Investigating aerosol–cloud interactions

Benjamin Stephen Grandey

Submitted for the degree of Doctor of Philosophy in Physics
Michaelmas Term 2011

Atmospheric, Oceanic and Planetary Physics
Department of Physics
University of Oxford

Investigating aerosol–cloud interactions

Benjamin Stephen Grandey, St John's College
Submitted for the degree of Doctor of Philosophy in Physics, Michaelmas Term 2011

Abstract

Microphysical and dynamical interactions between aerosols and clouds are associated with some of the largest uncertainties in projections of future climate. Many possible aerosol effects on clouds have been suggested, but large uncertainties remain. In order to improve model projections of future climate, it is essential that we improve our quantitative understanding of anthropogenic aerosol effects. Several studies investigating interactions between satellite-observed aerosol and cloud properties have been published in recent years. However, the observed relationships are not necessarily due to aerosol effects on clouds. They may be due to cloud and precipitation effects on aerosol, meteorological covariation, observational data errors or methodological errors. An analysis of methodological errors arising through climatological spatial gradients is performed. For region sizes larger than $4^\circ \times 4^\circ$, commonly used in the literature, spurious spatial variations in retrieved cloud and aerosol properties are found to introduce widespread significant errors to calculations of aerosol–cloud relationships. Small scale analysis prior to error-weighted aggregation to larger region sizes is recommended. Appropriate ways of quantifying relationships between aerosol optical depth (τ) and cloud properties are considered, and results are presented for three satellite datasets. There is much disagreement in observed relationships between τ and liquid cloud droplet number concentration and between τ and liquid cloud droplet effective radius, particularly over land. However, all three satellite datasets are in agreement about strong positive relationships between τ and cloud top height and between τ and cloud fraction (f_c). Using reanalysis τ data, which are less affected by retrieval artifacts, it is suggested that a large part of the observed f_c–τ signal may be due to cloud contamination of τ. General circulation model simulations further demonstrate that positive f_c–τ relationships may primarily arise due to covariation with relative humidity, and that negative f_c–τ relationships may arise due to scavenging of aerosol by precipitation. A new method of investigating the contribution of meteorological covariation to the observed relationships is introduced. Extratropical cyclone storm-centric composites of retrieved aerosol and cloud properties are investigated. A storm-centric description of the synoptics is found to be capable of explaining spurious f_c–τ relationships, although the spurious relationships explained are considerably smaller than observed relationships.

Acknowledgements

Many people have contributed to the work of this thesis, both directly, by providing specific input, and indirectly, by supporting me. Although not everyone can be mentioned here, I would like to name and thank a few people individually.

I would like to start by thanking **Philip Stier** who has provided extensive supervision support over the last three years (and previously, during my Masters project). Philip has gone out of his way to teach me about good research practice and creative thinking. He is an inspiring mentor. Many thanks are also due to **Till Wagner** and **Don Grainger** for acting as informal supervisors, providing much valuable input.

I would also like to thank **Johannes Quaas** and **Stefan Kinne** for the useful email conversations and for hosting me for a visit to the Max Planck Institute for Meteorology in Hamburg. **Kevin Hodges** has provided much assistance with configuring and running TRACK, his storm-tracking program. In addition to many conversations (and departmental doughnuts!), **Chris Arnold** kindly produced some AATSR data files for me.

Rosalind West and **Zak Kipling** have been wonderful office mates. In addition to countless helpful conversations, Rosalind has proof-read most of this thesis, while Zak has always been willing to share from his incredible source of computing knowledge.

Much of my learning in atmospheric physics has come from educational conversations with many people. In addition to those mentioned above, I would like to thank **Ed Gryspeerdt** and **Andy Sayer**.

The staff in AOPP perform valuable work. Special thanks are due to **Sarah Harrington**. Thanks also to **Monika Porada**, **Lucy Li**, **Russell Jones** and **Mark Munro**.

I have enjoyed many lunch breaks over the years with friends from AOPP. Recent lunches with **Jaemin Lee**, **Xiaoming Zhai** and **Luis Guanter** have been particularly fun and helpful for me during this taxing writing period.

Over the years I have been blessed by the pastoral support and prayers of friends including **Ramin Lolachi** and **Jo Eberhardt** (formerly Barstow) in AOPP. Jo also proof-read some of this thesis.

I am thankful for having had supportive housemates over the last two and a half years. Particular mention should go to **Wilson Ong**, who often went out of his way to cook for me in September, and to **Stephen Hibbs**, **Tim Kovoor** and **Jeremy Moses**, who have been brothers of encouragement to me.

I am very blessed to have been given a generous, loving and supportive fiancée, who has shown great patience when I have been tired and discouraged recently. I am looking forward with hope to being able to join **Ailene Chou** in Singapore in the near future. She has provided the main inspiration for me to strive to complete this DPhil as early as possible.

My parents, **Michael Grandey** and **Elisabeth Grandey**, and sister, **Rachel Grandey**, have all shown steadfast love and support over the years. I am thankful to have been blessed with such an amazing family.

Finally, I would like to thank the One to whom all thanks is due: my Creator, the Father of my Lord and Saviour Jesus Christ.

Benjamin Grandey, October 2011, Oxford

Contents

List of Figures

List of Tables

Chapter 1

Introduction

1.1 Aerosols, clouds and climate

1.1.1 Atmospheric aerosols and cloud droplets

Atmospheric *aerosols* are solid or liquid particles suspended in the atmosphere, with diameters generally between a few nanometers and a few micrometers (Seinfeld and Pandis, 1998). The Earth's atmosphere contains many different kinds of aerosols, of both anthropogenic and natural origin. Particular categories of aerosol which are considered to play an important role with regard to climate are sulphate, organic carbon, black carbon, nitrate, mineral dust and sea-salt aerosols (e.g., Haywood and Boucher, 2000).

1.1.2 Direct and indirect aerosol effects on climate

The optical and microphysical properties of aerosols may give rise to several radiative effects in the Earth's atmosphere. Figure 1.1 contains a schematic illustrating some of these potential effects.

The *direct aerosol effect* refers to scattering and absorption of shortwave and longwave radiation by atmospheric aerosols. The direct effect radiative perturbation due to a given aerosol is dependent on the vertical distribution of the aerosol, the *albedo* (reflectivity) of the Earth's surface beneath and any clouds present (e.g. Haywood and Shine, 1995; Stier et al., 2007). For example, for aerosols over a surface with a high albedo, such as snow or cloud, any absorption by the aerosol may dominate over scattering effects, leading to a net warming effect.

Heating due to the absorption of shortwave radiation by tropospheric aerosols can lead to in-

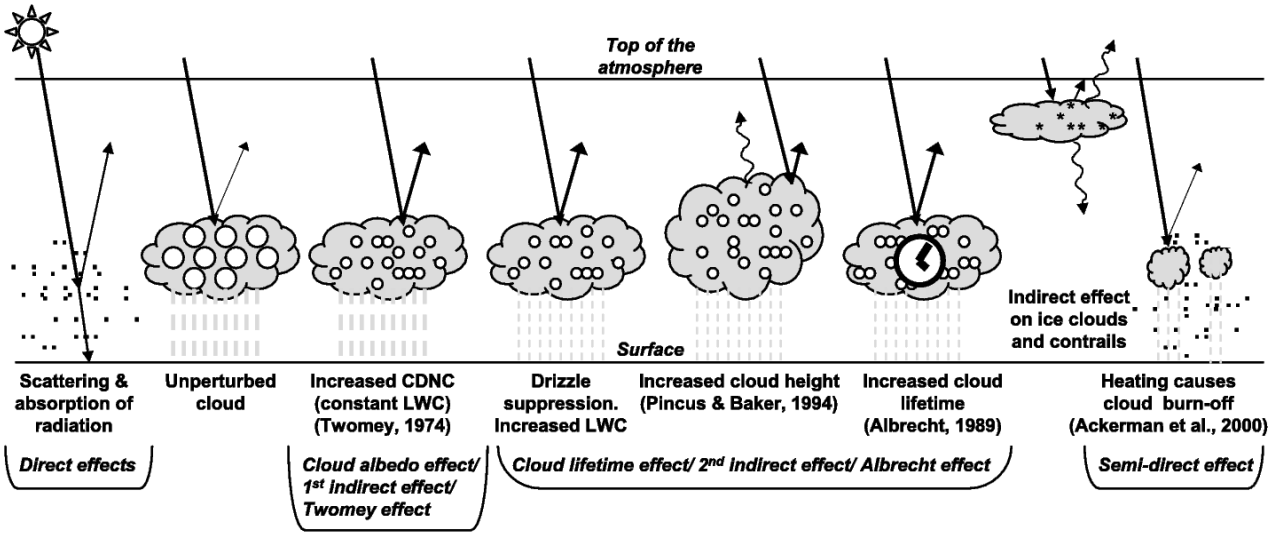

Figure 1.1: Schematic diagram showing the various radiative mechanisms associated with cloud effects that have been identified in relation to aerosols. The small black dots represent aerosol particles, the larger open circles cloud droplets. Straight lines represent the incident and reflected solar radiation, and wavy lines represent terrestrial radiation. The unperturbed cloud contains larger cloud drops because only natural aerosols are available as cloud condensation nuclei, while the perturbed cloud contains a greater number of smaller cloud drops because both natural and anthropogenic aerosols are available as cloud condensation nuclei. The vertical grey dashes represent rainfall, and LWC refers to liquid water content. [From Forster, P., Ramaswamy, V., Artaxo, P., Berntsen, T., Betts, R., Fahey, D. W., Haywood, J., Lean, J., Lowe, D. C., Myhre, G., Nganga, J., Prinn, R., Raga, G., Schultz, M., and Van Dorland, R.: Changes in Atmospheric Constituents and in Radiative Forcing. In: Climate Change 2007: The Physical Science Basis. Contribution of Working Group 1 to the Fourth Assessment Report of the Intergovernmental Panel on Climate Change, Cambridge University Press, 2007, Figure 2.10. Reproduced with permission from the IPCC.]

creased temperatures in the aerosol layer, decreasing relative humidity and changing tropospheric stability. This can significantly affect cloud lifetime, and is known as the *semi-direct aerosol effect*. For example, a modelling study showed that absorption of shortwave radiation by black carbon aerosol can lead to an enhanced daytime clearing of trade cumulus clouds over the northern Indian Ocean (Ackerman et al., 2000).

Indirect aerosol effects are the radiative effects which aerosols can have through microphysical interactions with clouds. Many aerosols are effective cloud condensation nuclei. A strong correlation between cloud condensation nuclei concentrations and aerosol optical depth has been observed (Andreae, 2009). Increasing the aerosol concentration in a cloud can lead to increased numbers of cloud condensation nuclei competing for water vapour which, in a cloud of constant liquid water content, in turn leads to a greater number of smaller droplets. This increases the albedo of the cloud, resulting in more shortwave radiation being reflected to space, and is referred to as the *cloud albedo effect* (Twomey, 1974, 1977). The decrease in droplet size may subsequently suppress precipitation.

The suppression of precipitation would enhance the retention of liquid water by the cloud, which may subsequently increase the lifetime of the cloud, an effect known as the *cloud lifetime effect* (Albrecht, 1989). The cloud top height can also be affected (Pincus and Baker, 1994). Other indirect effects have been suggested, such as the *glaciation indirect effect*, proposed by Lohmann (2002), whereby black carbon aerosols act as effective ice nuclei and can therefore enhance precipitation.

A complex interplay between different aerosol effects and feedbacks may exist in any given real-world situation. For example, Koren et al. (2008) propose that for clouds in smoky conditions over the Amazon, microphysical (indirect) aerosol effects dominate for low aerosol conditions and radiative (semi-direct) aerosol effects on the clouds dominate in high aerosol conditions.

It is worth noting that most aerosols have a much shorter lifetime than greenhouse gases, and so have a much stronger regional distribution and remain in the atmosphere for a much shorter period of time. Since many aerosol species can lead to health problems (see e.g. Bell et al., 2004; Kennedy, 2007), increasingly cleaner technologies are being employed in order to decrease aerosol emissions. Indeed, European emissions of sulphur have decreased by 70 % since 1980, and European emissions of oxides of nitrogen have decreased by 25–30 %, although emissions are currently increasing in developing regions (Grennfelt and Hov, 2005). As aerosol precursor emissions stabilise and then decrease, the atmospheric concentration of aerosols is also likely to stabilise and then decrease, due to their short lifetime. Under these conditions, future warming due to the increasing greenhouse gas concentrations will increasingly dominate over aerosol radiative effects (Andreae et al., 2005; Kiehl, 2007). Uncertainties in the size of aerosol radiative effects lead to uncertainties in the sensitivity of the climate's response to greenhouse gas forcing, because aerosol effects may currently offset much of the warming due to greenhouse gases. In order to accurately forecast future warming trends, it is therefore important to quantify the significance of aerosol effects in the present, and to reduce the large uncertainty in the radiative forcing due to aerosols.

1.1.3 Radiative forcing, climate feedbacks and projection uncertainties

Radiative forcing due to a change in an external driver of climate change is defined as "the change in net (down minus up) irradiance (solar plus longwave; in Wm^{-2}) at the tropopause after allowing for stratospheric temperatures to readjust to radiative equilibrium, but with surface and tropospheric temperatures and state held fixed at unperturbed values" (Forster et al., 2007). Positive radiative forcings

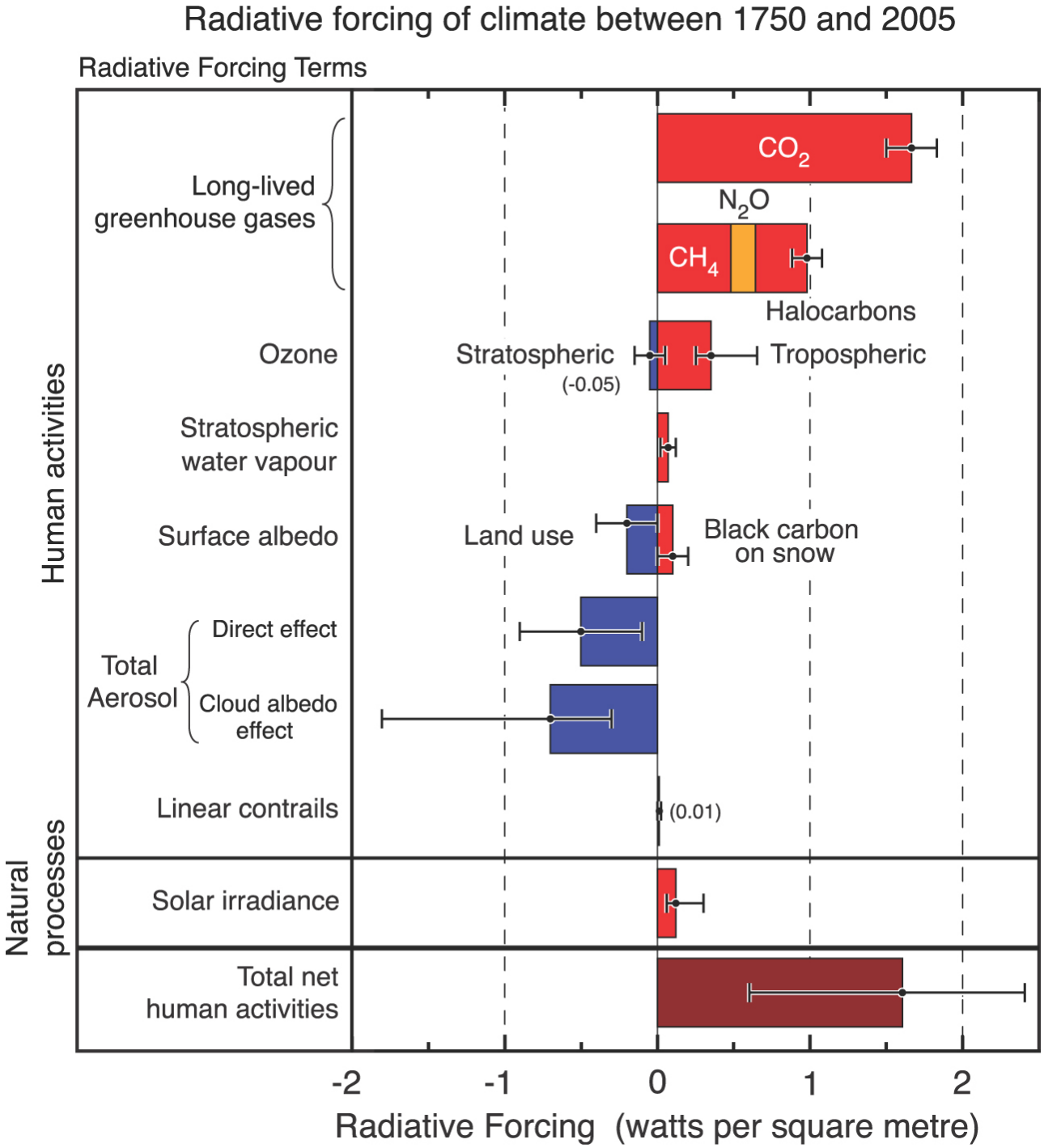

Figure 1.2: Summary of the principal components of the radiative forcing of climate change. The values represent the forcings in 2005 relative to the start of the industrial era (about 1750). Human activities cause significant changes in long-lived gases, ozone, water vapour, surface albedo, aerosols and contrails. The only increase in natural forcing of any significance between 1750 and 2005 occurred in solar irradiance. The thin black line attached to each coloured bar represents the range of uncertainty for the respective value. [From Forster, P., Ramaswamy, V., Artaxo, P., Berntsen, T., Betts, R., Fahey, D. W., Haywood, J., Lean, J., Lowe, D. C., Myhre, G., Nganga, J., Prinn, R., Raga, G., Schultz, M., and Van Dorland, R.: Changes in Atmospheric Constituents and in Radiative Forcing. In: Climate Change 2007: The Physical Science Basis. Contribution of Working Group 1 to the Fourth Assessment Report of the Intergovernmental Panel on Climate Change, Cambridge University Press, 2007, FAQ 2.1 Figure 2. Reproduced with permission from the IPCC.]

lead to a warming of the climate system. Significant forcings regularly considered in attribution studies are those caused by changes in the solar constant, greenhouse gas concentrations, tropospheric sulphate aerosols and stratospheric volcanic aerosols (e.g. Stone et al., 2007). It is worth noting that radiative forcing generally refers to the radiative effect of an anthropogenic driver or another external driver, such as solar irradiance changes, between pre-industrial times and the present day. Natural aerosol, such as sea-salt and mineral dust, may exert a radiative effect on the climate system but this would not generally be considered a radiative forcing. Figure 1.2 summarises the climatic radiative forcing components identified by Forster et al. (2007).

Many mechanisms act either to intensify or to oppose changes in the climate system. These effects are known as *climate feedbacks*. For example, if a surface-air temperature increase in polar regions reduces snow cover, the surface albedo will be reduced and less solar radiation will be reflected, creating a positive feedback mechanism leading to a greater warming in these regions. Other major climate feedbacks are those associated with clouds, water vapour, the lapse rate and the cryosphere (Bony et al., 2006).

Climate feedbacks determine the *climate response* to a given radiative forcing, as the climate system readjusts to radiative equilibrium. Early climate model studies suggested a linear relationship between equilibrium surface temperature change (ΔT) and radiative forcing (ΔF):

$$\Delta T = \lambda \Delta F \tag{1.1}$$

where λ is the *climate sensitivity parameter* (Rotstayn and Penner, 2001). Although λ is generally considered to be independent of the specific forcing mechanism, it may not be completely independent (Hansen and Nazarenko, 2004). Further discussion about the use of radiative forcing, particularly in relation to aerosol indirect effects, is provided by Haywood et al. (2009).

As shown in Figure 1.2, Forster et al. (2007) estimate an aerosol direct effect radiative forcing of -0.5 [-0.9 to -0.1] Wm^{-2} and a cloud albedo effect of -0.7 [-1.8 to -0.3] Wm^{-2}. Due to their interaction with the hydrological cycle, the other indirect effects and semi-direct effect are not considered as radiative forcings by Forster et al. (2007). However, Lohmann and Feichter (2005) estimate an effective cloud lifetime effect radiative forcing of -1.2 [-1.9 to -0.5] Wm^{-2}, leading to a total net anthropogenic radiative forcing of 0.4 [-0.3 to 2.4] Wm^{-2}. As can be seen, there is a large uncertainty in the total anthropogenic radiative forcing, and most of this uncertainty is due to

uncertainties in the size of aerosol effects.

1.2 Observational tools

Observations play an integral role in helping us to improve our understanding of the highly complex processes which occur in the atmosphere. They often highlight new avenues for investigation, form the basis for scientific hypotheses, and act as the plumb line by which theories must be assessed. As the physicist Richard Feynman famously said, "if it disagrees with experiment it is wrong" (Feynman, 2007). This applies as much to atmospheric science as it does to fundamental physics. Observations help scientific research to remain rooted in reality.

Many observational datasets of the atmosphere exist. Some are produced using in situ surface, ship and aircraft measurements, such as those gathered during the Variability of the American Monsoon System (VAMOS) Ocean–Cloud–Atmosphere–Land Study Regional Experiment (VOCALS-REx) field campaign (Wood et al., 2007). Other datasets contain data that have been remotely sensed from the surface, such as the aerosol data retrieved from the AErosol RObotic NETwork (AERONET) (Holben et al., 1998). Observational datasets retrieved from satellite data provide aerosol and cloud data over large regional and global scales. These satellite datasets are widely used for aerosol–cloud interaction studies.

1.2.1 Satellite platforms

Terra

Terra, also known as Earth Observing System (EOS) AM-1, was launched on 18th December 1999 and acts as a platform for a number of instruments: ASTER (Advanced Spaceborne Thermal Emission and Reflection Radiometer), CERES (Clouds and Earth's Radiant Energy System), MISR (Multiangle Imaging SpectroRadiometer), MODIS (MODerate resolution Imaging Spectroradiometer) and MOPITT (Measurements Of Pollution In The Troposphere) (NASA, 2009b). It is in a sun-synchronous orbit with a 10:30 A.M. equatorial crossing time (Kaufman et al., 1998).

Envisat

Envisat, launched in March 2002, is in a sun-synchronous orbit with a southwards equatorial crossing time of 10:00 A.M. (ESA, 2009). It carries ASAR (Advanced Synthetic Aperture Radar), MERIS (Medium Resolution Imaging Spectrometer), AATSR (Advanced-Along Track Scanning Radiometer), RA-2 (Radar Altimeter 2), GOMOS (a medium resolution spectrometer), MIPAS (Michelson Interferometer for Passive Atmospheric Sounding), SCIAMACHY (an imaging spectrometer), DORIS (Doppler Orbitography and Radio-positioning Integrated by Satellite) and LRR (Laser Retro-Reflector).

Aqua

Aqua, sometimes referred to by the pre-launch name EOS PM-1, was launched on 4th May 2002 (Parkinson, 2003). Like Terra, it has CERES and MODIS instruments onboard, in addition to AIRS (Atmospheric Infrared Sounder), AMSR-E (Advanced Microwave Scanning Radiometer for the Earth Observing System), AMSU-A (Advanced Microwave Sounding Unit-A) and HSB (Humidity Sounder for Brazil). Aqua flies in a sun-synchronous orbit with a northwards equatorial crossing time of 1:30 P.M.. It is the first member, with respect to both launch date and orbital position, of the afternoon A-Train constellation of satellites (Figure 1.3). These satellites fly in close formation, so there is potential to combine data from different instruments in order to produce improved data products (e.g. Jeong and Hsu, 2008).

PARASOL

Another member of the A-train, Polarization and Anisotropy of Reflectances for Atmospheric Sciences coupled with Observations from a Lidar (PARASOL), was launched on 18th December 2004 (CNES, 2009b). It carries a POLDER (POLarization and Directionality of the Earth's Reflectances) instrument.

CloudSat

CloudSat, also part of the A-Train, was launched on 28th April 2006, and carries the first satellite Cloud Profiling Radar (CPR) (Colorado State University, 2009).

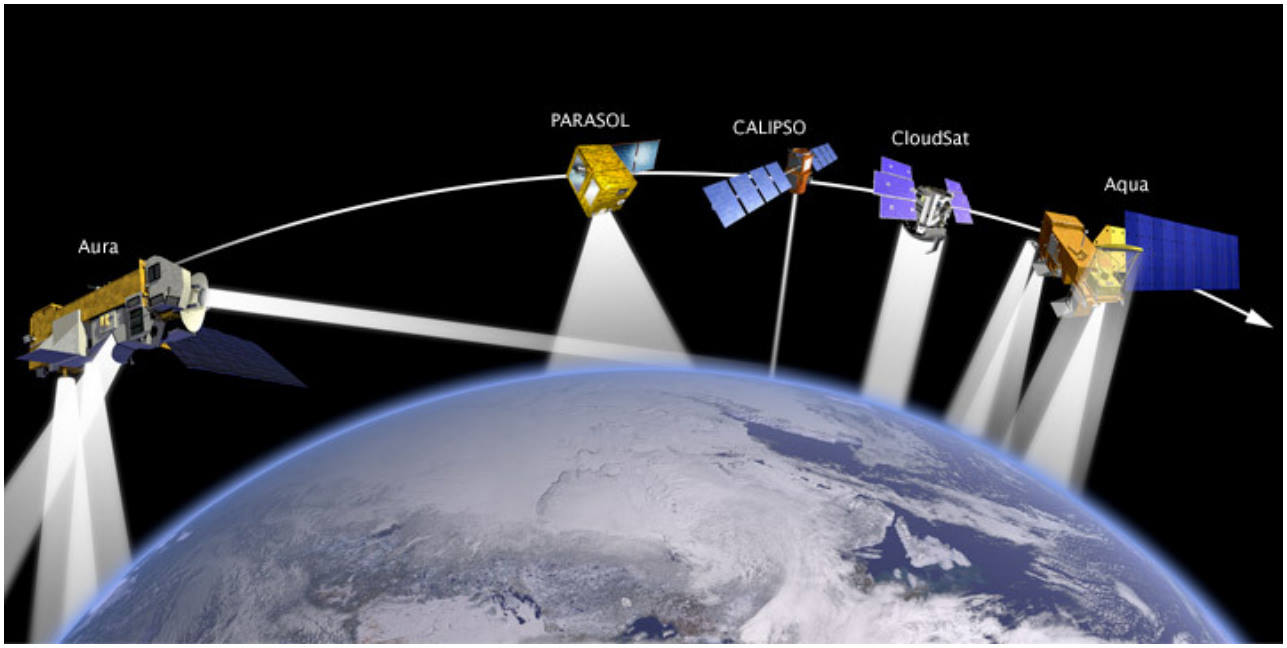

Figure 1.3: A graphic depicting the satellites that make up the A-train. [Graphic taken from NASA, 2010.]

CALIPSO

The Cloud–Aerosol Lidar and Infrared Pathfinder Satellite Observation (CALIPSO) satellite, another part of the A-Train, was also launched on 28th April 2006 (CNES, 2009a). The payload consists of CALIOP (Cloud-Aerosol LIdar with Orthogonal Polarization), IRR (Imaging Infrared Radiometer) and WFC (Wide Field Camera), all co-aligned (NASA, 2009a).

1.2.2 Satellite instrumentation

ATSR, ATSR-2 and AATSR

The Along-Track Scanning Radiometer (ATSR) was launched on ERS-1; ATSR-2 is on ERS-2; the Advanced Along-Track Scanning Radiometer (AATSR) is on Envisat (RAL, 2003). The primary purpose of ATSR is to measure sea-surface temperatures (Mutlow, 1993). However, aerosol and cloud retrievals also exist for these satellites (University of Oxford, 2009b).

MODIS

The MODerate resolution Imaging Spectroradiometer (MODIS) has 36 bands in the visible and infrared, with nadir resolutions of 250–1000 m, and has a cross track swath width of 2330 km (Barnes et al., 1998). There are MODIS instruments on both Terra and Aqua. They provide complete global

coverage every 1–2 days (NASA, 2009f). Terra-MODIS data from 24th February 2000 – present and Aqua-MODIS data from 3rd July 2002 – present are available (NASA, 2009c). MODIS atmospheric data products include aerosol and cloud properties, as well as water vapour (NASA, 2009e). MODIS also provides land data, such as vegetation indices (Huete et al., 2002), and ocean data, such as chlorophyll concentration (Esaias et al., 1998).

MISR

The Multi-angle Imaging SpectroRadiometer (MISR), on Terra, images the Earth in nine different view directions (Diner et al., 1998). It can provide cloud height data, in addition to other cloud and aerosol properties (NASA, 2009d). The swath width is 360 km.

POLDER-1, POLDER-2 and PARASOL

The POLarization and Directionality of the Earth's Reflectances (POLDER) instrument, designed to measure polarized and directional reflected solar radiation, has a swath width of approximately 2200 km and a resolution of 6×7 km^2 (Deschamps et al., 1994). Measuring polarized and directional reflectances allows it to differentiate between radiation scattered in the atmosphere and that reflected by the Earth's surface, allowing improved observations of clouds, aerosols, the land surface and oceans (CNES, 2009c). Data are available from three POLDER instruments: POLDER-1, on ADEOS-1, from November 1996 – June 1997; POLDER-2, on ADEOS-2, from April 2003 – October 2003; the third POLDER instrument, on PARASOL, from December 2004 onwards (Université Lille 1, 2009). PARASOL is intended to observe clouds and aerosols (CNES, 2009b).

CloudSat CPR

The CloudSat Cloud Profiling Radar (CPR) operates at 94-GHz (3 mm wavelength), has a horizontal footprint of 1.4 km $\times$ 3.5 km and has a vertical resolution of 250 m (Posselt et al., 2008). It measures several cloud parameters, and a cloud classification product is available.

CALIOP

The Cloud-Aerosol LIdar with Orthogonal Polarization (CALIOP), on CALIPSO, has been producing cloud and aerosol data since 2006, much of which has a horizontal resolution of 330 m and a

vertical resolution of 30–60 m (Winker et al., 2007).

1.2.3 Assessment of using satellite data for aerosol-cloud studies

In comparison to field campaigns, which provide datasets limited in both spatial and temporal extent, satellite sensors can provide global datasets extending over several years. Although AERONET releases aerosol data retrieved at many locations on Earth, the coverage is severely limited compared with that of many satellite datasets. The large datasets offered by satellite instruments are invaluable for statistical studies of the atmosphere and the processes which occur there.

However, satellites have a number of limitations. Cloud profiling radars, such as that onboard CloudSat, and lidars, such as CALIOP, can provide vertically resolved cloud and aerosol data, but they resolve only one horizontal dimension; radiometers, such as MODIS, often have large two-dimensional horizontal coverage but generally have no vertical resolution when retrieving aerosol and cloud properties. One limitation of particular interest here is that radiometers cannot retrieve both aerosol and cloud properties simultaneously: if a pixel is identified as cloudy, a cloud retrieval will be attempted; if a pixel is identified as cloud-free, an aerosol retrieval will be attempted. So radiometer retrieved aerosol and cloud properties are rarely completely co-located horizontally[1]. Also, radiometer products rarely allow vertical co-location to be tested: retrieved cloud properties are often that of the top of the highest layer of cloud and may not be representative of cloud below; retrieved aerosol properties are often column averages or totals and do not provide information on the location of the aerosol, which may be in defined layers.

Satellite data have the potential to provide an observational top-down constraint on relationships between aerosol and cloud properties. However, if taken in isolation of model data, they do not readily lend themselves to bottom-up process-based investigation. A discussion of modelling tools is provided in Section 1.3.

1.2.4 Choice of satellite data

For large-scale statistical studies of aerosols and clouds, datasets providing extensive horizontal coverage are highly desirable. Several satellite radiometers fulfill this criterion.

[1] By using PARASOL data together with other data from the A-train, Waquet et al. (2009) have demonstrated that it may sometimes be possible to retrieve properties of aerosols above clouds.

MODIS

MODIS data are available at two overpass times (Terra 10:30 A.M.; Aqua 1:30 P.M.), the data cover several years, the spatial resolution is high and the swath is wide compared to many radiometers. MODIS aerosol and cloud products have undergone several validation and comparison studies (e.g. Remer et al., 2005; Wu et al., 2009), and these products are commonly used in aerosol–cloud interaction studies (see Section 1.4). MODIS data are therefore used extensively in this research.

Due to the longer available time period, Terra-MODIS data are used in Chapter 2. However, in order to match the overpass time sampling of the model data used in Chapter 3, the results presented in Chapters 3–6 use Aqua-MODIS data. Although it is not of direct relevance to the current work, it is worth noting that data from other A-Train instruments could readily be used in combination with Aqua-MODIS data in future projects. The choice between Terra and Aqua for the MODIS data in this thesis should make little difference to the presented results. Although one published study has sought to take advantage of the overpass time differences between Aqua-MODIS and Terra-MODIS (Meskhidze et al., 2009), the differences between the datasets are generally quite small.

Several official MODIS Science Team Atmosphere irregularly gridded level 2 retrieved datasets are available (NASA, 2009e,c). In Chapters 5 and 6, retrieved aerosol and cloud properties from the MODIS Science Team Atmosphere Collection 5 Level 2 Joint Product are used (Remer et al., 2005; Platnick et al., 2003). The aerosol data are provided at approximately 10 km $\times$ 10 km and the cloud data at 5 km $\times$ 5 km on an irregular instrument grid. As will be explained in Chapters 5 and 6, these data will be regridded to a coordinate system centred on extratropical cyclones.

Regularly gridded $1^\circ \times 1^\circ$ level 3 daily and monthly averaged versions of these aerosol and cloud data are also available (Hubanks et al., 2008). In Chapters 2 and 3, MODIS Science Team Atmosphere Collection 5 level 3 daily data are used. The advantage of the regular grid is that data for large regions and time periods can be analysed much faster than when using considerably larger volumes of higher resolution irregularly gridded level 2 data. It is commonly assumed that level 3 aerosol and cloud data for a given day and $1^\circ \times 1^\circ$ grid box can be assumed to be co-located, since aerosol properties far away from sources have significant autocorrelations at scales of order 1° and one day (Anderson et al., 2003). This assumption of co-location is used here.

In addition to the MODIS Science Team data mentioned above, an independent cloud retrieval from the MODIS radiances has been produced by the CERES Team (Minnis et al., 2004). These

CERES Team cloud data are released with MODIS Science Team Collection 4 aerosol data as part of the CERES Single Scanner Footprint (SSF) Aqua and Terra level 2 products (NASA, 2011b). Much of these data have been gridded to 2.5° × 2.5° daily level 3 data by Johannes Quaas (Quaas et al., 2009). Some of these level 3 data are used in Chapter 3.

AATSR

The Global Retrieval of ATSR cloud Parameters and Evaluation (GRAPE) project (University of Oxford, 2009a) is developing a retrieval scheme capable of retrieving aerosol and cloud parameters from ATSR, ATSR-2 and AATSR data (Oxford-RAL Retrieval of Aerosols and Clouds, ORAC University of Oxford, 2009b). Much of the retrieved aerosol data have been released as part of the GlobAEROSOL project (Thomas et al., 2009). One distinguishing feature of the ORAC aerosol retrieval is that it uses a wind speed dependent sea-surface reflectance model (Sayer et al., 2010a). GlobAEROSOL level 2 data are used alongside MODIS Science Team level 2 aerosol data in Chapter 5 as an independent dataset. These GlobAEROSOL level 2 aerosol data are provided at approximately 10 km × 10 km resolution on a sinusoidal grid.

In order to provide another satellite dataset independent of the MODIS Science Team and MODIS CERES Team level 3 data, daily level 3 GlobAEROSOL and ORAC cloud data are used in Chapter 3. The ORAC level 3 daily cloud data have been gridded by Chris Arnold[2].

1.2.5 Retrieved aerosol and cloud properties

Satellite radiometers observe radiances (or reflectances) over different wavelength bands. Retrievals use inverse methods in an attempt to estimate physical properties of a scene using one or more of the observed radiances. This normally involves simplified forward models which are used to create lookup tables of the radiances which would be observed for a certain combination of physical properties, such as liquid cloud droplet effective radius (r_e) and cloud optical depth (τ_c; see section on cloud properties below). Some optimal estimation retrievals, such as ORAC mentioned above, incorporate prior estimates of the physical properties using Bayes' theorem.

One example of a retrieval scheme is the MODIS Science Team cloud retrieval of optical and microphysical properties described by Platnick et al. (2003). Overcast pixels with accompanying

[2]Chris Arnold, Atmospheric, Oceanic and Planetary Physics, Department of Physics, University of Oxford.

thermodynamic phases are identified using a decision tree of cloud mask tests, infrared radiances, near-infrared radiances and retrieved cloud top temperature data. For example, if a pixel is identified as being overcast with liquid cloud, then a joint retieval of r_e and τ_c is subsequently attempted. The retrieval uses two wavelength bands: a water-absorbing band (1.6, 2.1 or $3.7\,\mu$m), which is most sensitive to particle size; and a non-absorbing band ($0.86\,\mu$m over ocean, $0.65\,\mu$m over land and $1.2\,\mu$m over ice/snow), which is most sensitive to cloud optical depth. The retrieval scheme includes atmospheric corrections for the radiances and uses surface albedo information. The forward model assumes a single plane-parallel cloud layer.

Many aerosol and cloud properties are retrieved using radiometer data. Generally, each pixel is either flagged as cloudy or cloud-free. If a pixel is flagged as cloudy, then a cloud retrieval may be attempted; if it is cloud-free, then an aerosol retrieval may be attempted. Some of the commonly retrieved properties which are of particular interest when investigating aerosol–cloud interactions are described below.

Aerosol properties

Aerosol optical depth (τ) is the total extinction at a given wavelength due to aerosol in an atmospheric column. The τ data used in this project have been retrieved at a wavelength of 550 nm. If a pixel with thin or broken cloud is mistakenly flagged as cloud-free, cloud contamination of the aerosol retrieval may occur, leading to an overestimation of τ. Using MODIS, CALIPSO, AERONET and Micro-Pulse Lidar Network data, Huang et al. (2011) observed cirrus contamination of τ over South-East Asia. Also, three-dimensional (3D) scattering of light from nearby clouds may also cause unreliably high τ to be retrieved (Várnai and Marshak, 2009). A strong correlation between cloud condensation nuclei concentration and aerosol optical depth τ has been observed (Andreae, 2009). This suggests that τ can be used as a proxy for cloud condensation nuclei concentration.

Aerosol extinction, and hence also τ, often varies with wavelength λ as $\lambda^{-\alpha}$, where α is the *Ångström exponent* (Seinfeld and Pandis, 1998). Therefore, α can be calculated as

$$\alpha = -\frac{\ln \frac{\tau_1}{\tau_2}}{\ln \frac{\lambda_1}{\lambda_2}} \tag{1.2}$$

where τ_1 and τ_2 are the aerosol optical depths retrieved at two different wavelengths λ_1 and λ_2 (Ignatov et al., 1998). The Ångström exponent α is a good indicator of the size of the aerosol

particles, with larger α corresponding to smaller particles (NASA, 2011a).

Another indicator of aerosol size which is sometimes retrieved is the aerosol *fine-mode fraction* (η), defined as the fraction of the total τ for which fine-mode aerosol is responsible (Remer et al., 2005). Larger values of η correspond to a greater proportion of small particles.

Although not a directly-retrieved quantity, *aerosol index* (AI) is often defined as

$$AI = \tau\,\alpha \tag{1.3}$$

(e.g. Suzuki et al., 2008). Like τ, AI is a measure of aerosol load in an atmospheric column. Since the size of the aerosol particles is taken into account via α, AI may provide a better measure of aerosol number burden than τ does (Nakajima et al., 2001). AI is therefore sometimes used as an alternative proxy for cloud condensation nuclei concentration in aerosol–cloud interaction studies (e.g. Bréon et al., 2002; Suzuki et al., 2008; Sorooshian et al., 2009, 2010).

Cloud properties

Liquid cloud droplet effective radius (r_e) is defined as

$$r_e = \frac{\int_0^\infty r\,\pi\,r^2\,n(r)\,\mathrm{d}r}{\int_0^\infty \pi\,r^2\,n(r)\,\mathrm{d}r} = \frac{\int_0^\infty r^3\,n(r)\,\mathrm{d}r}{\int_0^\infty r^2\,n(r)\,\mathrm{d}r} \tag{1.4}$$

where r is liquid cloud droplet radius and $n(r)$ is the cloud droplet size distribution (Hansen and Travis, 1974; Nakajima and King, 1990). Retrieved r_e provides an estimate of the size of the droplets near the top of liquid water clouds. Thin clouds are more likely to have unreliable r_e measurements, and the retrieval may be less reliable when $r_e < 4\,\mu\mathrm{m}$ (Nakajima and King, 1990). Retrievals of r_e generally assume plane-parallel clouds, so are likely to be more reliable for stratus and stratocumulus cloud fields than they are for broken cloud fields with more complicated 3-D geometry (Marshak et al., 2006; Vant-Hull et al., 2007). Drizzle may also affect r_e retrievals, although this effect appears to be smaller than 3-D effects (Zinner et al., 2010). Absorbing aerosol layers above cloud may lead to biases in retrieved r_e (Haywood et al., 2004). Retrieved r_e can be dependent on the wavelengths used (Platnick, 2000; Zinner et al., 2010). Bréon and Doutriaux-Boucher (2005) find a poor correlation between MODIS and POLDER r_e over land, with a better correlation over ocean, although MODIS r_e is generally higher.

Liquid water path (w) is the total mass of liquid water in an atmospheric column. Assuming vertically homogeneous r_e, the MODIS retrieval calculates w as

$$w = \frac{2}{3} \rho_l \tau_c r_e \tag{1.5}$$

where τ_c is the liquid cloud optical depth (see below) and ρ_l is the density of liquid water (Platnick, 2000). If linear growth of r_e with height and constant cloud droplet number concentration are assumed (see discussion of liquid cloud droplet number concentration below), then an adiabatic correction should be applied (Wood and Hartmann, 2006):

$$w = \frac{5}{9} \rho_l \tau_c r_e. \tag{1.6}$$

Due to the linearity with r_e, much of the discussion of the reliability of r_e above also applies here. Seethala and Horváth (2010) found that adiabatically corrected MODIS r_e agreed well with Advanced Microwave Scanning Radiometer-EOS (AMSR-E) w for scenes with a high cloud fraction. However, disagreement was found in broken cloud scenes, most likely due to 3-D effects.

Cloud optical depth (τ_c) is the total extinction at a given wavelength due to cloud water (liquid, ice or both) in an atmospheric column (Platnick et al., 2003). Retrievals of τ_c may also be susceptible to 3-D effects and sub-pixel heterogeneity (Várnai and Marshak, 2002). However, much of the bias is cancelled when averaging over 50 km $\times$ 50 km areas, although some remains. Overlying absorbing aerosol layers may lead to low biases in retrieved τ_c (Haywood et al., 2004).

Cloud top pressure (p_{top}) is the average pressure at the top of all clouds (liquid and ice) in a given region. *Cloud top temperature* (T_{top}) is the average temperature at the top of all clouds (liquid and ice) in a given region. Both p_{top} and T_{top} are good indicators of cloud top height. The heights of many clouds are often slightly underestimated by radiometer retrievals, probably due to insufficient correction for cloud transparency (Minnis et al., 2011; Sayer et al., 2011).

Cloud fraction (f_c) is the total fractional cover of all clouds (liquid and ice) in a given region. It is often calculated by counting the proportion of cloudy pixels (Platnick et al., 2003). It is therefore dependent on resolution and cloud-flagging thresholds, making it difficult to compare absolute values of f_c between different datasets.

Liquid cloud droplet number concentration

Although not a directly-retrieved quantity, *liquid cloud droplet number concentration* (N_d) is sometimes estimated using the adiabatic approximation:

$$N_d = \gamma \, {\tau_c}^{\frac{1}{2}} \, {r_e}^{-\frac{5}{2}} \tag{1.7}$$

where $\gamma = 1.37 \times 10^{-5} \, \mathrm{m}^{-\frac{1}{2}}$ (Brenguier et al., 2000; Quaas et al., 2006) or $\gamma = 1.125 \times 10^{-5} \, \mathrm{m}^{-\frac{1}{2}}$ (Bennartz, 2007; George and Wood, 2010), depending on assumptions about constants relating to atmospheric conditions. A simplified derivation of this equation is provided in Appendix A. Four assumptions are made:

1. Liquid cloud water content, and hence mean liquid cloud droplet volume, both increase linearly with height above the cloud base. This assumption of adiabaticity requires an absence of both precipitation and entrainment. It has been observed to approximately hold for relatively thin non-precipitating marine stratocumulus clouds (Pawlowska and Brenguier, 2000; Zuidema et al., 2005). However, it is a far weaker assumption for many other types of clouds, including most continental clouds which are often subadiabatic (Kim et al., 2005).

2. Liquid cloud droplet number concentration is constant with height for any given cloud. In reality, entrainment and scavenging by drizzle may cause N_d to decrease with height (Pawlowska and Brenguier, 2000).

3. Cloud droplet size distributions are such that $r_e = \beta \, r_v$, where r_v is the mean volume radius (Equation A.2) and β is a constant which can be determined from in situ measurements (Martin et al., 1994). This relationship was derived for stratocumulus clouds with little entrainment. However, entrainment and scavenging by precipitation may not significantly affect the size distribution (Pawlowska and Brenguier, 2000). The results of Martin et al. (1994) give β values of 1.08 over ocean and 1.14 over land (Rotstayn and Liu, 2003). In reality, cloud droplet spectral dispersion and hence β may both increase with N_d, with values of β up to 1.6 being observed (Liu and Daum, 2002). It is worth noting that $\gamma \propto \beta^2$ (Equations 1.7 and A.11), so a 40% increase in β would lead to a doubling of N_d derived from Equation 1.7. However, Brenguier et al. (2011) find that although β can be highly variable, it does not appear to increase

with N_d.

4. Retrieved r_e is representative of the true r_e at the top of the cloud. A discussion about the reliability of satellite-retrieved r_e has already been provided above. It is worth noting that r_e is most reliable for homogeneous cloud fields, such as stratocumulus clouds.

It can be seen that Equation 1.7 is likely most suitable for non-precipitating stratocumulus cloud fields with little entrainment. It has been shown to be in good agreement with aircraft-measured N_d for stratocumulus clouds in the Southeast Pacific with cloud fractions greater than 0.8 (Bretherton et al., 2010). However, it may not be a good approximation for other cloud regimes. Further discussion about the validity of Equation 1.7 is provided elsewhere (e.g., Kubar et al., 2009).

The N_d data used in Chapters 2 and3 have been calculated by applying Equation (1.7) to retrieved liquid τ_c and r_e data. The Quaas et al. (2006) value of $\gamma = 1.37 \times 10^{-5}\,\mathrm{m}^{-\frac{1}{2}}$ is used. Following Quaas et al. (2006), clouds with $\tau_c < 4$ and $r_e < 4\,\mu\mathrm{m}$ are excluded when calculating N_d. Removing clouds with $\tau_c < 4$ implicitly removes clouds with small w in the calculation of N_d (Equation 1.5). For $r_e = 10\,\mu\mathrm{m}$, this corresponds to excluding clouds with $w < 27\,\mathrm{gm}^{-2}$.

It is worth noting that the first three assumptions stated above are also used in the majority of general circulation model (GCM) cloud microphysics parameterizations used for assessing the cloud albedo effect. Discussions of this are provided in Chen and Penner (2005) and Barahona and Nenes (2007). Converting from satellite-retrieved r_e to N_d using Equation 1.7 is effectively the inverse of how models convert N_d to r_e using the adiabatic approximation, although different constants may be used.

1.3 Modelling tools

1.3.1 General circulation models and parameterization uncertainties

Modern climate prediction, like weather forecasting, relies heavily on complex numerical models used to simulate the Earth's atmosphere-ocean system (Meehl et al., 2007). These so-called *general circulation models* (GCMs) contain either a dynamic ocean, a dynamic atmosphere or both coupled together. There are a number of state-of-the-art GCMs which are currently being used by different research facilities around the world (see e.g. Table 8.1 of Randall et al., 2007). Each model simulates

physical processes slightly differently.

Many physical processes, such as cloud formation, occur on scales too small to be resolved by GCMs, so these processes must be parameterized (e.g. Arakawa, 2004). There is a wide range of potentially valid parameter values that can be employed for a given GCM (Randall et al., 2007). One technique that is regularly used in probabilistic climate forecasting is to run an experiment using several different GCMs, generating a *multi-model ensemble* (e.g. Lambert and Boer, 2001). An alternative approach is to vary the values of parameters in a single model, testing different parameter combinations, generating a *perturbed physics ensemble* (e.g. Stainforth et al., 2005; Piani et al., 2005). Unfortunately, generating even modest-sized ensembles for a given experiment can be computationally expensive.

Climate*prediction*.net is a distributed computing project, using volunteers' computers distributed around the world to generate large perturbed physics ensembles for a number of climate experiments (Stainforth et al., 2002). Using climate*prediction*.net data, Sanderson et al. (2008b) find that the response to greenhouse-gas forcing is dependent on two climate feedbacks largely regulated by two parameters: the *entrainment coefficient*, associated with the cloud convection parametrization, and the *ice fall speed*, which affects cloud cover and humidity. Much of the variation in *climate sensitivity*, the equilibrium temperature response for a doubling of atmospheric carbon dioxide, also appears to be due to parameters associated with clouds (Sanderson et al., 2008a).

Bony and Dufresne (2005) demonstrate that marine boundary layer clouds are a dominant source of uncertainty in tropical cloud feedbacks in GCMs. A review by Stephens (2005) highlights that much of the uncertainty in model projections of climate change is due to cloud feedbacks in models. Much work needs to be done in order to improve cloud parameterizations in GCMs, and hence improve predictions of future climate.

1.3.2 Assessment of using general circulation models for aerosol–cloud studies

Many GCMs have aerosol and cloud modules which attempt to simulate aerosol indirect effects (Penner et al., 2006). Unlike the real atmosphere, aerosol emissions and hence concentrations can be artificially modified. Alternatively, it is often possible to switch GCM microphysics components on or off. This can allow the physical reasons for relationships between aerosol and cloud properties to be probed (e.g. Lohmann et al., 2006). Whereas satellite data can be used to provide a global

top-down constraint on relationships between aerosol and cloud properties, GCMs can provide a complementary bottom-up process-based investigation of these relationships, facilitating attribution of observed relationships to physical processes.

1.3.3 Cloud-resolving models and large-eddy simulations

Due to the computational expense of running simulations on a global scale, GCMs cannot normally be run at a high enough resolution to resolve cloud processes such as convection, so clouds must be parametrized in GCMs. However, numerical models have been designed to explicitly simulate individual clouds. Cloud-scale convection can be explicitly analysed and the effects of detailed microphysics schemes can be tested. Large-eddy simulations (LESs) are capable of resolving large-scale turbulence but require small-scale turbulence to be parametrized (Jacobson, 2005).

1.3.4 Choice of modelling tools

In order to investigate interactions between aerosol and cloud properties on a large global scale, GCM results, as opposed to cloud-resolving model results, are used alongside satellite data in this thesis. The modelling tools used are briefly described below.

AeroCom indirect effects experiment GCM data

Aerosol and cloud top data output from a number of different GCMs during the Aerosol Comparisons between Observations and Models (AeroCom) indirect effects intercomparison project (Quaas et al., 2009) are used in Chapter 3. The contributing atmospheric GCMs are as follows: four different versions of Community Atmosphere Model (CAM); the ECHAM5 GCM with the HAM aerosol scheme; the Geophysical Fluid Dynamics Laboratory (GFDL) GCM; the Goddard Institute for Space Studies (GISS) GCM; the Hadley Centre Global Environmental Model (HadGEM); the LMDZ GCM with the INCA aerosol scheme; the Spectral Radiation-Transport Model for Aerosol Species (SPRINTARS) model. The cloud albedo effect and the cloud lifetime effect on stratiform liquid clouds are parameterized. Aerosol effects on convection are not represented. Sea surface temperatures and sea-ice cover are prescribed. The data used in Chapter 3 are from simulations with year 2000 aerosol and precursor emissions and greenhouse gas concentrations. All data are provided at $2.5^\circ \times 2.5^\circ$ spatial resolution and daily temporal resolution. All data are sampled at local times near 1:30 P.M., matching

the overpass time of the Aqua satellite and hence the Aqua-MODIS instrument. The cloud data are sampled at cloud top, as viewed from above. Further details are provided in (Quaas et al., 2009). Only median results from this model ensemble are shown in Chapter 3.

ECMWF ERA-40 and ERA-Interim

The European Centre for Medium Range Weather Forecasts (ECMWF) provides global meteorological reanalysis (ERA) data (ECMWF, 2011a). Like weather forecast data, these data are output from a GCM. Observations have been assimilated in order to provide an optimal estimation of the state of the atmosphere at a given location and time. The ERA-40 project covers mid-1957 to 2001, while the more recent ERA-Interim project covers 1979 to mid-2011 (at the time of writing).

ERA-Interim zonal and meridional components of the 10-metre wind, mean sea level pressure and relative vorticity at 850 hPa are used in Chapters 5 and 6. ERA-Interim relative humidity at 850 hPa is also used in Chapter 5. ERA-40 data are used as the meteorological input for nudging ECHAM5 in Chapter 4.

MACC

The Monitoring Atmospheric Composition and Climate (MACC) project provides a reanalysis of many aerosol and chemistry properties (MACC, 2011). Aerosol optical depth is assimilated from satellite observations. As the time of writing, these data are currently available for 2003–2008 (ECMWF, 2011b). MACC reanalysis aerosol optical depth data are used alongside Aqua-MODIS data in Chapter 5.

ECHAM5-HAM

ECHAM5 is an atmospheric GCM primarily developed at the Max Planck Institute for Meteorology (Roeckner et al., 2003; Max Planck Institute for Meteorology, 2011). ECHAM5-HAM contains a aerosol model, HAM, which contains prognostic modal aerosol populations, size-distributions and compositions (Stier et al., 2005). Advanced aerosol microphysics for sulphate, black carbon, particulate organic matter, sea salt and mineral dust are represented in HAM. This aerosol model has been coupled to the cloud microphysics scheme in ECHAM5, allowing the cloud albedo and cloud lifetime aerosol effects to be represented (Lohmann et al., 2007). Two cloud cover schemes are available: the

Sundqvist scheme, parameterized using relative humidity as the only input (Sundqvist et al., 1989); and the statistical Tompkins scheme, which uses a prognostic probability density function of water vapour, considering processes such as convection, turbulence and microphysics (Tompkins, 2002). ECHAM5-HAM is used in Chapters 4 and 5.

1.4 Published aerosol–cloud interaction studies

Aerosol effects on clouds and their potential significance to the climate system are currently poorly understood, as shown in Section 1.1. Much work needs to be done in order to improve our understanding of these effects. Several studies investigating interactions between observed cloud and aerosol properties have been published in recent years. A brief survey of the findings of some of these studies, categorised according to potential aerosol–cloud interactions and implications, is provided below.

It is worth noting from the outset that an observed correlation between an aerosol property and a cloud property may not necessarily be due to aerosol effects on the cloud. We explore potential explanations for spurious correlations in Section 1.5.

1.4.1 Cloud albedo effect: Liquid cloud droplet number concentration and liquid cloud droplet effective radius

Theoretical considerations predict that, for constant liquid water path (w), the cloud albedo effect (E_r) with respect to liquid cloud droplet effective radius (r_e) can be written as

$$E_r = -\left.\frac{\partial \ln r_e}{\partial \ln \tau}\right|_w \tag{1.8}$$

where τ is the aerosol optical depth, assuming that τ is a suitable proxy for cloud condensation nuclei concentration (Feingold et al., 2001; Andreae, 2009). The requirement of constant w can be removed by instead considering the cloud albedo effect (E_N) with respect to cloud droplet number concentration (N_d) (Feingold et al., 2001; McComiskey et al., 2009)[3].

$$E_N = \frac{\mathrm{d} \ln N_d}{\mathrm{d} \ln \tau} = 3E_r. \tag{1.9}$$

[3]In fact, Equation 1.9 is more fundamentally related to the conceptual cloud albedo effect than Equation 1.8.

The cloud albedo effect predicts that higher cloud condensation nuclei concentrations should lead to higher N_d and, for clouds of constant w, smaller r_e. Since both τ and aerosol index (AI) may be suitable proxies for cloud condensation nuclei concentration, this suggests that higher τ or AI may lead to higher N_d and lower r_e.

Many observational studies looking at the cloud albedo effect have been published. Quaas et al. (2008) found that higher MODIS τ is generally associated with higher CERES SSF N_d for clouds with a liquid water path $w > 20\,\mathrm{gm}^{-2}$. Similarly, a surface remote sensing study has shown that, for stratus clouds off the Californian coast, a positive correlation between N_d and aerosol concentration exists (McComiskey et al., 2009). They consider different liquid water path (w) and spatial resolution constraints.

Using POLDER monthly data, Bréon et al. (2002) observed a negative correlation between r_e and aerosol index (AI). Selecting North Atlantic stratiform clouds, Kaufman et al. (2005) found a negative correlation between MODIS gridded daily τ and r_e. They performed a multiple regression analysis to investigate the contribution of meteorology to this observed relationship. Using ATSR-2 data for different regions and seasons, Bulgin et al. (2008) generally observed negative correlations between τ and r_e for clouds below 3 km, although positive correlations were also sometimes observed. Kiran et al. (2009) claimed that a decrease in r_e observed during break spells in the Indian monsoon is due to an increase in aerosol transport to the continental tropical convergence zone during the break spells. Using MODIS, AMSR-E and CERES data, Li et al. (2010) found a negative relationship between r_e and retrieved cloud condensation nuclei concentration for non-precipitating clouds in the presence of Saharan dust aerosol. The strength of this relationship increased when the data were further categorised by w. Yuan et al. (2011b) considered the special case of a Hawaiian volcano which released a steady plume of sulphur dioxide in 2008. Accounting for potential orographic effects, they found that an increase in sulphate aerosol appears to lead to a decrease in r_e.

Satellite-observed aerosol and cloud may have different vertical distributions and may not actually interact. Using CALIPSO vertical profile data, Costantino and Bréon (2010) found that a much stronger correlation between PARASOL r_e and MODIS AI exists for mixed aerosol–cloud cases than for non-mixed layers in the South-Eastern Atlantic stratocumulus region.

Aircraft in situ studies have the advantage that information about aerosol properties and cloud properties can be gathered at the same location both horizontally and vertically. Positive correlations

between aerosol concentration and N_d have been observed for stratocumulus clouds (e.g. Twohy et al., 2005; Lu et al., 2007). Berg et al. (2011) conducted a flight study near Oklahoma City. They used carbon monoxide (CO) concentration as a proxy for aerosol load. N_d was found to increase with both updraft velocity and CO concentration. r_e decreased with CO concentration.

Models are often used to complement observational data. Suzuki et al. (2008) showed that negative correlations exist between r_e and AI for different liquid water clouds in data produced by NICAM-SPRINTARS (Nonhydrostatic Icosahedral Atmospheric Model - Spectral Radiation-Transport Model for Aerosol Species), a global cloud resolving model with a horizontal resolution of 7 km coupled with an aerosol transport model. They showed that these findings are consistent with similar results observed in MODIS data. Menon et al. (2008) compared aerosol–cloud relationships observed in MODIS and CERES satellite data with those produced by the GISS (Goddard Institute for Space Studies) GCM. They ran three GCM simulations: one with no aerosol microphysical effects on clouds; one with aerosol microphysical effects on low-level liquid clouds; one with winds nudged to reanalysis data, in addition to the microphysical effects. They observed that r_e decreases with increasing τ in the satellite data. A similar relationship, although weaker, was present in the data from GCM runs which included aerosol–cloud microphysical effects. Quaas et al. (2009) showed that data from ten GCMs (Section 1.3.4 AeroCom) produced positive relationships between τ and N_d, in general agreement with satellite data.

1.4.2 Cloud lifetime effect: Liquid water path and total cloud fraction

Conceptually, the cloud lifetime effect predicts that, due to the suppression of precipitation, a positive correlation should exist between liquid water path (w) and τ. Increased cloud lifetime should also lead to a positive correlation between total cloud fraction (f_c) and τ. Although the cloud lifetime effect is also associated with suppression of precipitation and cloud height, these are discussed later.

Using MODIS gridded daily mean data, Koren et al. (2005) found a positive correlation between f_c and τ for convective clouds over the North Atlantic Ocean. Similarly, Kaufman et al. (2005) (Section 1.4.1) found a positive f_c–τ relationship for North Atlantic stratiform clouds. However, using the ECHAM4 GCM and running a simulation with aerosol microphysical effects on clouds switched off, Lohmann et al. (2006) demonstrated that much of this increase in f_c associated with high τ conditions is not due to aerosol indirect effects and may be due to dynamical effects. Furthermore,

Quaas et al. (2006) used ECHAM5-HAM to show that a large part of the f_c-τ relationship may be explainable by hygroscopic swelling of aerosols in high relative humidity condition (Section 1.5.3). The study by Menon et al. (2008) (Section 1.4.1) found that high τ conditions correspond to high f_c. However, the nudged GISS GCM simulation results suggested that much of this correspondence may be due to synoptic conditions. The Yuan et al. (2011b) study (Section 1.4.1) observed an increase in trade wind cumulus f_c with the presence of volcanic sulphate aerosol.

Surprisingly, the study by Suzuki et al. (2008) (see Section 1.4.1) suggested that w may decrease slightly with increasing AI, a relationship observed in both the MODIS and NICAM-SPRINTARS data. This is inconsistent with the basic conceptual model of the cloud lifetime effect.

Using a single cloud model and LESs, Jiang et al. (2006) found that aerosols may increase the lifetime of shallow cumulus clouds. However, their study suggested that, in addition to suppressing precipitation, smaller droplets can also lead to increased evaporation which would act to reduce the lifetime of the cloud. In some situations, it is therefore possible that an inverse cloud lifetime effect may sometimes occur.

1.4.3 Aerosol effects on precipitation and cloud top height

By modifying the cloud droplet size distribution, aerosols may have the potential to affect precipitation-forming processes in clouds. Rosenfeld and Lensky (1998) observed that precipitation-forming processes appear to be different for marine and continental convective clouds, and that marine clouds are modified as they move inland into more continental aerosol conditions. They also found that high aerosol conditions, due to biomass burning and urban air pollution, can significantly suppress precipitation. Air pollution has been observed to completely inhibit precipitation in some cases (Rosenfeld, 2000).

Through the suppression of precipitation, it is possible that increasing aerosol concentrations may allow convective clouds to grow to a greater cloud top height. Koren et al. (2005) (see Section 1.4.2) found a negative correlation between cloud top pressure and τ in the North Atlantic, providing evidence in support of this theory. Combining chemical transport model τ and meteorological reanalysis data with MODIS data in an attempt to compensate for cloud contamination and meteorological covariation (Section 1.5.3), Koren et al. (2010) found that invigoration of deep convection over the Atlantic by aerosols remained.

An in situ aircraft study over the Amazon found that smoke aerosols decrease cloud droplet sizes and suppress precipitation (Andreae et al., 2004). As a result, clouds could extend to greater heights, transporting water, aerosols and latent heat higher in the atmosphere, leading to an increase in thunderstorms and hail. Rosenfeld et al. (2008) provided a similar conceptual model explaining why increased cloud condensation nuclei concentrations can suppress precipitation in some clouds but enhance convection and precipitation in other clouds. The findings of Meskhidze et al. (2009), who used Terra and Aqua MODIS data to look at morning–afternoon differences, support the theory that aerosols may enhance convection over the Amazon.

Using a combination of MODIS, CloudSat and AMSR-E data alongside a cloud parcel model and an LES, Sorooshian et al. (2009) also found that precipitation decreases with increasing τ for tropical liquid clouds. Clouds with intermediate w appear most susceptible to suppression of precipitation by aerosols. When w is low, there is little potential for rain regardless of aerosol availability; when w is high, clouds are likely to precipitate anyway. By attempting to separate the aerosol–cloud interaction and cloud–precipitation components, Sorooshian et al. (2010) provided further evidence for the proposed causal mechanism.

For the trade wind cumulus clouds investigated by Yuan et al. (2011b) (Section 1.4.1), volcanic sulphate aerosol appears to suppress precipitation. Using a satellite-based lightning detector, Yuan et al. (2011a) found that there is also some evidence to suggest that volcanic aerosol may also sometimes increase lightning occurrence through the enhancement of deep convection. However, the increase in lightning occurrence may be due to electrification of ash which has been observed to be charged at distances over 1200 km from a volcanic source (Harrison et al., 2010).

Many LES modelling experiments have been performed in order to investigate the effect of aerosols on precipitation. However, there is little agreement between these studies, with both positive and negative effects on precipitation being observed for different conditions (Khain, 2009).

Using an LES, Feingold et al. (2010) suggested that oscillations between open and closed cell stratocumulus regimes may be modulated by aerosol effects on precipitation. The relationship between precipitation and cloud has been quantitatively compared to the analogous relationship between predator and prey populations in a biological system (Koren and Feingold, 2011).

1.4.4 Local aerosol effects with a global scope

Andreae et al. (2004) (see Section 1.4.3) suggested that the suppression of precipitation in the Amazon could affect the global circulation and water cycle. An ECHAM4 GCM study by Nober et al. (2003) supports the idea that the suppression of precipitation and enhancement of convection by aerosols can affect the global circulation.

Other mechanisms may exist by which aerosol effects could have a global scope. Evan et al. (2008) used satellite observations and a simple model to investigate how aerosol changes have affected cyclone development in the tropical Atlantic. They argued that a reduction in aerosol direct radiative forcing would lead to higher sea-surface temperatures which could result in an increased frequency of tropical cyclones. Since tropical cyclones probably play an important role in regulating stratospheric humidity (Romps and Kuang, 2009), they may in turn affect climate and stratospheric ozone (Shindell, 2001).

A modelling study by Wang (2007) suggested that heating of the atmosphere via solar absorption by black carbon aerosols may significantly affect large-scale tropical convection. Similarly, these absorbing aerosols may also affect the Indian summer monsoon circulation (Wang et al., 2009). These large-scale circulation impacts could have a significant impact on precipitation over large regions of the globe. Using a GCM, Bollasina et al. (2011) suggest that an observed decrease in Indian monsoonal rainfall is due to circulation changes induced by both aerosol direct and indirect effects.

1.4.5 Relative humidity and the direct effect

Interactions between aerosols and clouds may also be indirectly contributing to underestimates of direct aerosol radiative forcing. τ has been observed to increase near clouds in both photometer and MODIS data, although MODIS retrievals may not be accurate in such cases (Redemann et al., 2009). This increase is most likely due to the hygroscopic swelling of aerosols (Seinfeld and Pandis, 1998) in the high humidity environments near clouds. Koren et al. (2007) argued that satellite measurements of τ are biased towards cloud-free environments, and these measurements are therefore unrepresentatively low because they do not include scenes where aerosols are hygroscopically large in the high humidity environments near clouds. Using aircraft observations collected during the Indian Ocean Experiment (INDOEX), Twohy et al. (2009) provided evidence that relative humidity

effects on aerosols in the vicinity of clouds can lead to a 35–65 % enhancement in direct radiative forcing. This follows an earlier modelling study by Haywood et al. (1997), who demonstrated that sub-grid scale variability of relative humidity and cloud could lead to underestimation of the direct radiative forcing due to sulphate aerosol in GCMs.

1.4.6 Dependence on specific conditions

Predicting how a cloud will respond to aerosol is complicated. Cui et al. (2006) conducted a study using an axisymmetric model of a mixed phase convective cloud in low wind-shear continental conditions and found that increasing aerosols led to stagnated cloud development, a lower cloud top, weaker updrafts and suppressed precipitation. They mentioned that cloud response to aerosols appears heavily dependent on the type of cloud and conditions. Using a numerical model of convective clouds, Altaratz et al. (2008) showed that aerosol effects are dependent on relative humidity conditions. Jones et al. (2009), who used MODIS data together with reanalysis data, suggested that synoptic conditions, aerosol type and the vertical location of an aerosol layer may be much more significant factors than τ. Using MODIS satellite and SPRINTARS model data, L'Ecuyer et al. (2009) suggested that sulphate and sea-salt aerosols may have opposite effects on clouds: sulphate aerosol can decrease precipitation and enhance vertical development, whereas sea-salt can increase precipitation and suppress vertical development. This is probably because hydrophilic sea-salt can act as a giant cloud condensation nucleus on which large droplets can grow.

1.5 Possible reasons for spurious aerosol–cloud relationships in satellite data

Various relationships between aerosols and cloud properties have been observed in satellite data, and many potential implications have been suggested in recent years. However, the observed relationships are not necessarily due to causal relationships between aerosols and clouds. They may be due to erroneous satellite data, spatiotemporal climatological factors and meteorological effects.

1.5.1 Satellite data errors

Satellite datasets are not completely reliable (Section 1.2.5). One potential problem of interest here is that of cloud contamination of aerosol retrievals leading to overestimates of τ. This cloud contamination is more likely in situations where there is thin or broken cloud. This has the potential to lead to spurious positive relationships between τ and f_c, as will be discussed in Chapter 4.

1.5.2 Spatiotemporal climatological gradient effects

Many regions of the world experience seasonal changes which may include pronounced seasonal cycles of aerosol and cloud properties. Many studies already aim to remove this temporal climatological factor by looking at individual seasons.

Similarly, different regions experience different climatological conditions. These spatially-varying aerosol and cloud climatologies may also often contribute towards observed relationships between aerosol and cloud properties. This may affect the results of many of the studies mentioned in Section 1.4 that analysed data on a relatively large regional scale: Bréon et al. (2002) conducted their analysis on a global scale of $360^\circ \times 105^\circ$; Kaufman et al. (2005) and Koren et al. (2005) used North Atlantic regions of order $100^\circ \times 25^\circ$; Bulgin et al. (2008) used regions of varying sizes, from $14^\circ \times 8^\circ$ to $360^\circ \times 105^\circ$; Quaas et al. (2008) used continental regions of order $100^\circ \times 40^\circ$; Koren et al. (2008) used a $26^\circ \times 19^\circ$ region; Jones et al. (2009) used $10^\circ \times 10^\circ$ regions. Aerosol type, cloud regime and synoptic regime climatologies may vary over such large-scale regions. If data are analysed for the region as a whole, false correlations may be introduced. For example, Figure 1.4 illustrates a hypothetical ocean region with two sub-regions: one characterised by low thin stratocumulus cloud and biomass burning aerosol; the other, more remote, characterised by thicker fragmented cumulus cloud and sea-salt aerosol with a generally lower τ. One potential spurious correlation introduced by treating the two sub-regions as one larger region would be the observation that higher τ corresponds to thinner clouds with a larger fractional coverage, relationships which may exist in neither of the sub-regions if they were to be analysed in isolation. Similarly, further spurious relationships between other cloud and aerosol properties may also be introduced by looking at large regions. Such spatial climatological gradient effects are investigated in Chapter 2.

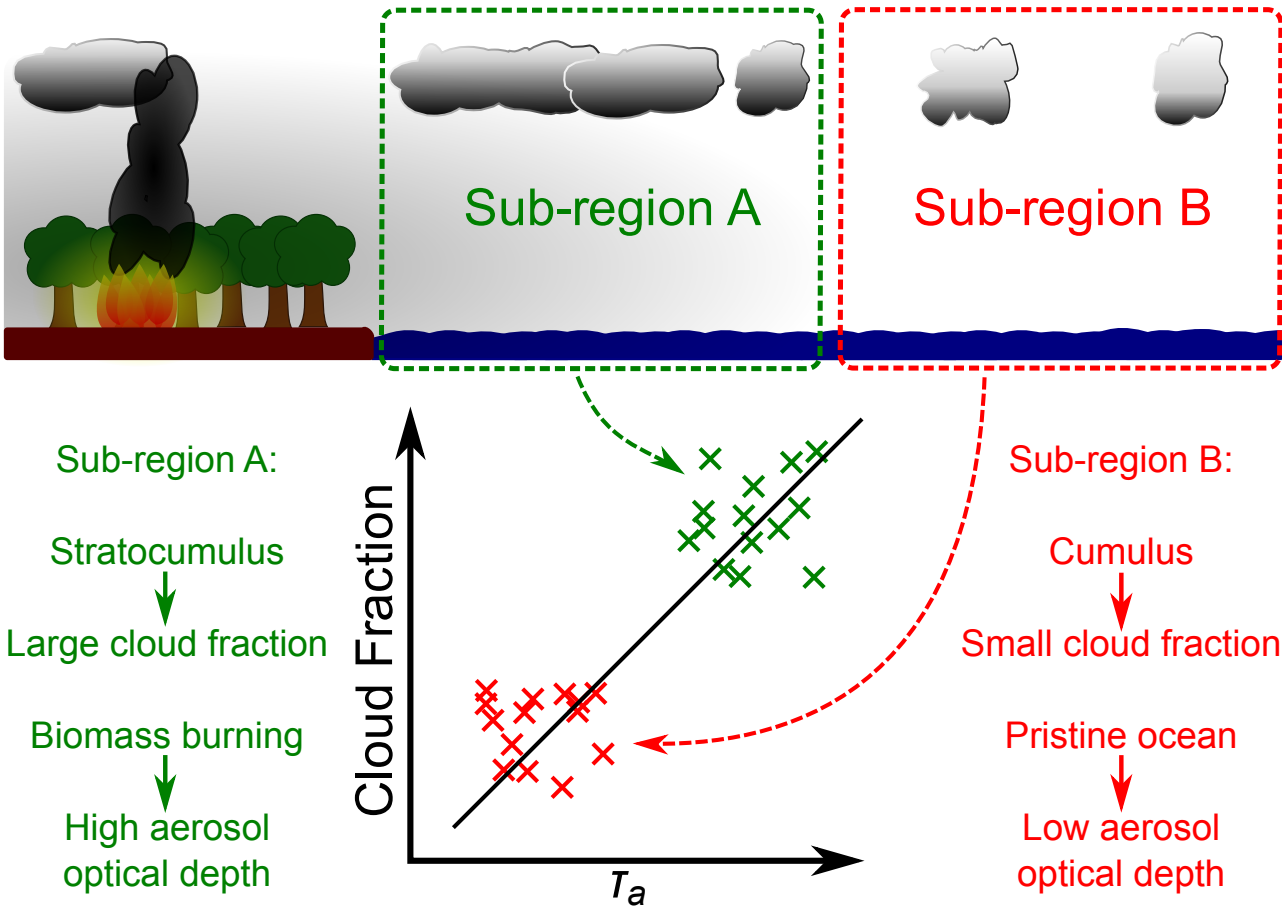

Figure 1.4: A schematic illustrating a hypothetical ocean region comprising two hypothetical sub-regions (sub-region A and sub-region B). Sub-region A is characterised by stratocumulus cloud and biomass burning aerosol; sub-region B is characterised by cumulus cloud in a pristine ocean environment. No statistically significant relationship between aerosol and cloud properties exists within each sub-region. However, analysing data for both sub-regions together leads to the spurious observation that high aerosol optical depth (τ) generally corresponds to a large cloud fractional coverage, as shown in the scatter plot.

1.5.3 Meteorological effects

Even if all large-scale climatological factors are correctly accounted for, smaller scale meteorological effects may also lead to spurious correlations between aerosol and cloud properties. As mentioned in Section 1.4.5, aerosols often swell hygroscopically in high humidity conditions, significantly increasing τ. Since cloud formation also depends on relative humidity, this could lead to spurious correlations between τ and cloud properties (Quaas et al., 2010). Engström and Ekman (2010) found that 10-metre wind speed can explain a large part of observed correlations between τ and f_c (see also Chapter 6). Some of the studies mentioned in Section 1.4 also aimed to account for potential meteorological contributions to observed relationships.

Most previous studies which consider potential meteorological contributions to observed aerosol–cloud relationships, including those mentioned above, have looked at simple local meteorological

variables such as relative humidity and wind speed. It is also possible that large-scale synoptic systems may often lead to spurious correlations between aerosols and clouds, causing correlations which may not be accounted for by considering simple local meteorological variables on their own.

Many studies have shown that extratropical cyclones and fronts are major drivers of large-scale cloud properties (Lau and Crane, 1995, 1997; Norris and Iacobellis, 2005; Wang and Rogers, 2001; Chang and Song, 2006; Field and Wood, 2007; Field et al., 2008). If these synoptic systems also affect aerosol properties, then they may lead to spurious relationships between aerosol and cloud properties.

Over land, synoptic conditions often appear to be a major factor affecting aerosol air pollution (Dharshana et al., 2010). Cold fronts have been observed to remove aerosols near the surface (e.g. Sheih et al., 1983; Jia et al., 2008).

Over ocean, high wind speeds and relative humidities associated with synoptic storms can lead to significantly increased aerosol optical depth (Glantz et al., 2009), due to both hygroscopic growth of aerosols (e.g. Seinfeld and Pandis, 1998) and increased sea salt emission (e.g. Woodcock, 1953; Lewis and Schwartz, 2004). Above a certain wind speed threshold, it is possible that sea salt concentrations near the surface may decrease due to scavenging by spray droplets (Pant et al., 2008). However, the question remains as to how extratropical cyclones may affect total column aerosol properties. This is investigated in Chapter 5. The extent to which extratropical cyclones may cause spurious correlations between retrieved aerosol and cloud properties is then investigated in Chapter 6.

1.6 Objectives of this project

The primary objective of this project is to improve our quantitative understanding of aerosol–cloud interactions and their role in the Earth's climate system. By developing new methods of analysing available satellite data, some of the possible reasons for observed relationships between aerosol and cloud properties will be explored. The outline below provides a summary of the questions investigated in each chapter.

Chapter 2

The first major area of focus will be the role of climatological spatial gradients, investigated in Chapter 2. Two questions are asked: What are sensible choices of spatial scale for aerosol–cloud interaction studies? What effect may spatial scale choices have on global estimates of radiative forcing due to the cloud albedo effect?

Chapter 3

Taking the recommendations of Chapter 2 into account, Chapter 3 will provide a global panoramic overview of observed relationships between aerosol and cloud properties. Two questions are investigated: What are appropriate ways of quantifying and presenting relationships between aerosol optical depth and different cloud properties on global scales? What relationships between aerosol optical depth and different cloud properties can be observed across the world for different satellite and GCM datasets?

Chapter 4

Reasons for the relationship between aerosol optical depth (τ) and cloud fraction (f_c) will be investigated in detail in Chapter 4. Three questions are considered: May the observed f_c–τ relationships be partly due to cloud contamination errors? Is ECHAM5-HAM capable of modelling the observed f_c–τ relationships? What are the reasons for the f_c–τ relationships in ECHAM5-HAM?

Chapters 5 and 6

The second next major area of focus will be the consideration of extratropical cyclones, investigated in Chapters 5 and 6. In Chapter 5, one question is asked: What effect do extratropical cyclones have on column aerosol properties over ocean? In Chapter 6, one question is considered: Can spurious relationships between aerosol and cloud properties be explained by considering simply the relative vorticity of extratropical cyclones and position relative to the storm centre?

Chapter 7

Finally, Chapter 7 will provide an overview of the main conclusions of this thesis, as well as mentioning possibilities for future work.

Chapter 2

A critical look at spatial scale choices in aerosol indirect effect studies

The text and figures in this chapter are those of Grandey and Stier (2010) (B. S. Grandey and P. Stier. A critical look at spatial scale choices in satellite-based aerosol indirect effect studies. *Atmos. Chem. Phys.*, 10:11459–11470, 2010, doi:10.5194/acp-10-11459-2010).

As discussed in Section 1.5.2, analysing satellite datasets over large regions may introduce spurious relationships between aerosol and cloud properties due to spatial variations in aerosol type, cloud regime and synoptic regime climatologies. In this chapter, the following two questions are asked:

1. What are sensible choices of spatial scale for aerosol–cloud interaction studies?

2. What effect may spatial scale choices have on global estimates of radiative forcing due to the cloud albedo effect?

A description of the datasets and methodology used in this chapter is provided in Section. 2.1. Results are presented in Section 2.2 and discussed, with reference to these two questions, in Section 2.3.

2.1 Method

2.1.1 Data

In this chapter, MODIS Science Team Collection 5 daily $1^\circ \times 1^\circ$ gridded level 3 products retrieved from Terra-MODIS radiances (MOD08_D3) for the ten-year period March 2000–February 2010 are used. The aerosol optical depth (τ) values are taken from the joint land and ocean mean aerosol optical depth dataset, retrieved at 550 nm.

For liquid cloud droplet effective radius (r_e), values from the quality-assured liquid cloud effective radius dataset are used. These data are retrieved using the 2.1 μm band and another band: 0.86 μm over ocean, 0.65 μm over land and 1.2 μm over ice/snow (Platnick et al., 2003). As mentioned in Section 1.2.5, r_e retrievals may be unreliable. However, the MODIS r_e product has been used in other studies (e.g., Kaufman et al., 2005; Kiran et al., 2009). It is a suitable product to use for investigating the effect of spatial scale choices on aerosol indirect effect studies.

Liquid cloud droplet effective number concentration (N_d) is calculated by applying Equation 1.7 to the liquid cloud optical depth and effective radius joint histogram. It is worth noting that the conclusions presented in Section 2.3 are not dependent on the validity of Equation 1.7, and that the current work also presents results for r_e, a directly retrieved cloud property. As discussed in Section 1.2.5, clouds with optical depths < 4 and $r_e < 4$ μm are excluded when calculating N_d. Identical sampling has not been applied to the quality-assured r_e used in this chapter. The results shown in Section 2.2 have not undergone a single-layer cloud constraint in the calculation of N_d. However, these results are relatively insensitive to the application of such a constraint, as will be shown in Appendix B.

2.1.2 Calculation of sensitivities

Following the method of Quaas et al. (2008), the sensitivity (b_ϕ) of a cloud property (ϕ) to τ is defined here as

$$b_\phi = \frac{\mathrm{d}\ln\phi}{\mathrm{d}\ln\tau}. \tag{2.1}$$

Of interest to this chapter is $b_{r_e} = \frac{\mathrm{dlnr_e}}{\mathrm{d}\ln\tau}$, the sensitivity of r_e, (cf. Equation 1.8) and $b_{N_d} = \frac{\mathrm{dlnN_d}}{\mathrm{d}\ln\tau}$, the sensitivity of N_d, (cf. Equation 1.9).

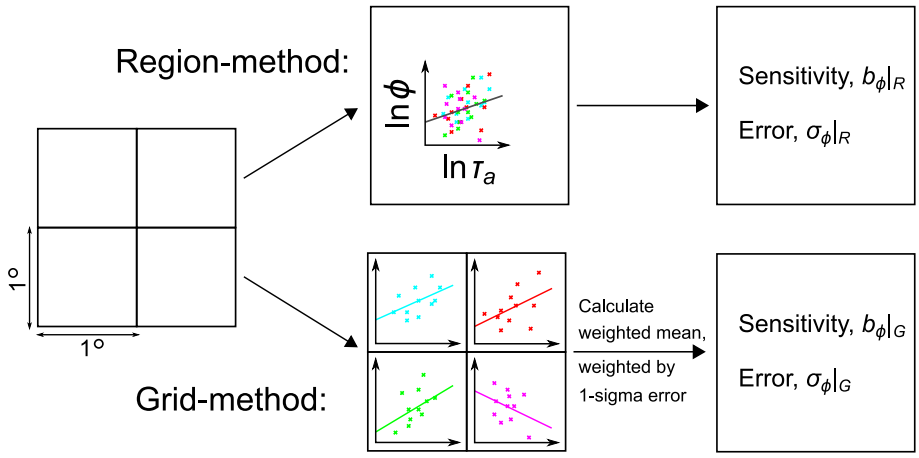

Figure 2.1: A schematic illustrating the methods used to calculate sensitivities, applied to a $2^\circ \times 2^\circ$ region. Each point in the scatter plot represents a $1^\circ \times 1^\circ$ grid box and day for which both cloud and aerosol data exist. The different colours are used to show data from different grid boxes. For simplicity, only a small number of data points are shown in this schematic.

When calculating sensitivities at $1^\circ \times 1^\circ$ resolution, Equation 2.1 is applied to data for a given season (December-January-February DJF, March-April-May MAM, June-July-August JJA or September-October-November SON) and $1^\circ \times 1^\circ$ grid box. This methodology can be thought of as calculating the linear regression slope of a scatter plot of $\ln \phi$ vs. $\ln \tau$, where each point represents a day for which both aerosol and cloud data exist for this grid box. The one-sigma error of the regression fit is also calculated.

When moving to larger regions, and ultimately the globe, there are two possible ways to extend this methodology, as illustrated in Figure 2.1. A single scatter plot for the entire region where different points represent different combinations of date and $1^\circ \times 1^\circ$ grid box, could be considered. This is the method used by Quaas et al. (2008, 2009) and is very similar to the methods used in many of the studies mentioned in Section 1.5.2 (Bréon et al., 2002; Kaufman et al., 2005; Bulgin et al., 2008). This is referred to here as the region-method, and its use is indicated by a subscript R, e.g. $b_{N_d}|_{\mathrm{R}}$. The region-method samples both temporal and spatial variability.

Alternatively, values of sensitivity for each individual $1^\circ \times 1^\circ$ grid box could be calculated, before calculating a mean, weighted by the one-sigma error, for the whole region. An error-weighted mean is used in order to reduce the impact of unreliable values with a large error, many of which may be outliers. This second method is referred to as the grid-method, indicated by a subscript G, e.g. $b_{N_d}|_{\mathrm{G}}$. The grid-method samples temporal variability only.

It is worth noting that the spatial scale choices being considered here are different from co-

location scale choice, another important consideration (McComiskey and Feingold, 2011). The co-location scale used here is $1^\circ \times 1^\circ$ for both the region-method and the grid-method.

In both the region-method and the grid-method, sensitivities with fewer than five contributing data points are excluded. Further significance testing is also applied, with sensitivities which are insignificant[1] at the two-sigma level being shown as white in Figures. 2.2, 2.3, 2.4 and 2.5. Both the region-method and the grid-method assume that cloud and aerosol measurements for different grid boxes and days are independent, an assumption which may cause the one-sigma errors calculated in this study to be too small. The validity and effect of this assumption will be discussed further in Appendix B.

As discussed in the introduction, the region-method has the potential to introduce a spurious sensitivity signal due to spurious spatial variations in cloud and aerosol climatologies. This will be demonstrated by randomly shuffling the temporal pairing of cloud and aerosol data within each season and $1^\circ \times 1^\circ$ grid box, assuming that aerosol and cloud properties for different days are independent. (See Figures. 2.2 and 2.4.) The application of this randomisation is indicated by a subscript Rand, e.g. $b_{N_d}|_{\mathrm{R,Rand}}$.

Although the grid-method has the obvious advantage of reducing spatial gradient methodological errors, the error weighting may lead to bias towards regions with a small error in the sensitivity. However, as will be discussed in Appendix B, this does not appear to be a major problem in this study.

In order to avoid errors due to retrievals behaving differently between ocean and land, ocean and land regions are analysed separately using a $1^\circ \times 1^\circ$ land mask.

Near the poles, where surface ice exists and satellite observations are at high solar zenith angles, properties retrieved from satellite data can often be unreliable (e.g., Liu et al., 2009). This problem is mostly avoided by limiting this study to regions between 60° N and 60° S.

A summary of the notation used in this chapter is provided for reference in Table 2.1.

[1] It is worth noting that a lack of statistical insignificance does not necessarily imply significance (e.g. Ambaum, 2010).

Table 2.1: A summary of the notation used in Chapter 2.

Symbol	Meaning
τ	aerosol optical depth
r_e	liquid cloud droplet effective radius
w	cloud liquid water path
τ_c	cloud optical depth
N_d	liquid cloud droplet effective number concentration
ϕ	a general cloud property, either r_e or N_d in this chapter
γ	constant in Equation 1.7; $=1.37\times10^{-5}\,\mathrm{m}^{-\frac{1}{2}}$
b_ϕ	the sensitivity, $\frac{\mathrm{d}\ln\phi}{\mathrm{d}\ln\tau}$, of a general cloud property to τ
b_{N_d}	sensitivity of N_d to τ
$b_{N_d}\vert_{\mathrm{R}}$	sensitivity of N_d to τ, calculated using the region-method
$b_{N_d}\vert_{\mathrm{G}}$	sensitivity of N_d to τ, calculated using the grid-method
$b_{N_d}\vert_{\mathrm{R,Rand}}$	sensitivity of N_d to τ, calculated using the region-method after data randomisation
$b_{N_d}\vert_{\mathrm{G,Rand}}$	sensitivity of N_d to τ, calculated using the grid-method after data randomisation
b_{r_e}	sensitivity of r_e to τ
$b_{r_e}\vert_{\mathrm{R}}$	sensitivity of r_e to τ, calculated using the region-method
$b_{r_e}\vert_{\mathrm{G}}$	sensitivity of r_e to τ, calculated using the grid-method
$b_{r_e}\vert_{\mathrm{R,Rand}}$	sensitivity of r_e to τ, calculated using the region-method after data randomisation
$b_{r_e}\vert_{\mathrm{G,Rand}}$	sensitivity of r_e to τ, calculated using the grid-method after data randomisation
DJF	Dec-Jan-Feb
MAM	Mar-Apr-May
JJA	Jun-Jul-Aug
SON	Sep-Oct-Nov

2.2 Results and discussion

The first column of Figure 2.2 shows the annual mean $b_{N_d}|_{\mathrm{R}}$ (region-method sensitivity of N_d to τ) for different region sizes. The sensitivities are calculated for each season and then an error-weighted annual mean is calculated. The top map, for $1^\circ\times1^\circ$ regions, shows positive sensitivities (red) over much of the ocean, indicating that higher τ generally corresponds with higher N_d over these areas, as predicted by the cloud albedo effect conceptual model. In contrast, negative sensitivities (blue) exist for some land areas, indicating that higher τ is associated with lower N_d. Much of the map is white, indicating that the calculated $b_{N_d}|_{\mathrm{R}}$ values were often not statistically significantly different from zero at the two-sigma confidence level. As the region size increases, the fraction of the globe containing statistically significant $b_{N_d}|_{\mathrm{R}}$ increases substantially.

For the grid-method, shown in the second column of Figure 2.2, the statistical significance of $b_{N_d}|_{\mathrm{G}}$ also improves substantially with increasing region size. The general spatial distribution of

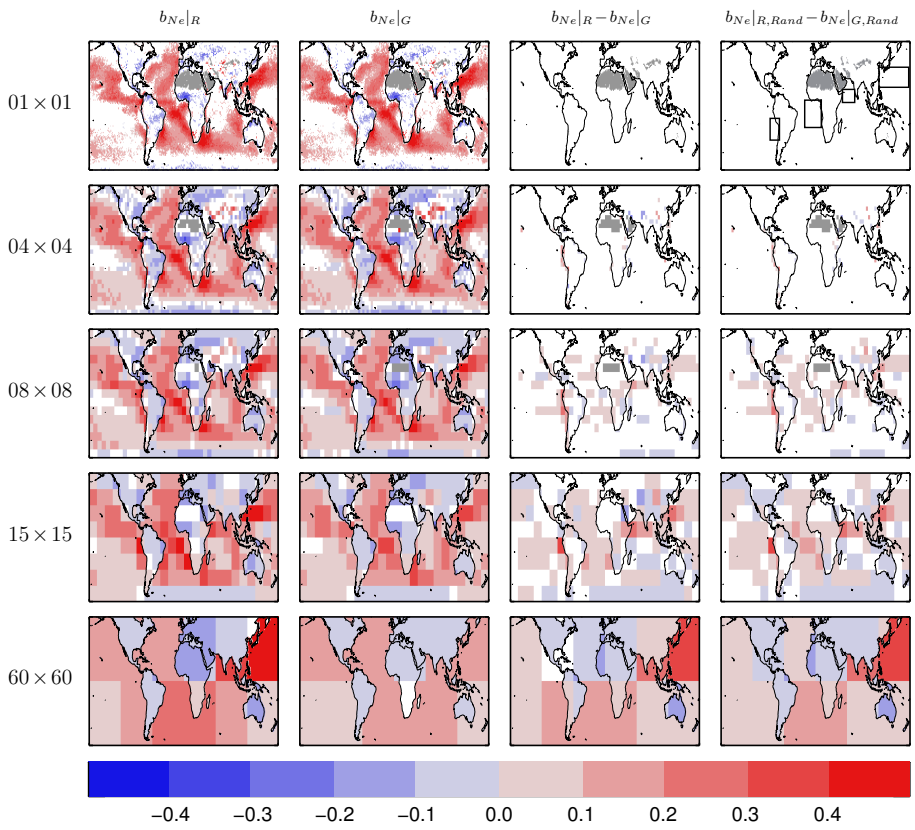

Figure 2.2: Annual (all seasons one-sigma error weighted) mean sensitivity of Terra-MODIS Collection 5 N_d (N_e in figure) to τ for different region sizes. The first column shows the results for the region-method; the second column is for the grid-method; the third column is the difference between the region-method and grid-method sensitivities; the fourth column is the difference when the data have first been randomised within each season and $1^\circ \times 1^\circ$ grid box. White regions are where the data are not significantly different from zero at two-sigma confidence, using the error from the sensitivity regression fit. Grey represents missing data. The four rectangles in the top right hand map indicate the regions commented on in Section 2.2.

grid-method sensitivities is similar to those of the region-method, with $b_{N_d}|_{\mathrm{G}}$ being mostly positive over the ocean and negative over land. However, some differences between $b_{N_d}|_{\mathrm{R}}$ and $b_{N_d}|_{\mathrm{G}}$ are also evident. For example, over the North-West Pacific, near East Asia, the $60^\circ \times 60^\circ$ $b_{N_d}|_{\mathrm{R}}$ is much larger than $b_{N_d}|_{\mathrm{G}}$.

The difference between $b_{N_d}|_{\mathrm{R}}$ and $b_{N_d}|_{\mathrm{G}}$ is shown in the third column of Figure 2.2. White shows where the difference is not significantly different from zero at the two-sigma confidence level. The region-method and grid-method only diverge at scales larger than $1^\circ \times 1^\circ$, so the $1^\circ \times 1^\circ$ $b_{N_d}|_{\mathrm{R}} - b_{N_d}|_{\mathrm{G}}$ map shows no difference between the two methods, as expected. At $4^\circ \times 4^\circ$, differences begin to appear along some of the coasts and land areas, probably due to surface albedo changes causing spatially-varying satellite retrieval errors. At $8^\circ \times 8^\circ$, many more differences can be seen, including over ocean areas. For $15^\circ \times 15^\circ$ and $60^\circ \times 60^\circ$, the presence of significant differences increases substantially.

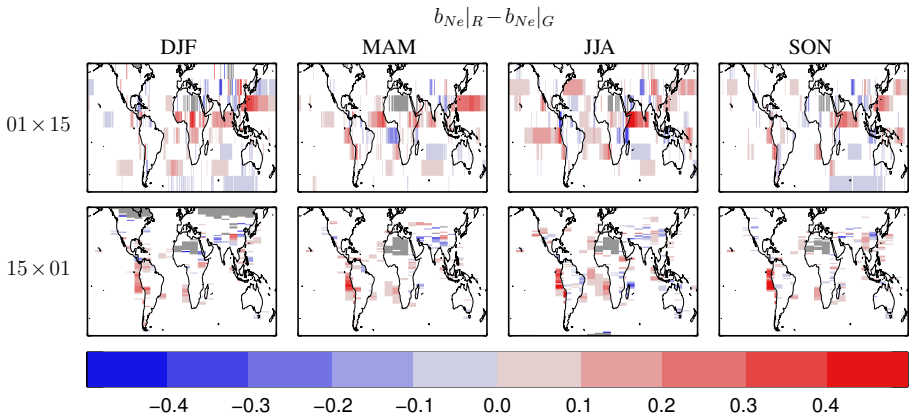

Figure 2.3: Difference in sensitivity of Terra-MODIS Collection 5 N_d (N_e in figure) to τ between the region-method and grid-method for different seasons and two different region shapes (meridional and zonal). White regions are where the data are not significantly different from zero at two-sigma confidence. Grey represents missing data.

These results for $b_{N_d}|_{\mathrm{R}}$, $b_{N_d}|_{\mathrm{G}}$ and $b_{N_d}|_{\mathrm{R}} - b_{N_d}|_{\mathrm{G}}$ are relatively insensitive to the application of a single-layer cloud constraint, as will be discussed in Appendix B.

In order to demonstrate that the observed differences occur due to spatial scale changes, the fourth column of Figure 2.2 shows the difference between the region-method and the grid-method for data which has been temporally randomised within each $1^\circ \times 1^\circ$ grid box and season prior to calculating the annual mean. This randomisation generally causes $b_{N_d}|_{\mathrm{G,Rand}}$ to become insignificantly different from zero, with a few statistically significant departures from zero being the result of noise. The dominant signal in $b_{N_d}|_{\mathrm{R,Rand}} - b_{N_d}|_{\mathrm{G,Rand}}$ is due to spatially-varying changes in N_d and/or τ within regions, either as a result of physical climatologies or surface albedo changes affecting satellite retrievals. The strong similarity between $b_{N_d}|_{\mathrm{R,Rand}} - b_{N_d}|_{\mathrm{G,Rand}}$ and $b_{N_d}|_{\mathrm{R}} - b_{N_d}|_{\mathrm{G}}$ demonstrates that these sensitivity differences arise as a result of varying climatologies and/or surface albedo within regions.

By looking at different region shapes, it is possible to investigate whether the $b_{N_d}|_{\mathrm{R}} - b_{N_d}|_{\mathrm{G}}$ differences are predominantly meridional or zonal in nature. Figure 2.3 shows the difference $b_{N_d}|_{\mathrm{R}} - b_{N_d}|_{\mathrm{G}}$ for different seasons and two different region definitions: $1^\circ \times 15^\circ$ (meridional) and $15^\circ \times 1^\circ$ (zonal). It can be seen that both meridional and zonal changes contribute, with meridional changes being more widespread over the open ocean.

Four ocean areas are worthy of particular mention: the Western North Pacific, to the east of China; the Arabian Sea, between the Horn of Africa and India; the Eastern South Pacific, near the South American coast; and the Eastern South Atlantic, near the African coast. These four regions are

indicated on the map at the top right of Figure 2.2. Below, each of these four regions is considered briefly.

Parts of the Western North Pacific, to the east of China, show a large difference between $b_{N_d}|_{\mathrm{R}}$ and $b_{N_d}|_{\mathrm{G}}$ at region-scales of $8^\circ \times 8^\circ$ and above (Figure 2.2), much of which is meridional (Figure 2.3). Aerosol properties are known to vary significantly within this region, often exhibiting a gradient in absorptivity and fine-mode fraction with distance from the coast (Choi et al., 2009). A significant part of this variation in aerosol properties is meridional.

The Arabian Sea, between the Horn of Africa and India, also shows a large meridional difference between $b_{N_d}|_{\mathrm{R}}$ and $b_{N_d}|_{\mathrm{G}}$, particularly during the summer months (Figure 2.3). This area often contains airborne dust originating from dust storms, with τ being higher in summer than in winter (Li and Ramanathan, 2002). The presence of dust often leads to situations where aerosol and cloud are misidentified (Brennan et al., 2005), leading to errors in retrieved properties. Since there is a strong meridional gradient in τ due to dust over the Arabian Sea (Li and Ramanathan, 2002), this may lead to a meridionally-varying contribution of contamination to retrieved properties.

The results presented here suggest that stratocumulus region indirect effect studies may be particularly susceptible to spatial scale choices. The Eastern South Pacific stratocumulus region, to the west of Peru and Chile, shows persistent differences between $b_{N_d}|_{\mathrm{R}}$ and $b_{N_d}|_{\mathrm{G}}$ (Figures 2.2 and 2.3). Interestingly, the Eastern South Atlantic stratocumulus region, to the west of Africa, shows a negative meridional difference in MAM but not in other seasons. Aerosol types and cloud properties are known to vary spatially within these regions (e.g., George and Wood, 2010), and variations may have a significant impact on observed aerosol indirect effects (Andrejczuk et al., 2008). These spatial variations must be taken into account when studying stratocumulus regions.

Figures 2.4 and 2.5 show b_{r_e} (the sensitivity of r_e to τ) which exhibits a very similar pattern to Figures 2.2 and 2.3, except for the inverted sign and colour bar range. For the first and second columns of Figure 2.4, blue regions show where b_{r_e} is negative, indicating that higher τ generally corresponds with smaller droplets, and red regions show where b_{r_e} is positive, indicating that higher τ corresponds with larger droplets. The aforementioned observations concerning the sensitivity of N_d also apply to the sensitivity of r_e. For example, the third column of Figure 2.4 shows that statistically significant differences between $b_{r_e}|_{\mathrm{G}}$ and $b_{r_e}|_{\mathrm{R}}$ emerge as the region size increases. These differences occur mainly along the coast and over land at $4^\circ \times 4^\circ$, but are found everywhere at $60^\circ \times 60^\circ$. As before, the

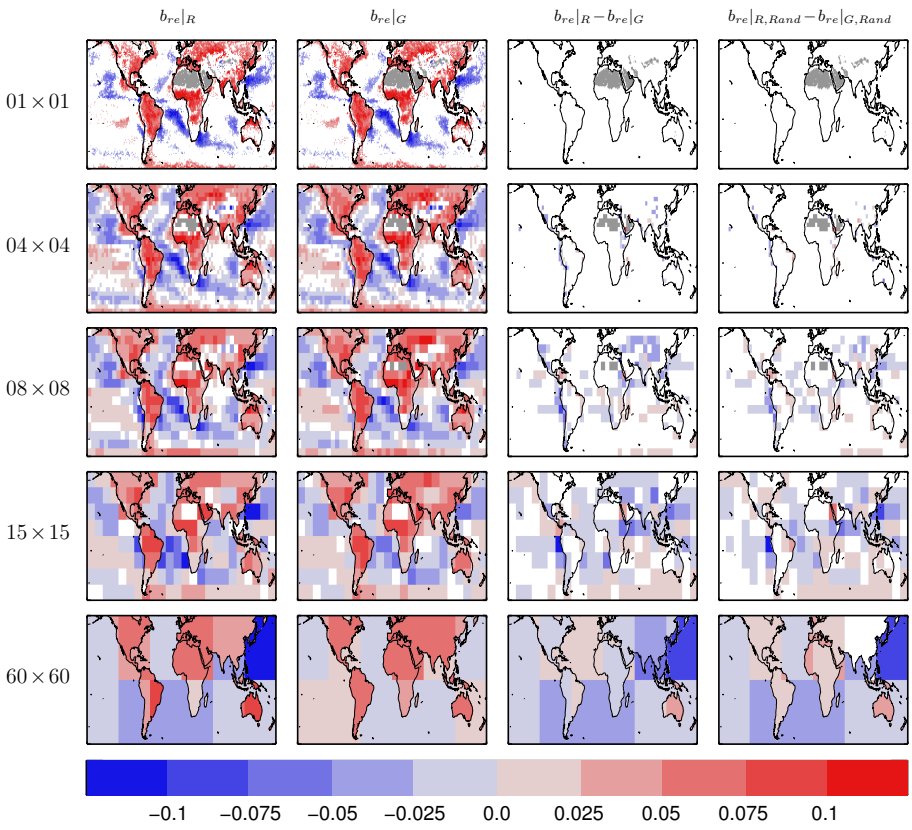

Figure 2.4: Same as Figure 2.2, but for sensitivity of Terra-MODIS Collection 5 r_e to τ.

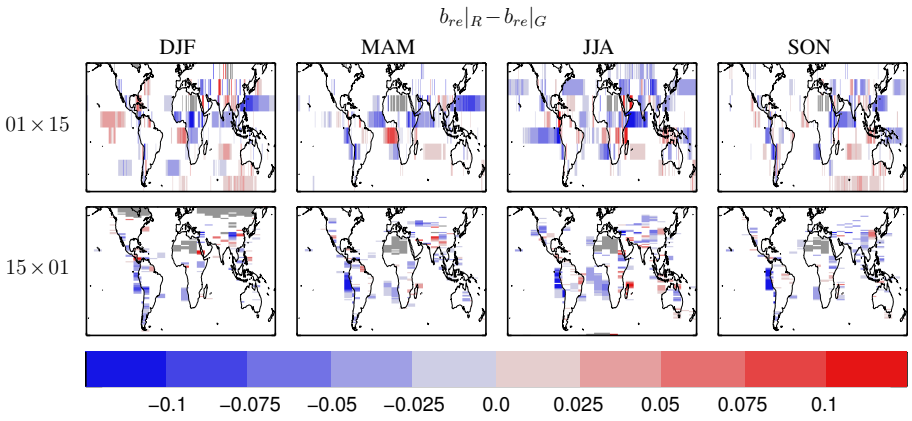

Figure 2.5: Same as Figure 2.3, but for sensitivity of Terra-MODIS Collection 5 r_e to τ.

fourth column shows that these differences are similar if the data have been randomly shuffled within each $1^\circ \times 1^\circ$ grid box. The four regions commented on above also show large $b_{r_e}|_{\mathrm{R}} - b_{r_e}|_{\mathrm{G}}$ differences in Figures 2.4 and 2.5.

Figure 2.6 shows the relative error introduced to the global average of b_{N_d} through the use of the region-method compared to the grid-method. As expected, this error increases with region size. This error generally acts such that the region-method leads to an overestimate of b_{N_d} compared to the grid-method. For the ocean-land combined and ocean-only sensitivities, this error increases rapidly

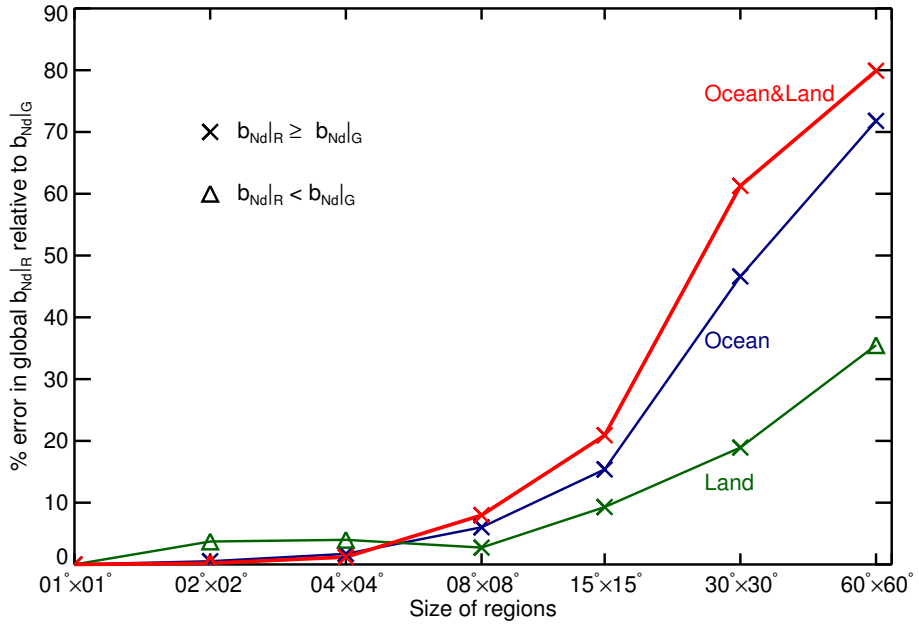

Figure 2.6: Absolute percentage error in the globally-averaged sensitivity of Terra-MODIS Collection 5 N_d to τ due to the region-method compared to the grid-method. The green data line is for land-only, the blue is for ocean-only and the red is for ocean and land combined. Crosses show where the region-method leads to an overestimate of the sensitivity (i.e. the error is positive), and triangles where the sensitivity is underestimated (the error is negative). As elsewhere in this study, weighting has been applied using the one-sigma error in the sensitivities. Latitudinal area weighting has not been applied.

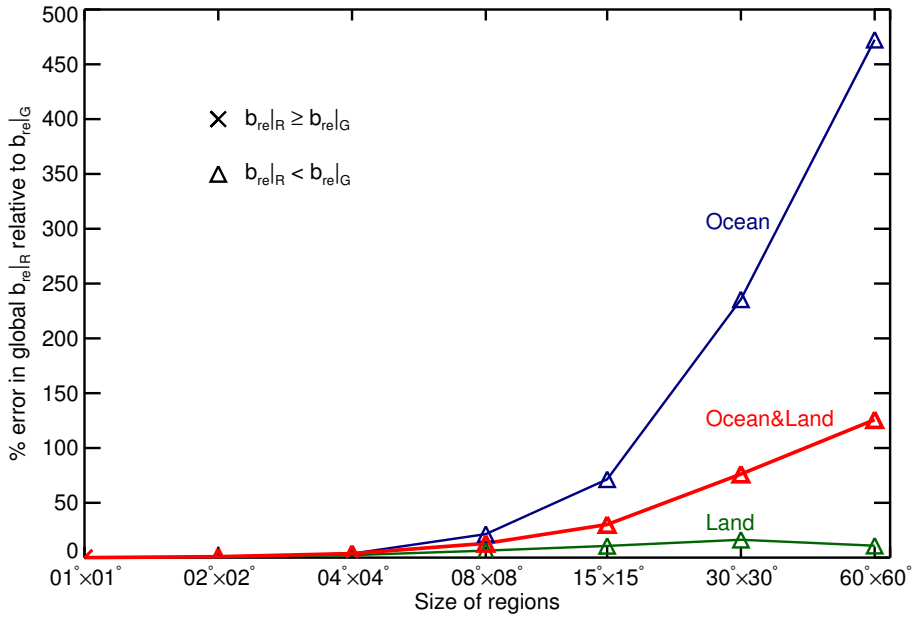

Figure 2.7: Same as Figure 2.6, but for sensitivity of Terra-MODIS Collection 5 r_e to τ.

to ∼5–10% between $4°\times4°$ and $8°\times8°$. It is at this scale that statistically significant differences begin to become apparent in many individual regions, as shown in Figure 2.2 and commented on earlier. Likewise, as can be seen in Figure 2.7, for r_e the region-method leads to large errors in b_{r_e} at region scales of $8°\times8°$ and larger. At $60°\times60°$, the ocean-only error in b_{r_e} grows to ∼470%.

Errors in sensitivities arising due to the region-method will propagate into associated estimates of cloud albedo effect radiative forcing. Quaas et al. (2008) use large-scale regions, of comparable size to the $60^\circ \times 60^\circ$ regions used here, to estimate radiative forcing. Their cloud albedo effect radiative forcing scales approximately linearly with b_{N_d}. As can be seen in Figure 2.6, the application of the region-method at $60^\circ \times 60^\circ$ gives rise to an 80% error (70% error for ocean-only). This would introduce an estimated error of approximately 80% to the Quaas et al. (2008) cloud albedo effect radiative forcing estimate, modifying their error estimate from $\pm 0.1\,\mathrm{W\,m^{-2}}$ to $\pm 0.2\,\mathrm{W\,m^{-2}}$. Quaas et al. (2008) clearly acknowledge that the uncertainty of their result is likely to be larger than $\pm 0.1\,\mathrm{W\,m^{-2}}$, due to data and methodological errors being difficult to account for. The current study helps to quantify a methodological error.

2.3 Conclusions

This chapter aimed to address two questions: What are sensible choices of spatial scale for aerosol–cloud interaction studies? What effect may spatial scale choices have on global estimates of radiative forcing due to the cloud albedo effect?

In order to address these questions, the effect of calculating aerosol–cloud relationships in satellite data over a variety of region sizes from $1^\circ \times 1^\circ$ to $60^\circ \times 60^\circ$ was investigated. Using MODIS satellite data, sensitivities (Equation 2.1) of derived N_d to τ and retrieved r_e to τ were calculated for these different spatial scale choices.

Generally, positive values of the sensitivity of derived N_d to τ are found for ocean regions, whilst negative values occur for many land regions. The spatial distribution of the sensitivity of retrieved r_e to τ shows the opposite pattern, with generally positive values for land regions and negative values for ocean regions. Differences in aerosol–cloud relationships between land and ocean may be related to regime dependent behaviour of aerosol indirect effects, as suggested by some large-eddy simulations (Haywood et al., 2009).

It was found that analysing datasets over large regional scales has the potential to introduce significant errors to aerosol indirect effect studies. For regions of size $4^\circ \times 4^\circ$, spatial scale errors are generally small ($\ll 10\%$ for the sensitivity of both N_d and r_e) but often become much more significant at region sizes of $8^\circ \times 8^\circ$ and larger. At larger region scales, these errors can become much larger. For

example, for regions of size $60^\circ \times 60^\circ$ the global ocean-only error in the sensitivity of r_e is $\sim 470\%$. The existence of these spatial scale errors appears to be robust to the application of a single-layer cloud constraint and also does not appear to be the result of a sampling bias due to error weighting.

In light of these findings, it seems sensible to recommend $4^\circ \times 4^\circ$ as the largest size of individual regions that should be used for analysis in aerosol indirect effect studies. Caution should be applied if looking at larger regions. If data exist at a higher gridded resolution (e.g. $1^\circ \times 1^\circ$), the possibility of analysing data at this higher resolution should be seriously considered. Results of calculations done at these small spatial scales can then be averaged over larger regions, allowing overall results to be calculated for large regions and the globe. Of course, it may not always be possible to conduct analyses at the small spatial scales recommended here. Dataset limitations may prohibit this, particularly when extra temporal and meteorological constraints reduce dataset size. Potential spatial scale methodological errors should be considered alongside other considerations.

The results presented in Section 2.2 suggest that stratocumulus regions are particularly susceptible to such methodological errors, and particular care must be taken when studying such regions.

For large regions, spatial scale errors may lead to large errors in estimates of global cloud albedo effect radiative forcing. For regions on the scale of $60^\circ \times 60^\circ$, this study suggests that this methodological error in radiative forcing is of order 80%. The corresponding ocean-only error in radiative forcing is of order 70%.

Another advantage of conducting analysis of aerosol–cloud relationships on small regional scales and presenting the results on maps is that it can provide an overview of how these relationships differ for different regions. This avoids the necessity of making prior assumptions about the homogeneity of these relationships across previously chosen large-scale regions.

This chapter focuses on the cloud properties, N_d and r_e, which are often of interest in cloud albedo effect studies. The methodological errors explored here highlight a potential source of inaccuracy in some of the cloud albedo effect studies mentioned in Section 1.4.1 (e.g., Bréon et al., 2002; Kaufman et al., 2005; Bulgin et al., 2008; Quaas et al., 2008). Although other cloud properties are not investigated here, it is likely that similar methodological errors may also affect the findings of studies which use large regions to investigate other aerosol indirect effects (e.g., Koren et al., 2005, 2008; Jones et al., 2009). However, the additional cloud type and meteorological constraints applied in several of these studies may make their results less susceptible to the spatial gradient effects discussed here.

Finally, it is worth noting that even small regions experience changes in cloud regime and aerosol conditions, often as a result of meteorology. This may lead to spurious correlations unaccounted for in this chapter, and is the basis for the work presented in Chapters 5 and 6. One possible further approach would be to investigate the contribution of temporal climatological gradients, analogous to the spatial gradients discussed here. However, although seasonal temporal scale choices should be considered, this would not fully account for meteorological effects. The development of more advanced methods to investigate the contribution of meteorology to observed aerosol–cloud relationships would be highly beneficial.

Chapter 3

Quantifying observed aerosol–cloud relationships on global scales

In the previous chapter, the effect of spatial scale choices in aerosol–cloud interaction studies was considered. It was recommended that analysis of relationships between aerosol and cloud properties be conducted using region sizes no larger than $4^\circ \times 4^\circ$, before averaging the results to larger regional scales where necessary. In addition to demonstrating an application of the spatial scale considerations, the work presented in Chapter 3 will provide a global panoramic overview of some observed relationships between aerosol and cloud properties, building on the results of earlier studies such as that by Quaas et al. (2009). Appropriate methods for quantifying the relationships will be considered. The following two questions are investigated:

1. What are appropriate ways of quantifying and presenting relationships between aerosol optical depth and different cloud properties on global scales?

2. What relationships between aerosol optical depth and different cloud properties can be observed across the world for different satellite and GCM datasets?

The data and methodology used to answer these questions are described in Section 3.1. The results are presented in Section 3.2. Conclusions are summarised in Section 3.3.

3.1 Method

3.1.1 Data

Data from a number of different satellite and GCM datasets are used in this chapter. As described in Section 1.2.4, daily level 3 Aqua-MODIS data from two different datasets are used: the official MODIS Science Team Atmosphere Collection 5 level 3 daily $1^\circ \times 1^\circ$ cloud and aerosol dataset (MYD08_D3, December 2002 – November 2008); and the CERES Single Scanner Footprint (SSF) dataset, which includes CERES Team cloud data alongside MODIS Science Team Collection 4 aerosol data, gridded to $2.5^\circ \times 2.5^\circ$ (2003–2005). A third satellite dataset combination used here is the AATSR GlobAEROSOL aerosol dataset and the AATSR ORAC cloud dataset, gridded to $1^\circ \times 1^\circ$ (Section 1.2.4, December 2002 – November 2006).

The AeroCom indirect effects intercomparison project used data from several different GCMs (Section 1.3.4; Quaas et al., 2009). These GCM data are also used here. They are sampled at a local time of 1:30 P.M., matching the overpass time of the Aqua satellite. They are provided at a spatial resolution of $2.5^\circ \times 2.5^\circ$.

A number of different cloud properties, explained in Section 1.2.5, are investigated in this chapter: liquid cloud droplet number concentration at cloud top (N_d; calculated using Equation 1.7 for the satellite datasets; directly output by the GCMs in the AeroCom model datasets), liquid cloud droplet effective radius at cloud top (r_e), cloud top temperature for all clouds (T_{top}) and total cloud fraction (f_c). Aerosol optical depth at 550 nm (τ) is used.

3.1.2 Analysis methodology

In order to investigate relationships between the cloud properties mentioned above and τ, the daily data are categorized into two cases: low τ conditions, where τ is less than the median for that grid-box, season and dataset; high τ conditions, where τ is greater than the median. Following this categorization, a mean for each grid box, season, property and dataset is calculated, before averaging across all four seasons. These means for low τ and high τ conditions, and the difference between them, are then shown on maps (e.g. Figures 3.1 and 3.2). Since this chapter does not aim to provide a comprehensive analysis of the GCM datasets and inter-model differences, the median results across the AeroCom models are shown rather than the results for every single model. The analysis is limited

to 60°S–60°N, because the satellite retrievals are likely to be less reliable near the poles.

Beyond looking at how the cloud properties change between low τ and high τ conditions, it would be interesting to mathematically quantify the relationships between the cloud properties and τ, as was done using sensitivities of N_d to τ in Chapter 2. When defining the sensitivity of N_d to τ as the ordinary least squares regression slope of $\ln N_d$ versus $\ln \tau$ in Chapter 2, it was implicitly assumed that N_d is dependent on τ and that a power law relationship between the two exists:

$$N_d(\tau, M) \propto \tau^b M \tag{3.1}$$

where b is a constant (the so-called sensitivity, $\frac{\mathrm{d} \ln N_d}{\mathrm{d} \ln \tau}$) and M represents other terms on which N_d is dependent, such as meteorological conditions. If this is true, and if τ is independent of M, then an ordinary least squares fit between N_d and τ would be appropriate, with ϵ becoming the error representing the other terms unaccounted for by τ:

$$\ln N_d = a + b \ln \tau + \epsilon \tag{3.2}$$

where a comes from the constant coefficient of proportionality for Equation 3.1 and $\epsilon = \ln M + \epsilon'$ is the error due to terms unaccounted for, such as meteorology and the error due to noise (ϵ'). A similar relationship was assumed for r_e. Three comments about these assumptions are noted below.

Firstly, it is assumed that a cloud property $\phi = \phi(\tau)$ is a function of τ, and that a linear relationship between these variables or transformations of these variable is appropriate. If this assumption that $\phi = \phi(\tau)$ is true, then a fit where ϕ residuals are minimized would be appropriate. As discussed throughout this thesis, especially in Section 1.5, observed relationships between ϕ and τ may not be due to aerosol indirect effects.

Secondly, it is assumed that τ is either independent of M or that τ and ϕ are functions of independent aspects of M, i.e. there is no covariance due to M. This may be a poor assumption, since both τ and ϕ may be dependent on common meteorological factors such as relative humidity and synoptic conditions, as mentioned in Section 1.5.3. In reality, depending on the covariance between M, ϕ and τ, part of M may be included in the constant b.

Thirdly, in order for an ordinary least squares fit to be valid, it is assumed that ϵ is normally distributed, and that ϵ' is independent of τ, i.e. there is no covariance between retrieval errors for τ

and ϕ. In reality, aerosol retrieval errors due to cloud contamination may be correlated with retrieved cloud properties, as mentioned in Section 1.5.1. This may lead to part of ϵ' being included in b.

Although these assumptions may not be fully valid, as noted above, such ordinary least squares fits are used here. It is important to remember that an observed relationship between τ and a cloud property ϕ may not indicate a causal indirect effect of the aerosol on cloud, and that the relationship may be largely due to meteorology or satellite retrieval errors. The aim of this chapter is simply to provide a global overview of these observed relationships in both satellite and GCM datasets. The use of three satellite datasets provides, to some extent, a possible constraint on the contribution of some possible retrieval errors. However, it is not unlikely that all three datasets may suffer from common retrieval errors, particularly those associated with cloud contamination of aerosol retrievals. The possible contribution of synoptic conditions is considered further in later chapters, particularly Chapter 6.

The shape of the ordinary least squares fit may not be obvious. For N_d and r_e, the two cloud properties used in Chapter 2, there are theoretical reasons for assuming a log-log relationship between these cloud properties and τ (Equations 1.8 and 1.9). For other cloud properties, a log-log relationship may not be appropriate. In this chapter, theoretical considerations are supplemented by an empirical test in order to decide whether to use log–log, lin–log or lin–lin[1] fits between the cloud properties and τ. The empirical measure chosen is the coefficient of determination (R^2), which is the square of the linear correlation coefficient and is a measure of goodness of fit. We apply this test to the MODIS Science Team Collection 5 dataset only, because this is the major satellite dataset used in this thesis. For each ϕ–τ combination, maps of R^2 are produced for log–log, lin–log and lin–lin fits (e.g. Figure 3.3).

After a fit has been chosen for each ϕ–τ combination, the regression slopes are calculated for each season and grid box. The results are regridded to $15^\circ \times 15^\circ$ using the grid-method of Chapter 2, weighting by the one-sigma error (e.g. Figure 3.4). As with the high τ and low τ condition means, the AeroCom model median for each $15^\circ \times 15^\circ$ region is shown, rather than the regression slopes for each model. Alongside the $15^\circ \times 15^\circ$ grid-method regression slope, correlation coefficients for the fit are calculated at the level 3 grid box resolution for each season before averaging across all four seasons. The number of ϕ–τ paired daily data points contributing towards the regression slopes

[1]The other possible combination of log–lin is not considered because it seems unphysical for a cloud property to be an exponential function of τ.

and correlations for each grid box are also shown. Again, the AeroCom model median correlation coefficient and number of points are shown for each grid box.

3.2 Results and discussion

3.2.1 Aerosol optical depth (τ)

The mean Aqua-MODIS Science Team Collection 5 τ field for the low τ days ($\tau <$ seasonal grid box median) averaged across all four seasons is shown in Figure 3.1(a). The purple and blue indicate low τ. The missing grey regions are due to the Collection 5 aerosol retrieval failing over bright surfaces, such as the Sahara Desert region of North Africa. The corresponding τ field for high τ conditions is shown in Figure 3.1(b). The second map contains much more green, yellow and red compared to the first, indicating higher τ, as expected by definition of the analysis. To the west of North Africa, the high τ due to dust storms is very evident. Also, anthropogenic aerosol over the Indo-Gangetic plain and East Asia is clearly visible. In general, the North Atlantic ocean has higher τ than the South Atlantic ocean due to the presence of more anthropogenic aerosol in the Northern Hemisphere. The band of high τ in the extratropical southern ocean is likely due to a combination of sea-salt emission and sea-surface reflectance effects, both dependent on the high wind speeds found in this region. This will be investigated further in Chapter 5. Figure 3.1(c) shows the difference between the two previous maps (high $-$ low). The ubiquitous red shows an increase in τ, as expected. It can be seen that regions with higher mean τ generally have a larger absolute difference between the low and the high τ means.

The second row, Figures 3.1(d)–(f), shows similar maps for the Aqua-MODIS Science Team Collection 4 τ, the τ data contained in the CERES SSF footprint. As can be seen, there are no missing regions in these Collection 4 fields. This is because the quality control on the level 3 τ data derived from the CERES SSF is less robust than for the more recent Collection 5 τ, so fewer retrievals over bright surfaces are dismissed in the CERES SSF Collection 4 than in Collection 5. It can be seen that in both the high and low τ cases, Collection 4 τ is generally very similar to Collection 5 τ over ocean. However, Collection 4 τ is generally much higher than Collection 5 τ over land (Bellouin et al., 2008). This is most likely due to poorer quality control in Collection 4 and the use of an improved retrieval in Collection 5. The very large difference between the two retrievals over Australia is likely

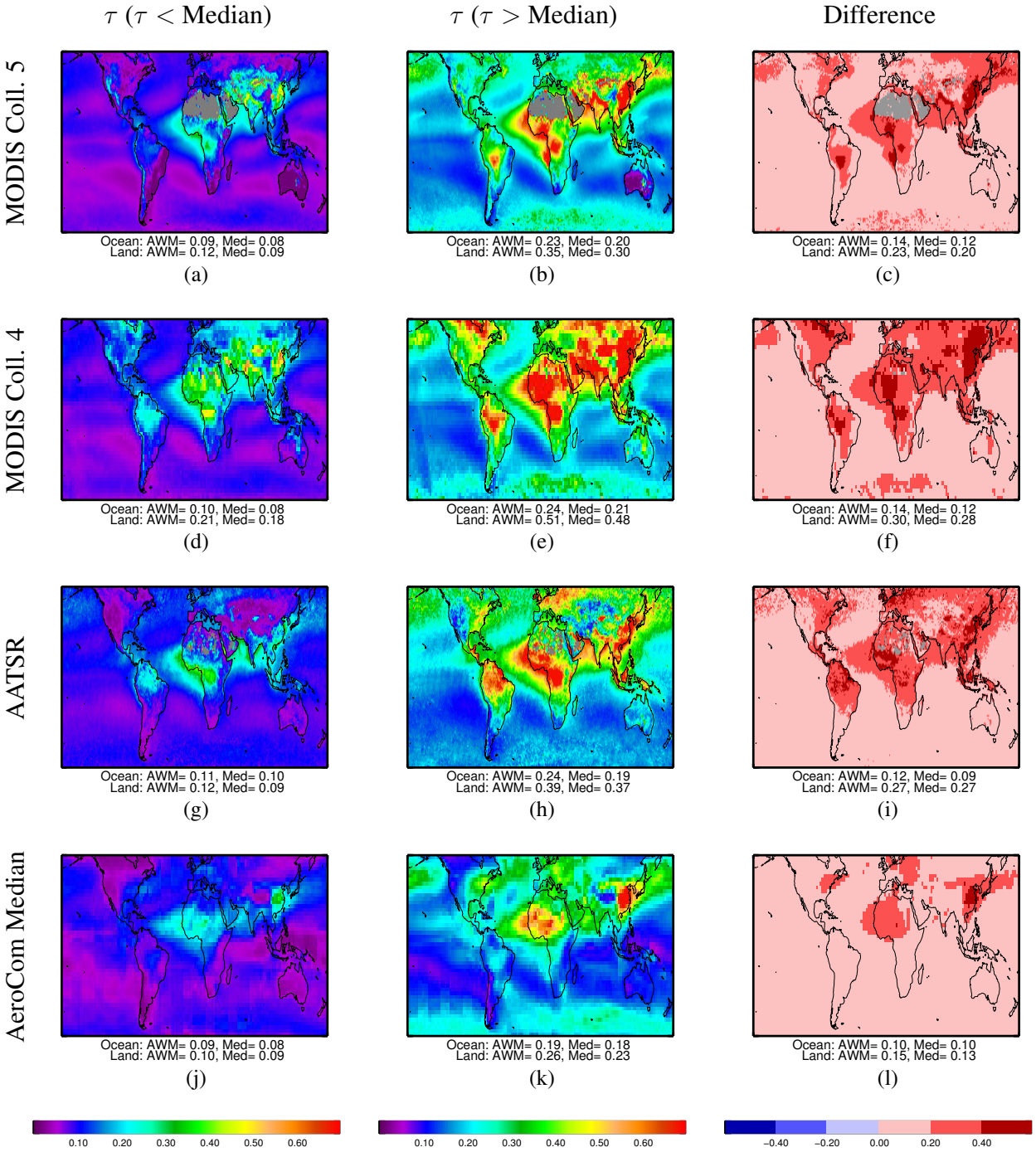

Figure 3.1: Annual (all seasons) mean aerosol optical depth (τ) for low τ ($\tau >$ seasonal grid box median; first column) and high τ ($\tau <$ seasonal grid box median; second column) conditions, and the difference between these (third column), for different satellite and model datasets: Aqua-MODIS Collection 5 (first row), Aqua-MODIS CERES SSF (which contains Collection 4 τ; second row), AATSR (GlobAEROSOL τ with ORAC cloud; third row) and the median of the AeroCom model results (fourth row). Grey represents missing data. An area-weighted mean (AWM) and median (Med) is provided beneath each map.

due to the bright surface. The difference map again shows an increase everywhere, as expected, and a similar spatial pattern to that for Collection 5. The increase over ocean is very similar to Collection 5, but the increase over land is much larger due to the presence of some significantly higher aerosol

retrievals most likely due to land retrieval and quality control differences, as mentioned above.

GlobAEROSOL AATSR τ, Figures 3.1(g)–(i), is generally similar to the Aqua-MODIS τ over ocean. One difference is that AATSR often sees lower τ than MODIS over the remote extratropical southern ocean, most likely due to the fact that the GlobAEROSOL retrieval has a wind speed dependent sea-surface reflectance correction. AATSR sees higher τ than MODIS over the North Atlantic ocean. Over land, AATSR is in much better agreement with MODIS Collection 5 than with Collection 4, except over the north of South America, Australia and Northern Europe.

The median low τ mean, high τ mean and difference for the AeroCom models are shown in Figures 3.1(j)–(l). Over ocean, the τ fields are comparable to those for the satellite datasets. There is a strong τ signal in the extratropical southern ocean, indicative of strong sea-salt emission. The visible vertical banding is due to sampling issues in one of the models, the Hadley Centre Model. The biomass burning contribution to τ appears to be poorly captured in the AeroCom Median, as evidenced by the low τ over northern South America and Sub-Saharan Africa compared to the satellite datasets. The difference map shows that there is a significantly smaller variation between low and high τ conditions than in the satellite datasets, particularly over land.

3.2.2 Liquid cloud droplet number concentration (N_d)

Figure 3.2(a) shows the mean Aqua-MODIS Science Team Collection 5 derived liquid cloud droplet number concentration (N_d) for conditions where daily τ is less than the seasonal median for that grid box. The grey regions of missing data over bright surfaces arise because there are no τ data here for categorization into low τ and high τ conditions. Over land, Collection 5 N_d is generally much higher than over ocean. As can be seen in the difference map, Figure 3.2(c), N_d generally increases over the ocean as one moves to high τ conditions, as expected from the conceptual cloud albedo effect. However, the blue over some land regions and the negative global mean and median for the land shows that Collection 5 N_d often decreases as one moves to high τ conditions over land.

Figure 3.3 shows the coefficient of determination (R^2), averaged over all four seasons, for log–log, lin–log and lin–lin regression fits of Collection 5 N_d versus τ. Blue shows very weak fits, while green and red show better fits. The spatial distribution of R^2 is similar for all three attempted fits. The global mean R^2 values, shown beneath the maps, are of order 0.03, showing that on average only 3% of the variance in N_d can be explained by τ using these regression fits. However, R^2 is much

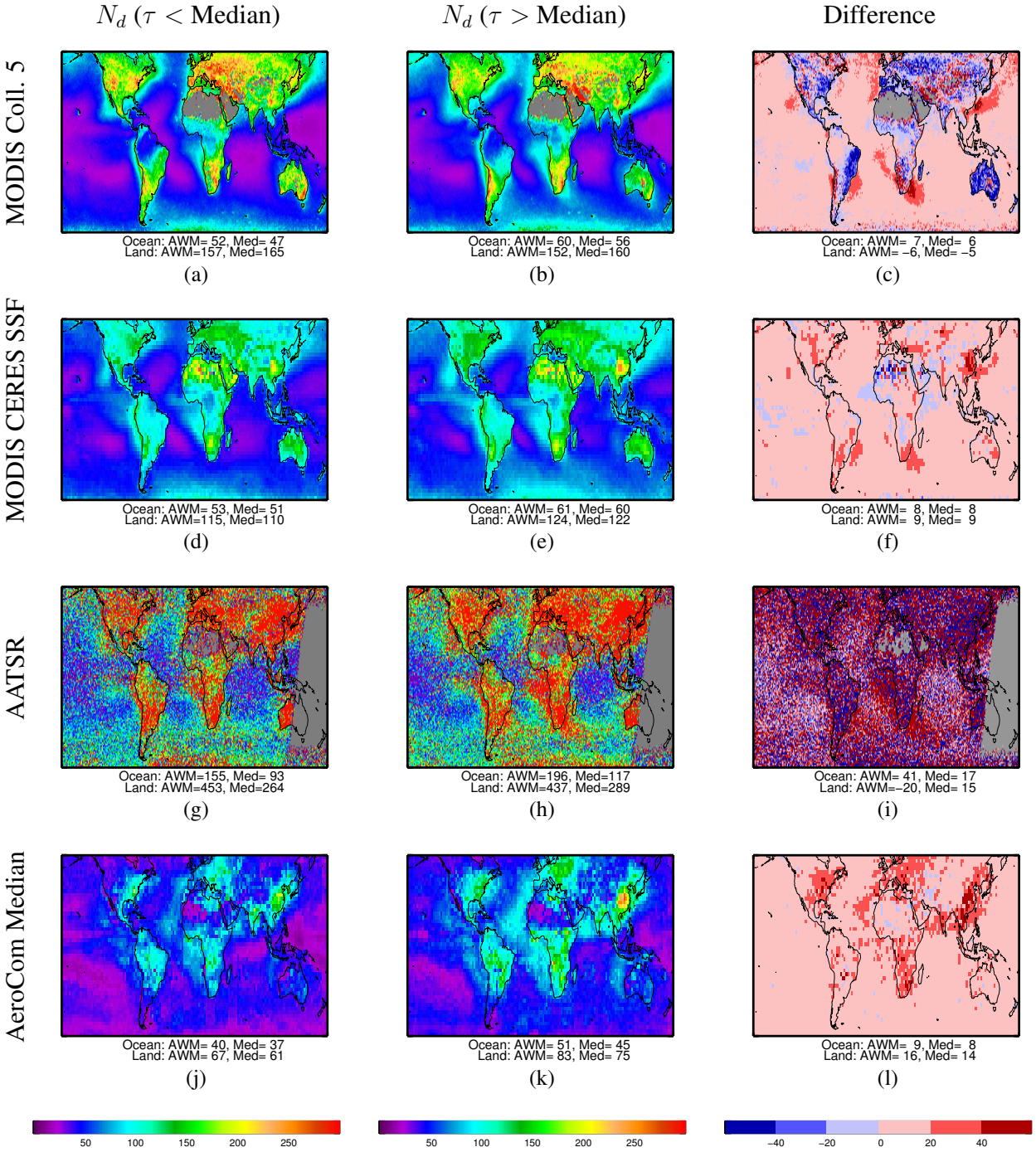

Figure 3.2: Same as Figure 3.1, but for mean liquid cloud droplet number concentration (N_d, cm^{-3}), again categorised according to low aerosol optical depth (τ) and high τ conditions. The reasons for the noise and missing values in the AATSR data are discussed in the text.

higher in the red areas, including the East Asian outflow region to the east of China, where at least 10% of the variance in N_d can be explained. By looking at the global means and medians, provided below each map, it can be seen that a log–log fit empirically appears to be the most successful of these three fits over ocean. This is consistent with the theoretical consideration of Equation 1.9, assuming that the cloud albedo effect is the major contributor to the relationship between τ and N_d.

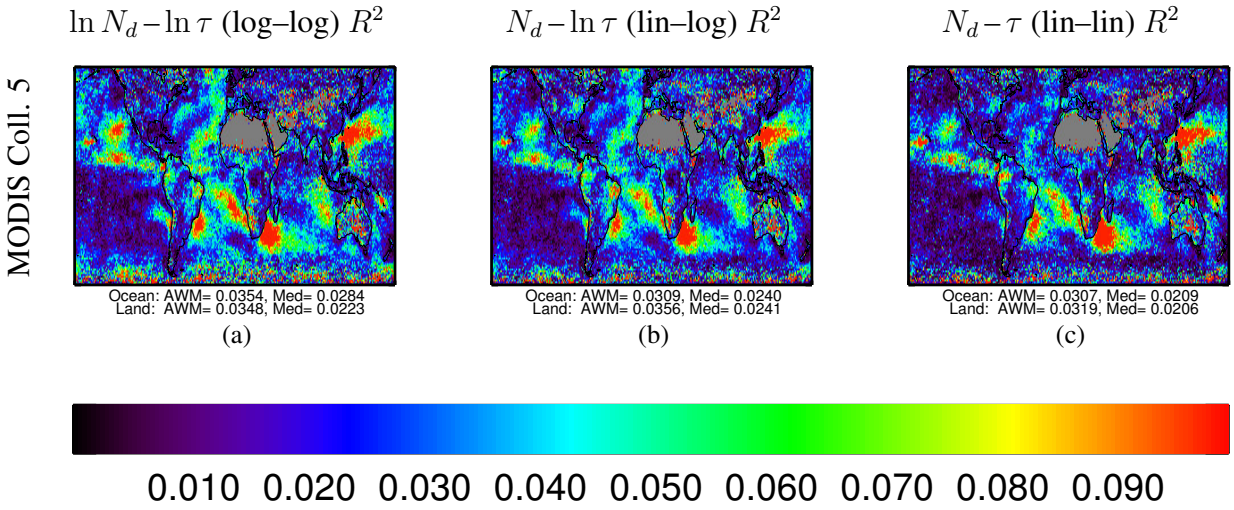

Figure 3.3: Annual mean (averaged over four seasons) coefficient of determination (R^2) for log–log (a), lin–log (b) and lin–lin (c) ordinary least squares fits of Aqua-MODIS Collection 5 derived liquid cloud droplet number concentration (N_d) to aerosol optical depth (τ). Grey represents missing data. An area-weighted mean (AWM) and median (Med) is provided beneath each map.

Over land, however, the lin–log fit appears to be more successful than the log–log fit. Due to the theoretical justification for using the log–log fit here, and also because much of the later part of this thesis focuses on ocean rather than land regions, the log–log fit is chosen here.

Figure 3.4(a) shows the log–log ordinary least squares regression slope of N_d versus τ for the Collection 5 data, averaged to $15^\circ \times 15^\circ$ using the grid-method of Chapter 2. This log–log regression slope was referred to as the sensitivity of N_d to τ in Chapter 2. The corresponding correlation coefficient (r) is shown in Figure 3.4(b), with orange showing positive correlations and purple showing negative correlations. In agreement with Figure 3.2(c), positive slopes and correlations are generally observed over the ocean, with negative values observed over many land regions. The global error-weighted means are $+0.146$ and -0.042 respectively. Regions with larger differences between low and high τ conditions often correspond to regions with steeper slopes and stronger correlations. Figure 3.4(c) shows the number of paired data points contributing to the slope and correlation calculations for each grid box. The presence of dark green over most of the world shows that there are generally hundreds of contributing data points for each grid box.

N_d derived from the Aqua-MODIS CERES SSF, Figures 3.2(d) and (e), has a similar spatial distribution to the Collection 5 N_d. However, the absolute values are lower over land. The difference in SSF N_d as one moves from low τ to high τ conditions, shown in Figure 3.2(f), is generally positive over both ocean and land, in contrast to the Collection 5 dataset which often had decreases over land.

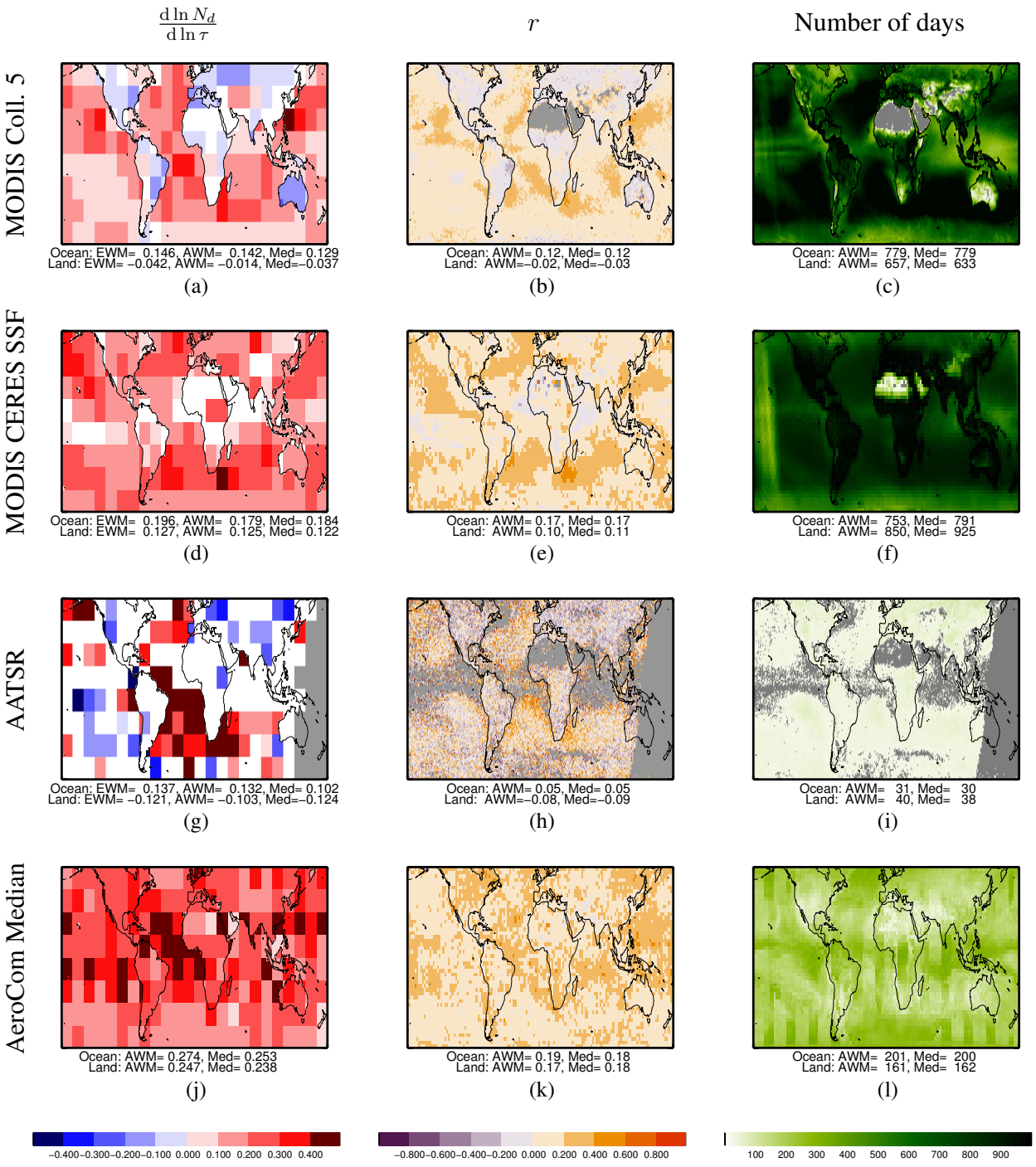

Figure 3.4: Results of a log–log ordinary least squares regression fit of liquid cloud droplet number concentration (N_d) to aerosol optical depth (τ) for different satellite and model datasets, assuming $\ln N_d = a + b \ln \tau + \epsilon$ where a and b are constants and ϵ is the error representing other terms not included in the linear model. First column: annual (all seasons one-sigma error weighted $15^\circ \times 15^\circ$ grid-method) mean regression coefficient $\frac{\mathrm{d}\ln N_d}{\mathrm{d}\ln\tau}$. White regions show where data are not significantly different from zero at two-sigma confidence. Grey represents missing data. Second column: annual mean correlation coefficient r. Third column: total number of days contributing paired data. An area-weighted mean (AWM) and median (Med) is provided beneath each map. For the satellite regression slopes, an error-weighted mean (EWM) is also provided.

Over ocean, the SSF N_d versus τ regressions slopes and correlations, shown in Figures 3.4(d) and (e), are generally slightly stronger than those of Collection 5. Again, it can be seen that the slopes and correlations are generally positive over land, in contrast to the Collection 5 values. These positive relationships over both land and ocean in the CERES SSF dataset have been previously observed by Quaas et al. (2008). The inconsistency between these datasets over land, where retrievals are less reliable, highlights the need to be careful when using satellite datasets. Although a signal may appear clear in one dataset, the use of a second dataset may show that the result is inconclusive and likely due to retrieval biases.

AATSR N_d, Figures 3.2(g) and (h), has a similar ocean-land contrast to the MODIS derived N_d data, although the absolute values for AATSR N_d are much higher. These higher N_d values are largely due to the fact that $N_d \propto r_e^{-\frac{5}{2}}$, so a small change in r_e can lead to a large change in N_d, and AATSR has much smaller retrieved r_e than either of the MODIS datasets (Figure 3.5). The missing data over the West Pacific are due to level 2 date mismatching between the level 3 gridded AATSR GlobAEROSOL aerosol and ORAC cloud datasets. The AATSR N_d differences, Figure 3.2(i), are much noisier than the MODIS N_d differences, likely because there is less AATSR input data, Figure 3.4(i). The global increase over ocean appears clear, with an increase in both the global mean and median, consistent with the two MODIS datasets. However, the global change over land is ambiguously noisy, with a negative mean and a positive median. By looking at the $15^\circ \times 15^\circ$ grid-method regression slopes, Figure 3.4(g), which have the advantage of error-weighting, a negative signal over land and some ocean regions becomes more evident. Strong positive slopes are observed over much of the Atlantic ocean. However, many regions, particularly land regions, have statistically insignificant slopes, probably due to the smaller amount of input data compared to MODIS. The global error-weighted mean slopes are $+0.137$ over ocean and -0.121 over land.

Over ocean, the global error-weighted mean slopes of satellite-derived N_d versus τ vary between $+0.137$ (AATSR) and $+0.196$ (MODIS CERES SSF). These generally positive relationships are consistent with the in situ aircraft studies of Twohy et al. (2005) and Lu et al. (2007), and the ground-based remote sensing study of McComiskey et al. (2009), who observed positive relationships between N_d and τ for stratocumulus clouds (Section 1.4.1). Over land, they vary between -0.121 (AATSR) and $+0.127$ (MODIS CERES SSF), providing no constraint on the sign of the relationships over land.

The AeroCom Median N_d, Figures 3.2(j) and (k), has a similar magnitude to the MODIS datasets over ocean, but is much lower than the satellite datasets over land. The difference, Figure 3.2(l), is again very similar to the MODIS datasets over ocean. It is almost always positive over land. The regression slopes and correlations, Figures 3.4(j,k), are positive over both ocean and land. The slopes are generally steeper than for the satellite datasets, with global error-weighted means of $+0.274$ for ocean and $+0.247$ for land.

3.2.3 Liquid cloud droplet effective radius (r_e)

As can be seen in Figures 3.5(a) and (b), for the Aqua-MODIS Collection 5 dataset, smaller liquid cloud droplet effective radii (r_e) are generally observed over land compared to over ocean. This is consistent with higher N_d being observed over land, as mentioned in the previous section. The spatial distribution of r_e is approximately inversely related to that of N_d, according to Equation 1.7. The difference in r_e as one moves from low to high τ conditions, Figure 3.5(c), generally shows a decrease over the ocean and an increase over land. This is also consistent with the N_d results discussed previously.

The global mean and median coefficients of determination, Figure 3.6, are highest for the lin–log fit over ocean and for the log–log fit over land. The log–log fit is chosen here, largely because theoretical considerations suggest that a log–log fit of r_e versus τ may be a good way to quantify the cloud albedo effect (Equation 1.8). The ocean R^2 values are generally lower for $\ln r_e$ versus $\ln \tau$ (mean 0.023) than they are for $\ln N_d$ versus $\ln \tau$ (mean of 0.035), suggesting that derived N_d may be more closely linked to τ than r_e is. This is consistent with the fact that Equation 1.8 assumes stratification according to liquid water path, something which is not accounted for here. However, the mean land R^2 value is higher for $\ln r_e$ versus $\ln \tau$ (0.041) than it is for $\ln N_d$ versus $\ln \tau$ (0.035), the reasons for which are unknown.

The Collection 5 $\ln r_e$ versus $\ln \tau$ regression slopes and correlation coefficients, Figures 3.7(a) and (b), are generally negative over ocean and positive over land, in agreement with the signs of the difference between low and high τ conditions. For the ocean slopes, more regions are statistically insignificant compared to the N_d slopes. This may be due to the lack of liquid water path stratification, as mentioned above.

Aqua-MODIS CERES SSF r_e values, Figures 3.5(d) and (e), are generally slightly smaller than

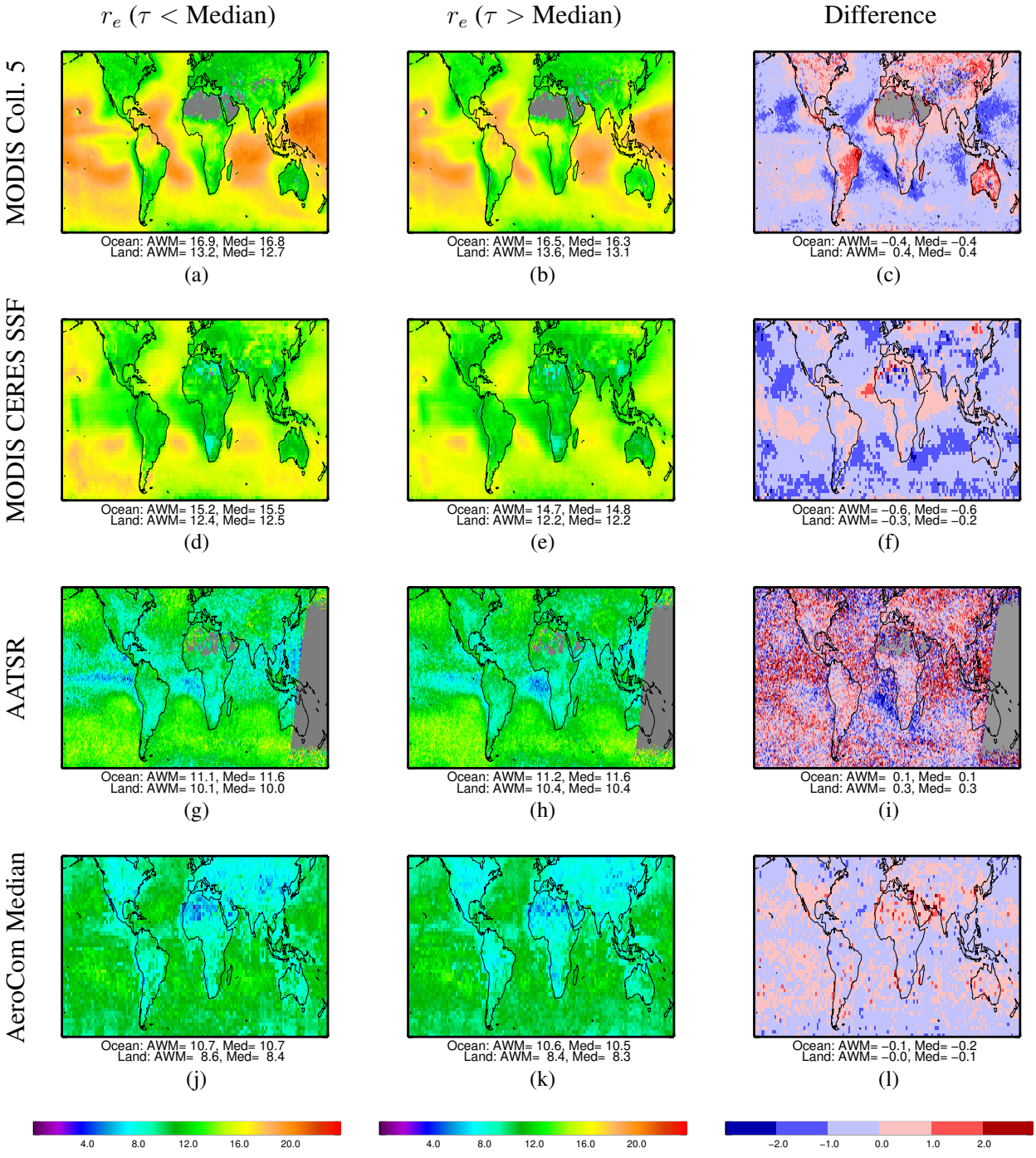

Figure 3.5: Same as Figure 3.1, but for mean liquid cloud droplet effective radius (r_e, μm).

the Collection 5 r_e. The mean r_e generally decreases as one moves from low to high Collection 4 τ conditions, as shown in Figure 3.5(f). The regression slopes and correlations, Figures 3.7(d) and (e), are likewise negative.

AATSR r_e, Figures 3.5(g) and (h), is much smaller than the MODIS retrieved r_e datasets. The land–ocean contrast is also weaker for AATSR than it is for the MODIS datasets. One further difference is that the AATSR r_e is very small to the east of Indonesia, whereas the MODIS Collection 5 r_e

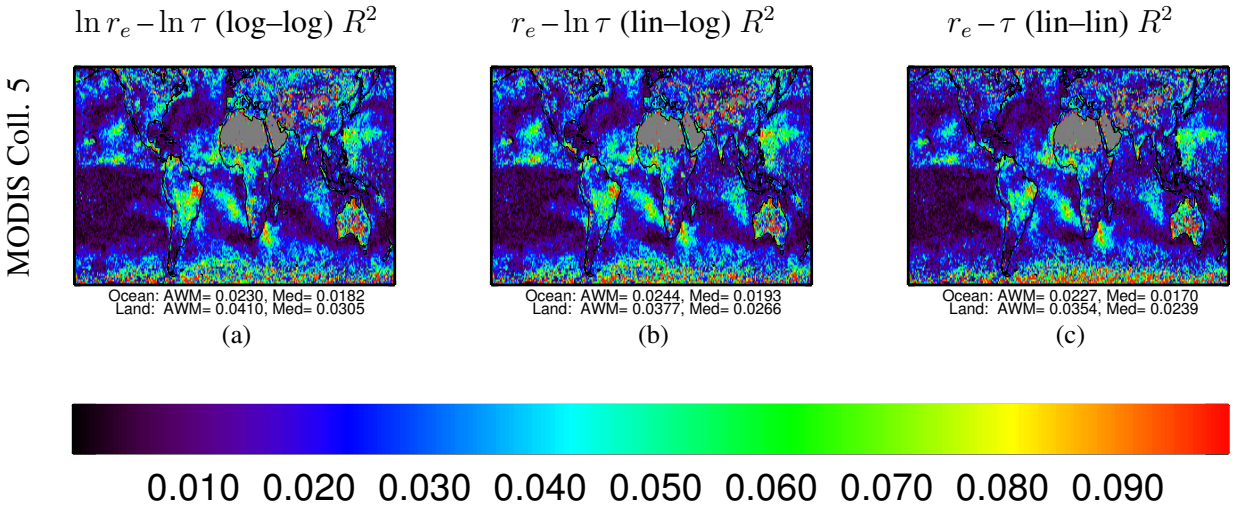

Figure 3.6: Same as Figure 3.3, but for fits of liquid cloud droplet effective radius (r_e) to aerosol optical depth (τ).

is large here. The difference in AATSR r_e between low and high τ conditions, Figure 3.5(i), is very noisy, although the global averages are positive over both land and ocean. The same is true for the $\ln r_e - \ln \tau$ correlation coefficients. This positive relationship between $\ln \tau$ and $\ln r_e$ is clearer for the regression slopes, particularly over ocean. This is in strong disagreement with the MODIS datasets.

Over ocean, the global error-weighted mean regression slopes of satellite-retrieved r_e versus τ vary between -0.042 (CERES SSF) and $+0.049$ (AATSR). Over land, they vary between -0.012 (CERES SSF) and $+0.042$ (AATSR). The strong disagreement between the three satellite datasets suggests that they provide very little constraint on the sign of relationships between τ and r_e over both ocean and land.

The AeroCom Median r_e data, Figures 3.5(j) and (k), are of a similar size to the AATSR r_e. The land–ocean contrast is stronger than in the AATSR dataset. The average differences between low and high τ conditions, Figure 3.5(l), are very slightly negative for both ocean and land, although positive differences are observed across much of the world. The same is true for the correlations, Figure 3.7(k). The global distribution of regression slopes, Figure 3.5(j), appears slightly noisy, although negative slopes dominate.

3.2.4 Cloud top temperature (T_{top})

The mean Aqua-MODIS Collection 5 cloud top temperatures (T_{top}) for low τ and high τ conditions are shown in Figures 3.8(a,b). All clouds, not just liquid clouds, contribute to T_{top}. Temperature

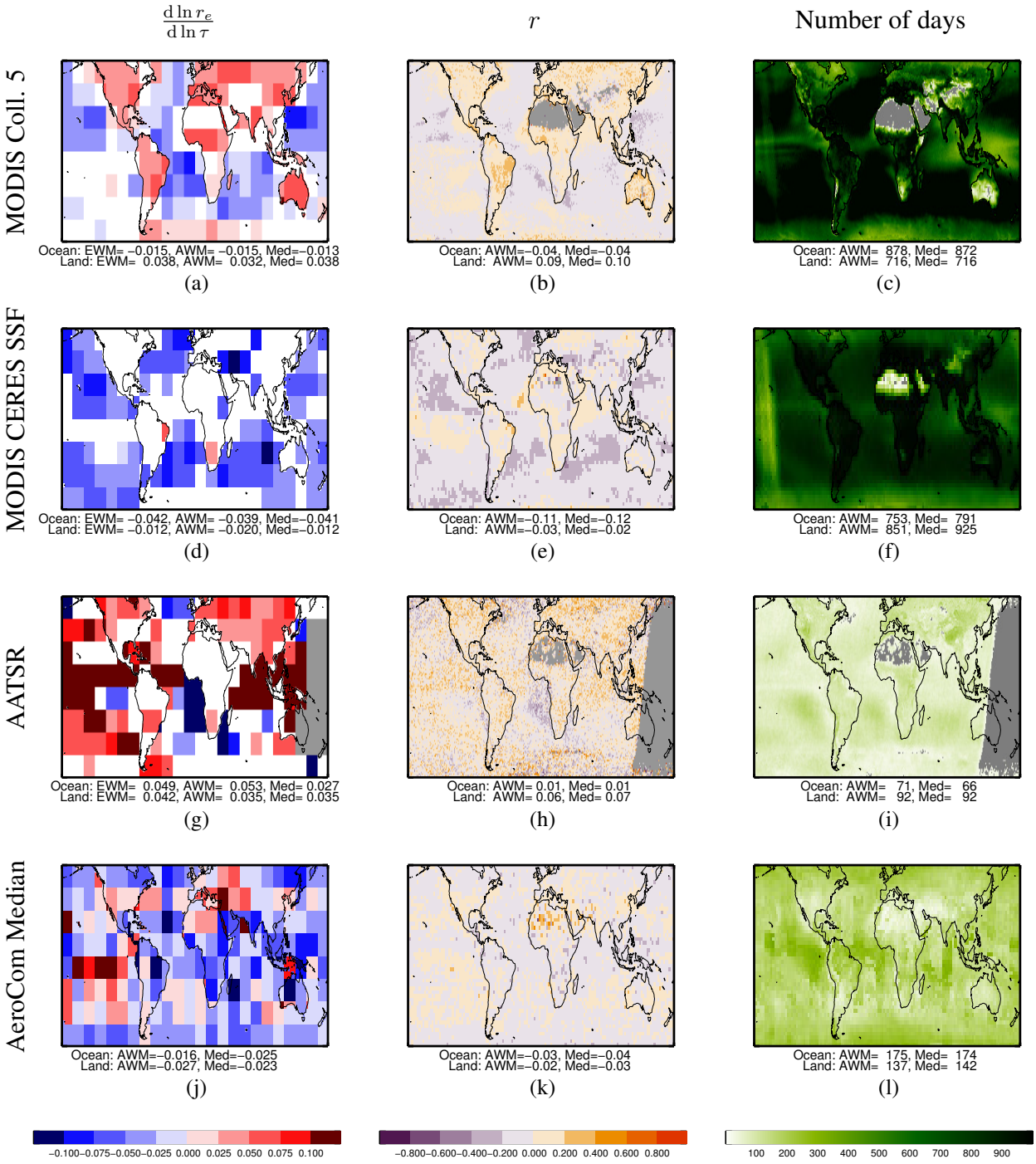

Figure 3.7: Same as Figure 3.4, but for results of a log–log ordinary least squares regression fit of liquid cloud droplet effective radius (r_e) to aerosol optical depth (τ), assuming $\ln r_e = a + b \ln \tau + \epsilon$.

generally decreases with height in the troposphere, so T_{top} is a good surrogate for cloud top height. Of course, T_{top} is also heavily dependent on location and season for a given cloud top height. Red regions show warm cloud tops, corresponding to lower clouds for a given region and season. It can be seen that over the ocean, warmer cloud tops are generally found towards the warmer equator. For the high τ conditions, cold cloud tops are observed near South-East Asia and over equatorial Africa,

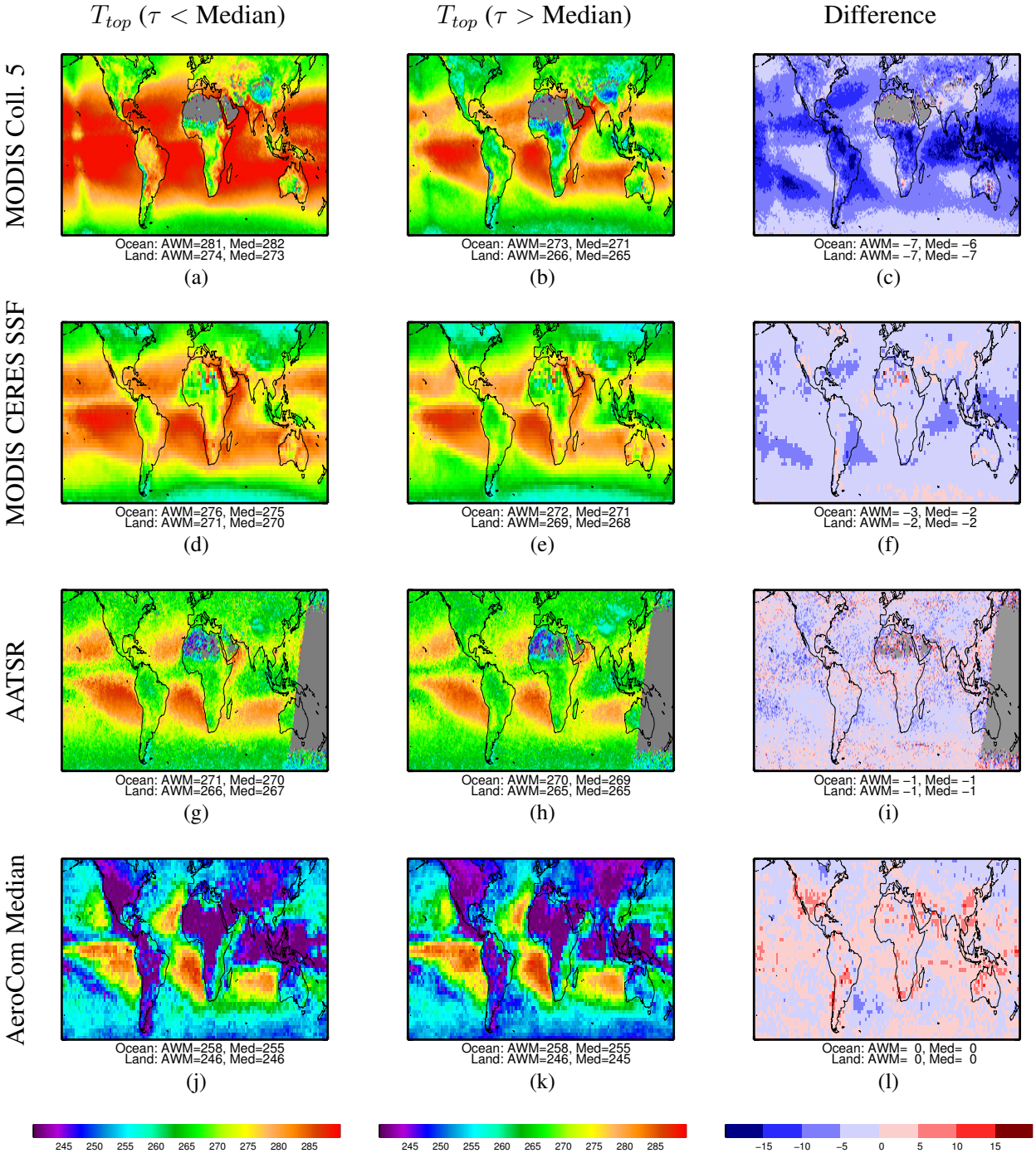

Figure 3.8: Same as Figure 3.1, but for mean cloud top temperature (T_{top}, K).

showing that high cloud tops frequently occur in these regions. As demonstrated by Figure 3.8(c), there is a global decrease in T_{top} (i.e. an increase in cloud top height) as one moves from low τ to high τ conditions, particularly near South-East Asia.

As can be seen in Figure 3.9, the largest mean and median coefficients of determination are found for the lin–lin fit of Collection 5 T_{top} versus τ for both ocean and land. In the absence of theoretical reasons for choosing a different fit, the empirically determined lin–lin fit is used here. The lin–lin R^2

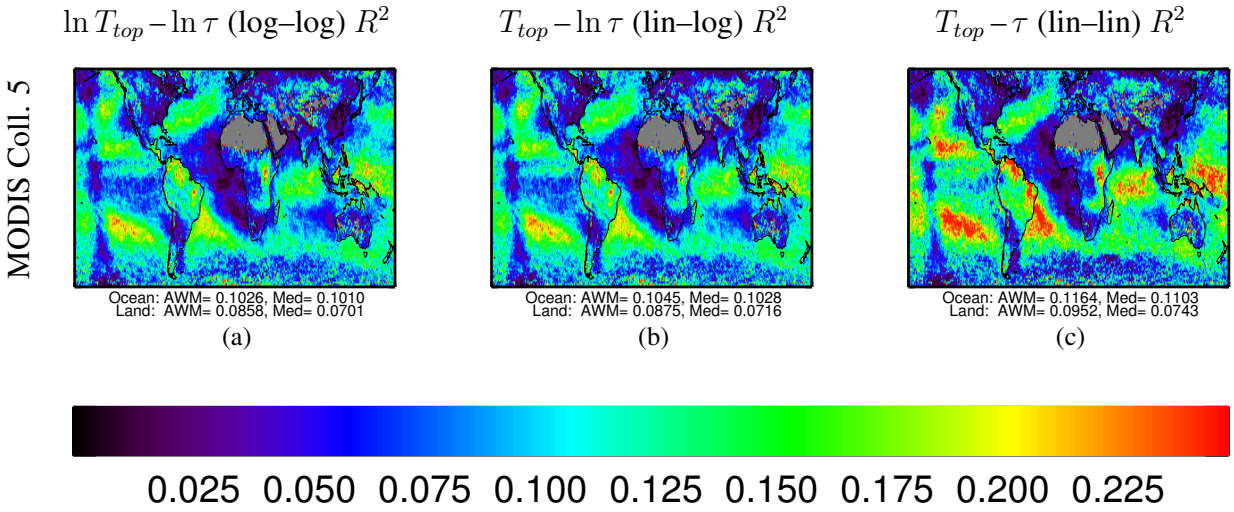

Figure 3.9: Same as Figure 3.3, but for fits of cloud top temperature (T_{top}) to aerosol optical depth (τ). Note differing colour scales.

global means are approximately 0.1 over both ocean and land, suggesting that approximately 10% of the variance in T_{top} can be generally be explained by τ. For some regions, notably parts of the subtropical Pacific ocean, the subtropical western South Atlantic ocean, the tropical Indian ocean and South-East Asia, R^2 is much larger, sometimes larger than 0.25. These values suggest that T_{top} is more closely linked to τ than either N_d or r_e is.

The corresponding regression slopes and correlations, Figures 3.10(a) and (b), are negative. Again, this demonstrates a positive relationship between Collection 5 τ and cloud top height. This was previously observed for convective clouds in the North Atlantic by Koren et al. (2005), who used an earlier collection of MODIS data. It is consistent with strong convective invigoration by aerosols (Section 1.4.3). However, it is also possible that this may be a spurious correlation caused by retrieval errors or synoptic conditions, discussed in Chapter 6.

Aqua-MODIS CERES SSF T_{top} data also generally decrease as one moves to higher τ conditions, as shown by Figures 3.8(d)–(f). However, the decreases are not found everywhere and they are not as strong as for the Collection 5 data. The same is true of the weaker correlations in Figure 3.10(e). For the regression slopes, most $15^\circ \times 15^\circ$ regions are statistically insignificant.

The relationship between τ and T_{top} is weaker still for the AATSR data (Figures 3.8i, 3.10g and 3.10h). The $15^\circ \times 15^\circ$ regions all have insignificant slopes, but the global error-weighted means are negative for both ocean and land.

Although the satellite datasets all show negative relationships between τ and T_{top}, the strength of

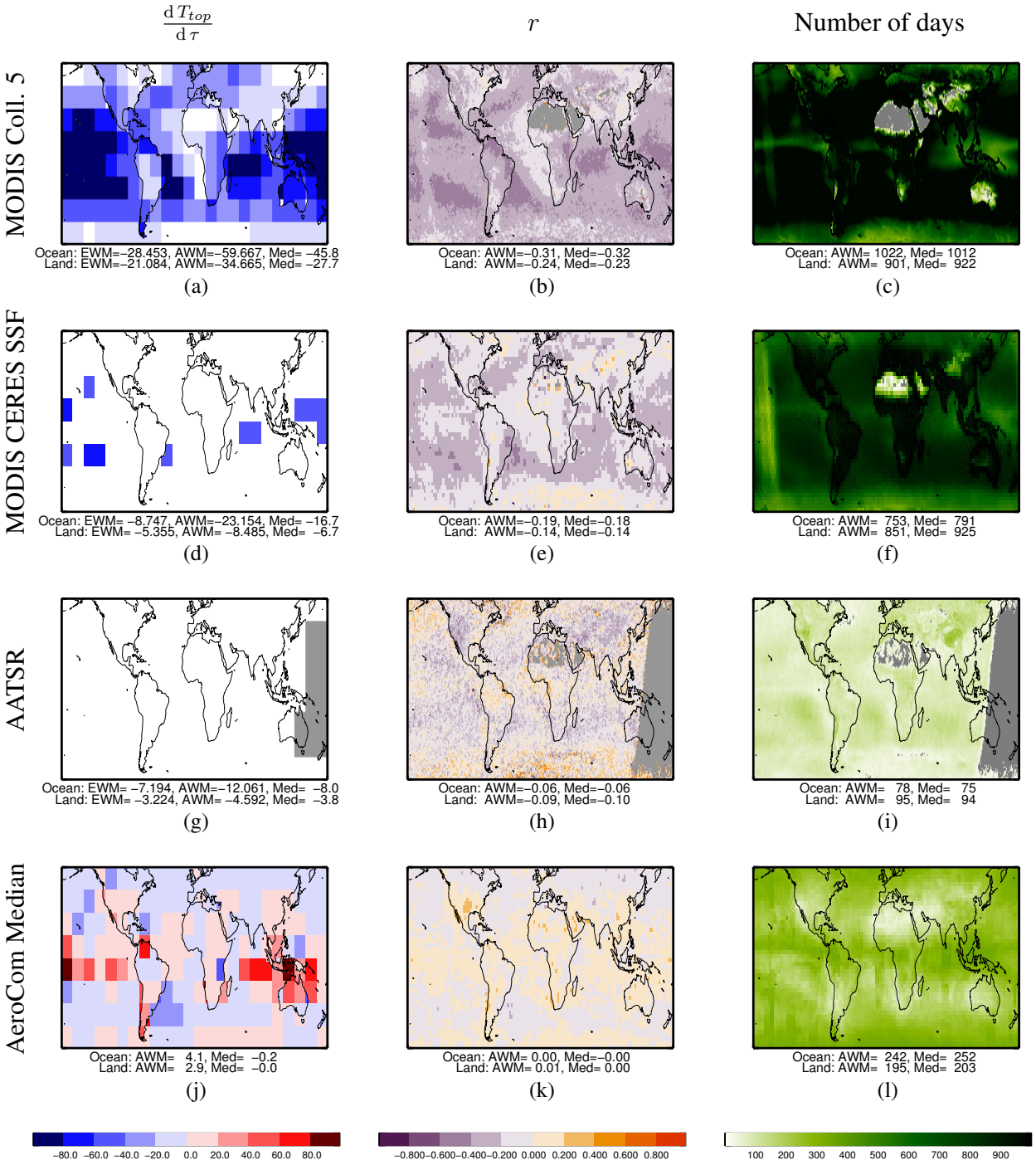

Figure 3.10: Same as Figure 3.4, but for results of a lin–lin ordinary least squares regression fit of cloud top temperature (T_{top}, K) to aerosol optical depth (τ), assuming $T_{top} = a + b\,\tau + \epsilon$.

these relationships are poorly constrained. The global error-weighted mean regression slopes vary between -7 K (AATSR) and -28 K (Collection 5) over ocean and between -3 K (AATSR) and -21 K (Collection 5) over land. The strong signal evident in the Aqua-MODIS Collection 5 data is not reproduced in the other satellite datasets, suggesting that retrieval errors may be responsible for this strong signal. As mentioned earlier, a very strong signal is observed in South-East Asia.

Thin tropical cirrus is known to be common here. When this is correctly identified as cloud, cold T_{top} values will be observed. However, it may sometimes be misidentified as aerosol, leading to contaminated erroneously high τ retrievals (Huang et al., 2011).

As can be seen in Figures 3.8(j) and (k), the AeroCom Median T_{top} data is generally much colder than the retrieved satellite data for both low τ and high τ conditions. This suggests that high clouds may be unrealistically common in the models, preventing lower clouds from being sampled. On average, there is no difference in T_{top} between low τ and high τ conditions for either the land or ocean, corroborated by the correlations (Figures 3.8i and 3.10k). However, in strong disagreement with the Aqua-MODIS Collection 5 data, strong positive relationships between τ and T_{top} are produced regionally over South-East Asia. It is worth noting that the AeroCom models used here do not include representations of aerosol effects on convection, so negative relationships between τ and T_{top} are not expected in the AeroCom Median. The positive relationships over South-East Asia may be due to wet scavenging of aerosol by convective precipitation. Although this hypothesis is not tested in this thesis, the contribution of convective wet scavenging to modelled relationships between τ and cloud fraction is investigated in Chapter 4.

3.2.5 Cloud fraction (f_c)

Figure 3.11(a) shows the Aqua-MODIS Collection 5 cloud fraction (f_c) for low τ conditions. As with T_{top}, f_c includes all clouds rather than just liquid clouds. High f_c data, indicated by red, orange and yellow, are observed in the extratropical storm-track ocean regions and in the inter-tropical convergence zone. Much lower f_c data, indicated by purple and blue, are observed over many land regions. As one moves to high τ conditions, Figure 3.11(b), f_c increases substantially. This is shown by the increase everywhere in Figure 3.11(c). Some of the largest increases are observed in the subtropics.

When choosing which fit to use, it is worth considering that a linear axis, as opposed to a logarithmic axis, probably makes most sense for f_c, which varies from 0 to 1. The coefficients of determination, Figure 3.12, suggest that a lin–log fit is the most appropriate choice. The global average R^2 values are approximately 0.2 for both ocean and land, higher than for any of the other cloud properties, suggesting that 20% of the variance in f_c can be explained by changes in τ.

The regression slopes and correlations, Figures 3.13(a) and (b), also show positive relationships between τ and f_c at all points. The Collection 5 $f_c - \ln \tau$ correlations are stronger than for any of the

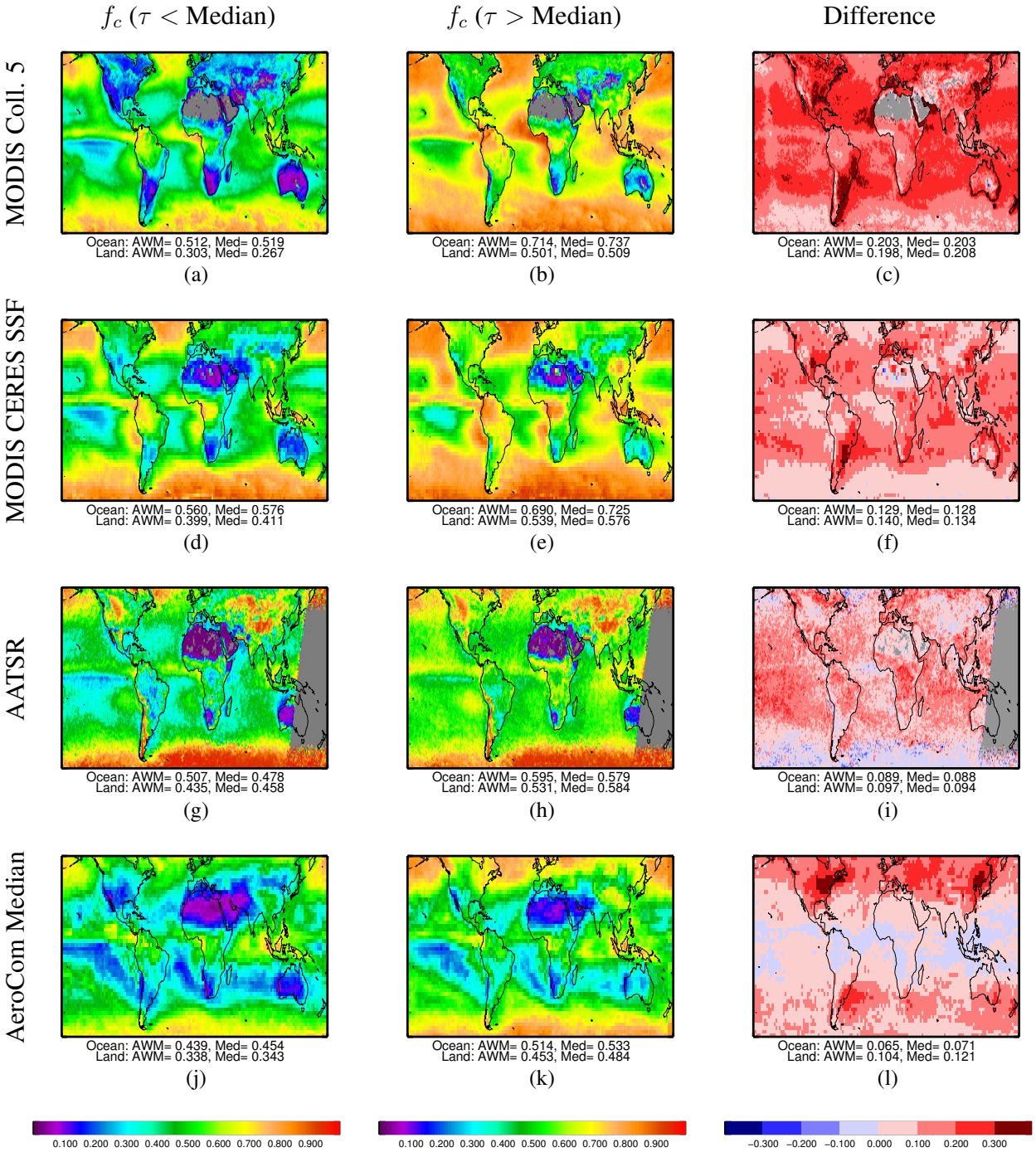

Figure 3.11: Same as Figure 3.1, but for mean cloud fraction f_c.

other ϕ–τ correlations, in agreement with the R^2 values mentioned above.

The Aqua-MODIS CERES SSF f_c data, Figures 3.11(d) and (e), are similar to the Collection 5 f_c data. Again, an increase is observed everywhere as one moves to high τ conditions, as can be seen in Figure 3.11(f). The regression slopes and correlations, Figures 3.13(d) and (e), are also positive. However, the differences, regression slopes and correlations are not as high as for the Collection 5 data.

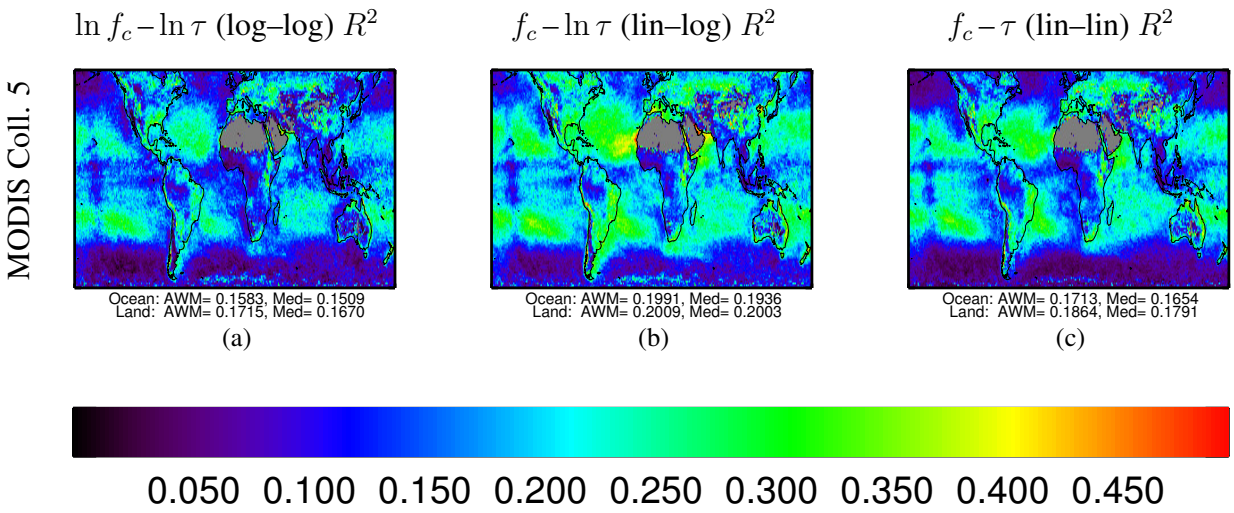

Figure 3.12: Same as Figure 3.3, but for fits of cloud fraction (f_c) to aerosol optical depth (τ).

AATSR f_c, Figures 3.11(g) and (h), has a similar spatial distribution to the Aqua-MODIS f_c datasets. A general increase in f_c as one moves to high τ conditions is also observed, Figure 3.11(i), although the increase is not as large as in the Aqua-MODIS datasets. Some decreases are observed in the Southern Ocean. The regression slopes are mostly positive and not statistically insignificant[2], and the correlations are generally positive. However, these positive signals are again weaker than in the two Aqua-MODIS datasets.

All three satellite datasets are in general agreement about a positive relationship between τ and f_c. The global mean differences in f_c between low and high τ conditions vary between $+0.09$ (AATSR) and $+0.20$ (Collection 5) over ocean and between $+0.10$ (AATSR) and $+0.20$ (Collection 5) over land. These observations are consistent with the conceptual cloud lifetime effect. However, satellite retrieval errors may also be able to explain the observations. Increasing f_c may increase the relative potential for sub-pixel cloud contamination of aerosol retrievals, causing spurious correlations between τ and f_c. Also, relative humidity or synoptic conditions may contribute towards the relationships. These will be discussed and investigated further in Chapters 4 and 6.

The AeroCom Median f_c, Figures 3.11(j) and (k), is generally lower than that observed in the satellite datasets. However, it is difficult to compare f_c between different datasets, because it is resolution-dependent. The differences, regression slopes and correlations, Figures 3.11(l), 3.13(j) and 3.13(k), generally show positive relationships between τ and f_c, in broad agreement with the

[2]As mentioned in the footnote in Section 2.1, statistical insignificance does not necessarily imply significance. Therefore, 'not statistically insignificant' is used instead of 'significant'.

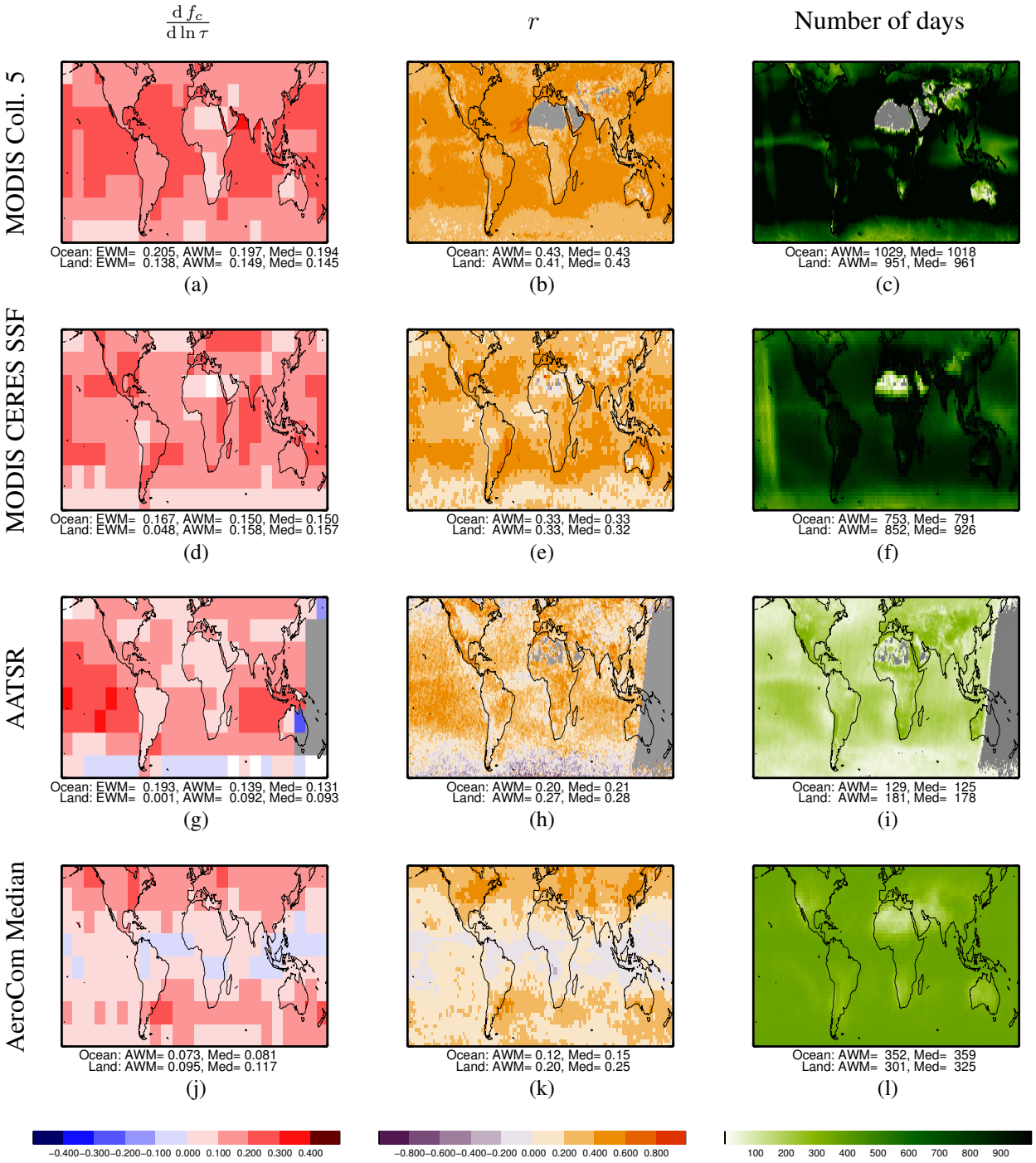

Figure 3.13: Same as Figure 3.4, but for results of a lin–log ordinary least squares regression fit of cloud fraction (f_c) to aerosol optical depth (τ), assuming $f_c = a + b \ln \tau + \epsilon$.

satellite datasets. However, in the tropics the relationship is much weaker than in any of the satellite datasets, and some negative slopes are observed in some equatorial regions. As with the T_{top} results over South-East Asia, the AeroCom Median completely fails to capture the relationships observed in the satellite datasets for the South-East Asian region. This may be due to wet scavenging, as will be discussed in Chapter 4.

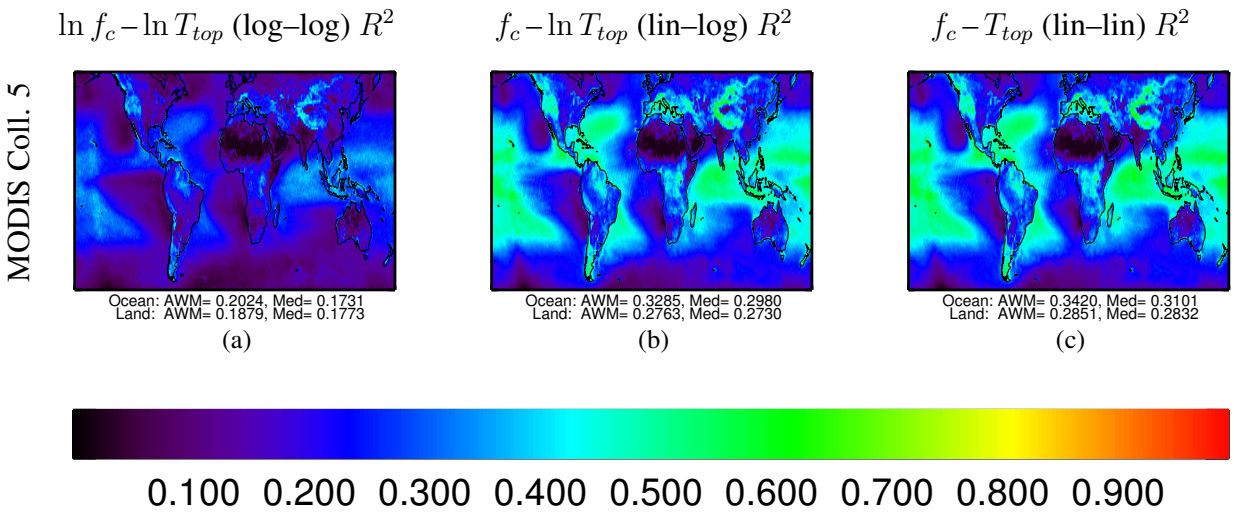

Figure 3.14: Same as Figure 3.3, but for fits of cloud fraction (f_c) to cloud top temperature (T_{top}, K).

3.2.6 Cloud top temperature – cloud fraction

In addition to investigating relationships between τ and cloud properties, it might also be instructive to consider relationships between cloud properties themselves. Relationships between T_{top} and f_c are presented briefly here.

A lin–lin fit of f_c versus T_{top} is chosen, because the coefficients of determination shown in Figure 3.14 empirically suggest that this is the most appropriate fit. The mean R^2 values, approximately 0.3 for both ocean and land, are larger than for any of the ϕ–τ combinations.

The Aqua-MODIS Collection 5 $15^\circ \times 15^\circ$ regression slopes, Figure 3.15(a), are consistently negative and not statistically insignificant. The correlations, Figure 3.15(b), are stronger than for any of the ϕ–τ combinations. As shown in Figure 3.15(c), there are more data points contributing to these slopes and correlations than there were for the ϕ–τ analyses. This is because there are almost always cloud retrievals within a $1^\circ \times 1^\circ$ grid box, whereas successful aerosol retrievals may not always exist, particularly for completely cloudy grid boxes.

The Aqua-MODIS CERES SSF regression slopes, Figure 3.15(d), are considerably steeper than those for Collection 5. The strongest slopes occur in the same locations as for Collection 5, namely in the subtropical South Pacific, South Atlantic and Indian Oceans. The correlations, Figure 3.15(e), are very similar to those for Collection 5, both in spatial distribution and magnitude.

The AATSR slopes, Figure 3.15(g), are also consistently negative and of a similar magnitude to the Aqua-MODIS Collection 5 slopes. The correlations, Figure 3.15(h), are slightly weaker than

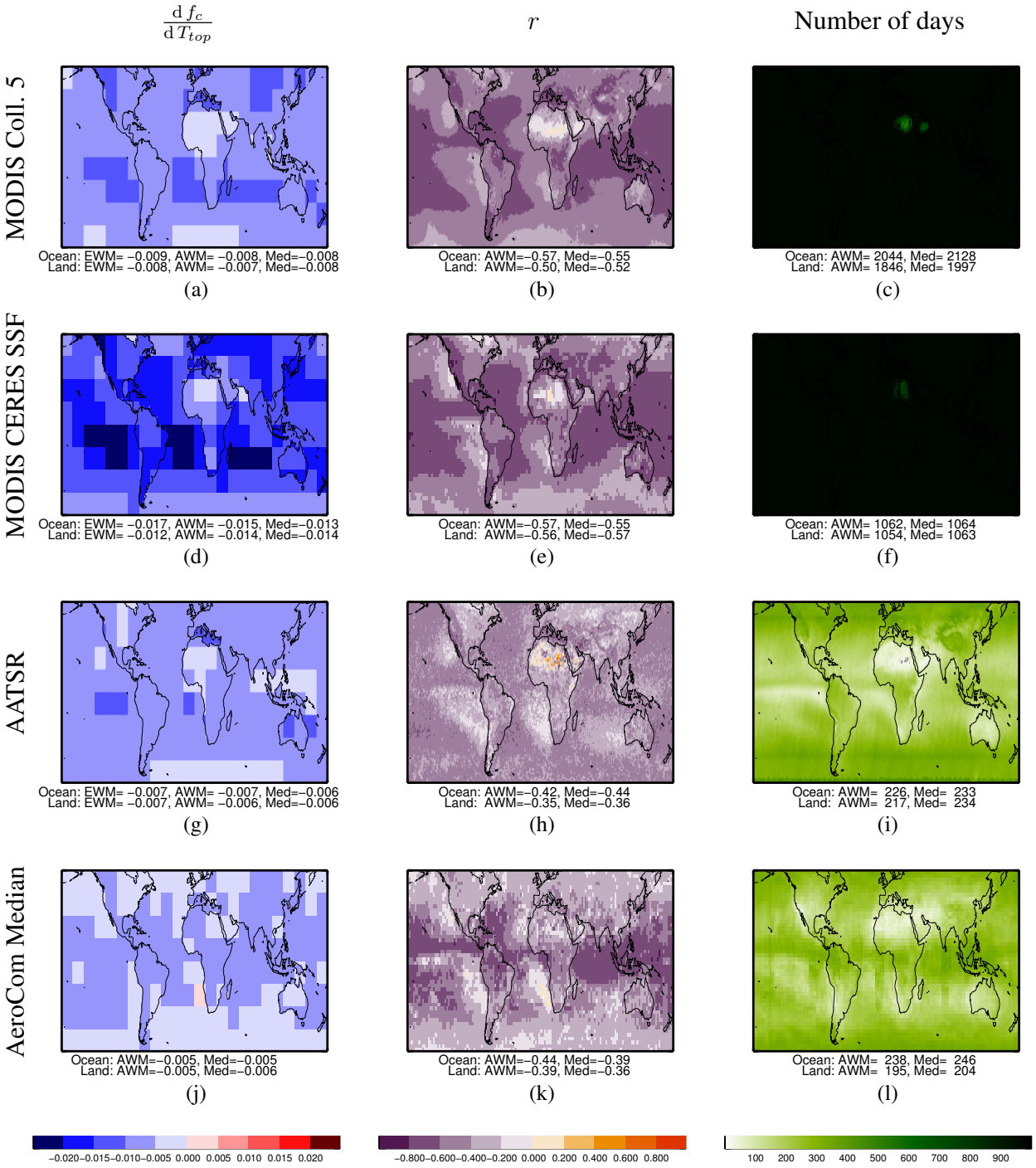

Figure 3.15: Same as Figure 3.4, but for results of a lin–lin ordinary least squares regression fit of cloud fraction (f_c) to cloud top temperature (T_{top}, K), assuming $f_c = a + b\,T_{top} + \epsilon$.

for either of the MODIS datasets, although they are still relatively strong. As can be seen in Figure 3.15(i), there are far fewer contributing data points than for the MODIS datasets.

The AeroCom Median slopes, Figure 3.15(j), are almost always negative, although they are slightly less steep than in any of the satellite datasets. The correlations, Figure 3.15(k), are in reasonable agreement with the satellite datasets.

Negative relationships between T_{top} and f_c are consistently observed, showing a positive relationship between cloud height and f_c. These relationships are likely explained by meteorology and cloud layer statistical considerations, discussed below.

Firstly, meteorological conditions which are conducive to the formation of high clouds may also be conducive to high cloud fractions. For example, frontal clouds near the centre of an extratropical cyclone often have high tops and also lead to high f_c, as will be discussed in Chapter 6. Also, high cirrus cloud often covers large regions. However, counterexamples, which potentially suggest the opposite relationship, also exist. For example, stratocumulus clouds are very low and yet often lead to high f_c. It is interesting to note that some of the weakest correlations occur in the stratocumulus regions to the west of the coasts of southern Africa, South America and California.

Secondly, even if clouds were randomly distributed in different atmospheric layers, it should be expected that situations with lots of cloud (high f_c) should also be situations where high cloud obscures much of the lower cloud below. Although no relationship between f_c and average cloud height would exist, a relationship between f_c and cloud top height would exist.

3.3 Conclusions

This chapter aimed to consider the following two questions: What are appropriate ways of quantifying and presenting relationships between aerosol optical depth (τ) and different cloud properties on global scales? What relationships between aerosol optical depth and different cloud properties can be observed across the world for different satellite and GCM datasets? The cloud properties investigated were liquid cloud droplet number concentration (N_d), liquid cloud droplet effective radius (r_e), cloud top temperature (T_{top}) and cloud fraction (f_c). The daily gridded satellite datasets used came from Aqua-MODIS Collection 5, Aqua-MODIS CERES SSF (which includes Collection 4 τ) and AATSR (GlobAEROSOL τ and ORAC cloud properties). Alongside these, GCM data from the AeroCom indirect effects intercomparison project was also used, with median model results being shown in this chapter.

Two methods of quantifying and presenting relationships between τ and the cloud properties were employed. Both methods involved displaying results on maps, in addition to providing global means. As mentioned in Section 2.3, maps have the advantage of being able to show how results vary

for different regions of the world, without needing to make assumptions about homogeneity across pre-defined regions.

First, the difference in mean cloud properties between low τ and high τ conditions, categorised according to seasonal grid-box τ medians, were shown on maps (e.g. Figure 3.5). These differences are relatively easy to understand conceptually, providing a measure of how the absolute value of a cloud property varies between low and high τ conditions.

Second, linear regression fits of each cloud property versus τ were calculated. The form of each fit was chosen based on theoretical considerations and empirical coefficients of determination for the Aqua-MODIS Collection 5 data (e.g. Figure 3.6). The following fits were chosen: $\ln N_d$ – $\ln \tau$ (log–log), $\ln r_e$ – $\ln \tau$ (log–log), T_{top} – τ (lin–lin) and f_c – $\ln \tau$ (lin–log). The regression slopes were averaged to $15^\circ \times 15^\circ$ using the grid-method of Chapter 2, in order to reduce noise and insignificance whilst also having a high enough resolution to show how the slopes vary for different parts of the world (e.g. Figure 3.4). For N_d and r_e, there are strong theoretical reasons for using such regression slopes to quantify the cloud albedo effect (Equations 1.9 and 1.8). For other cloud properties, such as T_{top} and f_c, the slopes still provide a quantitative measure of how the cloud property varies with τ. However, assumptions are made about the nature of the relationship, and only three forms of fit (log–log, lin–log and lin–lin) are tested although other fits might be more successful. Correlation coefficients were shown on maps alongside the regression slopes. The coefficients of determination (the square of these correlation coefficients) indicate how much of the variance in the cloud property can be explained by the fit against τ.

Both methods of quantifying and displaying relationships between cloud properties and τ were used in this chapter, both being appropriate tools for investigating the relationships. For N_d and r_e, the second method is probably the most useful because this is a common way to quantify the cloud albedo effect. For T_{top} and f_c, the choice of method may vary according to the situation. For example, the first method is used in Chapter 4, because of its simplicity in providing an indication of how cloud fraction varies between low and high τ conditions, whereas the second method is used in Chapter 6.

Over ocean, N_d is generally positively correlated with τ in all three of the satellite datasets, as predicted by the cloud albedo effect. The global error-weighted mean regression slopes of $\ln N_d$ versus $\ln \tau$ vary between $+0.14$ and $+0.20$ for the results presented here. Over land, there is much more disagreement about the signs of the relationships, with the global error-weighted mean slopes

varying between -0.12 and $+0.13$. The lower bounds are produced by AATSR and the upper bounds by Aqua-MODIS CERES SSF over both ocean and land. The AeroCom Median produces positive relationships over both ocean and land, with slopes that are steeper than observed in the satellite datasets.

The satellite datasets provide little constraint on the r_e–τ relationships, with global error-weighted mean $\ln r_w$ versus $\ln \tau$ regression slopes varying in the ranges -0.042 to $+0.049$ over ocean and -0.012 to $+0.042$ over land. The lower and upper bounds are provided by Aqua-MODIS CERES SSF and AATSR respectively. Liquid water path is not accounted for in these calculations. For the AeroCom Median, the slopes are generally negative.

All three satellite datasets generally observe negative relationships between T_{top} and τ, indicating positive relationships between cloud top height and τ. The global error-weighted mean regression slopes vary in the ranges -7 K to -28 K over ocean and -3 K to -21 K over land, with the lower bounds from AATSR and the upper bounds from Aqua-MODIS Collection 5. The median of the AeroCom models, which do not include representations of aerosol effects on convection, generally produces far weaker relationships than the satellite datasets.

Positive relationships between f_c and τ are almost always observed in all three satellite datasets. The correlation coefficients are larger than for any of the other cloud properties. The global mean differences in f_c between low and high τ conditions vary in the ranges $+0.09$ to $+0.20$ over ocean and $+0.10$ to $+0.20$ over land. AATSR and Collection 5 provide the lower and the upper bounds respectively. The AeroCom Median also generally produces positive relationships, although negative relationships are sometimes observed in the tropics.

Strong negative relationships between f_c and T_{top} are found in all three satellite datasets and also in the AeroCom Median. It is suggested that these f_c–T_{top} relationships may either be due to meteorological covariance or arise as a statistical outcome of having clouds randomly distributed in different atmospheric layers.

Many of the observed relationships between cloud properties and τ are consistent with aerosol indirect effects on clouds. In particular, the cloud albedo effect predicts positive relationships between N_d and τ, as observed over ocean. Positive relationships between cloud top height and τ and between f_c and τ have also been predicted and have been observed elsewhere (Section 1.4). However, other possible explanations for these relationships exist (Section 1.5). In this chapter, the possible

contribution of spatial climatological effects has been accounted for by following the methodological recommendations of Chapter 2. The potential contributions of satellite data errors and meteorological effects remain outstanding. In Chapters 5 and 6, one possible approach for investigating the role of large-scale meteorological conditions is proposed. But before this, Chapter 4 considers the possible explanations for relationships between f_c and τ.

Chapter 4

Investigating the relationship between aerosol optical depth and cloud fraction using satellite, reanalysis and GCM data

The previous chapter presented global relationships between observed aerosol optical depth (τ) and cloud properties. All three satellite datasets generally showed globally strong positive relationships between τ and cloud fraction (f_c). In this chapter, we further investigate the f_c–τ relationships.

As mentioned in Section 1.5, many possible reasons for observed relationships between aerosol and cloud properties exist. Following Quaas et al. (2010), of particular relevance to the f_c–τ relationships are the following potential mechanisms:

1. The spatial scale effects discussed in Chapter 2 may lead to spurious f_c–τ relationships. This potential problem has already been avoided in the results presented in the previous chapter and will continue to be avoided in the current chapter.

2. Satellite data errors may lead to positive f_c–τ relationships. Pixels in thin and broken cloud fields, with high f_c, may be mistakenly flagged as cloud-free when they are contaminated by cloud, leading to erroneously high τ retrievals (Huang et al., 2011). Furthermore, three-dimensional scattering of light by inhomogeneous clouds may also lead to erroneously high τ retrievals (Várnai and Marshak, 2009). A possible way to avoid these problems may be to combine satellite-retrieved f_c data with reanalysis-forecast τ data, assuming that these τ data do not suffer from residual cloud contamination due to assimilation from satellite datasets.

Koren et al. (2010) follow a similar approach by combining chemical transport model τ data with MODIS cloud data when investigating deep convective clouds over the Atlantic ocean. GCM data should not suffer from this problem.

3. The simple aerosol cloud lifetime effect conceptual model would predict positive f_c–τ relationships (Albrecht, 1989), assuming τ is a suitable surrogate for cloud condensation nuclei concentration (Andreae, 2009). Many GCMs attempt to simulate this effect by coupling aerosol to the stratiform cloud microphysics scheme, an effect that can often be switched on or off, although a large model error may exist.

4. Relative humidity may drive positive f_c–τ relationships (Quaas et al., 2010). Cloud fraction generally increases with relative humidity. Aerosols swell hygroscopically in high relative humidity conditions, increasing τ (Seinfeld and Pandis, 1998). GCMs should be able to reproduce this effect, particularly as cloud cover parameterizations are generally heavily dependent on relative humidity (e.g. Sundqvist et al., 1989), although there may be significant model errors. GCM-modelled dry τ, which assumes no hygroscopic aerosol growth, allows for this relative humidity effect to be accounted for, as demonstrated by Quaas et al. (2010).

5. Other meteorological factors may lead to spurious f_c–τ relationships. For example, 10-metre wind speed is capable of explaining a significant part of observed f_c–τ relationships (Engström and Ekman, 2010). A potential contribution of large-scale extratropical cyclones is considered in Chapter 6. GCMs should be capable of reproducing these meteorological effects.

6. Wet scavenging of aerosols by precipitation (Seinfeld and Pandis, 1998) might lead to negative f_c–τ relationships. This assumes that higher f_c corresponds to a higher probability of precipitation. GCM aerosol modules all simulate wet scavenging as the major removal mechanism for atmospheric aerosol.

7. Cloud processing of aerosols may alter the optical properties of aerosols. Most aerosol particles created in clouds are very small and therefore unlikely to significantly increase τ, and larger particles are often scavenged (Seinfeld and Pandis, 1998). However, some larger particles may also be produced (Su et al., 2008). It has been suggested that, far away from sources, aerosol particles have been cycled through clouds approximately three times (Pruppacher and Jaenicke, 1995).

In order to investigate some of these possible mechanisms, two additional tools are used in this chapter. Firstly, Monitoring Atmospheric Composition and Climate (MACC) project reanalysis-forecast τ data (MACC, 2011; Section 1.3.4) are used in an attempt to compensate for cloud contamination in the Aqua-MODIS τ data (second point above). Secondly, the ECHAM5-HAM GCM (Section 1.3) is used to investigate the cloud lifetime effect, relative humidity and wet scavenging contributions (third, fourth and sixth points above).

The following questions are asked in this chapter:

1. May the observed f_c–τ relationships be partly due to cloud contamination errors?
2. Is ECHAM5-HAM capable of modelling the observed f_c–τ relationships?
3. What are the reasons for the f_c–τ relationships in ECHAM5-HAM?

4.1 Method

The satellite data used in this chapter are from the official Aqua-MODIS Science Team Collection 5 level 3 daily $1^\circ \times 1^\circ$ cloud and aerosol dataset (MYD08_D3; Section 1.2.4). Total cloud fraction (f_c) and aerosol optical depth at 550 nm (τ) are of interest here. The data used in this chapter cover 2003–2007.

As mentioned above, cloud contamination of τ retrievals may cause spurious f_c–τ relationships, something that may be avoidable by pairing satellite-derived f_c with τ from a reanalysis-forecast aerosol dataset. However, residual cloud contamination may remain and model errors may be introduced. The reanalysis-forecast τ data used in this chapter are from the MACC project (MACC, 2011, Section 1.3.4), interpolated from $1.125^\circ \times 1.125^\circ$ to $1^\circ \times 1^\circ$ in order to match the MODIS data. MACC data from two different forecast time-steps, relative to the assimilation time of 00 UTC, are used: t + 3 hour; t + 24 hour from assimilation the previous day. The t + 24 hour forecast τ is likely to have less residual cloud contamination but more model error than the t + 3 hour forecast τ. It is assumed that the reanalysis-forecast τ at a particular time during the day are representative of the τ at the satellite overpass time, corresponding to the f_c data. As with the Aqua-MODIS data, the MACC τ data used here cover 2003–2007.

Data from the ECHAM5-HAM GCM are also used (Section 1.3). As mentioned in Section 1.3, the HAM aerosol model has been coupled to the cloud microphysics, allowing the cloud albedo

and cloud lifetime aerosol effects to be represented. Of particular interest here is the cloud lifetime effect on f_c. Six simulations are performed. Three of these use the Sundqvist cloud cover scheme, which parameterizes f_c using relative humidity as the only input (Sundqvist et al., 1989); three use the statistical Tompkins cloud cover scheme, which uses a prognostic probability density function of water vapour, considering processes such as convection, turbulence and microphysics (Tompkins, 2002). For each cloud cover scheme, three simulations are conducted: a Control run, with aerosol indirect effects represented; a NoAIE run, with no aerosol indirect effects (fixed N_d); a NoConvScav run, with aerosol indirect effects represented but with no convective wet scavenging of aerosols. All simulations use year 2000 present-day aerosol and precursor emissions (Dentener et al., 2006). All simulations are nudged to year 2000 meteorology using ERA-40 reanalysis data, preceded by a three month spin-up period from October 1999. All simulations are run at T63 horizontal and L31 vertical resolution. Data are output everywhere at 6 hourly temporal and $1.875^\circ \times 1.875^\circ$ spatial resolution. The f_c data are calculated assuming maximum-random overlap of cloud layers (Stubenrauch et al., 2008). In addition to τ from all simulations, dry τ output from the Control simulations is also used. Following Quaas et al. (2010), dry τ is calculated by reducing the extinction coefficient of each aerosol mode by the volume fraction of water for that mode, approximating the τ that would be calculated if there was no hygroscopic swelling of the aerosols.

As in the previous chapter, the daily data are categorized into two cases: low τ conditions, where τ is less than the median for that grid-box, season and dataset; high τ conditions, where τ is greater than the median. The mean f_c for each grid-box, season and dataset is then calculated for low τ and high τ conditions, before averaging across all four seasons to show annual mean fields. Again, the analysis is limited to 60°S–60°N.

4.2 Results and discussion

Figure 4.1(a) shows the annual mean Aqua-MODIS Collection 5 total cloud fraction (f_c) for low aerosol optical depth (τ) conditions, where τ is less than the seasonal grid box median for each grid box and season. Purple and blue indicate low f_c values, while yellow, orange and red indicate high f_c values. Extratropical land areas often have low f_c whereas the extratropical oceans and the Inter-Tropical Convergence Zone (ITCZ) have high f_c.

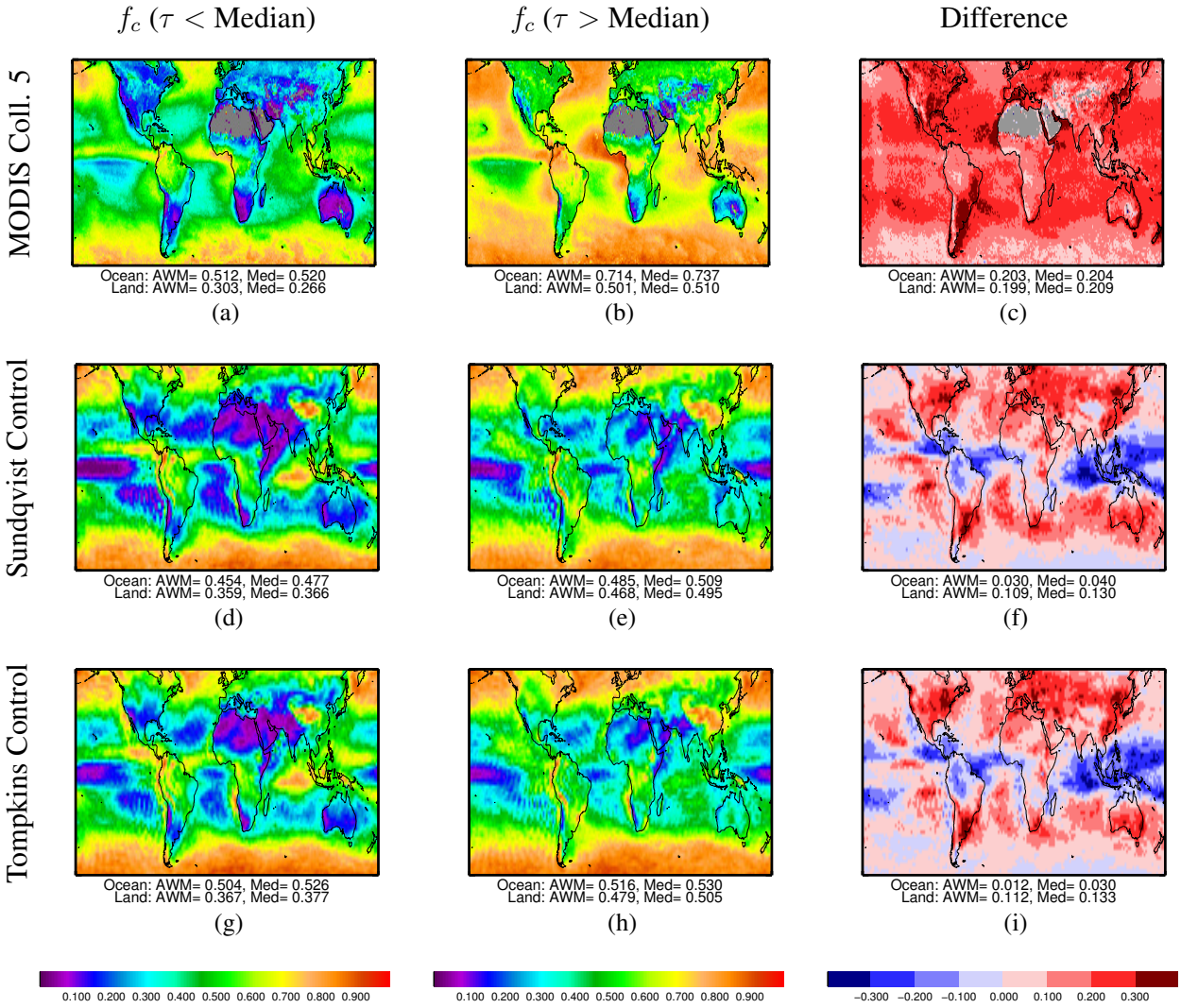

Figure 4.1: Annual (all seasons) mean cloud fraction (f_c) for low τ (τ < seasonal grid box median; first column) and high τ (τ > seasonal grid box median; second column) conditions, and the difference between these (third column), for Aqua-MODIS Collection 5 (first row), the ECHAM5-HAM Sundqvist Control simulation (second row) and the ECHAM5-HAM Tompkins Control simulation (third row). Grey represents missing data. The area-weighted mean (AWM) and median (Med) for both ocean and land are shown beneath each map. The first row is very similar to that of Figure 3.11.

Figure 4.1(b) shows the corresponding annual mean f_c for high τ conditions, where τ is greater than the seasonal grid box median. It can be clearly seen that f_c generally increases between low τ and high τ conditions, indicating positive f_c–τ relationships. This has been observed in other studies, such as those by Koren et al. (2005) and Kaufman et al. (2005) who investigated clouds over the North Atlantic ocean using earlier MODIS data. Figure 4.1(c), the differences in f_c between low and high τ conditions, shows that these positive f_c–τ relationships are global. Particularly strong relationships, shown in darker shades of red, are found over the subtropical oceans, southern South America and eastern North America. The relationship over the extratropical southern oceans is weaker. Over

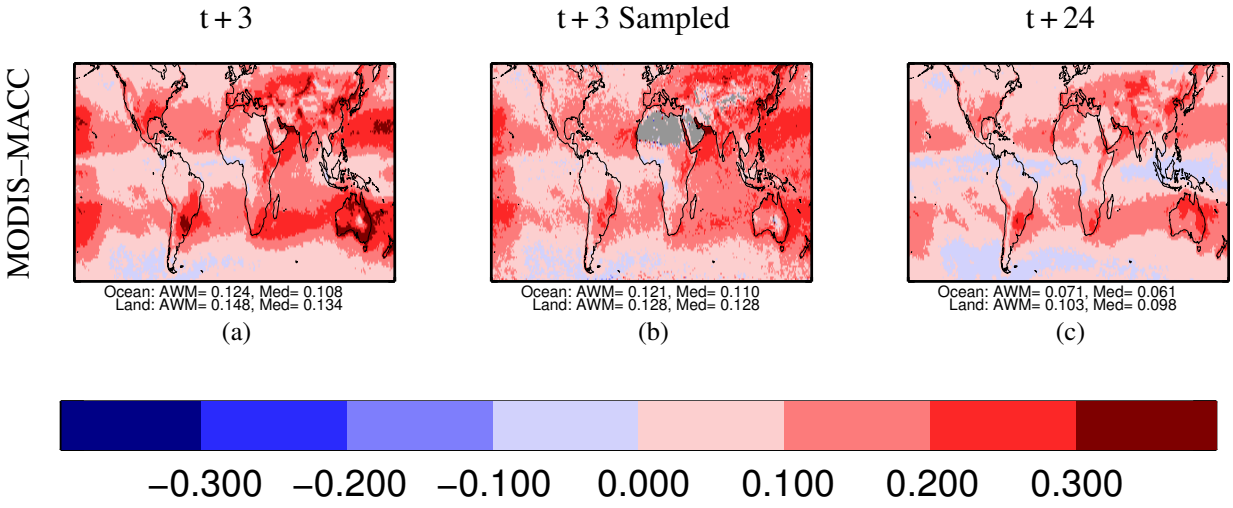

Figure 4.2: Annual (all seasons) mean difference in cloud fraction (f_c) between low τ ($\tau <$ seasonal grid box median) and high τ ($\tau >$ seasonal grid box median) conditions for Aqua-MODIS Collection 5 f_c combined with three different versions of MACC τ: (a) MACC t + 3 hour τ; (b) MACC t + 3 hour τ sampled where Aqua-MODIS Collection 5 τ exist; (c) MACC t + 24 hour τ. The area-weighted mean (AWM) and median (Med) for both ocean and land are shown beneath each map.

ocean, there is a mean increase in f_c of 0.20 from 0.51 to 0.71; over land, there is also a mean increase of 0.20 from 0.30 to 0.50.

An increase of 0.2 in f_c is relatively large. For example, assuming an idealised ocean albedo of 0.0 and a cloud albedo of 0.5, a 0.2 increase in f_c may lead to an albedo increase of order 0.1 over ocean. Given a solar constant of $1370\,\mathrm{Wm}^{-2}$, averaged to $340\,\mathrm{Wm}^{-2}$ across the surface of the earth, an albedo increase of 0.1 would correspond to a shortwave radiation decrease of order $30\,\mathrm{Wm}^{-2}$ at the top of the atmosphere. Of course, this shortwave decrease might be offset be a sizeable longwave increase, particularly if the cover of high clouds increases.

In the previous chapter, two other satellite datasets (Aqua-MODIS CERES SSF; AATSR ORAC f_c with GlobAEROSOL τ) were also investigated. It was shown that positive f_c–τ relationships also exist for these datasets, although the relationships are not as strong as in the Aqua-MODIS Collection 5 data (Figure 3.11).

As previously stated, the positive f_c–τ relationships are not necessarily due to aerosol indirect effects on cloud. Cloud contamination of aerosol retrievals provides one potential explanation. In an attempt to provide an approximate correction for this, the Aqua-MODIS Collection 5 f_c data are paired with MACC reanalysis-forecast τ data. The results of categorising according to low and high MACC t + 3 hour τ conditions are shown in Figure 4.2(a). Globally positive f_c–τ relationships are again evident, although they are generally weaker than cases when MODIS τ is used. The relation-

ships are still strong over the extratropical ocean, and the relationships are even larger than before for parts of the extratropical North Pacific. For a few small regions, notably parts of the extratropical South Pacific, the extratropical South Atlantic and the equatorial Atlantic oceans, weak negative f_c–τ relationships are observed, indicated by pale blue. Over ocean, the global mean increase is now 0.12; over land, the increase is 0.15.

It is worth noting that the data contributing to Figures 4.1(c) and 4.2(a) sample different situations: MODIS τ retrievals do not exist for completely cloudy grid boxes, whereas MACC τ data exist everywhere. Sampling differences such as these often impact results (Sayer et al., 2010b). In order to investigate the impact of this sampling difference, 4.2(b) shows the corresponding results for when the MACC t + 3 hour τ are sampled according to Aqua-MODIS τ data availability. As can be seen, Figures 4.2(a) and (b) are relatively similar, showing that the sampling choice does not have a large impact. The sampled data generally produce slightly weaker f_c–τ relationships, particularly over land.

Some residual cloud contamination may remain in the MACC τ data due to the assimilation of satellite-retrieved τ. This contamination should decrease for longer forecast times from assimilation, although model errors will increase as the forecast length increases. The MACC–MODIS f_c–τ relationships for a longer MACC forecast of t + 24 hour are shown in 4.2(c). The relationships are generally weaker than for t + 3 hour, although the spatial patterns are similar. Negative f_c–τ relationships are more evident in the tropics for the t + 24 hour τ data. Over ocean, the global mean increase is 0.07; over land, the increase is 0.10. This suggests that cloud contamination may account for approximately one half of the observed global increase in f_c over ocean. However, it is difficult to disentangle the contributions from residual cloud contamination and model errors.

Results for the ECHAM5-HAM Sundqvist Control simulation are shown in Figures 4.1(d)–(f). The global mean f_c is lower than the MODIS f_c. However, it is worth noting that it is difficult to compare absolute values of f_c between different datasets, because f_c is dependent on resolution. The differences in f_c between low and high τ conditions bear much similarity to those for the MODIS–MACC combinations. The spatial distribution of positive and negative relationships is remarkably similar between the Sundqvist Control and the MODIS–MACC t + 24 hour data, although the relationships are generally stronger in the Sundqvist Control. The strong positive f_c–τ relationships observed over the subtropical oceans, southern South America, North America, Asia and Australia

are of similar size to those for the MODIS–MACC combinations. Further agreement is found in the extratropical ocean, where the relationships are weaker, with some weak negative relationships in the extratropical southern oceans. As observed in the MODIS–MACC t + 24 hour data, negative f_c–τ relationships are found over parts of the tropics, particularly South-East Asia, although these negative relationships are much stronger in the Sundqvist Control data. These negative relationships, which occur primarily over the tropical ocean, greatly reduce the global mean increase in f_c to 0.03 over ocean. Over land, the global mean increase is 0.11, comparable to the MODIS–MACC t + 24 hour results.

The f_c results for the ECHAM5-HAM Tompkins Control simulation, shown in Figures 4.1(g)–(i), are similar to those for the Sundqvist Control. The global mean f_c values are slightly larger in the Tompkins Control due to tuning differences between the two cloud schemes. Over ocean, the subtropical positive f_c–τ relationships are slightly weaker in the Tompkins Control than in the Sundqvist Control, leading to a smaller global ocean mean f_c increase of 0.01. Over land, the global mean increase is 0.11 for the Tompkins Control, very similar to that for the Sundqvist Control.

Seven possible mechanisms for f_c–τ relationships were suggested at the beginning of this chapter. The first of these, namely spatial gradient effects, has been avoided by conducting the analysis on small regions of $1^\circ \times 1^\circ$ and displaying the results on maps. The second of these, namely cloud contamination of τ, has been partially mitigated in the MODIS–MACC results and does not impact the ECHAM5-HAM model results. Four possible mechanisms remain for explaining the ECHAM5-HAM Control results. Two of these would predict positive f_c–τ relationships: the aerosol cloud lifetime effect and hygroscopic growth of aerosol in high relativity humidity conditions. One would predict negative f_c–τ relationships: wet scavenging of aerosol by precipitation. The contributions of these three effects to the ECHAM5-HAM Control results are now investigated. The two remaining possible mechanisms, whereby spurious f_c–τ relationships are caused by other meteorological factors or cloud processing of aerosols, are not tested here.

First, the contribution of the cloud lifetime effect is investigated. The ECHAM5-HAM Control simulations contained a representation of the cloud albedo and cloud lifetime effects. These aerosol indirect effects were not included in the ECHAM5-HAM NoAIE simulations. The differences in f_c between low and high τ conditions for these NoAIE simulations are shown in Figures 4.3(a) and (d). For both the Sundqvist and the Tompkins cloud cover schemes, the differences in f_c for the NoAIE

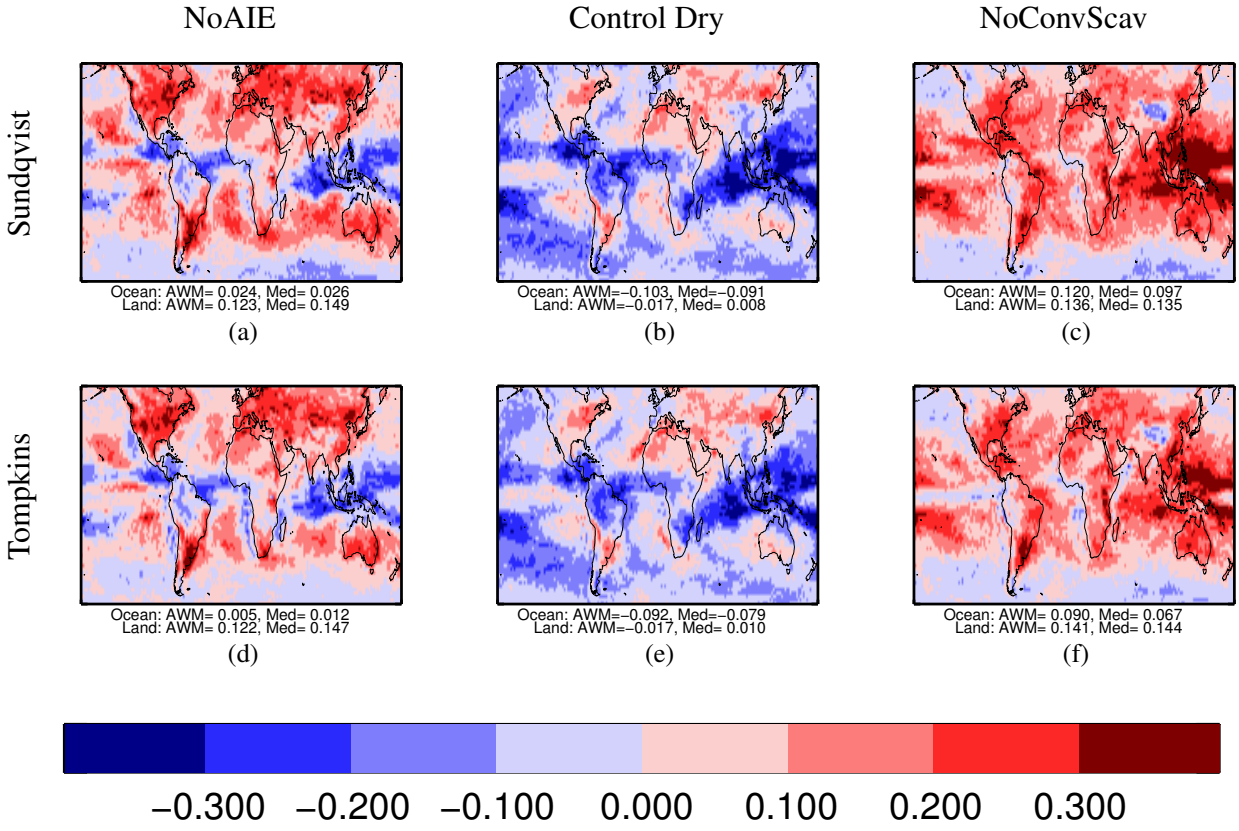

Figure 4.3: Same as Figure 4.2 but for six different ECHAM5-HAM simulations.

simulations are similar to those for the Control simulations. A slight weakening of positive f_c–τ relationships occurs over many subtropical ocean areas, and the differences in the southern Indian Ocean become more negative. However, a slight strengthening of positive f_c–τ relationships occurs over land for the NoAIE runs, opposite from what would be expected from the conceptual cloud lifetime effect. These results suggest that the model simulated indirect effects are not the primary mechanism responsible for the positive f_c–τ relationships observed in the Control simulations. This is consistent with the findings of Lohmann et al. (2006) and Quaas et al. (2010).

Second, the contribution of relative humidity is investigated. In order to do this, dry τ from the Control simulations is used instead of total τ. The radiative calculation of dry τ assumes that the aerosol particles have not grown hygroscopically, providing a measure of column aerosol amount that is independent of humidity. The annual mean total τ and dry τ fields for the the Sundqvist Control simulation are shown in Figures 4.4(a) and (b). The fields are very similar for the Tompkins Control and the NoAIE simulations. Because τ is heavily dependent on aerosol size, dry τ is generally much lower than τ, as can be seen.

The f_c differences between low and high dry τ conditions in the Control runs are shown in Fig-

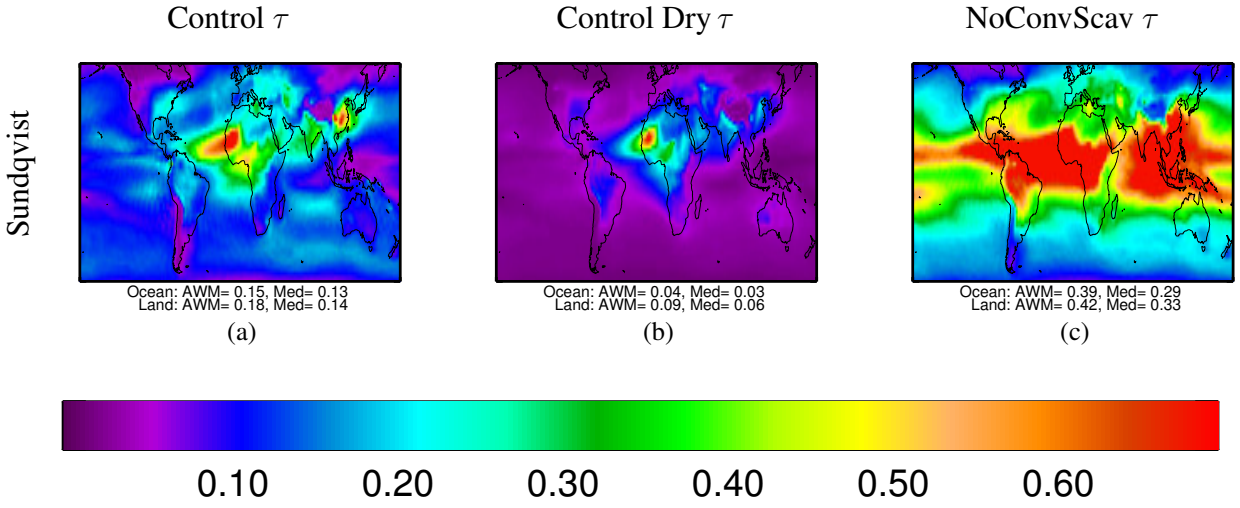

Figure 4.4: Annual (all seasons) mean aerosol optical depth (τ) for ECHAM5-HAM simulations. The area-weighted means (AWM) and median (Med) for both ocean and land are shown beneath each map. The Tompkins simulations have very similar annual mean τ fields to the respective Sundqvist simulations. The NoAIE simulations have very similar annual mean τ fields to the Control simulations.

ures 4.3(b) and (e). It can be clearly seen that using dry τ removes the majority of the positive f_c–τ relationships over ocean. Many land areas retain positive f_c – dry τ relationships. However, these positive relationships are significantly weakened compared to when total τ is used. A global mean negative f_c – dry τ relationship is found over both ocean and land for both the Sundqvist and the Tompkins Control runs. These results demonstrate that relative humidity is the primary driver for the positive f_c–τ relationships in ECHAM5-HAM, in agreement with Quaas et al. (2010).

Third, the contribution of wet scavenging is investigated. The negative f_c–τ relationships in the Control runs are generally found in the tropics, where convective precipitation dominates, constituting 95% of the 20°S–20°N precipitation in the Sundqvist Control. It is these negative relationships which are of interest here, so wet scavenging by convective precipitation is switched off for the NoConvScav simulations. Scavenging by stratiform cloud precipitation remains. Wet scavenging is a major removal mechanism for aerosol in ECHAM5-HAM. As a result, τ is generally much higher in the the NoConvScav simulations compared to the Control simulations, particularly in the tropics, as can be seen by comparing Figures 4.4(a) and (c). The lifetime of aerosols in GCMs is typically approximately two weeks when scavenging is turned on. Switching off convective scavenging increases τ by a factor of approximately three, suggesting a lifetime of approximately six weeks for the NoConvScav simulation. Therefore the three month spin-up should allow these concentrations to reach an equilibrium by the start of the year 2000 analysis period.

Figures 4.3(c) and (f) show the f_c differences between low and high τ conditions for the NoConvScav simulations. Most of the negative f_c–τ relationships found in the tropics of the Control simulation are removed, becoming positive in the NoConvScav simulations. This demonstrates that wet scavenging by convective precipitation is the primary reason for the strong negative f_c–τ relationships found in the tropics of the Control simulations. Interestingly, the f_c–τ relationships become more negative for many extratropical ocean areas in the NoConvScav simulations compared to the Control Simulations. This may be because wet scavenging by stratiform cloud precipitation may become a more significant aerosol removal mechanism in the NoConvScav runs, leading to more negative relationships in regions where stratiform precipitation dominates.

4.3 Conclusions

Regularly gridded daily data were categorised into low aerosol optical depth (τ) conditions and high τ conditions, based on the median τ for each grid box and season, for several datasets. Annual mean cloud fraction (f_c) was calculated for low and high τ conditions, based on the τ categorisation. The difference in annual mean f_c was also calculated, and the results were shown on maps.

For the Aqua-MODIS daily level 3 τ and f_c data, globally consistent increases in f_c between low and high τ conditions were found, indicating positive f_c–τ relationships. A global mean f_c increase of 0.2 was observed for both ocean and land.

Categorising the Aqua-MODIS f_c data according to MACC reanalysis-forecast t + 3 hour τ data generally resulted in a weakening of the observed positive f_c–τ relationships. It was demonstrated that the weakening was not due to sampling differences. The positive relationships were weakened further for a longer MACC forecast period of t + 24 hour. This provides some evidence to suggest that part of the positive f_c–τ relationships observed in the MODIS data may be due to retrieval errors, although the weakening of the relationships may also be due to MACC model errors. Positive f_c–τ relationships were still observed to dominate globally for the MODIS–MACC combinations, particularly in the tropics. However, negative relationships emerged over the parts of the tropics and extratropical southern oceans in the t + 24 hour data. Over ocean, global mean f_c increases of 0.12 and 0.07 were found for t + 3 hour and t + 24 hour respectively. Over land, global mean f_c increases of 0.15 and 0.10 were found.

The results of the ECHAM5-HAM Control simulations generally agreed well with the MACC-MODIS results in the subtropics and extratropics. In agreement with the MODIS–MACC t + 24 hour results, negative f_c–τ relationships were found in parts of the tropics. However, these negative relationships were found to be much stronger in the ECHAM5-HAM Control simulations. By running NoAIE simulations, in which aerosol indirect effects were switched off, it was demonstrated that the cloud lifetime effect is not the primary contributor to positive f_c–τ relationships in ECHAM5-HAM. Rather, the positive relationships are primarily due to the hygroscopic swelling of aerosols in high relative humidity conditions, as was demonstrated by using dry τ instead of total τ. By running No-ConvScav simulations, in which convective wet scavenging was switched off, it was demonstrated that the negative f_c–τ relationships in the tropics are primarily due to wet scavenging by convective precipitation in ECHAM5-HAM. These results were similar for both the Sundqvist and the Tompkins cloud cover schemes.

This chapter investigated the possible contributions of satellite data errors, aerosol indirect effects, relative humidity and wet scavenging to observed relationships between τ and f_c. The following two chapters consider the possible contribution of extratropical cyclones.

Chapter 5

The effect of extratropical cyclones on column aerosol properties over ocean

Most of the work presented in this chapter, excluding that which uses the MACC data, has been published in Grandey et al. (2011) (B. S. Grandey, P. Stier, T. M. Wagner, R. G. Grainger and K. I. Hodges, The effect of extratropical cyclones on satellite-retrieved aerosol properties over ocean, *Geophys. Res. Lett.*, 38, L13805, 2011, doi: 10.1029/2011GL047703).

Meteorological effects may lead to spurious correlations between aerosol and cloud properties, as discussed in Section 1.5.3. It is therefore important to understand the effect synoptic systems may have on cloud and aerosol properties.

Previous compositing studies have looked at the dynamical structure of extratropical cyclones (e.g. Catto et al., 2010) and the effect that extratropical cyclones have on clouds over ocean (Lau and Crane, 1995, 1997; Norris and Iacobellis, 2005; Wang and Rogers, 2001; Chang and Song, 2006; Field and Wood, 2007; Field et al., 2008). This chapter seeks to complement these previous studies through the production of storm-centric composites of satellite-retrieved total column aerosol properties over ocean. In this chapter, the following question is asked:

1. What effect do extratropical cyclones have on column aerosol properties over ocean?

The compositing methodology and the data used in this chapter are introduced in Section 5.1. The

results are presented and discussed in Section 5.2. A summary of the main conclusions is provided in Section 5.3.

5.1 Method

In this chapter, storm-centric composites are produced using satellite-retrieved aerosol properties over ocean from both the MODerate resolution Imaging Spectroradiometer (MODIS) on Aqua and the Advanced Along-Track Scanning Radiometer (AATSR) on ENVISAT. Aerosol optical depth at 550 nm (τ) and fine-mode fraction data from the MODIS Science Team Collection 5 Atmosphere Level 2 Joint Product are used (Remer et al., 2005). The MODIS aerosol data are provided at approximately 10 km $\times$ 10 km resolution. No wind speed dependent sea-surface reflectance correction is applied in the Collection 5 aerosol retrieval. Five years (2003–2007) of MODIS data, covering all seasons, are used.

In order to allow comparison with an independent aerosol dataset which has a wind speed dependent sea-surface reflectance correction, AATSR τ and Ångström exponent data retrieved by the Oxford-RAL Retrieval of Aerosols and Clouds (ORAC) as part of the GlobAEROSOL project are also used (Thomas et al., 2009; Sayer et al., 2010a, Section 1.2.4). Each GlobAEROSOL daily file provides data on a 10 km $\times$ 10 km sinusoidal grid. The accuracy of both of these retrieval algorithms is discussed in Kokhanovsky et al. (2010). Again, data covering 2003–2007 are used.

Relative vorticity at 850 hPa, zonal and meridional components of the 10-metre wind, mean sea level pressure (p_0) and 850 hPa relative humidity (RH) are provided in European Centre for Medium Range Weather Forecasts (ECMWF) ERA-Interim reanalysis data. The reanalysis data used here are at 6 hourly temporal and $1.5^\circ \times 1.5^\circ$ spatial resolution. Wind speed (u) is calculated using the 10-metre wind vector components. The data used in this chapter cover 2003–2007.

MACC project reanalysis aerosol data for 2003–2007 are also used here (MACC, 2011, Section 1.3.4). The aerosol optical depth (τ) is available for different aerosol components. Results for the sea-salt τ (including aerosol water) as well as the total τ are presented in this chapter. The aerosol data are not available at the assimilation time-step of 00 UTC, so the closest forecast time-step, t + 3 hour, is chosen.

One year of ECHAM5-HAM GCM data are also used (Section 1.3). Two ECHAM5-HAM runs

are conducted: one with year 2000 present-day (PD) aerosol and precursor emissions and one with pre-industrial (PI) aerosol and precursor emissions Dentener et al. (2006). These emission datasets are those used for the AeroCom experiment. The meteorology is nudged to ERA-40 reanalysis data for the year 2000. The GCM is run at T63 horizontal and L31 vertical resolution. Data are output everywhere at 6 hourly temporal and $1.875^\circ \times 1.875^\circ$ spatial resolution. ECHAM5-HAM τ, total precipitation rate, relative vorticity at 850 hPa, p_0 and 10-metre winds are used in this chapter.

Extratropical cyclones are tracked using TRACK, which uses an adaptive tracking algorithm to objectively identify and track meteorological features in GCM data (Hodges, 1995, 1999). TRACK has been configured to track the 850 hPa relative vorticity associated with extratropical cyclones, henceforth referred to as storms. Storms which persist for less than two days or move a distance of less than 1000 km are not considered. For analysing the MODIS, AATSR and MACC aerosol data, extratropical cyclones are tracked in the ERA-Interim 850 hPa relative vorticity field covering 2003–2007. For analysing the ECHAM5-HAM data, extratropical cyclones are tracked separately in the 850 hPa relative vorticity field of the ECHAM5-HAM PI run, which has been nudged to meteorology for the year 2000.

For each storm at each model time-step, p_0, RH, the wind data and the model (MACC or ECHAM5-HAM) aerosol data are regridded at 200 km $\times$ 200 km resolution on a 4000 km $\times$ 4000 km domain centred on the storm. In order to produce storm-centric satellite-retrieved aerosol data, the tracked cyclone locations and relative vorticities are interpolated to five minute temporal resolution, using a parametric cubic spline with time as the parameter. If Aqua-MODIS or AATSR retrieved aerosol data exist within a 4000 km $\times$ 4000 km storm-centric domain, then the aerosol data are re-gridded at 25 km $\times$ 25 km resolution on the storm-centric domain.

The storm-centric regularly gridded model and satellite data for individual storms are then composited. The advantages of looking at a composite storm are that data coverage of the storm-centric domain will be increased significantly, that noise will be reduced and that background variability will be largely removed, making some statistically relevant large-scale structure more evident than in individual cases. In order to reduce the unrepresentative influence of extreme aerosol events, the composites are produced using medians.

In order to compare against average conditions, the reanalysis and satellite data are also regridded with respect to storm tracks which have been translated temporally by one year. This allows for the

production of all-conditions composites from data which are blind as to whether or not a storm is present in the domain but which also have the same seasonal and locational sampling as the storm-centric composites. All-conditions composites are not constructed for the ECHAM5-HAM data due to there only being one year of ECHAM5-HAM data.

Composites for storms over the North Atlantic ocean (NA; 50°W–10°W, 30°N–55°N) and South Atlantic ocean (SA; 50°W–10°E, 55°S–30°S) are compared. A minimum 850 hPa relative vorticity threshold of 7×10^{-5} s^{-1} has been chosen, leading to median storm-centre p_0 values of 988 hPa and 980 hPa for the NA and the SA respectively.

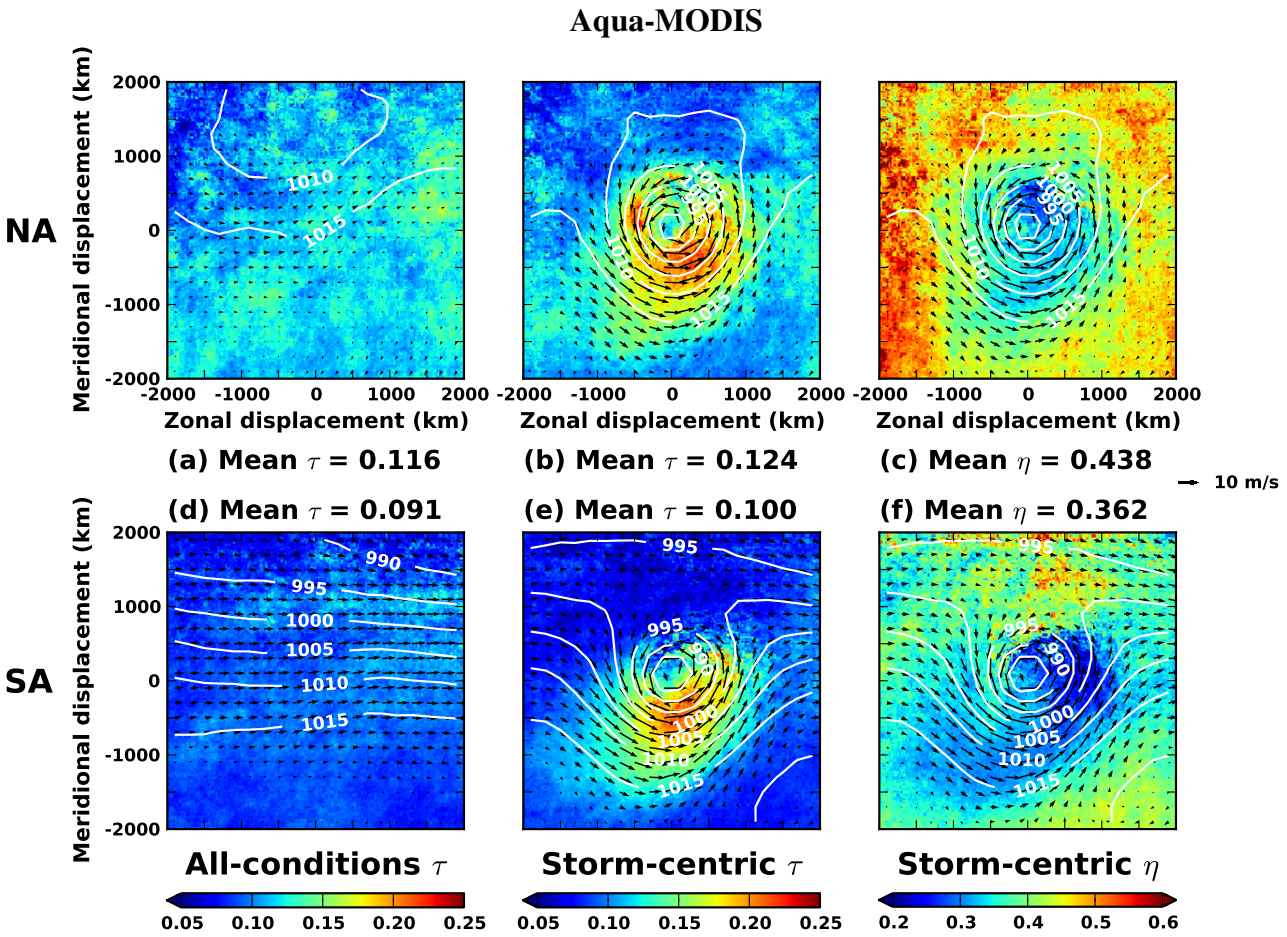

Figure 5.1: Aqua-MODIS Collection 5 all-conditions aerosol optical depth (τ; a, d), storm-centric τ (b, e) and storm-centric fine-mode fraction (η; c, f) median composites for the North Atlantic (NA; a–c) and the South Atlantic (SA; d–f) oceans. Composite ERA-Interim mean sea level pressure (p_0, hPa; white contours) and wind vectors (black arrows) are over-plotted. The wind vector scale is provided at the right-hand edge. Positive meridional displacements are poleward of the storm centre. The data cover 2003–2007. A minimum 850 hPa relative vorticity threshold of 7×10^{-5} s^{-1} is used.

5.2 Results and discussion

Figures 5.1(a) and (d) show all-conditions MODIS τ composites for the NA and the SA. Although some noise is evident, these composite fields are relatively smooth and no large-scale structure is evident. It can be seen that the NA generally experiences higher τ than the SA, most likely due to anthropogenic aerosol pollution advected from North America.

Storm-centric τ composites are shown in Figures 5.1(b) and (e). Towards the edge of the domains, τ is similar to that of the corresponding all-conditions composites, with higher τ for the NA than the SA. However, towards the centre of the domain it can be seen that storms can have a strong effect on τ compared to average conditions. For both the NA and the SA, τ increases near the centre of the storm-centric composites, peaking equatorward of the low pressure centre.

In order to provide an indication of the size distribution of the observed aerosol, storm-centric MODIS fine-mode fraction is shown in Figures 5.1(c) and (f). Near the edge of the storm domain it can be seen that fine-mode fraction is higher for the NA than the SA, consistent with there being more anthropogenic fine-mode aerosol in the NA. In the regions of higher u near the centre of the composites, where the enhanced τ was also observed, fine-mode fraction is smaller, indicating the presence of larger aerosols.

Two physical mechanisms may explain the increase in τ and decrease in fine-mode fraction towards the centre of the composite storms. First, increasing u will result in increased sea-salt emission (Lewis and Schwartz, 2004). Bubble bursting during whitecap generation is the primary mechanism for sea-salt aerosol emission. These whitecaps generally form at wind speeds of $4\,\mathrm{ms}^{-1}$ and greater (O'Dowd and de Leeuw, 2007). The whitecap fractional coverage, and hence sea-salt emission, increases as u increases, forming a basis for emission parameterizations (Gong, 2003). However, the Gong (2003) emission parameterization may overestimate emission at high u, and it may underestimate emission at low u if sea-surface temperature is not taken into account (Jaeglé et al., 2011). Uncertainties remain concerning the emission flux of aerosol from the ocean surface (de Leeuw et al., 2011). Sea-salt aerosol is often large, so increasing u would result in a decrease in fine-mode fraction alongside an increase in τ, as observed.

Second, RH, shown in Figure 5.2, is higher nearer the centre of the storm, leading to hygroscopic growth of aerosol particles (Seinfeld and Pandis, 1998). This too would result in a decrease in fine-mode fraction as well as an increase in τ.

In addition to the two physical mechanisms mentioned above, it is possible that the results observed in Figure 5.1 may be due to a retrieval error. Increasing u leads to a brightening of the ocean surface. This would lead to an increase in retrieved τ and may also affect fine-mode fraction. This sea-surface reflectance effect is not corrected for in the MODIS Collection 5 aerosol data. It is also worth noting that some of the aerosol retrievals may be contaminated by cloud such as thin cirrus (e.g. Huang et al., 2011), although this would not explain the storm-centric τ and fine-mode fraction patterns shown in Figure 5.1.

In order to investigate the possible contribution of a surface reflectance retrieval error to these observations, Figure 5.3 shows similar composites for GlobAEROSOL AATSR data. The GlobAEROSOL AATSR retrieval has a wind speed dependent sea-surface reflectance correction, although some residual sea-surface reflectance contamination may remain. This retrieval is independent of the MODIS retrieval.

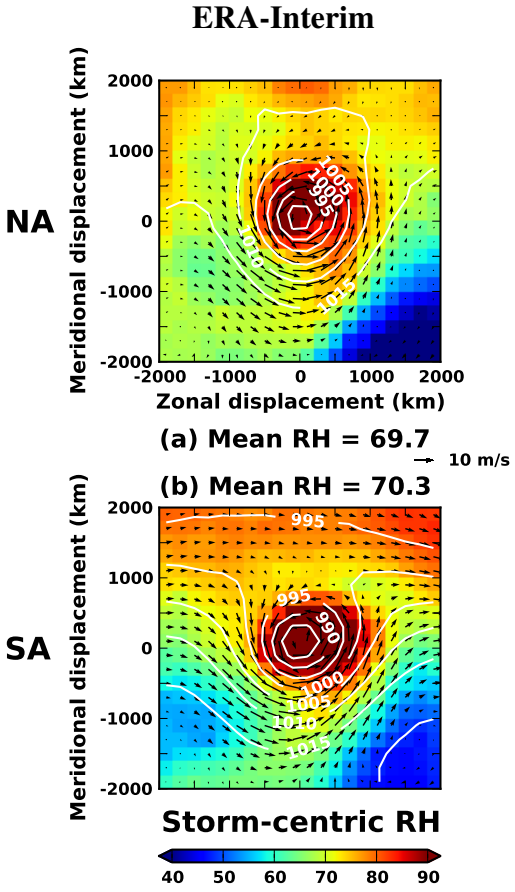

Figure 5.2: ECMWF ERA-Interim storm-centric 850 hPa relative humidity (RH, %) median composites for the North Atlantic (NA; a) and the South Atlantic (SA; b) oceans. Composite ERA-Interim mean sea level pressure (p_0, hPa; white contours) and wind vectors (black arrows) are over-plotted. The wind vector scale is provided at the right-hand edge. Positive meridional displacements are poleward of the storm centre. The data cover 2003–2007. A minimum 850 hPa relative vorticity threshold of 7×10^{-5} s^{-1} is used.

As can be seen in Figure 5.3, the AATSR composites provide incomplete coverage and are significantly noisier than the MODIS composites shown in Figure 5.1. This is due to AATSR having a smaller swath width than MODIS. The presence of missing data in the poleward part of the AATSR composites is due to there being fewer AATSR retrievals at high latitudes compared to lower latitudes.

However, despite the noise, the AATSR composites have a similar structure to the MODIS composites. The all-conditions τ is higher in the NA than in the SA. The GlobAEROSOL AATSR τ observations are higher than the MODIS τ observations in the NA. AATSR τ is generally higher in regions of higher u towards the centre of the storm domains compared to regions of lower u. The third column of Figure 5.3 shows storm-centric composites of Ångström exponent, which is inversely related to aerosol size. It can be seen that aerosol size increases towards the centre of the composite storms, as was also observed in the MODIS composites.

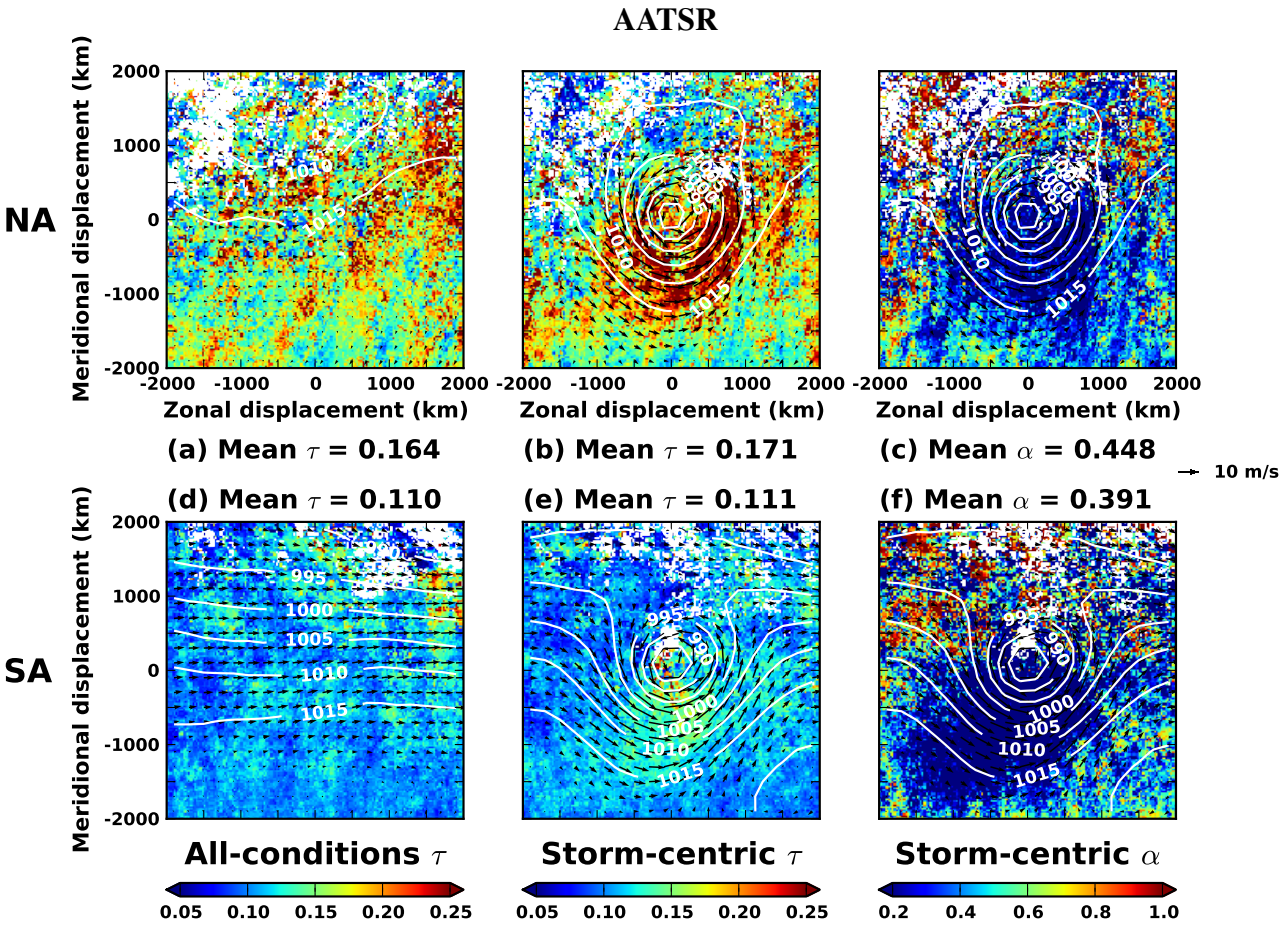

Figure 5.3: Same as Figure 5.1, but for GlobAEROSOL AATSR all-conditions aerosol optical depth (τ; a, d), storm-centric τ (b, e) and storm-centric Ångström exponent (α; c, f) median composites. White fill represents missing data.

Both the MODIS and AATSR datasets indicate an increase in τ near the centre of the composite storms. The fact that these observations apply to two independent satellite datasets, one of which has a wind speed dependent sea-surface reflectance correction, suggests that surface reflectance effects cannot fully account for these observations. Therefore, one or both of the physical mechanisms of sea salt emission and hygroscopic growth must be a major contributor to these observations.

As mentioned above, both RH and u generally increase towards the centre of the storm domain. As can be seen in Figure 5.2, storm-centric composite RH generally peaks very close to the centre of the storm domain, being negatively correlated to p_0, with p_0–RH pattern correlation coefficients (Glickman, 2000) of $r = -0.75$ and $r = -0.93$ for the NA and the SA respectively. Storm-centric composite u is also correlated to p_0, with p_0–u $r = -0.76$ and $r = -0.41$ for the NA and the SA respectively, but u peaks equatorward of the storm centre. As can be seen in Figures 5.1 and 5.3, storm-centric τ also peaks equatorward of the storm centre, with a similar spatial pattern to the winds. Visual comparison of τ and the wind fields of the storm-centric composites in Figures 5.1 and 5.3 suggests that u is the dominant explanatory variable for τ.

This is investigated further by looking at u–τ and RH–τ pattern correlations. Storm-centric τ is regridded to the 200 km $\times$ 200 km resolution of the u and RH fields. Figure 5.4(a) shows an example scatter plot of NA storm-centric MODIS τ against u. As can be seen, there is an approximately linear relationship between u and τ, with a good pattern correlation ($r = 0.83$). A linear relationship between u and τ is consistent with the findings of Smirnov et al. (2003) and other studies referenced by them. By comparison, the scatter plot of NA storm-centric MODIS τ against RH, Figure 5.4(b), shows a much weaker and less linear relationship between RH and τ ($r = 0.32$). This supports the argument that u is the primary explanatory variable for NA storm-centric MODIS τ. The u–RH pattern correlation ($r = 0.62$) is stronger than the RH–τ correlation, suggesting that non-orthoganality between u and RH may be driving the RH–τ correlation. Interestingly, for fixed u, looking along a vertical line in Figure 5.4(a) or a fixed color in Figure 5.4(b), there often appears to be a negative RH–τ correlation, opposite to that which would be expected for the conceptual aerosol hygroscopic growth model.

A linear regression model, of form $\tau(u) = a + bu$, has been fitted to the NA storm-centric τ data shown in Figure 5.4(a). The resulting coefficients are shown in the first row of Table 5.1. This model has then be used to make a prediction of τ using u as the only input field. The resulting NA storm-

centric $\tau(u)$ is shown in Figure 5.4(c). By visual inspection of Figures 5.1(b) and 5.4(c), it can be clearly seen that a linear regression model based only on u is capable of reproducing the significant features of NA storm-centric MODIS τ.

For comparison, Figures 5.4(d)–(f) show corresponding scatter plots and predicted $\tau(u)$ for NA storm-centric AATSR τ. It can be seen that a linear relationship between u and τ is less clear here than it is for the MODIS data. A lower pattern correlation is found, probably due to a combination of increased noise in the AATSR data and surface reflectance effects in the MODIS data. However, as with the MODIS data, it can be seen that u is a more appropriate explanatory variable than RH.

The first four rows in Table 5.1 contain u–τ and RH–τ pattern correlation coefficients, as well as u linear regression model coefficients, for the different MODIS/AATSR and NA/SA combinations. The r values show that τ is always more strongly correlated to u than to RH.

For both MODIS and AATSR separately, the intercept (a) is lower in the NA than in the SA, consistent with higher background pollution in the NA. The slopes (b) for NA MODIS, SA MODIS and NA AATSR $\tau(u)$ are comparable. However, b is much lower for SA AATSR $\tau(u)$. The reason for the higher MODIS and NA AATSR b may be that MODIS overestimates the u–τ relationship due to surface reflectance effects and AATSR amplifies high τ. The values of a and b calculated here for SA storm-centric composite AATSR τ ($a = 0.0813$, $b = 0.0034 \pm 0.0003$) are similar to those previously found for the remote southern ocean by Huang et al. (2010) ($a = 0.0850 \pm 0.0002$, $b = 0.0040 \pm 0.0002$) who used temporally and spatially matched τ and u data in their analysis.

	u			RH
	b ($\mathrm{m^{-1}s}$)	a	r	r
NA MODIS τ	0.0097±0.0003	0.0496	0.83	0.32
SA MODIS τ	0.0111±0.0004	0.0041	0.83	0.22
NA AATSR τ	0.0089±0.0006	0.0997	0.57	0.17
SA AATSR τ	0.0034±0.0003	0.0813	0.54	0.19
NA MODIS η	-0.0184±0.0007	0.5793	-0.80	-0.38
SA MODIS η	-0.0115±0.0007	0.4621	-0.61	-0.21
NA AATSR α	-0.0388±0.0033	0.7575	-0.51	-0.05
SA AATSR α	-0.0461±0.0038	0.8030	-0.52	0.04

Table 5.1: Linear regression slopes (b), intercepts (a) and pattern correlation coefficients (r) of aerosol properties (aerosol optical depth τ, fine-mode fraction η and Ångström exponent α) against wind speed (u) across the North Atlantic (NA) and South Atlantic (SA) storm-centric composite domains. The final column contains r for aerosol properties against relative humidity (RH). The pattern correlation coefficients between u and RH are 0.62 and 0.54 for the NA and the SA respectively.

The final four rows of Table 5.1 show pattern correlation coefficients and u linear regression model coefficients for the aerosol size parameters. These also show strong relationships with u, although the linear models for the size parameters do not work quite as well as for the $\tau(u)$ models.

In order to test further the hypothesis that much of the observed storm-centric τ is due to sea-salt emission, composites are produced using MACC reanalysis τ data. Figures 5.5(a) and (b) show all-conditions composites of the MACC total τ data. For the NA, the mean MACC τ is comparable to that of AATSR, being higher than that of MODIS. For the SA, MACC τ is higher than in either of the satellite datasets. There is an unexplained peak in MACC τ in the centre of the NA all-conditions composite, a feature which is unobserved in the satellite all-conditions NA composites. It is possible that this disagreement with the satellite datasets may be due to sampling difference (Sayer et al., 2010b). Low τ values are observed at the polewards end of both the NA and the SA all-conditions

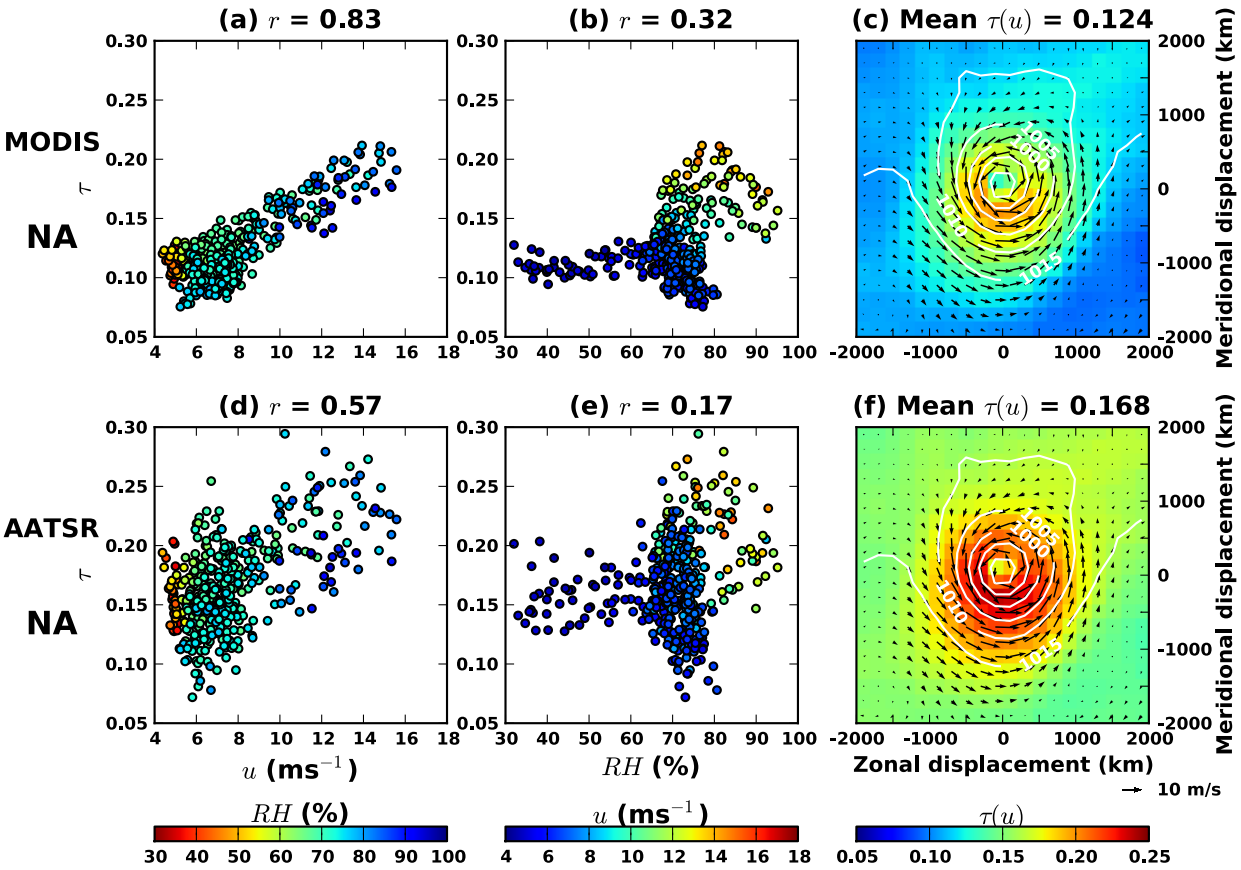

Figure 5.4: (a) Scatter plot of North Atlantic (NA) storm-centric composited Aqua-MODIS aerosol optical depth (τ) against wind speed (u) colored according to relative humidity (RH). Each point in the scatter plot corresponds to a 200 km $\times$ 200 km grid point in Figure 1(b). (b) A similar scatter plot for τ against RH, colored according to u. (c) u-fitted linear model predicted $\tau(u)$ based on the coefficients in the first row of Table 5.1: $\tau(u) = 0.0496 + 0.0097u$. (d–f) Similar to (a–c), but for NA AATSR τ. Similar scatter plots and u linear model predictions for the other MODIS and AATSR aerosol properties for both the NA and the South Atlantic (SA) can be viewed in Appendix C.

composites.

The NA storm-centric composite of MACC total τ, Figure 5.5(b), is quantitively similar to that of AATSR, once again being higher than that of MODIS. As for the all-conditions composites, the SA storm-centric composite of MACC τ, Figure 5.5(e), is higher on average than in either of the satellite datasets. Both have the strong peak in τ near the storm-centre, a very similar feature to that observed in the satellite composites. Storm-centric composites of MACC sea-salt τ, Figures 5.5(c) and (f), demonstrate that this peak is primarily due to sea-salt in the MACC data. The peak matches the wind speed field more closely than the RH field. This provides further evidence that the increase in τ near the centre of the storm-centric composites is due to increased emission of sea-salt via increased wind

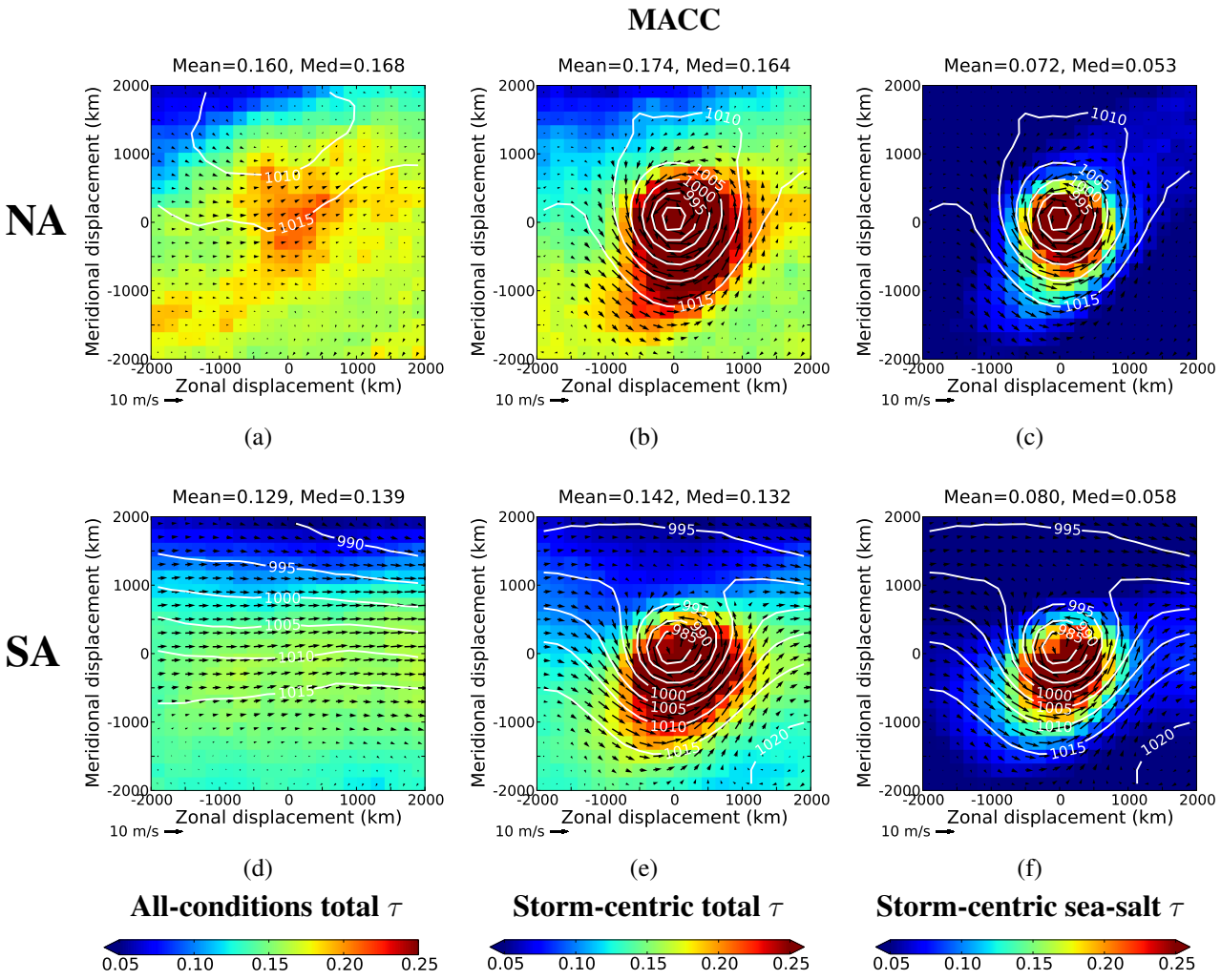

Figure 5.5: MACC Reanalysis t + 3 hour forecast all-conditions total aerosol optical depth (τ; a, d), storm-centric total τ (b, e) and storm-centric sea-salt τ (c, f) median composites for the North Atlantic (NA; a–c) and the South Atlantic (SA; d–f) oceans. Composite ERA-Interim mean sea level pressure (p_0, hPa; white contours) and wind vectors (black arrows) are over-plotted. The wind vector scale is provided at the bottom left-hand edge of each plot. Positive meridional displacements are poleward of the storm centre. The data cover 2003–2007. A minimum 850 hPa relative vorticity threshold of 7×10^{-5} s^{-1} is used.

speeds.

Corresponding storm-centric median composites of ECHAM5-HAM total τ for the present-day (PD) run over the NA and the SA are shown in Figures 5.6(a) and (d) respectively. An enhancement in τ equatorward of the storm centre is again clearly visible. These are generally lower than the storm-centric τ for the MODIS, AATSR and MACC datasets, particularly in the polar air westward and poleward of the storm centre. In agreement with the other datasets, storm-centric τ is higher over the NA compared to over the SA. The τ composites for the pre-industrial (PI) run are shown in Figures 5.6(b) and (e). For the NA, there is a large decrease in τ between the PD and PI runs,

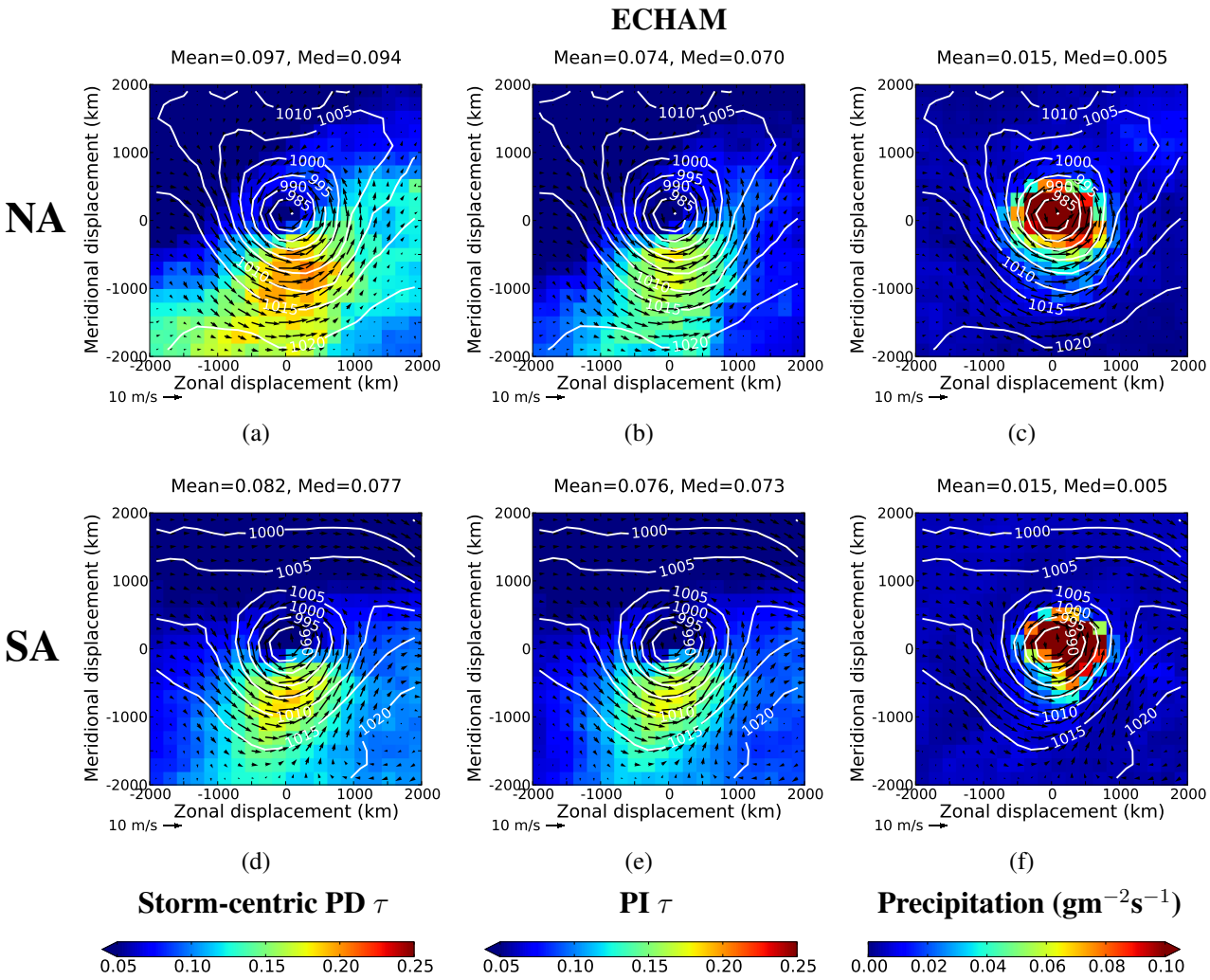

Figure 5.6: Storm-centric median composites of ECHAM5-HAM present-day (PD) aerosol optical depth (τ; a, d), pre-industrial (PI) τ (b, e) and PD total precipitation rate (c, f) over the North Atlantic ocean (NA; a–c) and the South Atlantic Ocean (SA; d–f). Composite ECHAM5-HAM mean sea level pressure (hPa; white contours) and wind vectors (black arrows) are over-plotted. The wind vector scale is provided at the bottom left-hand edge of each plot. Positive meridional displacements are poleward of the storm centre. The data cover one year, with meteorology nudged to the year 2000. A minimum 850 hPa relative vorticity threshold of 7×10^{-5} s^{-1} is used.

consistent with a decrease in the background anthropogenic aerosol concentrations. For the SA, where there is less anthropogenic aerosol, the decrease is much smaller. In fact, the storm-centric τ is similar for PI NA, PD SA and PI SA, demonstrating that the main reason for higher storm-centric τ over the NA is due to higher anthropogenic aerosol concentrations compared to over the SA.

Comparing Figure 5.6(a) with Figure 5.4(c), it can be seen that the ECHAM5-HAM τ does not match the wind field as closely as might be expected. In particular, the ECHAM5-HAM τ is very low at the storm centre, and it peaks slightly further equatorward than the region of maximum wind speed. The 'hole' in τ in the immediate vicinity of the storm centre may be due to model precipitation scavenging much of the aerosol. Storm-centric median composites of ECHAM5-HAM total precipitation rate are shown in Figures 5.6(c) and (f). It can be seen that the region of maximum of precipitation corresponds closely to the 'hole' of low τ. It is possible that too much aerosol may have been scavenged by the model precipitation, and that this might be responsible for the particularly low τ in the polar air.

5.3 Conclusions

As demonstrated, midlatitude synoptic storm systems have a significant effect on storm-centric composite aerosol properties, with retrieved aerosol optical depth and aerosol size increasing substantially in regions of high wind speed near the centre of extratropical cyclones over ocean. By producing composites of both MODIS Collection 5 aerosol data, which have no wind speed dependent sea-surface reflectance correction, and GlobAerosol AATSR aerosol data, which do have a wind speed dependent sea-surface reflectance correction, it has been shown that sea-surface reflectance effects alone cannot account for the observed storm-centric aerosol signals. Pattern correlations and linear regression models, applied across the storm-centric composite domains, have shown that wind speed is a suitable explanatory variable for the aerosol properties. The results are consistent with wind speed dependent emission of sea-salt. Further evidence in support of this interpretation has been provided by composites of MACC reanalysis sea-salt aerosol optical depth data.

Higher satellite-retrieved τ data were observed in the North Atlantic ocean composites compared to the South Atlantic ocean composites. Composites of ECHAM5-HAM pre-industrial and present-day aerosol simulations confirmed that this difference is primarily due to higher anthro-

pogenic aerosol concentrations in the North Atlantic ocean.

Midlatitude storms are also a major driver of variation in cloud properties (Field and Wood, 2007). The extent to which extratropical cyclones may be responsible for driving satellite-observed relationships between midlatitude aerosol and cloud properties will be explored in Chapter 6.

Chapter 6

The contribution of extratropical cyclones to observed aerosol–cloud relationships

In Chapter 5, it was shown that the high wind speeds associated with extratropical cyclones can increase sea-salt emission, increasing the aerosol optical depth and decreasing the fine-mode fraction. Other studies (e.g. Field and Wood, 2007) have shown that these synoptic systems can affect cloud properties. In both cases, storm-centric compositing has been shown to be a fruitful approach. Here, the storm-centric compositing methodology is applied to the investigation of observed relationships between aerosols and clouds. The relative vorticity of each storm and position relative to the storm centre are considered in an attempt to provide a simplified description of the large-scale forcing of aerosols and clouds by extratropical cyclones. The following question is considered in this chapter:

1. Can spurious relationships between aerosol and cloud properties be explained by considering simply the relative vorticity of extratropical cyclones and position relative to the storm centre?

The data and methodology used are explained in Section 6.1. Results are presented and discussed in Section 6.2. Conclusions are summarised in Section 6.3.

6.1 Method

This chapter uses daytime data from the MODIS Science Team Collection 5 Atmosphere Level 2 Joint Product for the Aqua satellite, covering 2003–2007 (Section 1.2.4). In addition to the $10\,\mathrm{km} \times 10\,\mathrm{km}$ aerosol optical depth (τ) data used in the previous chapter, this chapter also uses

$5\,\text{km} \times 5\,\text{km}$ cloud top temperature (T_{top}) and cloud fraction (f_c) data. Liquid cloud top properties, such as liquid cloud droplet number concentration, are not investigated here because much of the extratropical cyclone domain is dominated by high clouds with cold tops, as will be shown. Strict ocean-retrieval-only masking is applied to the τ data only. Retrievals of T_{top} and f_c are likely to be far less sensitive to surface albedo changes between land and ocean. As in the previous chapter, ERA-Interim $850\,\text{hPa}$ relative vorticity (ω), zonal and meridional components of the 10-metre wind and mean sea level pressure are also used.

The storm-centric gridding methodology is almost identical to that explained in Section 5.1. Here, the level 2 satellite data are gridded to a lower resolution of $200\,\text{km} \times 200\,\text{km}$, the same as the ERA-Interim data, since this seems to be a sensible choice of co-location scale for much of the aerosol–cloud interaction analysis. At this scale, the assumption of clear-sky τ being representative for the grid box should hold, such that τ can be assumed to be co-located with T_{top} and f_c (Anderson et al., 2003).

First, in order to illustrate how τ, T_{top} and f_c change between weaker and stronger storms, median composites for a weaker relative vorticity range of $3 < \omega < 5{\times}10^{-5}\,\text{s}^{-1}$ are shown alongside those for the stronger vorticity range of $\omega > 7{\times}10^{-5}\,\text{s}^{-1}$ used in Chapter 5. The weaker vorticity range was chosen to sample a similar number of storms to the stronger vorticity range. To provide an indication of the data spread within each of these vorticity ranges, lower and upper quartile composites are produced to complement the median composites. For example, Figure 6.3 shows the T_{top} composites for the North Atlantic (NA) ocean. Over the NA ocean, the median storm-centre mean sea level pressures are $1008\,\text{hPa}$ for the weaker range and $998\,\text{hPa}$ for the stronger range. Over the SA, these median pressure minima are $990\,\text{hPa}$ and $980\,\text{hPa}$.

Second, following Chapter 3, regression slopes and correlations of the cloud properties versus τ are calculated for the all-conditions data and for the storm-centric data. This is done for each $200\,\text{km} \times 200\,\text{km}$ grid box in the domain. The full range of vorticities, $\omega > 1{\times}10^{-5}\,\text{s}^{-1}$, are used for the regression and correlation calculations. Following Chapter 3, a lin–lin fit is used for T_{top} versus τ and a lin–log fit is used for f_c versus τ. For example, the regression slopes and correlations of NA T_{top} versus τ are shown in the first two columns of Figure 6.5.

Third, in order to investigate the extent to which storm strength may be able to explain the observed relationships, the τ and cloud property data are shuffled for each grid box within narrow

vorticity ranges of $1\times10^{-5}\,\mathrm{s}^{-1}$ before recalculating the regression slopes and correlations. By randomising the pairing of the cloud and τ data before calculating the relationships, the contributions due to retrieval errors and aerosol–cloud interactions are largely removed. However, they may not be completely removed because some correctly matched cloud property and τ pairs may remain after shuffling, most likely for stronger storms with $\omega > 10\times10^{-5}\,\mathrm{s}^{-1}$ where there are fewer storms in a given $1\times10^{-5}\,\mathrm{s}^{-1}$ interval. Because this shuffling occurs within narrow ω ranges, the shuffled cloud and τ data remain functions of ω. So the calculated relationships between shuffled τ and the cloud properties represent the synoptic component which can be explained by ω and position in the storm-centric domain. Of course, no strong relationships should be found for the shuffled all-conditions data which are also included as a control. For example, the third and fourth columns of Figure 6.5 show the regression slopes and correlations of NA T_{top} versus τ, where the data was first shuffled within each narrow vorticity range.

Most of the results for the NA (50°W–10°W, 30°N–55°N) and the South Atlantic ocean (SA; 50°W–10°E, 55°S–30°S) are shown in this chapter. The SA T_{top} and f_c median, lower quartile and upper quartile composites are shown in Appendix D.

6.2 Results and discussion

6.2.1 Aerosol optical depth (τ)

Figures 6.1(a)–(c) show the lower quartile, median and upper quartile storm-centric composites of Aqua-MODIS Collection 5 Aerosol Optical Depth (τ) for North Atlantic ocean (NA) storms with relative vorticity (ω) in the range $3 < \omega < 5\times10^{-5}\,\mathrm{s}^{-1}$. The lower quartile composite has low τ across most of the domain, indicated by the blue, with a slight enhancement in the region of high wind speeds to the south-east of the storm centre. There is also a slight enhancement in the south-east corner of the domain, far away from the storm-centre, most likely due to background conditions in the North Atlantic. In the median composite, a slight enhancement is also visible just to the south-east of the storm centre, but is weak compared to the background. A decrease in the south-western and northern parts of the domain is visible in the median composite, likely due in part to the low wind speeds here, although frontal clearance and the advection of polar air may also play a role. This decrease is more striking in the upper quartile composite, showing that high τ values are uncommon

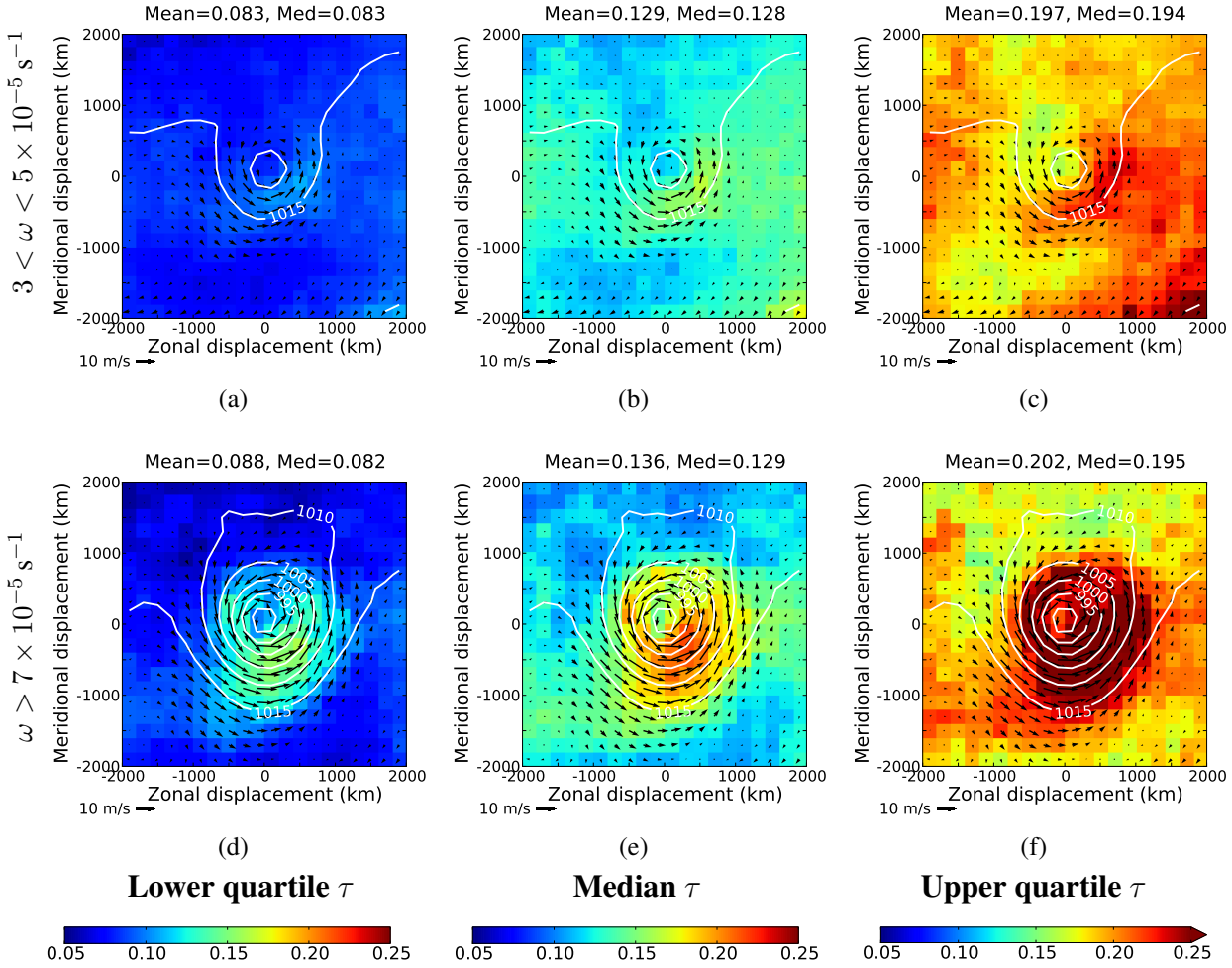

Figure 6.1: Storm-centric (a, d) lower quartile, (b, e) median and (c, f) upper quartile composites of Aqua-MODIS aerosol optical depth (τ) for two 850 hPa relative vorticity (ω) ranges for the North Atlantic ocean. Median composites of ERA-Interim mean sea level pressure (p_0; white contours) and wind vectors (black arrows) are over-plotted. The wind vector scale is provided at the bottom left-hand edge of each composite. Positive meridional displacements are poleward of the storm centre. The data cover 2003–2007.

to the north-west of the storm centre and in the south-western part of the domain for this vorticity range.

Figures 6.1(d)–(f) show corresponding composites for a stronger vorticity range of $\omega > 7{\times}10^{-5}$ s^{-1}. This stronger vorticity range is the same as that used in Chapter 5, so the median is similar to that shown in Figure 5.1(b) apart from the difference in resolution. Much of the discussion in Chapter 5 applies here too. The strong enhancement of τ in the regions of high wind speed to the south and east of the storm centre is visible in both the lower quartile and the upper quartile composites in addition to the median composite. This storm-centric enhancement is much stronger for the stronger vorticity range than it is for the weaker vorticity range commented on above.

For both vorticity ranges, there is an average τ increase of order 0.05 between the lower quartile

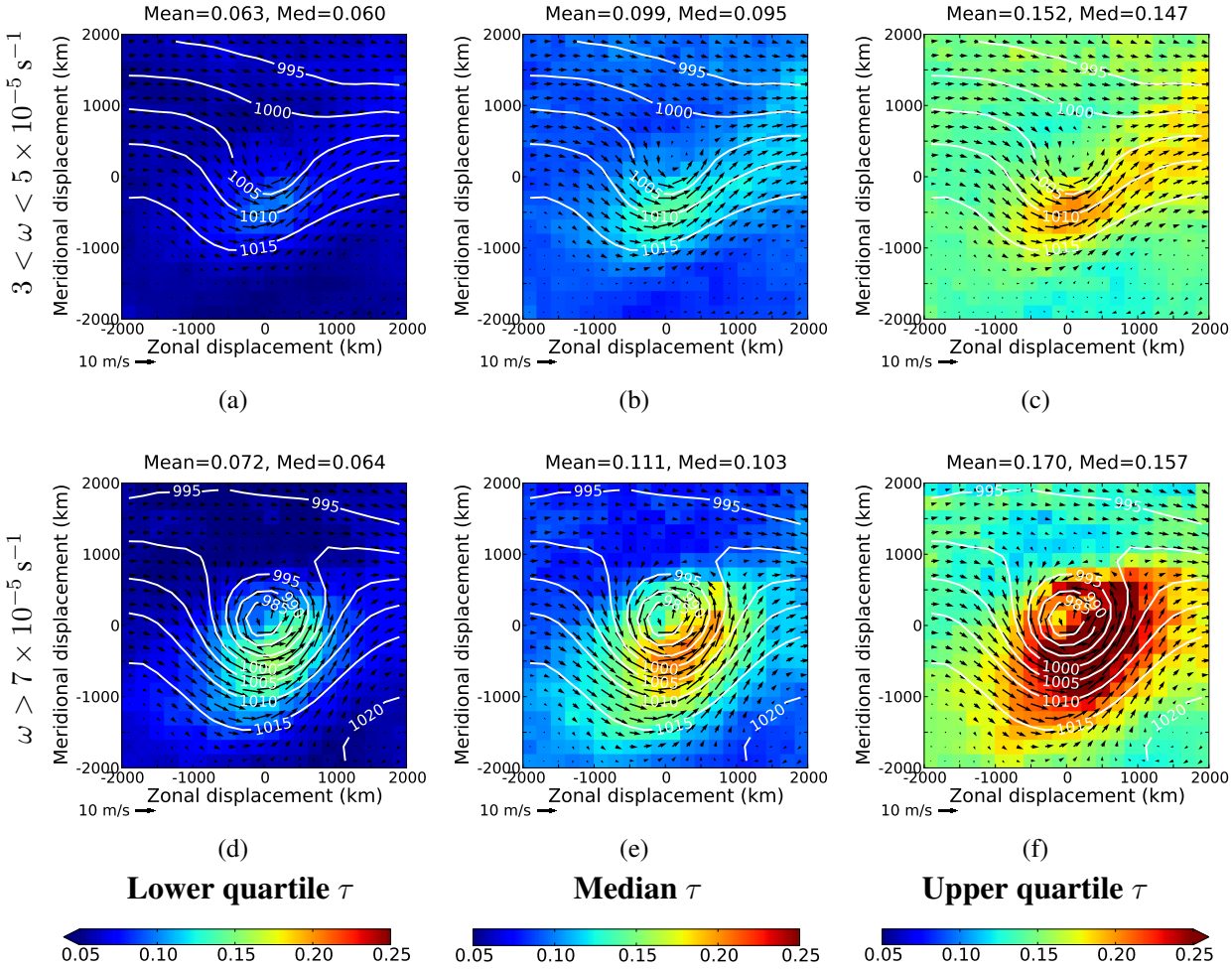

Figure 6.2: Same as Figure 6.1, but for Aqua-MODIS aerosol optical depth (τ) over the South Atlantic ocean.

and median composites, and an increase of order 0.07 between the median and the upper quartile composites. This is quite a large spread compared to the average enhancement of less than 0.01 due to the change in vorticity. However, near the centre of the storm domain, the signal due to the vorticity change is of order 0.05, comparable to the average differences between the medians and the quartiles.

The corresponding South Atlantic ocean (SA) composites can be seen in Figure 6.2 . They are similar to those for the NA, but with a lower background τ level as observed in Chapter 5.

6.2.2 Cloud top temperature (T_{top})

Figures 6.3(a)–(c) show the lower quartile, median and upper quartile storm-centric composites of Aqua-MODIS Collection 5 cloud top temperature (T_{top}) for NA storms with relative vorticity in the range $3 < \omega < 5{\times}10^{-5}\,\mathrm{s}^{-1}$. The lower quartile tends towards sampling scenes where cold high

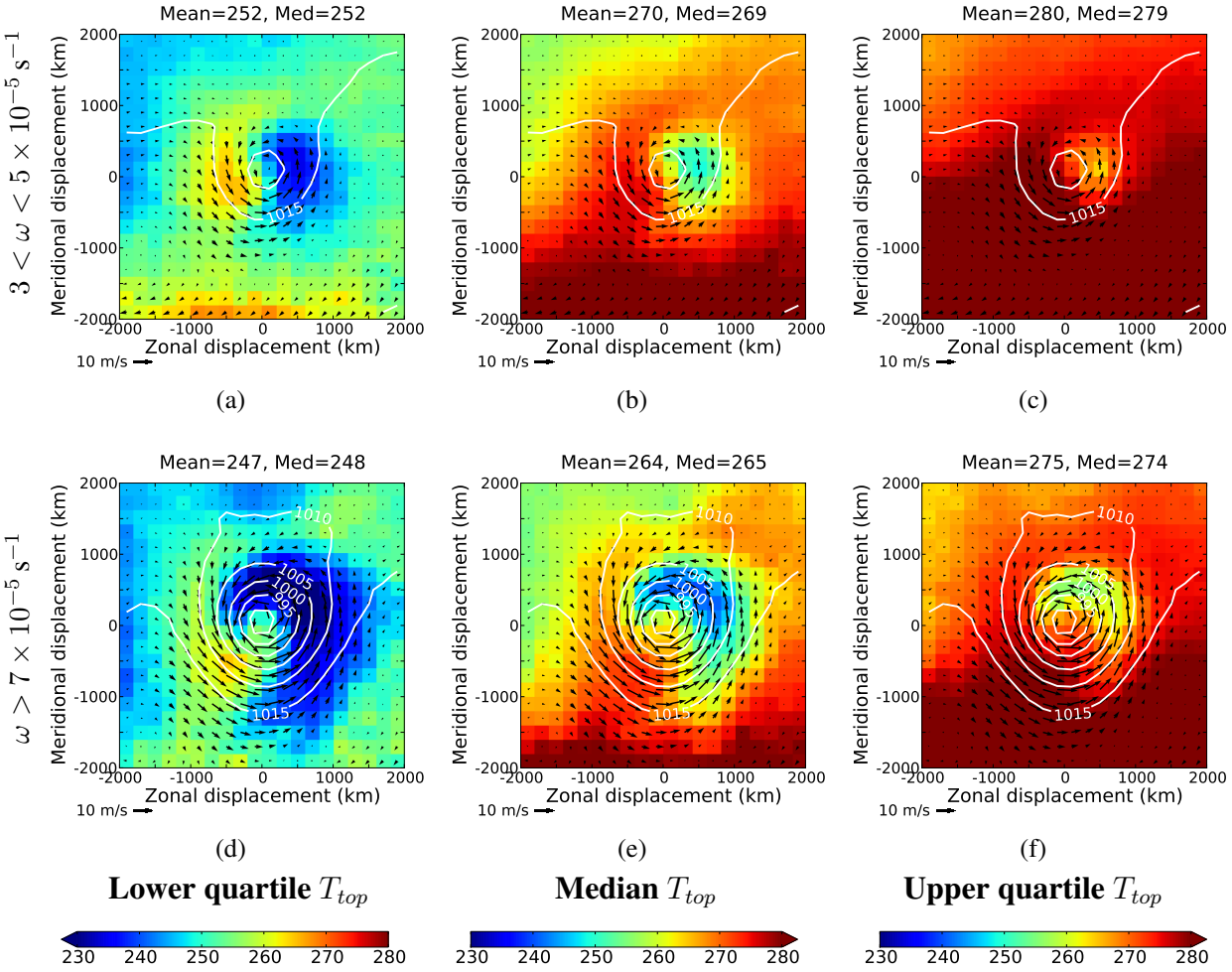

Figure 6.3: Same as Figure 6.1, but for Aqua-MODIS cloud top temperature (T_{top}, K) over the North Atlantic ocean.

cloud dominates, whereas the upper quartile tends towards scenes where warm low cloud can be seen. A shield of colder higher cloud can be discerned to the east of the storm centre in all three of the composites. Relatively cold cloud can also be seen in the advected cold polar air in the north-west of the storm-centric domain. In the lower quartile, a band of warmer cloud can be seen to the west of the storm centre, indicating a general absence of high clouds here. A general meridional gradient in T_{top} exists, with warmer clouds generally observed at the equatorward edge of the domain.

The composites for the stronger vorticity range of $\omega > 7 \times 10^{-5}$ s^{-1} are shown in Figures 6.3(d)–(f). It can be seen from the mean sea level pressure contours, shown in white, that deeper pressure minima occur for these stronger storms. These composites have similar general features to those commented on above. The shield of cold high cloud is larger and colder for the stronger vorticity range than it is for the weaker vorticity range. This is to be expected, since this shield of high cloud is synoptically driven.

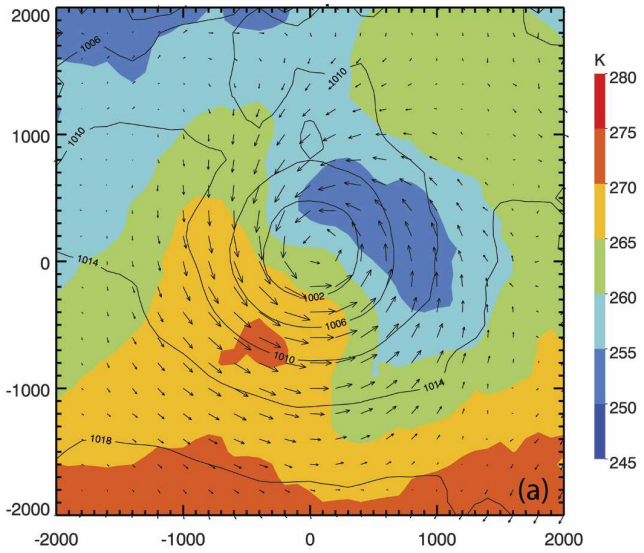

Figure 6.4: Terra-MODIS level 3 cloud top temperature (T_{top}) storm-centric mean composite for the North Atlantic ocean, produced by Field and Wood (2007). Note the different colour scale compared to Figure 6.3. [From Field, P. R. and Wood, R.: Precipitation and Cloud Structure in Midlatitude Cyclones, J. Climate, 20, 233–254, doi:10.1175/JCLI3998.1, 2007. ©American Meteorological Society. Reprinted with permission.]

For comparison, the NA T_{top} mean composite plot of Field and Wood (2007) is shown in Figure 6.4. Field and Wood (2007) used a different storm identification and compositing methodology to that used here, identifying extratropical cyclones based on surface pressure gradients and minima. Their mean composite of T_{top} has similar features to the median composites produced here and shown in Figure 6.3. The T_{top} values of the Field and Wood (2007) composite are somewhere between those for the two vorticity ranges used here. Similarly, their mean storm-centre mean sea level pressure of approximately 1000 hPa is between the median storm-centre values of 1008 hPa and 988 hPa for the NA composites produced here.

For both vorticity ranges, the domain average increase in T_{top} between the lower quartile and the median is approximately 17 K. The increase between the median and the upper quartile is approximately 10 K. The domain average decrease between the weaker composites and the stronger composites is of order 5 K, considerably smaller than the spread between the quartiles. However, the strengthening of the high cloud shield can result in some grid boxes seeing decreases of up to 20 K.

The SA T_{top} composites are very similar, so they are not shown in this chapter. For reference, they can be viewed in Appendix D Figure D.1.

Relationships between T_{top} and τ are now investigated in a storm-centric context. Figure 6.5(a) shows the regression slopes of T_{top} versus τ for each grid box of the NA all-conditions gridded data. It can be seen that negative regression slopes, indicated by blue, are found almost everywhere in

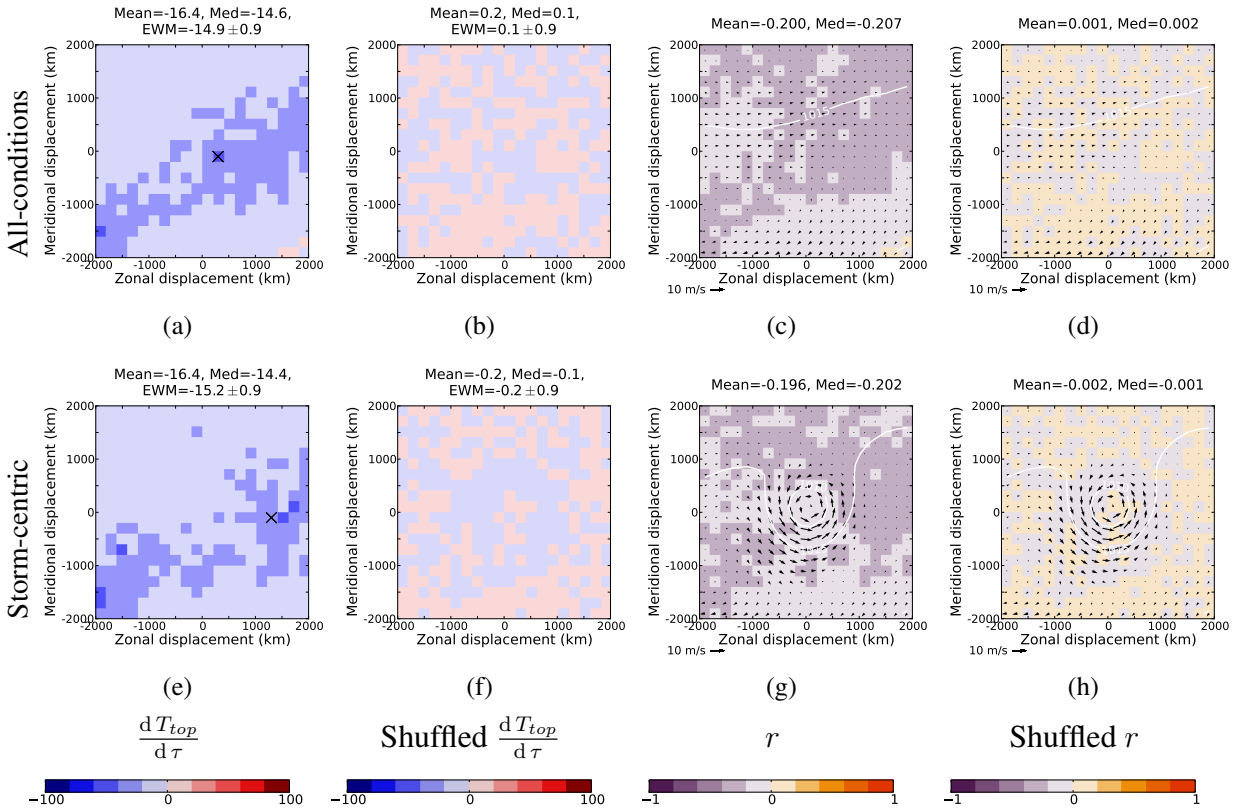

Figure 6.5: (a) All-conditions results of a lin–lin ordinary least squares regression fit of Aqua-MODIS cloud top temperature (T_{top}, K) versus aerosol optical depth (τ) over the North Atlantic ocean. Non-stippled slopes are statistically insignificant at the two-sigma confidence level. (b) Similar to (a), but for T_{top} and τ data which has been shuffled within each narrow relative vorticity range. (c) Linear Pearson correlation coefficients (r) corresponding to the slopes shown in (a). Median composites of ERA-Interim mean sea level pressure (p_0; white contours) and wind vectors (black arrows) are over-plotted. (d) Correlation coefficients corresponding to the slopes of the shuffled data shown in (b). (e)–(g) Similar to (a)–(d), but for storm-centric data rather than all-conditions data.

the domain. Taken individually, almost all of these regression slopes are statistically insignificant at two-sigma confidence, indicated by the lack of stippling. However, the error-weighted mean (EWM) for the whole domain is an order of magnitude larger than the associated one-sigma error. Since these regression slopes are for all-conditions, it would be expected that they should be similar to the NA T_{top} versus τ regression slopes calculated in Chapter 3. Comparison of the NA portion of Figure 3.10(a) with Figure 6.5(a) reveals that this appears to be the case.

The corresponding storm-centric regression slopes are shown in Figure 6.5(e). As mentioned in Section 6.1, the full vorticity range of all tracked storms is used. It can be seen that the storm-centric regression slopes are very similar to those for all-conditions. The storm-centric EWM of $-15.2\,\mathrm{K}$ is slightly steeper than the all-conditions EWM of $-14.9\,\mathrm{K}$. However, the one-sigma error of $0.9\,\mathrm{K}$ suggests that this smaller difference may be insignificant. This shows that analysing relationships

between NA T_{top} and τ in a storm-centric context appears to make little discernible difference to the results.

As outlined in Section 6.1, the T_{top} and τ data are next shuffled for each grid box within narrow vorticity ranges of $1\times10^{-5}\,\mathrm{s}^{-1}$. The regression slopes are then recalculated. This random shuffling largely removes spurious correlations between T_{top} and τ induced by indirect effects and correlated retrieval errors. The simplified large-scale synoptic contribution described by ω and position in the storm domain is retained. Since ω and position are meaningless references for the all-conditions data, it should be expected that the shuffled all-conditions slopes should be approximately zero. This is indeed the case, as Figure 6.5(b) shows. The all-conditions slope EWM of $0.1\,\mathrm{K}$ is an order of magnitude smaller than that for the non-shuffled all-conditions data and it is much smaller than the associated one-sigma error of $0.9\,\mathrm{K}$, rendering it insignificantly different from zero.

The slopes for the shuffled storm-centric data, shown in Figure 6.5(f), are also very small. The EWM of $-0.2\,\mathrm{K}$ is slightly steeper than for the shuffled all-conditions data, but it is still much smaller than both the one-sigma error and the non-shuffled EWM. These results show that there is no evidence to suggest that large-scale ω and position relative to the storm centre, representing a simplified description of synoptic forcing by extratropical cyclones, can explain spurious relationships between τ and T_{top}.

The all-conditions and storm-centric correlation coefficients (r), shown in Figures 6.5(c) and (g), are also very similar to one another. The observed correlations are negative, of order -0.2 on average, and comparable to the NA correlations shown in Figure 3.10(b). The correlations for the shuffled all-conditions and storm-centric data are shown in Figures 6.5(d) and (h). They are two orders of magnitude smaller than for the non-shuffled data. These observations for the correlation coefficients are consistent with those made for the regression slopes.

Corresponding regression slopes and correlations for the SA are shown in Figure 6.6. The latitudes have been inverted, with the poleward (southward) direction pointing to the top of the page. The EWM regression slopes for the non-shuffled data are stronger for the SA than for the NA, and there is a stronger meridional gradient, with the slopes becoming steeper nearer the equator. This stronger meridional gradient in the SA is also apparent in Figure 3.10(b). As was the case for the NA results, the difference between the all-conditions and the storm-centric EWM regression slopes is statistically insignificant, being smaller than the one-sigma error. Although the storm-centric shuffled

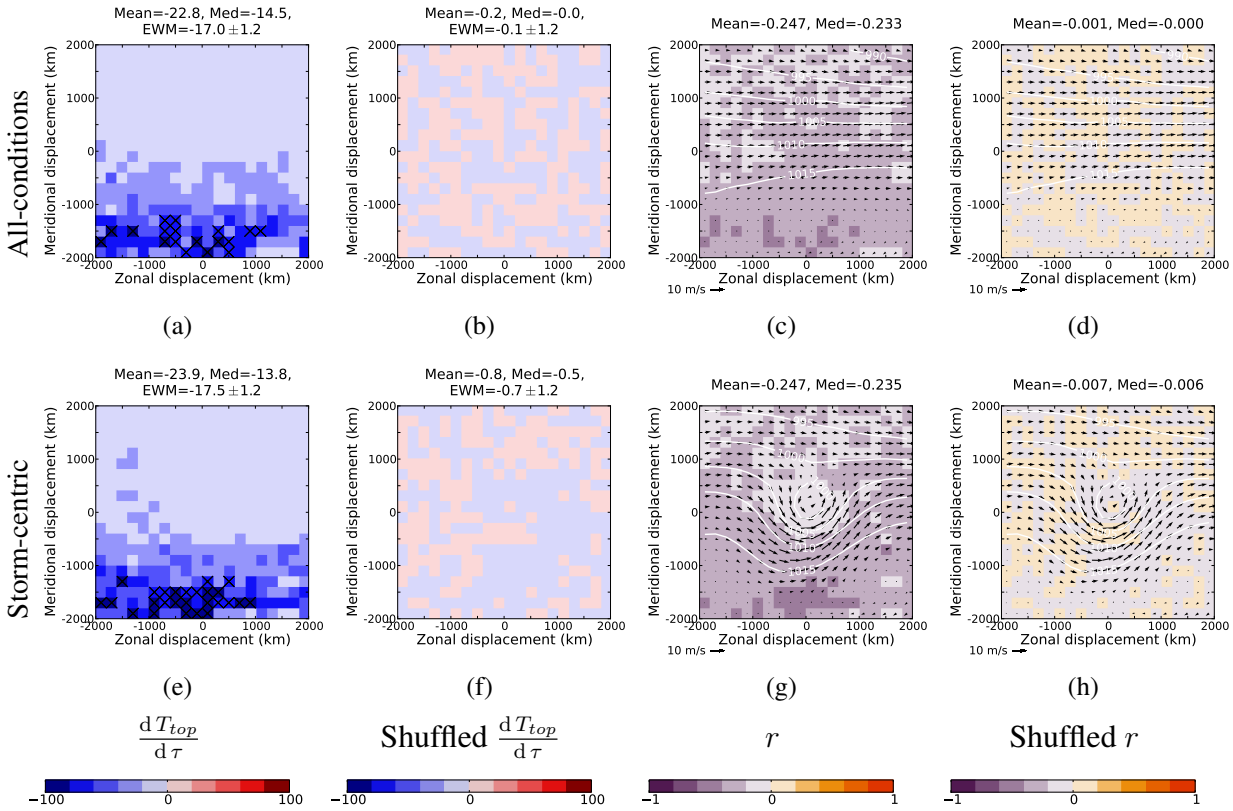

Figure 6.6: Similar to Figure 6.5, but for lin–lin fits of cloud top temperature (T_{top}) versus aerosol optical depth (τ) over the South Atlantic ocean.

regression slope EWM of -0.7 K is steeper than for the NA, it is still statistically insignificant. Similar remarks can be made for the SA correlations as were made for the NA correlations. Again, there is no evidence to suggest that the simplified description of large-scale synoptic forcing, described by ω and position in storm domain, can explain spurious relationships between τ and T_{top}.

6.2.3 Cloud fraction (f_c)

The lower quartile, median and upper quartile storm-centric composites of Aqua-MODIS Collection 5 cloud fraction (f_c) for storms with vorticity in the range $3 < \omega < 5{\times}10^{-5}\,\mathrm{s}^{-1}$ are shown in Figures 6.7(a)–(c). Blue indicates low f_c while red indicates high f_c. It can be seen there are often very high f_c values in the polewards part and the centre of the storm domain. Even in the lower quartile, f_c values larger than 0.8 are observed towards the centre of the storm domain. This feature corresponds to the cloud shield with cold T_{top} commented on above. In the upper quartile, the entire domain contains large f_c values, with the upper quartile composite domain mean being 0.965.

It is worth noting that these large fractional cloud covers may affect τ data in two ways. First,

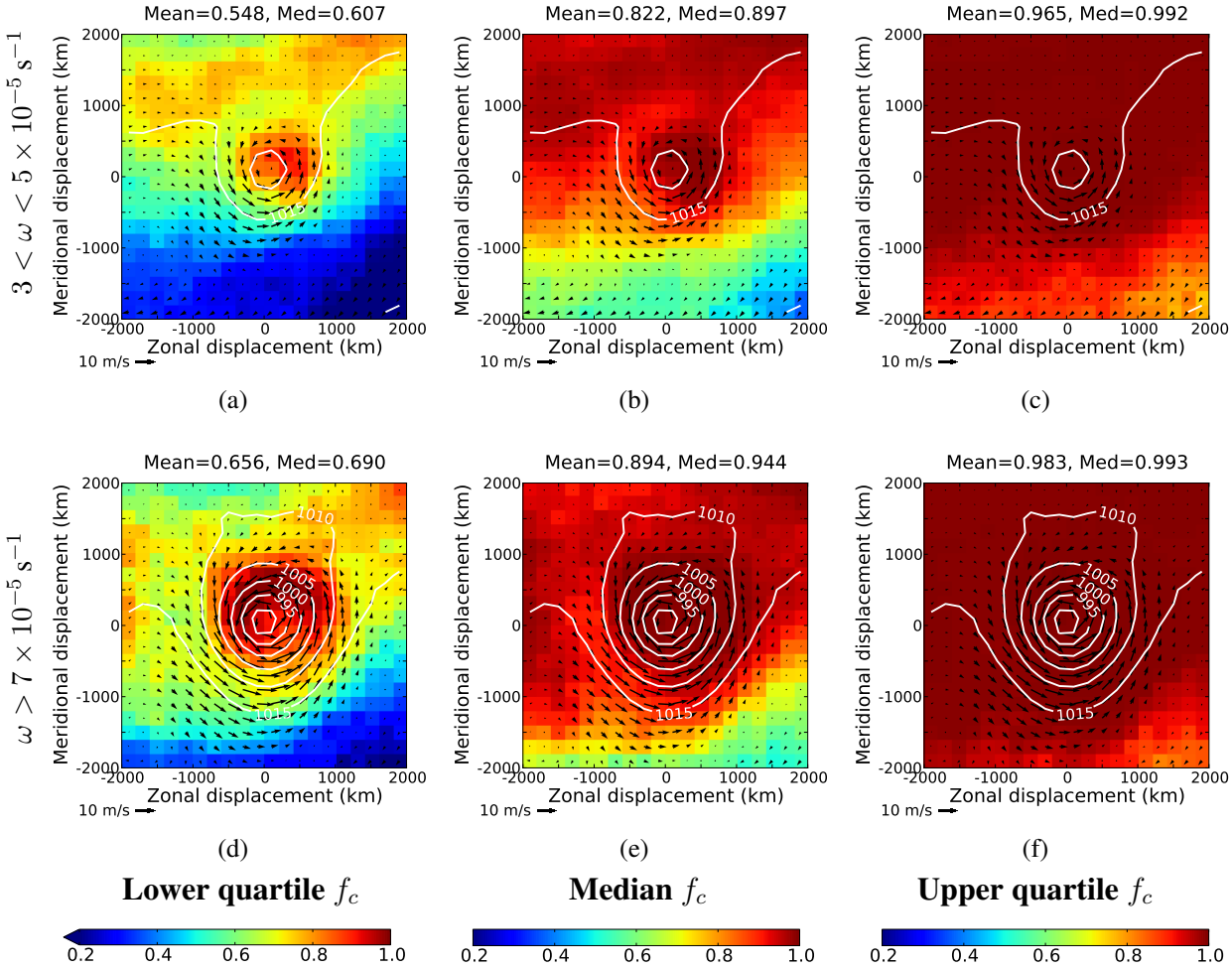

Figure 6.7: Same as Figure 6.1, but for Aqua-MODIS cloud fraction (f_c) over the North Atlantic ocean.

no aerosol retrievals will occur for grid boxes with complete cloud cover, biasing the τ data towards situations with lower f_c values. Second, cloud contamination of τ may be correlated with f_c, as mentioned in Section 5.2. However, the τ composites do not show a general meridional gradient in τ, only an enhancement near the storm centre, whereas the f_c composites show a strong meridional gradient. This suggests that potential cloud contamination cannot explain the observed τ composites shown in Figure 6.1. However, it is possible that cloud contamination may still contribute towards observed relationships between aerosol and cloud properties, as discussed in Chapter 4.

Figures 6.7(d)–(f) show the lower quartile, median and upper quartile storm-centric f_c composites for the stronger vorticity range of $\omega > 7{\times}10^{-5}\,\mathrm{s}^{-1}$. These composites have similar spatial patterns to those for the weaker vorticity range, but with higher values of f_c. The domain mean f_c differences between the two vorticity ranges are approximately 0.1, 0.07 and 0.02 for the lower quartile, median and upper quartile composites respectively. This shows that storm strength can have a large effect

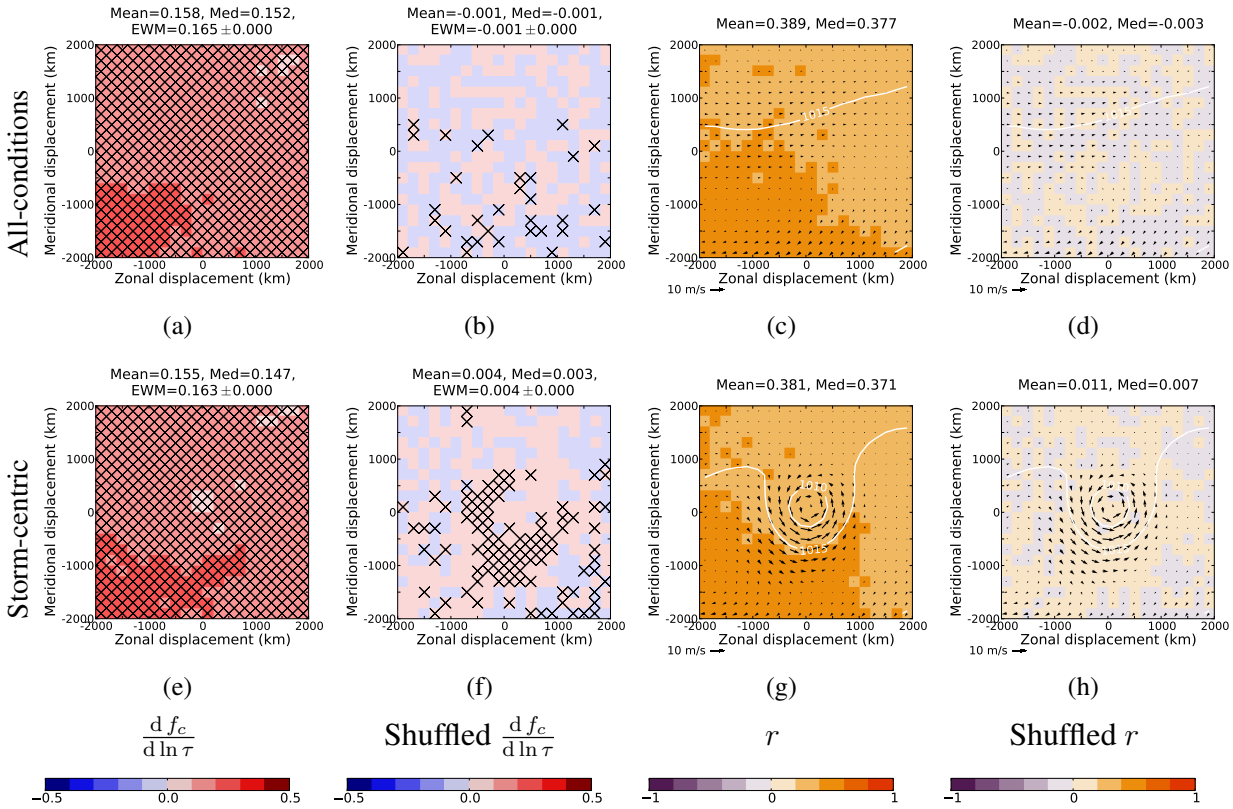

Figure 6.8: Similar to Figure 6.5, but for lin–log fits of cloud fraction (f_c) versus aerosol optical depth (τ) over the North Atlantic ocean.

on f_c. However, the domain mean differences between the lower quartile and the median, of order 0.2–0.3, and between the median and upper quartile, of order 0.1, show that there is also a large variation within each of these vorticity ranges.

The corresponding SA f_c composites are very similar to those for the NA, so they are not shown here. For reference, they are included in Appendix D Figure D.2.

It has been shown that both τ and f_c generally increase with storm strength, suggesting that the large-scale synoptic conditions of extratropical cyclones may lead to spurious relationships between these two variables. Quantitative relationships between τ and f_c are now investigated.

Figure 6.8(a) shows the all-conditions regression slopes of f_c versus $\ln\tau$. Positive slopes, shown in red, are observed everywhere in the all-conditions domain, approximately consistent with the NA part of Figure 3.13(a). In contrast to the T_{top} versus τ regression slopes of Figure 6.5 which were insignificant for most grid boxes when considered individually, no grid box of Figure 6.8(a) has a statistically insignificant f_c versus $\ln\tau$ regression slope, as shown by the ubiquitous stippling.

The corresponding storm-centric regression slopes, shown in Figure 6.8(e), are similarly non-

insignificant. The storm-centric regression slopes are very similar to those for all-conditions. There is a slight weakening in the centre of the storm domain, possibly due to there being little variation in the high f_c values found here. The EWM is very slightly smaller, being 0.163 compared to 0.165. The errors on these EWMs are more than two orders of magnitude smaller than the EWMs themselves.

As done previously for the T_{top} and τ data, the f_c and τ data for each grid box are next shuffled within each vorticity range of $1\times10^{-5}\,\mathrm{s}^{-1}$. The regression slopes are then recalculated across the full vorticity range. The NA all-conditions results are shown in Figure 6.8(b). A mixture of positive and negative slopes are observed. It would be expected that these regression slopes for the shuffled all-conditions data should be statistically indistinguishable from zero. The magnitude of the EWM is larger than the one-sigma error. However, it is two orders of magnitude smaller than the all-conditions EWM for the non-shuffled data and is also opposite in sign, -0.001 compared to 0.165. This indicates that the shuffling methodology is working approximately as expected.

Figure 6.8(f) shows the regression slopes for the shuffled NA storm-centric data. Many individual slopes just to the south and west of the domain centre are positive and non-insignificant, suggesting that the simplified description of the large-scale synoptics investigated here may indeed explain a spurious contribution to observed relationships between f_c and τ. This part of the domain, to the south of the storm centre, is also where the winds are strongest. The non-insignificant EWM of 0.004, which is also larger than the all-conditions EWM of -0.001, also supports this suggestion. However, this EWM is still almost two orders of magnitude smaller than the non-shuffled EWM of 0.163. Although the simplified large-scale synoptics, described by storm vorticity and position in the storm domain, may explain a spurious contribution to relationships between f_c and τ, this contribution is very small compared to the total observed f_c–$\ln\tau$ relationships.

Similar conclusions can be made for the f_c–$\ln\tau$ correlation coefficients. The all-conditions and storm-centric correlation coefficients, shown in Figures 6.8(c) and (g), are very similar to each other and are consistently positive. They are again approximately comparable to the NA correlations shown in Figure 3.13(b). The f_c–$\ln\tau$ correlations, of order 0.4, are approximately twice as strong as the T_{top}–τ correlations, of order -0.2, as can be seen by comparing Figures 6.8(c) and (g) with Figures 6.5(c) and (g).

The correlations for the shuffled NA all-conditions f_c and $\ln\tau$ data, shown in Figures 6.8(d), are more than two orders of magnitude smaller. The mean of -0.002 has an opposite sign to that

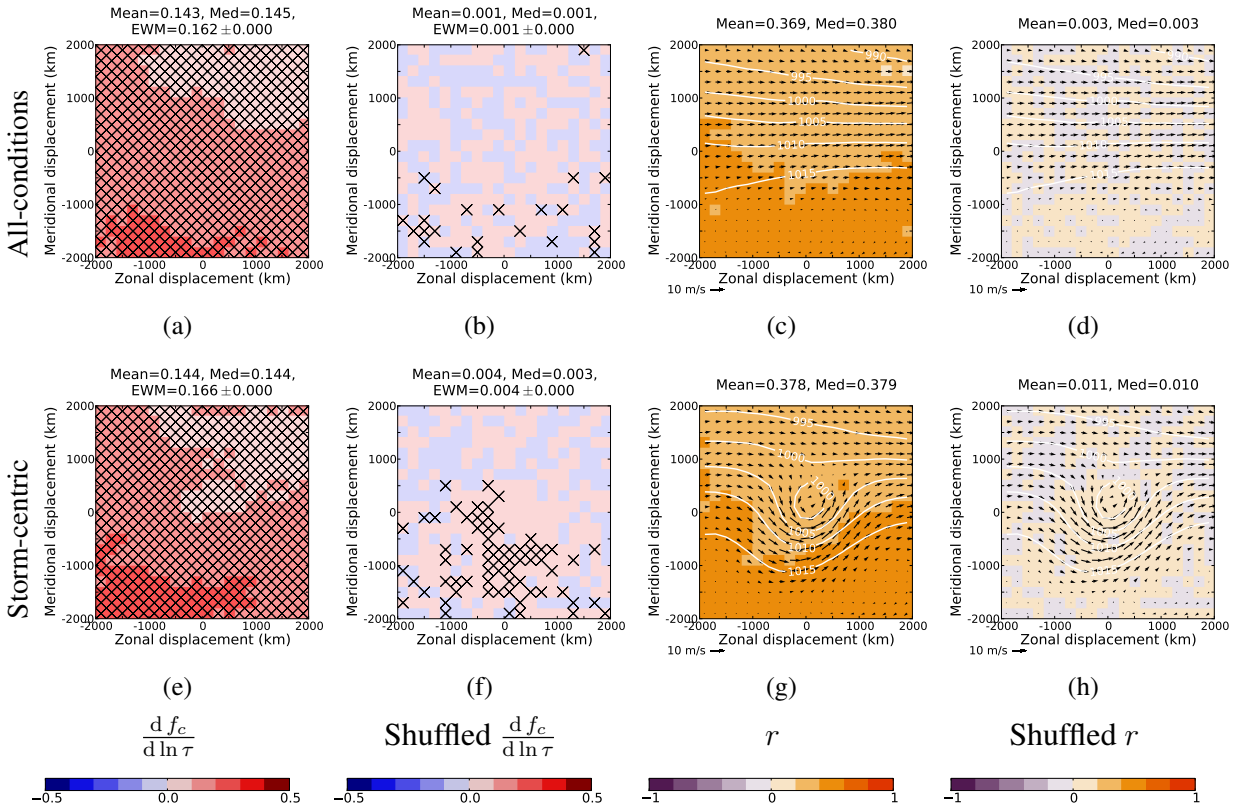

Figure 6.9: Similar to Figure 6.5, but for lin–log fits of cloud fraction (f_c) versus aerosol optical depth (τ) over the South Atlantic ocean.

for the non-shuffled all-conditions data and is close to zero, consistent with the regression slopes. The correlations for the shuffled storm-centric data, shown in Figure 6.8(h), are mostly positive, particularly near the storm centre. The mean of 0.011 is stronger than that for the shuffled all-conditions data, but it is still much smaller than the correlations for the non-shuffled data. Again, this suggests that the simplified description of the synoptics categorised here may be capable of explaining a spurious contribution to relationships between f_c and $\ln\tau$, but this contribution is much smaller than the total observed relationships.

Corresponding results for the SA are shown in Figure 6.9. One difference compared to the NA is that there is a stronger meridional gradient in the regression slopes, consistent with the regression slopes shown in Figure 3.13(a). Apart from this difference, the results are very similar to those for the NA. They provide further support for the conclusion that the simplified description of the large-scale synoptics can explain spurious relationships between τ and f_c, but that the spurious relationships are much weaker than observed relationships between τ and f_c.

6.3 Conclusions

In Chapter 5, it was shown that extratropical cyclones affect Aqua-MODIS retrieved aerosol optical depth (τ) over ocean. In this chapter, it was further demonstrated that on average for a given position in the storm-centric domain, stronger storms generally lead to higher τ than weaker storms, particularly near the storm centre. However, this enhancement is generally smaller than the variability in τ for a given storm strength and position in the storm-centric domain, probably due to variations in local wind speeds.

Storm-centric composites of cloud properties were also investigated in this chapter, building on the previous work of Lau and Crane (1995, 1997), Norris and Iacobellis (2005), Wang and Rogers (2001), Chang and Song (2006), Field and Wood (2007) and Field et al. (2008). It was found that the median composites of cloud top temperature (T_{top}) reveal a cold high cloud shield to the north and east of the storm centre. The extent and height of this shield increases with storm strength. The domain average T_{top} is colder for stronger storms compared to weaker storms. However, as for the τ fields, the variability between the quartiles for a given storm strength is generally larger than the difference due to vorticity changes, except for some grid boxes near the centre of the storm domain.

The cloud fraction (f_c) composites show a general increase in f_c with storm strength. However, once again the variability between the quartiles for a given storm strength is generally larger than the difference between different storm strengths.

Because storm strength has been shown to affect τ, T_{top} and f_c, it seemed plausible to hypothesize that extratropical cyclones may cause spurious relationships between these three properties. Storm-centric regression slopes and correlation coefficients of T_{top} versus τ and f_c versus $\ln \tau$ were calculated, following Chapter 3. The observed relationships were comparable to those observed for the Aqua-MODIS Collection 5 data in Chapter 3.

The τ, T_{top} and f_c were then shuffled within narrow ranges of storm vorticity, before recalculating the regressions slopes and correlations. This was done in an attempt to remove correlations due to retrieval errors and genuine aerosol–cloud interactions. By choosing narrow ranges of storm vorticity and retaining position in the storm domain, a simplified description of the large-scale synoptics of extratropical cyclones was investigated. This was done in order to answer the question asked at the beginning of the chapter: Can spurious relationships between aerosol and cloud properties be explained by considering simply the relative vorticity of extratropical cyclones and position relative

to the storm centre?

The T_{top} versus τ regression slopes for the shuffled data were insignificant, even when averaged across the storm-centric domain. This showed that the simplified description of the synoptics, described by storm vorticity and position relative to the storm centre, is incapable of explaining spurious relationships between T_{top} and τ for the data used here.

However, the f_c versus $\ln \tau$ regression slopes for the shuffled data were often found to be non-insignificant. This suggests that the simplified description of the large-scale synoptics can explain spurious relationships between f_c and τ. However, these spurious relationships are far smaller than observed relationships between f_c and τ, which may be better explained by cloud contamination, relative humidity (Chapter 4) and descriptions of meteorology based on local field variables such as winds Engström and Ekman (2010). Many of the non-insignificant slopes were found just to the south of the storm centre, where the winds are generally strongest. This suggests that the synoptically induced winds, which were largely found to explain the observed storm-centric τ composites (Chapter 5), may be the mechanism by which the simplified large-scale synoptics can explain spurious relationships between f_c and τ.

Chapter 7

Conclusions and future work

The climatic importance of aerosol–cloud interactions has been under investigation for over three decades. Twomey (1974, 1977) suggested that cloud albedo changes induced by aerosols might have a significant effect on the planetary albedo and climate, an effect now known as the cloud albedo effect or first aerosol indirect effect. Since then, many other aerosol indirect effects on climate via aerosol–cloud interactions have been proposed.

In recent years, there has been a considerable increase in the availability of in situ and satellite remote sensing data of aerosol and cloud properties. These observational data have been complemented by increasingly complex computer models. Many strong relationships between aerosol and cloud properties have been observed. However, the contributions from different potential aerosol indirect effects are still poorly understood, leading to some of the largest uncertainties in radiative forcing and future climate change (Forster et al., 2007). This is because aerosols, clouds and their interactions within the atmosphere represent a highly complex system. It is very difficult to establish the causal pathways for observed relationships between aerosol and cloud properties. Alongside genuine aerosol indirect effects on clouds, many other possible mechanisms may contribute to the observed relationships: cloud and precipitation effects on aerosol; meteorological covariation; observational data errors; and methodological errors, such as those arising from climatological spatial gradient effects.

The work presented in this thesis was conducted in an attempt to improve our quantitative understanding of aerosol–cloud interactions and their role in the Earth's climate system. Some of the potential reasons for observed relationships between aerosol and cloud properties have been investigated, building on the work of others. Potential methodological improvements have been identified.

New methodological techniques have been developed. General circulation model (GCM) experiments have been conducted alongside extensive analysis of satellite and reanalysis data.

Main conclusions are summarised in Section 7.1 below. Of course, much more work remains to be done in this important field, and some suggestions for future work are provided in Section 7.2.

7.1 Conclusions

Analysing satellite datasets over large regions may introduce spurious relationships between aerosol and cloud properties due to spatial variations in aerosol type, cloud regime and synoptic regime climatologies. This potential problem has largely been overlooked in previous aerosol–cloud interaction studies. In Chapter 2, which has mostly been published in Grandey and Stier (2010), two questions were asked: What are sensible choices of spatial scale for aerosol–cloud interaction studies? What effect may spatial scale choices have on global estimates of radiative forcing due to the cloud albedo effect?

Using regularly gridded daily data retrieved from the MODerate resolution Imaging Spectroradiometer (MODIS) instrument on the Terra satellite, relationships between aerosol optical depth (τ), derived liquid cloud droplet effective number concentration (N_d) and liquid cloud droplet effective radius (r_e) were calculated at different spatial scales. Log–log regression slope fits were used because log–log relationships between N_d and τ and between r_e and τ are often used to provide a measure of the cloud albedo effect. Maps of these slopes were produced for different methodological spatial scale choices.

Generally, positive slopes of $\ln N_d$ versus $\ln \tau$ were found over the ocean regions, in agreement with the conceptual cloud albedo effect. However, negative slopes occurred for many land regions. The spatial distribution of the $\ln r_e$ versus $\ln \tau$ slopes showed approximately the opposite pattern, with generally positive values for land regions and negative values for ocean regions.

It was found that for region sizes larger than $4^\circ \times 4^\circ$, spurious spatial variations in retrieved cloud and aerosol properties can introduce widespread significant errors to calculations of the regression slopes. For regions on the scale of $60^\circ \times 60^\circ$, representative of the regional scales used in several other aerosol–cloud interaction studies, these methodological errors may lead to an overestimate in global cloud albedo effect radiative forcing of order 80% relative to that calculated for regions on the

scale of $1^\circ \times 1^\circ$.

Although Chapter 2 focused on N_d and r_e, similar methodological considerations of spatial gradients may likely apply for analysis of relationships between other cloud properties and τ. It is recommended that analysis in aerosol indirect effect studies should be conducted on small regional scales no larger than $4^\circ \times 4^\circ$, before averaging the results to larger regional scales if necessary. In addition to avoiding errors due to spatial gradients, conducting the analysis at a resolution of order $1^\circ \times 1^\circ$ and presenting the results on a map can be an effective way to provide an overview of how aerosol–cloud relationships vary for different parts of the globe, without making prior assumptions about the homogeneity of these relationships across large regional scales.

Following the recommendations of Chapter 2, relationships between τ and various cloud properties were presented in Chapter 3. Two questions were asked: What are appropriate ways of quantifying and presenting relationships between aerosol optical depth and different cloud properties on global scales? What relationships between aerosol optical depth and different cloud properties can be observed across the world for different satellite and GCM datasets?

Four cloud properties were investigated: N_d, r_e, cloud top temperature (T_{top}) and cloud fraction (f_c). Regularly gridded daily versions of three satellite datasets were compared: cloud and aerosol data retrieved by the MODIS Science Team using radiances from the MODIS instrument on board the Aqua satellite (Aqua-MODIS Collection 5); cloud data retrieved by the Clouds and Earth's Radiant Energy System (CERES) Team using Aqua-MODIS radiances together with MODIS Science Team Collection 4 τ (Aqua-MODIS CERES Single Scanner Footprint, SSF); and Oxford-RAL retrieval of Aerosols and Clouds (ORAC) cloud data together with GlobAEROSOL τ data, retrieved using radiances from the Advanced Along-Track Scanning Radiometer (AATSR) on board Envisat. GCM data from the Aerosol Comparisons between Observations and Models (AeroCom) indirect effects intercomparison project were also used.

Appropriate ways of quantifying and presenting the relationships were considered. First, maps of the mean difference in a cloud property between low and high τ conditions, categorised according to seasonal grid-box median τ, were produced. Second, maps of regression slopes and correlation coefficients were also produced. The shapes of the regression fits were chosen based on both theoretical considerations and empirical coefficient of determination goodness-of-fit tests. The following fits were chosen: $\ln N_d$ versus $\ln \tau$ (log–log), $\ln r_e$ versus $\ln \tau$ (log–log), T_{top} versus τ (lin–lin) and

f_c versus $\ln \tau$ (lin–log).

In all three satellite datasets positive N_d–τ relationships were generally observed over ocean. The global error-weighted mean regression slopes of $\ln N_d$ versus $\ln \tau$ varied between 0.14 and 0.20 over ocean, suggesting a variation in cloud albedo effect radiative forcing of up to approximately 40%, depending on the satellite dataset used. There was much less agreement on the sign of the relationships over land.

There was also little agreement between the satellite datasets for the sign of the r_e–τ relationships over both ocean and land, providing little constraint on these relationships. However, stratification by liquid water path was not performed here.

Negative T_{top}–τ relationships were generally observed over both ocean and land in all three satellite datasets, showing that cloud top height and τ are positively correlated. The global error-weighted mean regression slopes of T_{top} versus τ varied in the ranges -7 K to -28 K over ocean and -3 K to -21 K over land.

Positive f_c–τ relationships were almost always observed over both ocean and land in all three satellite datasets. These relationships were stronger than for any of the relationships between the other cloud properties and τ. The global mean differences in f_c between low and high τ conditions were found to vary in the ranges 0.09 to 0.20 over ocean and 0.10 to 0.20 over land. The strong f_c–τ relationships have potentially large implications for climate, particularly if part of the relationship is due to aerosol increasing the lifetime of the cloud through suppression of precipitation: a change of 0.2 in global f_c could lead to a negative shortwave radiative effect of approximately $30\,\mathrm{Wm}^{-2}$, an order of magnitude larger than the positive forcing due to greenhouse gases, although this might partly be offset by a positive longwave radiative effect, particularly if the f_c increase is for high clouds. However, many different mechanisms may be responsible for f_c–τ relationships.

The main reasons for f_c–τ relationships were investigated in Chapter 4. The first question asked in Chapter 4 considered the possible contribution of cloud contamination of retrieved τ data: May the observed f_c–τ relationships be partly due to cloud contamination errors? In an attempt to remove cloud contamination from the τ data, state-of-the-art reanalysis-forecast τ data from the Monitoring Atmospheric Composition and Climate (MACC) project were combined with Aqua-MODIS Collection 5 f_c data. Two forecast time-steps of t + 3 hr and t + 24 hr after assimilation were used. The later forecast time-step of t + 24 hr should contain less cloud contamination but introduce more model

error compared to the earlier time-step of t + 3 hr. Over ocean, the global mean f_c increase of 0.20 between low and high τ conditions for the Collection 5 data was reduced to 0.12 and 0.07 when the t + 3 hour and t + 24 hour MACC data were used respectively. Over land, the global mean f_c increase of 0.20 was reduced to 0.15 and 0.10 when the MACC data were used. Although it is difficult to separate the contribution due to additional model error from the contribution due to reduced cloud contamination, these results suggest that cloud contamination may account for approximately half of the f_c–τ signal observed in the Aqua-MODIS Collection 5 data.

Even after the attempted partial mitigation of cloud contamination, strong positive f_c–τ relationships were found to remain for most of the world in the MODIS–MACC data. The strongest positive relationships were found to remain in the subtropics. Negative relationships appeared over much of the tropics when t + 24 hour MACC data were used. In order to further investigate the reasons for these relationships, the ECHAM5-HAM GCM was used. The second question of Chapter 4 considered the suitability of using ECHAM5-HAM here: Is ECHAM5-HAM capable of modelling the observed f_c–τ relationships? Positive f_c–τ relationships, generally of similar magnitude to those observed with the MODIS–MACC combination, were found in the subtropics and extratropics in the ECHAM5-HAM data. ECHAM5-HAM produced negative f_c–τ relationships in many parts of the tropics, in general agreement with the MODIS–MACC t + 24 hour combination, although the negative relationships were much stronger in ECHAM5-HAM. Overall, ECHAM5-HAM appeared to capture many of the observed relationships reasonably well.

Having established that ECHAM5-HAM appears to be a suitable hypothesis testing tool for probing the reasons behind the f_c–τ relationships, a third question was asked in Chapter 4: What are the reasons for the f_c–τ relationships in ECHAM5-HAM? Running simulations with no representation of the cloud lifetime effect did not remove the positive relationships, showing that the cloud lifetime effect was not the major contributor to the positive f_c–τ relationships in the model. By replacing τ with dry τ, it was demonstrated that these positive relationships are primarily due to hygroscopic growth of aerosol in high relative humidity environments. The negative f_c–τ relationships in the modelled tropics can be explained by wet scavenging of convective precipitation, as was demonstrated by switching convective wet scavenging off in ECHAM5-HAM. In order to test the sensitivity of these results to the choice of stratiform cloud cover parameterization in the model, the simulations were repeated for two different stratiform cloud cover schemes. The observations were consistent for both

cloud schemes.

Although the contribution of relative humidity to f_c–τ relationships was investigated in Chapter 4, the possible contribution of other meteorological factors was not analysed. Engström and Ekman (2010) demonstrated that 10-metre wind speed can explain part of the observed f_c–τ relationships. Meteorological field variables, such as wind speed, are often affected by large-scale synoptic systems such as extratropical cyclones. Looking at these large-scale systems, rather than the local meteorological field variables used in other studies, might provide a complementary view of the meteorological contribution to relationships between aerosol and cloud properties.

Several previous studies have investigated the impact of extratropical cyclones on cloud properties (e.g. Field and Wood, 2007). Chapter 5, much of which has been published in Grandey et al. (2011), complements these previous studies by investigating the effect of extratropical cyclones on aerosol properties over ocean. The following question was asked: What effect do extratropical cyclones have on column aerosol properties over ocean? In order to answer this question, extratropical cyclones were tracked using European Centre for Medium Range Weather Forecasts (ECMWF) meteorological reanalysis (ERA-Interim) 850 hPa relative vorticity data. Storm-centric composites of Aqua-MODIS Collection 5 and AATSR τ and aerosol size parameters were produced for the North Atlantic and the South Atlantic oceans.

It was found that τ and aerosol size both increase near the centre of the composite extratropical cyclones. Using composites of ECMWF ERA-Interim reanalysis data, it was demonstrated that wind speed is a considerably more likely explanatory variable than relative humidity for the aerosol observations. A comparison of composites for both MODIS and AATSR, the latter of which uses a wind speed dependent sea-surface reflectance model in the aerosol retrieval, suggested that although surface reflectance effects may contribute towards some of the observations, wind speed dependent emission of sea salt also appears to make a significant contribution to the observed aerosol properties. Further evidence in support of the suggestion that part of the enhancement in τ is due to sea-salt emission was provided by composites of MACC reanalysis-forecast sea-salt τ.

Satellite-retrieved τ data were found to be higher in the North Atlantic ocean composites compared to the South Atlantic ocean composites. By performing two ECHAM5-HAM simulations, one with pre-industrial aerosol and precursor emissions and the other with present-day emissions, it was demonstrated that the differences between the North Atlantic and the South Atlantic ocean τ com-

posites are primarily due to the presence of more anthropogenic aerosol in the Northern Hemisphere.

In Chapter 6 it was further shown that τ generally increases with the relative vorticity of an extratropical cyclone in addition to being dependent on position relative to the centre of the cyclone. By comparing storm-centric composites of T_{top} and f_c, it was shown that these cloud properties are also partly dependent on relative vorticity and position in the storm domain. However, variability in τ, T_{top} and f_c within a given vorticity range was often larger than the average change in these properties between weaker storms and stronger storms.

As mentioned above, previous studies have attempted to use local meteorological field variables in order to identify spurious contributions to relationships between aerosol and cloud properties. Chapter 6 proposed an alternative method of investigating a meteorological contribution: Can spurious T_{top}–τ and f_c–τ relationships be explained by considering simply the relative vorticity of extratropical cyclones and position relative to the storm centre? This question was investigated by shuffling the pairing of the aerosol and cloud data within narrow bins of vorticity for each position in the storm-centric domain. Regression slopes and correlations were calculated for each position both before and after shuffling. Although T_{top} and τ were both found to vary with storm vorticity, no statistically robust relationship between T_{top} and τ was found for the shuffled storm-centric data. However, a weak positive relationship between f_c and τ was found in the shuffled storm-centric data, although the regression slope was found to be two orders of magnitude weaker than was found for the non-shuffled data. This shows that the simplified description of the synoptics is capable of explaining spurious f_c–τ relationships, although the spurious relationships explained are far smaller than observed relationships.

Summary

This thesis has provided an overview of observed relationships between retrieved τ and four cloud properties: N_d, r_e, T_{top} and f_c. Appropriate ways of quantifying and presenting the observed relationships have been considered. By comparing three different satellite datasets, areas of agreement and disagreement have been identified, providing observational constraints on the relationships. For example, it was shown that global estimates of cloud albedo effect radiative forcing over ocean may vary by up to 40% depending on the satellite N_d dataset used.

Reasons for many of the observed relationships have been investigated. It was found that cli-

matological spatial gradients of aerosol and cloud properties may have introduced methodological errors to several published studies looking at aerosol–cloud interactions. These errors may lead to global cloud albedo effect radiative forcing overestimates of up to 80%. Following this finding, methodological improvements have been recommended and implemented in this thesis.

Strong positive relationships between f_c and τ were observed in all three satellite datasets over land and ocean, with potentially major implications for climate. However, by combining reanalysis-forecast τ data with the satellite f_c, it was demonstrated that approximately half of the positive f_c–τ signal may be due to cloud contamination of the satellite-retrieved τ data. By performing several GCM simulations, it was further demonstrated that most of the remaining positive f_c–τ signal can probably be explained by covariation with relative humidity. Negative f_c–τ relationships may also arise due to scavenging of aerosols by precipitation. The cloud lifetime effect does not appear to be the primary explanatory mechanism for observed f_c–τ relationships.

A new method of investigating the contribution of meteorological covariation to observed relationships between aerosol and cloud properties has been introduced. The variation of aerosol and cloud properties with a simplified description of the large-scale synoptics of extratropical cyclones has been investigated. Extratropical cyclones have been shown to affect retrieved τ and aerosol size, with a large part of this signal likely arising due to enhanced emission of sea-salt in regions of higher wind speed. They have also been shown to affect T_{top} and f_c. A simplified description of extratropical cyclones, based on storm relative vorticity and position in the storm domain, produced no statistically robust explanation for T_{top}–τ relationships. However, this simplified description of extratropical cyclones was found to explain spurious f_c–τ relationships, although the spurious relationships explained are far smaller than observed relationships.

The work presented in this thesis has improved our understanding of the reasons for observed relationships between aerosol and cloud properties. Improved methodologies have been suggested and implemented, contributing to the investigation of aerosol–cloud interactions and their role within the climate system.

7.2 Future work

Much work remains to be done in order to improve our understanding of aerosol–cloud–climate interactions. Following ideas introduced in this thesis, four potential avenues for further research are mentioned below.

Satellite data

The differences between different satellite datasets demonstrate the lack of reliability of many retrieved cloud and aerosol properties. Much work remains to be done in the development of physically consistent and reliable retrievals of cloud properties from satellite data. Of particular relevance is the consideration of three-dimensional light scattering effects. Future satellite missions should be carefully designed alongside more advanced retrieval considerations.

Reanalysis aerosol data

Reanalysis-forecast τ data were combined with satellite-retrieved f_c data in Chapter 4 in an attempt to account for satellite retrieval errors such as cloud contamination of τ. As mentioned, residual cloud contamination may remain due to assimilation, and model errors might also be introduced. It would be expected that residual cloud contamination would decrease and model errors would increase for later forecast time-steps, when more time has passed since assimilation. It would be interesting to test the sensitivity of the f_c–τ relationships to the choice of forecast time-step. It would also be interesting to apply this approach to relationships between other cloud properties and τ.

The availability of increasingly reliable aerosol reanalysis data would be highly beneficial for future studies. Further development of aerosol models and assimilation of observations is an important area. In addition to the ideal of providing aerosol data that are hopefully not affected by cloud contamination, the aerosol fields in reanalysis data are continuous, allowing co-location of aerosol properties with satellite-retrieved cloud properties even when there are no retrieved aerosol data available.

General circulation models

The ECHAM5-HAM GCM proved to be a useful hypothesis testing tool in Chapter 4, allowing the reasons for the observed f_c–τ relationships to be investigated in greater detail than would have been

possible with observations only. Many more interesting results may be found through the creative use of GCMs alongside observational datasets.

The use of more than one satellite dataset in Chapters 3 and 5 provided an indication of the reliability of the observations. It would be interesting to repeat the GCM modelling parts of Chapter 4 with another GCM, in order to test whether the given explanations for the ECHAM5-GCM behaviour apply more widely.

The development of improved representations of aerosols and clouds in GCMs would be very useful for studies investigating global aerosol–cloud interactions. Of course, improvements here would also help with improving projections of future climate, which depend heavily on GCM simulations.

Consideration of large-scale synoptic systems

As an alternative to using local meteorological field variables to account for spurious relationships between aerosol and cloud properties, Chapter 6 introduced the possibility of considering large-scale synoptic systems instead. The approach used, whereby data were categorised according to position in the storm-centric domain and storm vorticity, proved to be partially successful. A combination of the storm-centric and local meteorological variable approaches might be more fruitful than either approach taken in isolation. Cloud and aerosol data could be categorised by position in the storm-centric domain and a local meteorological variable, providing a basis for future work.

Bibliography

Ackerman, A. S., Toon, O. B., Stevens, D. E., Heymsfield, A. J., Ramanathan, V., and Welton, E. J.: Reduction of tropical cloudiness by soot, Science, 288, 1042–1047, doi:10.1126/science.288.5468.1042, 2000.

Albrecht, B. A.: Aerosols, Cloud Microphysics, and Fractional Cloudiness, Science, 245, 1227–1230, 1989.

Altaratz, O., Koren, I., and Reisin, T.: Humidity impact on the aerosol effect in warm cumulus clouds, Geophys. Res. Lett., 35, L17 804, doi:10.1029/2008GL034178, 2008.

Ambaum, M. H. P.: Significance Tests in Climate Science, J. Climate, 23, 5927–5932, doi:10.1175/2010JCLI3746.1, 2010.

Anderson, T. L., Charlson, R. J., Winker, D. M., Ogren, J. A., and Holmén, K.: Mesoscale variations of tropospheric aerosols, J. Atmos. Sci., 60, 119–136, 2003.

Andreae, M. O.: Correlation between cloud condensation nuclei concentration and aerosol optical thickness in remote and polluted regions, Atmos. Chem. Phys., 9, 543–556, 2009.

Andreae, M. O., Rosenfeld, D., Artaxo, P., Costa, A. A., Frank, G. P., Longo, K. M., and Silva-Dias, M. A. F.: Smoking Rain Clouds over the Amazon, Science, 303, 1337–1342, 2004.

Andreae, M. O., Jones, C. D., and Cox, P. M.: Strong present-day aerosol cooling implies a hot future, Nature, 435, 1187–1190, doi:10.1038/nature03671, 2005.

Andrejczuk, M., Reisner, J. M., Henson, B., Dubey, M. K., and Jeffery, C. A.: The potential impacts of pollution on a nondrizzling stratus deck: Does aerosol number matter more than type?, J. Geophys. Res., p. D19204, doi:10.1029/2007JD009445, 2008.

Arakawa, A.: The cumulus parameterization problem: Past, present, and future, J. Climate, 17, 2493–2525, 2004.

Barahona, D. and Nenes, A.: Parameterization of cloud droplet formation in large-scale models: Including effects of entrainment, J. Geophys. Res., 112, D16 206, doi:10.1029/2007JD008473, 2007.

Barnes, W. L., Pagano, T. S., and Salomonson, V. V.: Prelaunch characteristics of the moderate resolution imaging spectroradiometer (MODIS) on EOS-AMI, IEEE T. Geosci. Remote, 36, 1088–1100, 1998.

Bell, M. L., Samet, J. M., and Dominici, F.: Time-series studies of particulate matter, Annu. Rev. Publ. Health, 25, 247–280, doi:10.1146/annurev.publhealth.25.102802.124329, 2004.

Bellouin, N., Jones, A., Haywood, J., and Christopher, S. A.: Updated estimate of aerosol direct radiative forcing from satellite observations and comparison against the Hadley Centre climate model, J. Geophys. Res., 113, D10 205, doi:10.1029/2007JD009385, 2008.

Bennartz, R.: Global assessment of marine boundary layer cloud droplet number concentration from satellite, J. Geophys. Res., 112, doi:10.1029/2006JD007547, 2007.

Berg, L. K., Berkowitz, C. M., Barnard, J. C., Senum, G., and Springston, S. R.: Observations of the first aerosol indirect effect in shallow cumuli, Geophys. Res. Lett., 38, L03 809, doi:10.1029/2010GL046047, 2011.

Bollasina, M. A., Ming, Y., and Ramaswamy, V.: Anthropogenic Aerosols and the Weakening of the South Asian Summer Monsoon, Science, doi:10.1126/science.1204994, 2011.

Bony, S. and Dufresne, J.-L.: Marine boundary layer clouds at the heart of tropical cloud feedback uncertainties in climate models, Geophys. Res. Lett., 32, doi:10.1029/2005GL023851, 2005.

Bony, S., Colman, R., Kattsov, V. M., Allan, R. P., Bretherton, C. S., Dufresne, J.-L., Hall, A., Hallegatte, S., Holland, M. M., Ingram, W., Randall, D. A., Soden, B. J., Tselioudis, G., and Webb, M. J.: How Well Do We Understand and Evaluate Climate Change Feedback Processes?, J. Climate, 19, 3445–3482, 2006.

Brenguier, J.-L., Pawlowska, H., Schüller, L., Preusker, R., Fischer, J., and Fouquart, Y.: Radiative properties of boundary layer clouds: Droplet effective radius versus number concentration, J. Atmos. Sci., 57, 803–821, 2000.

Brenguier, J.-L., Burnet, F., and Geoffroy, O.: Cloud optical thickness and liquid water path – does the k coefficient vary with droplet concentration?, Atmos. Chem. Phys., 11, 9771–9786, doi:10.5194/acp-11-9771-2011, URL http://www.atmos-chem-phys.net/11/9771/2011/, 2011.

Brennan, J. I., Kaufman, Y. J., Koren, I., and Li, R. R.: Aerosol–Cloud Interaction—Misclassification of MODIS Clouds in Heavy Aerosol, IEEE T. Geosci. Remote, 43, 911–915, doi:10.1109/TGRS.2005.844662, 2005.

Bréon, F.-M. and Doutriaux-Boucher, M.: A Comparison of Cloud Droplet Radii Measured From Space, IEEE T. Geosci. Remote, 43, 1796–1805, doi:10.1109/TGRS.2005.852838, 2005.

Bréon, F.-M., D., T., and Generoso, S.: Aerosol Effect on Cloud Droplet Size Monitored from Satellite, Science, 295, 834–838, doi:10.1126/science.1066434, 2002.

Bretherton, C. S., Wood, R., George, R. C., Leon, D., Allen, G., and Zheng, X.: Southeast Pacific stratocumulus clouds, precipitation and boundary layer structure sampled along 20 S during VOCALS-REx, Atmos. Chem. Phys., 10, 10 639–10 654, doi:10.5194/acp-10-10639-2010, URL http://www.atmos-chem-phys.net/10/10639/2010/, 2010.

Bulgin, C. E., Palmer, P. I., Thomas, G. E., Arnold, C. P. G., Campmany, E., Carboni, E., Grainger, R. G., Poulsen, C., Siddans, R., and Lawrence, B. N.: Regional and seasonal variations of the Twomey indirect effect as observed by the ATSR-2 satellite instrument, Geophys. Res. Lett., 35, L02 811, doi:10.1029/2007GL031394, 2008.

Catto, J. L., Shaffrey, L. C., and Hodges, K. I.: Can Climate Models Capture the Structure of Extratropical Cyclones?, J. Climate, 23, 1621–1635, doi:10.1175/2009JCLI3318.1, 2010.

Chang, E. K. M. and Song, S.: The Seasonal Cycles in the Distribution and Precipitation around Cyclones in the Western North Pacific and Atlantic, J. Atmos. Sci., 63, 815–839, 2006.

Chen, Y. and Penner, J. E.: Uncertainty analysis for estimates of the first indirect aerosol effect, Atmos. Chem. Phys., 5, 2935–2948, doi:10.5194/acp-5-2935-2005, URL http://www.atmos-chem-phys.net/5/2935/2005/, 2005.

Choi, Y.-S., Ho, C.-H., Oh, H.-R., Park, R. J., and Song, C.-G.: Estimating bulk optical properties of aerosols over the western North Pacific by using MODIS and CERES measurements, Atmos Environ, 43, 5654–5660, doi:10.1016/j.atmosenv.2009.07.036, 2009.

CNES: CALIPSO: Mission studying the atmosphere, http://smsc.cnes.fr/CALIPSO/ [Accessed 24th August 2009], 2009a.

CNES: PARASOL: Mission studying the atmosphere, http://smsc.cnes.fr/PARASOL/ [Accessed 22nd August 2009], 2009b.

CNES: POLDER: Atmosphere, Land and Ocean mission, http://smsc.cnes.fr/POLDER/ [Accessed 22nd August 2009], 2009c.

Colorado State University: CLOUDSAT, http://eospso.gsfc.nasa.gov/ [Accessed 22nd August 2009], 2009.

Costantino, L. and Bréon, F. M.: Analysis of aerosol-cloud interaction from multi-sensor satellite observations, Geophys. Res. Lett., 37, L11 801, doi:10.1029/2009GL041828, 2010.

Cui, Z., Carslaw, K. S., Yin, Y., and Davies, S.: A numerical study of aerosol effects on the dynamics and microphysics of a deep convective cloud in a continental environment, J. Geophys. Res., 111, doi:10.1029/2005JD005981, 2006.

de Leeuw, G., Andreas, E. L., Anguelova, M. D., Fairall, C. W., Lewis, E. R., O'Dowd, C., Schulz, M., and Schwartz, S. E.: Production flux of sea spray aerosol, Rev. Geophys., 49, RG2001, doi:10.1029/2010RG000349, 2011.

Dentener, F., Kinne, S., Bond, T., Boucher, O., Cofala, J., Generoso, S., Ginoux, P., Gong, S., Hoelzemann, J. J. and Ito, A., Marelli, L., Penner, J. E., Putaud, J. P., Textor, . C., Schulz, M., van der Werf, G. R., and Wilson, J.: Emissions of primary aerosol and precursor gases in the years 2000 and 1750 prescribed data-sets for AeroCom, Atmos. Chem. Phys., 6, 4321–4344, doi:10.5194/acp-6-4321-2006, 2006.

Deschamps, P.-Y., Breon, F.-M., Leroy, M., Podaire, A., Bricaud, A., Buriez, J.-C., and Seze, G.: POLDER mission: instrument characteristics and scientific objectives, IEEE T. Geosci. Remote, 32, 598–614, doi:10.1109/36.297978, 1994.

Dharshana, K. G. T., Kravtsov, S., and Kahl, J. D. W.: Relationship between synoptic weather disturbances and particulate matter air pollution over the United States, J. Geophys. Res., 115, D24 219, doi:10.1029/2010JD014852, 2010.

Diner, D. J., Beckert, J. C., Reilly, T. H., Bruegge, C. J., Conel, J. E., Kahn, R. A., Martonchik, J. V., Ackerman, T. P., Davies, R., Gerstl, S. A. W., Gordon, H. R., Muller, J.-P., Myneni, R. B., Sellers, P. J., Pinty, B., and Verstraete, M. M.: Multi-angle imaging spectroradiometer (MISR) instrument description and experiment overview, IEEE T. Geosci. Remote, 36, 1072–1087, 1998.

ECMWF: ERA Project, http://www.ecmwf.int/research/era/do/get/index [Accessed 10th August 2011], 2011a.

ECMWF: MACC Re-analysis, http://data-portal.ecmwf.int/data/d/macc_reanalysis [Accessed 10th August 2011], 2011b.

Engström, A. and Ekman, A. M. L.: Impact of meteorological factors on the correlation between aerosol optical depth and cloud fraction, Geophys. Res. Lett., 37, L18 814, doi:10.1029/2010GL044361, 2010.

ESA: Envisat ESA Mission, `http://envisat.esa.int/` [Accessed 24th August 2009], 2009.

Esaias, W. E., Abbott, M. R., Barton, I., Brown, O. B., Campbell, J. W., Carder, K. L., Clark, D. K., Evans, R. H., Hoge, F. E., Gordon, H. R., Balch, W. M., Letelier, R., and Minnett, P. J.: An overview of MODIS capabilities for ocean science observations, IEEE T. Geosci. Remote, 36, 1250–1265, 1998.

Evan, A. T., Heidinger, A. K., Bennartz, R., Bennington, V., Mahowald, N. M. amd Corrada-Bravo, H., Velden, C. S., Myhre, G., and Kossin, J. P.: Ocean temperature forcing by aerosols across the Atlantic tropical cyclone development region, Geochem. Geophy. Geosy., 9, Q05V04, doi:10.1029/2007GC001774, 2008.

Feingold, G., Remer, L. A., Ramaprasad, J., and Kaufman, Y. J.: Analysis of smoke impact on clouds in Brazilian biomass burning regions: An extension of Twomey's approach, J. Geophys. Res., 106, 22,907–22,922, doi:10.1029/2001JD000732, 2001.

Feingold, G., Koren, I., Wang, H., Xue, H., and Brewer, W. A.: Precipitation-generated oscillations in open cellular cloud fields, Nature, 466, 849–852, doi:10.1038/nature09314, 2010.

Feynman, R. P.: The Character of the Physical Law, Penguin, 2007.

Field, P. R. and Wood, R.: Precipitation and Cloud Structure in Midlatitude Cyclones, J. Climate, 20, 233–254, doi:10.1175/JCLI3998.1, 2007.

Field, P. R., Gettelman, A., Neale, R. B., Wood, R., Rasch, P. J., and Morrison, H.: Midlatitude Cyclone Compositing to Constrain Climate Model Behaviour Using Satellite Observations, J. Climate, 21, 5887–5903, doi:10.1175/2008JCLI2235.1, 2008.

Forster, P., Ramaswamy, V., Artaxo, P., Berntsen, T., Betts, R., Fahey, D. W., Haywood, J., Lean, J., Lowe, D. C., Myhre, G., Nganga, J., Prinn, R., Raga, G., Schultz, M., and Van Dorland, R.: Changes in Atmospheric Constituents and in Radiative Forcing. In: Climate Change 2007: The Physical Science Basis. Contribution of Working Group 1 to the Fourth Assessment Report of the Intergovernmental Panel on Climate Change, Cambridge University Press, 2007.

George, R. C. and Wood, R.: Subseasonal variability of low cloud radiative properties of the southeast Pacific Ocean, Atmos. Chem. Phys., 10, 4047–4063, 2010.

Glantz, P., Nilsson, E. D., and von Hoyningen-Huene, W.: Estimating a relationship between aerosol optical thickness and surface wind speed over the ocean, Atmos. Res., 92, 58–68, doi:10.1016/j.atmosres.2008.08.010, 2009.

Glickman, T., ed.: Glossary of Meteorology. 2nd Edition, Amer. Meteor. Soc., 2000.

Gong, S. L.: A parameterization of sea-salt aerosol source function for sub- and super-micron particles, Global Biogeochem. Cy., 17, 1097, doi:10.1029/2003GB002079, 2003.

Grandey, B. S. and Stier, P.: A critical look at spatial scale choices in satellite-based aerosol indirect effect studies, Atmos. Chem. Phys., 10, 11 459–11 470, doi:10.5194/acp-10-11459-2010, 2010.

Grandey, B. S., Stier, P., Wagner, T. M., Grainger, R. G., and Hodges, K. I.: The effect of extratropical cyclones on satelliteretrieved aerosol properties over ocean, Geophys. Res. Lett., 38, L13 805, doi: 10.1029/2011GL047703, 2011.

Grennfelt, P. and Hov, O.: Regional air pollution at a turning point, Ambio, 34, 2–10, 2005.

Hansen, J. and Nazarenko, L.: Soot climate forcing via snow and ice albedos, P. Natl. Acad. Sci. USA, 101, 423–428, doi:10.1073/pnas.2237157100, 2004.

Hansen, J. E. and Travis, L. D.: Light scattering in planetary atmospheres, Space Science Reviews, 16, 527–610, doi:10.1007/BF00168069, 1974.

Harrison, R. G., Nicoll, K. A., Ulanowski, Z., and Mather, T. A.: Self-charging of the Eyjafjallajökull volcanic ash plume, Environ. Res. Lett., 5, 024 004, doi:10.1088/1748-9326/5/2/024004, 2010.

Haywood, J. and Boucher, O.: Estimates of the direct and indirect radiative forcing due to tropospheric aerosols: A review, Rev. Geophys., 38, 513–543, doi:10.1029/1999RG000078, 2000.

Haywood, J. M. and Shine, K. P.: The effect of anthropogenic sulfate and soot aerosol on the clear sky planetary radiation budget, Geophys. Res. Lett., 22, 603–606, 1995.

Haywood, J. M., Ramaswamy, V., and Donner, L. J.: A limited-area-model case study of the effects of sub-grid scale variations in relative humidity and cloud upon the direct radiative forcing of sulfate aerosol, Geophys. Res. Lett., 24, 143–146, doi:10.1029/96GL03812, 1997.

Haywood, J. M., Osborne, S. R., and Abel, S. J.: The effect of overlying absorbing aerosol layers on remote sensing retrievals of cloud effective radius and cloud optical depth, Q. J. Roy. Meteor. Soc., 130, 779–800, doi:10.1256/qj.03.100, 2004.

Haywood, J. M., Donner, L., Jones, A., and Golaz, J.-C.: Global Indirect Radiative Forcing Caused by Aerosols, in: Clouds in the Perturbed Climate System: Their Relationship to Energy Balance, Atmospheric Dynamics, and Precipitation, edited by J. Heintzenberg and R. J. Charlson, MIT Press, 2009.

Hodges, K. I.: Feature Tracking on the Unit Sphere, Mon. Weather Rev., 123, 3458–3465, 1995.

Hodges, K. I.: Adaptive Constraints for Feature Tracking, Mon. Weather Rev., 127, 1362–1373, 1999.

Holben, B. N., Eck, T. F., Slutsker, I., Tanré, D., Buis, J. P., Setzer, A., Vermote, E., Reagan, J. A., Kaufman, Y. J., Nakajima, T., Lavenu, F., Jankowiak, I., and Smirnov, A.: AERONET - A federated instrument network and data archive for aerosol characterization, Remote Sens. Environ., 66, 1–16, doi:10.1016/S0034-4257(98)00031-5, 1998.

Huang, H., Thomas, G. E., and Grainger, R. G.: Relationship between wind speed and aerosol optical depth over remote ocean, Atmos. Chem. Phys., 10, 5943–5950, doi:10.5194/acp-10-5943-2010, URL `http://www.atmos-chem-phys.net/10/5943/2010/`, 2010.

Huang, J., Hsu, N. C., Tsay, S.-C., Jeong, M.-J., Holben, B. N., Berkoff, T. A., and Welton, E. J.: Susceptibility of aerosol optical thickness retrievals to thin cirrus contamination during the BASE-ASIA campaign, J. Geophys. Res., 116, D08 214, doi:10.1029/2010JD014910, 2011.

Hubanks, P. A., King, M. D., Platnick, S. A., and Pincus, R. A.: MODIS Atmosphere L3 Gridded Product Algorithm Theoretical Basis Document. ATBD Reference Number: ATBD-MOD-30., `http://modis-atmos.gsfc.nasa.gov/_docs/L3_ATBD_2008_12_04.pdf` [Accessed 18th August 2009], 2008.

Huete, A., Didan, K., Miura, T., Rodriguez, E. P., Gao, X., and Ferreira, L. G.: Overview of the radiometric and biophysical performance of the MODIS vegetation indices, Remote Sens. Environ., 83, 195–213, doi:10.1016/S0034-4257(02)00096-2, 2002.

Ignatov, A., Stowe, L., and Singh, R.: Sensitivity study of the Angstrom exponent derived from AVHRR over the oceans, Adv. Space Res., 21, 439–442, 1998.

Jacobson, M. Z.: Fundamentals of Atmospheric Modeling, Second Edition, Cambridge University Press, 2005.

Jaeglé, L., Quinn, P. K., Bates, T. S., Alexander, B., and Lin, J.-T.: Global distribution of sea salt aerosols: new constraints from in situ and remote sensing observations, Atmos. Chem. Phys., 11, 3137–3157, doi:10.5194/acp-11-3137-2011, URL http://www.atmos-chem-phys.net/11/3137/2011/, 2011.

Jeong, M.-J. and Hsu, N. C.: Retrievals of aerosol single-scattering albedo and effective aerosol layer height for biomass-burning smoke: Synergy derived from "A-Train" sensors, Geophys. Res. Lett., 35, L24 801, doi:10.1029/2008GL036279, 2008.

Jia, Y., Rahn, K. A., He, K., Wen, T., and Wang, Y.: A novel technique for quanifying the regional component of urban aerosol solely from its sawtooth cycles, J. Geophys. Res., 113, D21 309, doi:10.1029/2008JD010389, 2008.

Jiang, H., Xue, H., Teller, A., Feingold, G., and Levin, Z.: Aerosol effects on the lifetime of shallow cumulus, Geophys. Res. Lett., 33, doi:10.1029/2006GL026024, 2006.

Jones, T. A., Christopher, S. A., and Quaas, J.: A six year satellite-based assessment of the regional variations in aerosol indirect effects, Atmos. Chem. Phys., 9, 4091–4114, 2009.

Kaufman, Y. J., Herring, D. D., Ranson, K. J., and Collatz, J. G.: Earth observing system AMI mission to earth, IEEE T. Geosci. Remote, 36, 1045–1055, 1998.

Kaufman, Y. J., Koren, I., Remer, L. A., Rosenfeld, D., and Rudich, Y.: The effect of smoke, dust, and pollution aerosol on shallow cloud development over the Atlantic Ocean, P. Natl. Acad. Sci. USA, 102, 11 207–11 212, doi:10.1073/pnas.0505191102, 2005.

Kennedy, I. M.: The health effects of combustion-generated aerosols, P. Combust. Inst., 31 II, 2757–2770, doi:10.1016/j.proci.2006.08.116, 2007.

Khain, A. P.: Notes on state-of-the-art investigations of aerosol effects on precipitation: a critical review, Environmental Research Letters, 4, 015 004, URL http://stacks.iop.org/1748-9326/4/i=1/a=015004, 2009.

Kiehl, J. T.: Twentieth century climate model response and climate sensitivity, Geophys. Res. Lett., 34, L22 710, doi:10.1029/2007GL031383, 2007.

Kim, B.-G., Klein, S. A., and Norris, J. R.: Continental liquid water cloud variability and its parameterization using Atmospheric Radiation Measurement data, J. Geophys. Res., 110, D15S08, doi:10.1029/2004JD005122, 2005.

Kiran, V. R., Rajeevan, M., Rao, S. V. B., and Rao, N. P.: Analysis of variations of cloud and aerosol properties associated with active and break spells of Indian summer monsoon using MODIS data, Geophys. Res. Lett., 36, L09 706, doi:10.1029/2008GL037135, 2009.

Kokhanovsky, A. A., Deuzé, J. L., Diner, D. J., Dubovik, O., Ducos, F., Emde, C., Garay, M. J., Grainger, R. G., Heckel, A., Herman, M., Katsev, I. L., Keller, J., Levy, R., North, P. R. J., Prikhach, A. S., Rozanov, V. V., Sayer, A. M., Ota, Y., Tanré, D., Thomas, G. E., and Zege, E. P.: The inter-comparison of major satellite aerosol retrieval algorithms using simulated intensity and polarization characteristics of reflected light, Atmos. Meas. Tech., 3, 909–932, doi:10.5194/amt-3-909-2010, URL `http://www.atmos-meas-tech.net/3/909/2010/`, 2010.

Koren, I. and Feingold, G.: Aerosol–cloud–precipitation system as a predator-prey problem, P. Natl. Acad. Sci. USA, 108, 12 227–12 232, doi:10.1073/pnas.1101777108, 2011.

Koren, I., Kaufman, Y. J., Rosenfeld, D., Remer, L. A., and Rudich, Y.: Aerosol invigoration and restructuring of the Atlantic convective clouds, Geophys. Res. Lett., 32, doi:10.1029/2005GL023187, 2005.

Koren, I., Remer, L. A., Kaufman, Y. J., Rudich, Y., and Martins, J. V.: On the twilight zone between clouds and aerosols, Geophys. Res. Lett., 34, doi:10.1029/2007GL029253, 2007.

Koren, I., Martins, J. V., Remer, L. A., and Afargan, H.: Smoke Invigorations Versus Inhibition of Clouds over the Amazon, Science, 321, 946–949, doi:10.1126/science.1159185, 2008.

Koren, I., Feingold, G., and Remer, L. A.: The invigoration of deep convective clouds over the Atlantic: aerosol effect, meteorology or retrieval artifact?, Atmos. Chem. Phys., 10, 8855–8872, doi:10.5194/acp-10-8855-2010, URL `http://www.atmos-chem-phys.net/10/8855/2010/`, 2010.

Kubar, T. L., Hartmann, D. L., and Wood, R.: Understanding the Importance of Microphysics and Macrophysics for Warm rain in Marine Low Clouds. Part I: Satellite Observations, J. Atmos. Sci., 66, 2953–2972, doi:10.1175/2009JAS3071.1, 2009.

Lambert, S. J. and Boer, G. J.: CMIP1 evaluation and intercomparison of coupled climate models, Clim. Dynam., 17, 83–106, 2001.

Lau, N.-C. and Crane, M. W.: A Satellite View of the Synoptic-Scale Organization of Cloud Properties in Midlatitude and Tropical Circulation Systems, Mon. Weather Rev., 123, 1984–2006, 1995.

Lau, N.-C. and Crane, M. W.: Comparing Satellite and Surface Observations of Cloud Patterns in Synoptic-Scale Circulation Systems, Mon. Weather Rev., 125, 3172–3189, 1997.

L'Ecuyer, T. S., Berg, W., Haynes, J., Lebsock, M., and Takemura, T.: Global observations of aerosol impacts on precipitation occurrence in warm maritime clouds, J. Geophys. Res., 114, D09 211, doi:10.1029/2008JD011273, 2009.

Lewis, E. R. and Schwartz, S. E.: Sea Salt Aerosol Production: Mechanisms, Methods, Measurements, and Models, American Geophysical Union, Washington, DC, 2004.

Li, F. and Ramanathan, V.: Winter to summer monsoon variation of aerosol optical depth over the tropical Indian Ocean, J. Geophys. Res., 107, doi:10.1029/2001JD000949, 2002.

Li, R., Min, Q.-L., and Harrison, L. C.: A Case Study: The Indirect Aerosol Effects of Mineral Dust on Warm Clouds, J. Atmos. Sci., 67, 805–816, doi:10.1175/2009JAS3235.1, 2010.

Liu, J. C., Schaaf, C., Strahler, A., Jiao, Z. T., Shuai, Y. M., Zhang, Q. L., Roman, M., Augustine, J. A., and Dutton, E. G.: Validation of Moderate Resolution Imaging Spectroradiometer (MODIS) albedo retrieval algorithm: Dependence of albedo on solar zenith angle, J. Geophys. Res., p. D01106, doi:10.1029/2008JD009969, 2009.

Liu, Y. and Daum, P. H.: Anthropogenic aerosols: Indirect warming effect from dispersion forcing, Nature, 419, 580–581, doi:10.1038/419580a, 2002.

Lohmann, U.: A glaciation indirect aerosol effect caused by soot aerosols, Geophys. Res. Lett., 29, doi:10.1029/2001GL014357, 2002.

Lohmann, U. and Feichter, J.: Global indirect aerosol effects: a review, Atmos. Chem. Phys., 5, 715–737, 2005.

Lohmann, U., Koren, I., and Kaufman, Y. J.: Disentangling the role of microphysical and dynamical effects in determining cloud properties over the Atlantic, Geophys. Res. Lett., 33, doi:10.1029/2005GL024625, 2006.

Lohmann, U., Stier, P., Hoose, C., Ferrachat, S., Kloster, S., Roeckner, E., and Zhang, J.: Cloud microphysics and aerosol indirect effects in the global climate model ECHAM5-HAM, Atmos. Chem. Phys., 7, 3425–3446, doi:10.5194/acp-7-3425-2007, URL http://www.atmos-chem-phys.net/7/3425/2007/, 2007.

Lu, M.-L., Conant, W. C., Jonsson, H. H., Varutbangkul, V., Flagan, R. C., and Seinfeld, J. H.: The Marine Stratus/Stratocumulus Experiment (MASE): Aerosol-cloud relationships in marine stratocumulus, J. Geophys. Res., 112, D10 209, doi:10.1029/2006JD007985, 2007.

MACC: Monitoring atmospheric composition and climate, http://www.gmes-atmosphere.eu [Accessed 10th August 2011], 2011.

Marshak, A., Platnick, S., Várnai, T., Wen, G., and Cahalan, R. F.: Impact of three-dimensional radiative effects on satellite retrievals of cloud droplet sizes, J. Geophys. Res., 111, D09 207, doi:10.1029/2005JD006686, 2006.

Martin, G. M., Johnson, D. W., and Spice, A.: The Measurement and Parameterization of Effective Radius of Droplets in Warm Stratocumulus Clouds, J. Atmos. Sci., 51, 1823–1842, doi:10.1175/1520-0469(1994)051⟨1823:TMAPOE⟩2.0.CO;2, 1994.

Max Planck Institute for Meteorology: ECHAM5, http://www.mpimet.mpg.de/en/science/models/ech [Accessed 10th August 2011], 2011.

McComiskey, A. and Feingold, G.: The scale problem in quantifying aerosol indirect effects, Atmos. Chem. Phys. Discuss., 11, 26 741–26 789, doi:10.5194/acpd-11-26741-2011, URL http://www.atmos-chem-phys-discuss.net/11/26741/2011/, 2011.

McComiskey, A., Feingold, G., Frisch, A. S., Turner, D. D., Miller, M. A., Chiu, J. C., Min, Q., and Ogren, J. A.: An assessment of aerosol-cloud interactions in marine stratus clouds based on surface remote sensing, J. Geophys. Res., 114, D09 203, doi:10.1029/2008JD011006, 2009.

Meehl, G. A., Stocker, T. F., Collins, W. D., Friedlingstein, P., Gaye, A. T., Gregory, J. M., Kitoh, A., Knutti, R., Murphy, J. M., Noda, A., Raper, S. C. B., Watterson, I. G., Weaver, A. J., and Zhao, Z.-C.: Global Climate Projections. In: Climate Change 2007: The Physical Science Basis. Contribution of Working Group 1 to the Fourth Assessment Report of the Intergovernmental Panel on Climate Change, Cambridge University Press, 2007.

Menon, S., Del Genio, A. D., Kaufman, Y., Bennartz, R., Koch, D., Loeb, N., and Orlikowski, D.: Analyzing signatures of aerosol-cloud interactions from satellite retrievals and the GISS GCM to constrain the aerosol indirect effect, J. Geophys. Res., 113, doi:10.1029/2007JD009442, 2008.

Meskhidze, N., Remer, L. A., Platnick, S., Negrón Juárez, R., Lichtenberger, A. M., and Aiyyer, A. R.: Exploring the differences in cloud properties observed by the Terra and Aqua MODIS sensors, Atmos. Chem. Phys., 9, 3461–3475, 2009.

Minnis, P., Young, D., Sun-Mack, S., Heck, P. W., Doelling, D. R., and Trepte, Q. Z.: CERES Cloud Property Retrievals from Imagers on TRMM, Terra, and Aqua, in: Proceedings of SPIE: Remote Sensing of Clouds and the Atmosphere VIII, edited by Schäfer, K. P., Comerón, A., Carleer, M. R., and Picard, R. H., vol. 5235, pp. 37–48, 2004.

Minnis, P., Sun-Mack, S., Chen, Y., Khaiyer, M. M., Yi, Y., Ayers, J. K., Brown, R. R., Dong, X., Gibson, S. C., Heck, P. W., Lin, B., Nordeen, M. L., Nguyen, L., Palikonda, R., Smith, W. L., Spangenberg, D. A., Trepte, Q. Z., and Xi, B.: CERES Edition-2 Cloud Property Retrievals Using TRMM VIRS and Terra and Aqua MODIS Data – Part II: Examples of Average Results and Comparisons With Other Data, IEEE T. Geosci. Remote, PP, 1–30, doi:10.1109/TGRS.2011.2144602, 2011.

Mutlow, C. T.: The ATSR instrument, Earth Observation Quarterly, 40, 14–15, 1993.

Nakajima, T. and King, M. D.: Determination of the Optical Thickness and Effective Particle Radius of Clouds from Reflected Solar Radiation Measurements. Part I: Theory., J. Atmos. Sci., 47, 1878–1893, 1990.

Nakajima, T., Higurashi, A., Kawamoto, K., and Penner, J. E.: A possible correlation between satellitederived cloud and aerosol microphysical parameters, Geophys. Res. Lett., 28, 1171–1174, doi: 10.1029/2000GL012186, 2001.

NASA: The Cloud-Aerosol Lidar and Infrared Pathfinder Satellite Observation (CALIPSO), `http://www-calipso.larc.nasa.gov/` [Accessed 24th August 2009], 2009a.

NASA: The Earth Observing System Project Science Office, `http://eospso.gsfc.nasa.gov/` [Accessed 22nd August 2009], 2009b.

NASA: LAADS Web: Level 1 and Atmosphere Archive Distribution System, `http://ladsweb.nascom.nasa.gov/index.html` [Accessed 21st August 2009], 2009c.

NASA: MISR: Multi-angle Imaging SpectroRadiometer, `http://www-misr.jpl.nasa.gov/index` [Accessed 21st August 2009], 2009d.

NASA: MODIS Atmosphere, `http://modis-atmos.gsfc.nasa.gov/index.html` [Accessed 21st August 2009], 2009e.

NASA: MODIS Web, `http://modis.gsfc.nasa.gov/` [Accessed 21st August 2009], 2009f.

NASA: NASA Earth Observatory, `http://earthobservatory.nasa.gov/` [Accessed 18th August 2010], 2010.

NASA: GES DISC: Aerosol Angstrom Exponent, `http://disc.sci.gsfc.nasa.gov/data-hol` [Accessed 15th June 2011], 2011a.

NASA: CERES SSF Data Sets, `http://eosweb.larc.nasa.gov/PRODOCS/ceres/level2_ss` [Accessed 14th June 2011], 2011b.

Nober, F. J., Graf, H. F., and Rosenfeld, D.: Sensitivity of the global circulation to the suppression of precipitation by anthropogenic aerosols, Global Planet. Change, 37, 57–80, 2003.

Norris, J. R. and Iacobellis, S. F.: North Pacific Cloud Feedbacks Inferred from Synoptic-Scale Dynamic and Thermodynamic Relationships, J. Climate, 18, 4862–4878, 2005.

O'Dowd, C. D. and de Leeuw, G.: Marine aerosol production: a review of the current knowledge, Phil. Trans. R. Soc. A, 365, 1753–1774, doi:10.1029/2003GB002079, 2007.

Pant, V., Deshpande, C. G., and Kamra, A. K.: On the aerosol number concentration–wind speed relationship during a severe cyclonic storm over south Indian Ocean, J. Geophys. Res., 113, D02 206, doi:10.1029/2006JD008035, 2008.

Parkinson, C. L.: Aqua: An Earth-Observing Satellite Mission to Examin Water and Other Climate Variables, IEEE T. Geosci. Remote, 41, 173–183, doi:10.1109/TGRS.2002.808319, 2003.

Pawlowska, H. and Brenguier, J.-L.: Microphysical properties of stratocumulus clouds during ACE-2, Tellus B, 52, 868–887, doi:10.1034/j.1600-0889.2000.00076.x, URL `http://dx.doi.org/10.1034/j.1600-0889.2000.00076.x`, 2000.

Penner, J. E., Quaas, J., Storelvmo, T., Takemura, T., Boucher, O., Guo, H., Kirkevåg, A., Kristjánsson, J. E., and Seland, O.: Model intercomparison of indirect aerosol effects, Atmos. Chem. Phys., 6, 3391–3405, 2006.

Piani, C., Frame, D. J., Stainforth, D. A., and Allen, M. R.: Constraints on climate change from a multi-thousand member ensemble of simulations, Geophys. Res. Lett., 32, 1–5, doi:10.1029/2005GL024452, 2005.

Pincus, R. and Baker, M. B.: Effect of precipitation on the albedo susceptibility of clouds in the marine boundary layer, Nature, 372, 250–252, 1994.

Platnick, S.: Vertical photon transport in cloud remote sensing problems, J. Geophys. Res., 105, 22,919–22,935, doi:10.1029/2000JD900333, 2000.

Platnick, S., King, M. D., Ackerman, S. A., Menzel, W. P., Baum, B. A., Riedi, J. C., and Frey, R. A.: The MODIS cloud products: algorithms and examples from Terra, IEEE T. Geosci. Remote, 41, 459–473, doi:10.1109/TGRS.2002.808301, 2003.

Posselt, D. J., Stephens, G. L., and Miller, M.: CLOUDSAT: Adding a New Dimension to a Classical View of Extratropical Cyclones, B. Am. Meteorol. Soc., 89, 599–609, 2008.

Pruppacher, H. R. and Jaenicke, R.: The processing of water vapor and aerosols by atmospheric clouds, a global estimate, Atmos. Res., 38, 283–295, 1995.

Quaas, J., Boucher, O., and Lohmann, U.: Constraining the total aerosol indirect effect in the LMDZ and ECHAM4 GCMs using MODIS satellite data, Atmos. Chem. Phys., 6, 947–955, 2006.

Quaas, J., Boucher, O., Bellouin, N., and Kinne, S.: Satellite-based estimate of the direct and indirect aerosol climate forcing, J. Geophys. Res., 113, doi:10.1029/2007JD008962, 2008.

Quaas, J., Ming, Y., Menon, S., Takemura, T., Wang, M., Penner, J. E., Gettelman, A., Lohmann, U., Bellouin, N., Boucher, O., Sayer, A., Thomas, G. E., McComiskey, A., Feingold, G., Hoose, C., Kristjánsson, J. E., Liu, X., Balkanski, Y., Donner, L. J., Ginoux, P. A., Stier, P., Grandey, B., Feichter, J., Sednev, I., Bauer, S. E., Koch, D., Grainger, R. G., Kirkevåg, A., Iversen, T., Seland, O., Easter, R., Ghan, S. J., Rasch, P. J., Morrison, H., Lamarque, J.-F., Iacono, M. J., Kinne, S., and

Schulz, M.: Aerosol indirect effects – general circulation model intercomparison and evaluation with satellite data, Atmos. Chem. Phys., 9, 8697–8717, 2009.

Quaas, J., Stevens, B., Stier, P., and Lohmann, U.: Interpreting the cloud cover aerosol optical depth relationship found in satellite data using a general circulation model, Atmospheric Chemistry and Physics, 10, 6129–6135, doi:10.5194/acp-10-6129-2010, URL http://www.atmos-chem-phys.net/10/6129/2010/, 2010.

RAL: The ATSR Project, http://www.atsr.rl.ac.uk/ [Accessed 21st August 2009], 2003.

Randall, D. A., Wood, R. A., Bony, S., Colman, R., Fichefet, T., Fyfe, J., Kattsov, V., Pitman, A., Shukla, J., Srinivasan, J., Stouffer, R. J., Sumi, A., and Taylor, K. E.: Climate Models and Their Evaluation. In: Climate Change 2007: The Physical Science Basis. Contribution of Working Group 1 to the Fourth Assessment Report of the Intergovernmental Panel on Climate Change, Cambridge University Press, 2007.

Redemann, J., Zhang, Q., Russell, P. B., Livingston, J. M., and Remer, L. A.: Case studies of aerosol remote sensing in the vicinity of clouds, J. Geophys. Res., 114, doi:10.1029/2008JD010774, 2009.

Remer, L. A., Kaufman, Y. J., Tanré, D., Mattoo, S., Chu, D. A., Martins, J. V., Li, R.-R., Ichoku, C., Levy, R. C., Kleidman, R. G., Eck, T. F., Vermote, E., and Holben, B. N.: The MODIS Aerosol Algorithm, Products, and Validation, J. Atmos. Sci., 62, 947–973, doi:10.1175/JAS3385.1, 2005.

Roeckner, E., Bäuml, G., Bonaventura, L., Brokopf, R., Esch, M., Giorgetta, M., Hagemann, S., Kirchner, I., Kornblueh, L., Manzini, E., Rhodin, A., Schlese, U., Schulzweida, U., and Tompkins, A.: The atmospheric general circulation model ECHAM5: Part I: Model description, report No. 349, Max Planck Institute for Meteorology, Hamburg, 127 pp., http://www.mpimet.mpg.de/fileadmin/publikationen/Reports/max_scirep_34
[Accessed 15th June 2011], 2003.

Romps, D. M. and Kuang, Z.: Overshooting convection in tropical cyclones, Geophys. Res. Lett., 36, L09 804, doi:10.1029/2009GL037396, 2009.

Rosenfeld, D.: Suppression of Rain and Snow by Urban and Industrial Air Pollution, Science, 287, 1793–1796, 2000.

Rosenfeld, D. and Lensky, I. M.: Satellite-Based Insights into Precipitation Formation Processes in Continental and Maritime Convective Clouds, B. Am. Meteorol. Soc., 79, 2457–2476, 1998.

Rosenfeld, D., Lohmann, U., Raga, G. B., O'Dowd, C. D., Kulmala, M., Fuzzi, S., Reissell, A., and Andreae, M. O.: Flood or Drought: How Do Aerosols Affect Precipitation?, Science, 321, 1309–1313, 2008.

Rotstayn, L. D. and Liu, Y.: Sensitivity of the First Indirect Aerosol Effect to an Increase of Cloud Droplet Spectral Dispersion with Droplet Number Concentration, J. Climate, 16, 3476–3481, doi:10.1175/1520-0442(2003)016⟨3476:SOTFIA⟩2.0.CO;2, 2003.

Rotstayn, L. D. and Penner, J. E.: Indirect Aerosol Forcing, Quasi Forcing, and Climate Response, J. Climate, 14, 2960–2975, doi:10.1175/1520-0442(2001)014⟨2960:IAFQFA⟩2.0.CO;2, 2001.

Sanderson, B. M., Knutti, R., Aina, T., Christensen, C., Faull, N., Frame, D. J., Ingram, W. J., Piani, C., Stainforth, D. A., Stone, D. A., and Allen, M. R.: Constraints on model response to greenhouse gas forcing and the role of subgrid-scale processes, J. Climate, 21, 2384–2400, doi:10.1175/2008JCLI1869.1, 2008a.

Sanderson, B. M., Piani, C., Ingram, W. J., Stone, D. A., and Allen, M. R.: Towards constraining climate sensitivity by linear analysis of feedback patterns in thousands of perturbed-physics GCM simulations, Clim. Dynam., 30, 175–190, doi:10.1007/s00382-007-0280-7, 2008b.

Sayer, A. M., Thomas, G. E., and Grainger, R. G.: A sea surface reflectance model for (A)ATSR, and application to aerosol retrievals, Atmos. Meas. Tech., 3, 813–838, doi:10.5194/amt-3-813-2010, URL http://www.atmos-meas-tech.net/3/813/2010/, 2010a.

Sayer, A. M., Thomas, G. E., Palmer, P. I., and Grainger, R. G.: Some implications of sampling choices on comparisons between satellite and model aerosol optical depth fields, Atmos. Chem. Phys., 10, 10 705–10 716, doi:10.5194/acp-10-10705-2010, URL http://www.atmos-chem-phys.net/10/10705/2010/, 2010b.

Sayer, A. M., Poulsen, C. A., Arnold, C., Campmany, E., Dean, S., Ewen, G. B. L., Grainger, R. G., Lawrence, B. N., Siddans, R., Thomas, G. E., and Watts, P. D.: Global retrieval of ATSR cloud parameters and evaluation (GRAPE): dataset assessment, Atmos. Chem. Phys., 11, 3913–3936, doi:10.5194/acp-11-3913-2011, URL http://www.atmos-chem-phys.net/11/3913/2011/, 2011.

Seethala, C. and Horváth, A.: Global assessment of AMSRE and MODIS cloud liquid water path retrievals in warm oceanic clouds, J. Geophys. Res., 115, D13 202, doi:10.1029/2009JD012662, 2010.

Seinfeld, J. H. and Pandis, S. N.: Atmospheric Chemistry and Physics: From Air Pollution to Climate Change, John Wiley & Sons, New York, NY, 1998.

Sheih, C. M., Johnson, S. A., and DePaul, F. T.: Case studies of aerosol size distribution and chemistry during passages of a cold and a warm front, Atmos Environ, 17, 1299–1306, doi:10.1016/0004-6981(83)90404-3, 1983.

Shindell, D. T.: Climate and ozone response to increased stratospheric water vapor, Geophys. Res. Lett., 28, 1551–1554, doi:10.1029/1999GL011197, 2001.

Smirnov, A., Holben, B. N., Eck, T. F., Dubovik, O., and Slutsker, I.: Effect of wind speed on columnar aerosol optical properties at Midway Island, J. Geophys. Res., 108, 4802, doi:10.1029/2003JD003879, 2003.

Sorooshian, A., Feingold, G., Lebsock, M. D., Jiang, H., and Stephens, G. L.: On the precipitation susceptibility of clouds to aerosol perturbations, Geophys. Res. Lett., 36, L13 803, doi:10.1029/2009GL038993, 2009.

Sorooshian, A., Feingold, G., Lebsock, M. D., Jiang, H., and Stephens, G. L.: Deconstructing the precipitation susceptibility construct: Improving methodology for aerosol-cloud precipitation studies, J. Geophys. Res., 115, D17 201, doi:10.1029/2009JD013426, 2010.

Stainforth, D., Kettleborough, J., Allen, M., Collins, M., Heaps, A., and Murphy, J.: Distributed computing for public-interest climate modeling research, Comput. Sci. Eng., 4, 82–89, doi:10.1109/5992.998644, 2002.

Stainforth, D. A., Aina, T., Christensen, C., Collins, M., Faull, N., Frame, D. J., Kettleborough, J. A., Knight, S., Martin, A., Murphy, J. M., Piani, C., Sexton, D., Smith, L. A., Spicer, R. A., Thorpe, A. J., and Allen, M. R.: Uncertainty in predictions of the climate response to rising levels of greenhouse gases, Nature, 433, 403–406, doi:10.1038/nature03301, 2005.

Stephens, G. L.: Cloud feedbacks in the climate system: A critical review, J. Climate, 18, 237–273, doi:10.1175/JCLI-3243.1, 2005.

Stier, P., Feichter, J., Kinne, S., Kloster, S., Vignati, E., Wilson, J., Ganzeveld, L., Tegen, I., Werner, M., Balkanski, Y., Schulz, M., Boucher, O., Minikin, A., and Petzold, A.: The aerosol-climate model ECHAM5-HAM, Atmos. Chem. Phys., 5, 1125–1156, doi:10.5194/acp-5-1125-2005, URL `http://www.atmos-chem-phys.net/5/1125/2005/`, 2005.

Stier, P., Seinfeld, J. H., Kinne, S., and Boucher, O.: Aerosol absorption and radiative forcing, Atmos. Chem. Phys., 7, 5237–5261, 2007.

Stone, D. A., Allen, M. R., Selten, F., Kliphuis, M., and Stott, P. A.: The detection and attribution of climate change using an ensemble of opportunity, J. Climate, 20, 504–516, doi:10.1175/JCLI3966.1, 2007.

Stubenrauch, C. J., Cros, S., Lamquin, N., Armante, R., Chedin, A., Crevoisier, C., and Scott, N. A.: Cloud properties from Atmospheric Infrared Sounder and evaluation with Cloud-Aerosol Lidar and Infrared Pathfinder Satellite Observations, J. Geophys. Res., 113, D00A10, doi:10.1029/2008JD009928, 2008.

Su, W., Schuster, G. L., Loeb, N. G., Rogers, R. R., Ferrare, R. A., Hostetler, C. A., Hair, J. W., and Obland, M. D.: Aerosol and cloud interaction observed from high spectral resolution lidar data, J. Geophys. Res., 113, D24 202, doi:10.1029/2008JD010588, 2008.

Sundqvist, H., Berge, E., and Kristjánsson, J. E.: Condensation and Cloud Parameterization Studies with a Mesoscale Numerical Weather Prediction Model, Mon. Weather Rev., 117, 1641–1657, doi:10.1175/1520-0493(1989)117⟨1641:CACPSW⟩2.0.CO;2, 1989.

Suzuki, K., Nakajima, T., Satoh, M., Tomita, H., Takemura, T., Nakajima, T. Y., and Stephens, G. L.: Global cloud-system-resolving simulation of aerosol effect on warm clouds, Geophys. Res. Lett., 35, doi:10.1029/2008GL035449, 2008.

Thomas, G. E., Carboni, E., Sayer, A. M., Poulson, C. A., Siddans, R., and Grainger, R. G.: Oxford-RAL Aerosol and Cloud (ORAC): aerosol retrievals from satellite radiometers, in: Satellite Aerosol Remote Sensing Over Land, edited by Kokhanovsky, A. A. and G. de Leeuw, Springer, 2009.

Tompkins, A. M.: A prognostic parameterization for the subgrid-scale variability of water vapor and clouds in large-scale models and its use to diagnose cloud cover, J. Atmos. Sci., 59, 1917–1942, doi:10.1175/1520-0469(2002)059⟨1917:APPFTS⟩2.0.CO;2, 2002.

Twohy, C. H., Petters, M. D., Snider, J. R., Stevens, B., Tahnk, W., Wetzel, M. andRussell, L., and Burne, F.: Evaluation of the aerosol indirect effect in marine stratocumulus clouds: Droplet number, size, liquid water path, and radiative impact, J. Geophys. Res., 110, D08 203, doi:10.1029/2004JD005116, 2005.

Twohy, C. H., Coakley Jr., J. A., and Tahnk, W. R.: Effect of changes in relative humidity on aerosol scattering near clouds, J. Geophys. Res., 114, D05 205, doi:10.1029/2008JD010991, 2009.

Twomey, S.: Pollution and the Planetary Albedo, Atmos Environ, 8, 1251–1256, 1974.

Twomey, S.: The Influence of Pollution on the Shortwave Albedo of Clouds, J. Atmos. Sci., 34, 1149–1152, 1977.

Université Lille 1: ICARE: Cloud-Aerosol-Water-Radiation Interactions, http://www.icare.univ-lille1.fr/ [Accessed 22nd August 2009], 2009.

University of Oxford: GRAPE: Global Retrieval of ATSR Cloud Parameters and Evaluation, http://www.atm.ox.ac.uk/project/grape/index.html [Accessed 21st August 2009], 2009a.

University of Oxford: Oxford-RAL Retrieval of Aerosol and Cloud (ORAC), http://www.atm.ox.ac.uk/project/ORAC/index.html [Accessed 21st August 2009], 2009b.

Vant-Hull, B., Marshak, A., Remer, L. A., and Li, Z. Q.: The effects of scattering angle and cumulus cloud geometry on satellite retrievals of cloud droplet effective radius, IEEE T. Geosci. Remote, 45, 1039–1045, doi:10.1109/TGRS.2006.890416, 2007.

Várnai, T. and Marshak, A.: Observations of Three-Dimensional Radiative Effects that Influence MODIS Cloud Optical Thickness Retrievals, J. Atmos. Sci., 59, 1607–1618, doi:10.1175/1520-0469(2002)059⟨1607:OOTDRE⟩2.0.CO;2, 2002.

Várnai, T. and Marshak, A.: MODIS observations of enhanced clear sky reflectance near clouds, Geophys. Res. Lett., 36, L06 807, doi:10.1029/2008GL037089, 2009.

Wang, C.: Impact of direct radiative forcing of black carbon aerosols on tropical convective precipitation, Geophys. Res. Lett., 34, L05 709, doi:10.1029/2006GL028416, 2007.

Wang, C., Kim, D., Ekman, A. M. L., Barth, M. C., and Rasch, P. J.: Impact of anthropogenic aerosols on Indian summer monsoon, Geophys. Res. Lett., 36, L21 704, doi:10.1029/2009GL040114, 2009.

Wang, C.-C. and Rogers, J. C.: A Composite Study of Explosive Cyclogenesis in Different Sectors of the North Atlantic. Part I: Cyclone Structure and Evolution, Mon. Weather Rev., 129, 1481–1499, 2001.

Waquet, F., Riedi, J., Labonnote, L. C., Goloub, P., Cairns, B., Deuzé, J.-L., and Tanré, D.: Aerosol Remote Sensing over Clouds Using A-Train Observations, J. Atmos. Sci., 66, 2468–2480, doi:10.1175/2009JAS3026.1, 2009.

Winker, D. M., Hunt, W. H., and McGill, M. J.: Initial performance assessment of CALIOP, Geophys. Res. Lett., 34, L19 803, doi:10.1029/2007GL030135, 2007.

Wood, R. and Hartmann, D. L.: Spatial Variability of Liquid Water Path in Marine Low Cloud: The Importance of Mesoscale Cellular Convection, J. Climate, 19, 1748–1764, doi:10.1175/JCLI3702.1, 2006.

Wood, R., Mecheso, C. R., Bretherton, C. S., Huebert, B., and Weller, R.: The VAMOS Ocean-Cloud-Atmosphere-Land Study (VOCALS), U.S. CLIVAR Variations, 5, 2007.

Woodcock, A. H.: Salt nuclei in marine air as a function of altitude and wind force, J. Meteor., 10, 362–371, 1953.

Wu, D. L., Ackerman, S. A., Davies, R., Diner, D. J., Garay, M. J., Kahn, B. H., Maddux, B. C., Moroney, C. M., Stephens, G. L., Veefkind, J. P., and Vaughan, M. A.: Vertical distributions and relationships of cloud occurrence frequency as observed by MISR, AIRS, MODIS, OMI, CALIPSO, and CloudSat, Geophys. Res. Lett., 36, L09 821, doi:10.1029/2009GL037464, 2009.

Yuan, T., Remer, L. A., Pickering, K. E., and Yu, H.: Observational evidence of aerosol enhancement of lightning activity and convective invigoration, Geophys. Res. Lett., 38, L04 701, doi:10.1029/2010GL046052, 2011a.

Yuan, T., Remer, L. A., and Yu, H.: Microphysical, macrophysical and radiative signatures of volcanic aerosols in trade wind cumulus observed by the A-Train, Atmos. Chem. Phys., 11, 7119–7132, doi:10.5194/acp-11-7119-2011, URL `http://www.atmos-chem-phys.net/11/7119/2011/`, 2011b.

Zinner, T., Wind, G., Platnick, S., and Ackerman, A. S.: Testing remote sensing on artificial observations: impact of drizzle and 3-D cloud structure on effective radius retrievals, Atmos. Chem. Phys., 10, 9535–9549, doi:10.5194/acp-10-9535-2010, URL `http://www.atmos-chem-phys.net/10/9535/2010/`, 2010.

Zuidema, P., Westwater, E. R., Fairall, C., and Hazen, D.: Ship-based liquid water path estimates in marine stratocumulus, J. Geophys. Res., 110, D20 206, doi:10.1029/2005JD005833, 2005.

Appendix A

Introduction

A.0.1 Adiabatic liquid cloud droplet number concentration

This appendix complements Chapter 1. A simplified derivation of Equation 1.7 is provided below. Constants, which have mostly been omitted from this derivation, can be found in Brenguier et al. (2000) and Quaas et al. (2006). A discussion of the assumptions is provided in Section 1.2.5.

Following Brenguier et al. (2000), the liquid water content in an adiabatically rising parcel increases linearly with height above cloud base (h). If the liquid cloud droplet number concentration (N_d) is constant, then the total volume (V_{tot}) of the droplets will also increase linearly with h:

$$V_{tot}(h) \propto h. \tag{A.1}$$

This volume growth is distributed among the droplets, causing the mean volume radius (r_v) to increase:

$$r_v(h) = \left(\frac{\int_0^\infty r^3\, n(r)\, \mathrm{d}r}{N_d} \right)^{\frac{1}{3}} \propto h^{\frac{1}{3}}\, N_d^{-\frac{1}{3}}. \tag{A.2}$$

In order to find an expression for liquid cloud droplet effective radius (r_e), it is assumed that $r_e = \beta\, r_v$, with the constant of proportionality (β) being calculated from in situ measurements (Martin et al., 1994). Hence,

$$r_e(h) \propto \beta\, h^{\frac{1}{3}}\, N_d^{-\frac{1}{3}}. \tag{A.3}$$

At the top of the cloud, r_e will be given by

$$r_e(H) \propto \beta\, H^{\frac{1}{3}}\, N_d^{-\frac{1}{3}}. \tag{A.4}$$

Extinction (k_{ext}) of short-wave radiation is proportional to the droplet surface area (Hansen and Travis, 1974):

$$k_{ext} \propto r_s^2 \, N_d \tag{A.5}$$

where r_s is the mean surface radius,

$$r_s = \left(\frac{\int_0^\infty r^2 \, n(r) \, \mathrm{d}r}{N_d} \right)^{\frac{1}{2}}. \tag{A.6}$$

From Equation 1.4, it can be seen that

$$r_e = \frac{r_v^3}{r_s^2}. \tag{A.7}$$

Hence, using Equations A.2 and A.3,

$$r_s(h) \propto \beta^{\frac{1}{2}} \, h^{\frac{1}{3}} \, N_d^{-\frac{1}{3}}. \tag{A.8}$$

Therefore, substituting into Equation A.5,

$$k_{ext}(h) \propto \beta \, h^{\frac{2}{3}} \, N_d^{\frac{1}{3}}. \tag{A.9}$$

The cloud optical depth (τ_c) can be found by integrating this over the depth of the cloud:

$$\tau_c = \int_0^H k_{ext}(h) \, \mathrm{d}h \propto \int_0^H \beta \, h^{\frac{2}{3}} \, N_d^{\frac{1}{3}} \, \mathrm{d}h \propto \beta \, H^{\frac{5}{3}} \, N_d^{-\frac{1}{3}}. \tag{A.10}$$

Eliminating H in Equations A.4 and A.10 gives the adiabatic approximation for N_d in terms of cloud-top r_e and τ_c:

$$N_d \propto \beta^2 \, {\tau_c}^{\frac{1}{2}} \, {r_e}^{-\frac{5}{2}}. \tag{A.11}$$

From the first assumption that liquid water content increases linearly with h, the liquid water path (w) can be found by integrating over the depth:

$$w \propto \int_0^H h \, \mathrm{d}h \propto H^2. \tag{A.12}$$

Substituting this into Equation A.4, adiabatic N_d can then be written in terms of cloud top r_e and w:

$$N_d \propto \beta^3 \, w^{\frac{1}{2}} \, {r_e}^{-3}. \tag{A.13}$$

Appendix B

A critical look at spatial scale choices in aerosol indirect effect studies

When calculating the sensitivities shown in Section 2.2, no single-layer-only cloud constraint was applied, a decision which has the potential to impact the results. The decision to use one-sigma error weighting also has the potential to impact the results through the introduction of a sampling bias. When calculating errors, it was assumed that data for different grid boxes and days are independent. The discussion below briefly discusses the implications of these three decisions, focusing on the N_d sensitivities. It is found that the N_d results are relatively robust with respect to these decisions. It is likely that the same would apply to the r_e results.

B.0.2 The effect of not applying a single-layer cloud constraint

The N_d and r_e results presented in Section 2.2 and the first row of Figure B.1 are for all liquid clouds (i.e. no single-layer cloud constraint has been applied). For comparison, the annual mean $60^\circ \times 60^\circ$ N_d sensitivities shown in the second row of Figure B.1 use N_d values calculated from the single-layer cloud histogram. As can be seen by comparison of the first and second rows, although some of the details may change, the application of a single-layer constraint does not appear to have a significant effect here. In particular, the general global picture of $b_{N_d}|_{\mathrm{R}} - b_{N_d}|_{\mathrm{G}}$ changes little.

B.0.3 The effect of one-sigma error weighting

Weighting by the one-sigma error when calculating $b_{N_d}|_{\mathrm{G}}$ for regions larger than $1^\circ \times 1^\circ$ and multi-season means of both $b_{N_d}|_{\mathrm{G}}$ and $b_{N_d}|_{\mathrm{R}}$ has the potential to introduce a bias towards regions and seasons with a low one-sigma error. In order to demonstrate that this potential problem does not appear to be the major contributor to the region and grid method differences discussed in this thesis, the third row of Figure B.1 shows annual mean $60^\circ \times 60^\circ$ N_d sensitivities calculated with no error weighting. As can be seen by comparison of the first and third rows of Figure B.1, the overall global picture remains similar.

B.0.4 The assumption of data independence

When calculating errors for the insignifance masks, it was assumed that data for different grid boxes and days are independent. This assumption may not be valid, because cloud and aerosol properties may often have significant autocorrelations at spatial scales greater than one degree and temporal scales longer than one day (e.g. Anderson et al., 2003). Due to this assumption of independence, the one-sigma errors calculated in this study may be too small.

In order to test the robustness of some of the results presented in Section 2.2 to the possibility of data dependence, let us consider a situation where only $\frac{1}{25}$ of our data may be truly independent. This will result in a scaling of the independence-assumed errors by a factor of $\sqrt{25} = 5$. When testing for insignificance, a two-sigma mask on the new errors would therefore correspond to a ten-sigma mask on the old independence-assumed errors, as shown in the final row of Figure B.1. Comparison of the final rows of Figs. 2.2 and B.1 shows that the possibility of data dependence may increase the number of regions where $b_{N_d}|_{\mathrm{R}} - b_{N_d}|_{\mathrm{G}}$ is insignificant. However, $b_{N_d}|_{\mathrm{R}} - b_{N_d}|_{\mathrm{G}}$ remains significant for the majority of regions.

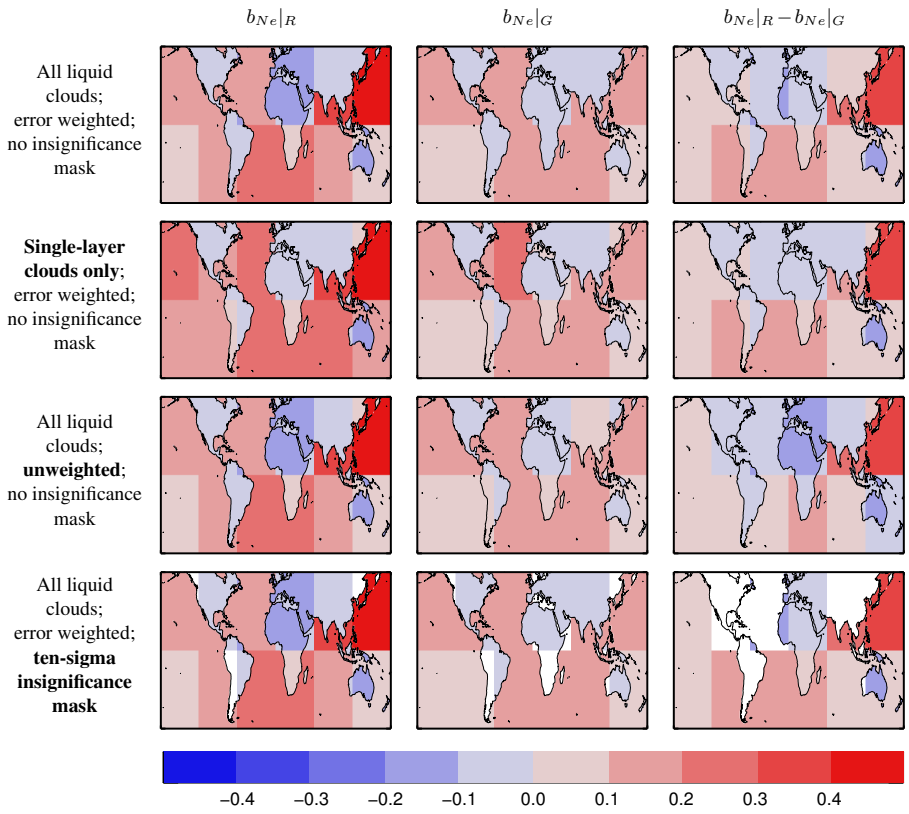

Figure B.1: Annual mean sensitivity of Terra-MODIS Collection 5 N_d to τ_a for regions of size $60^\circ \times 60^\circ$. The first column shows the results for the region-method; the second column is for the grid-method; the third column is the difference between the region-method and grid-method sensitivities. The first row shows the results for when the single-layer cloud constraint is not applied to the calculation of N_d and for when one-sigma error weighting is used to combine sensitivities for $1^\circ \times 1^\circ$ grid boxes to $60^\circ \times 60^\circ$ regions (grid-method) and sensitivities for individual seasons to annual means (both methods), like the b_{N_d} results shown in Figure 2.2; the second row shows the results for when the single-layer cloud contraint is applied to the calculation of N_d; the third row shows the results for when error weighting is not used; the fourth row shows the results for when a ten-sigma insignifcance mask is applied. No insignificance mask has been applied to the first three rows.

Appendix C

The effect of extratropical cyclones on column aerosol properties over ocean

The figures in this appendix supplement the results and discussion of Chapter 5.

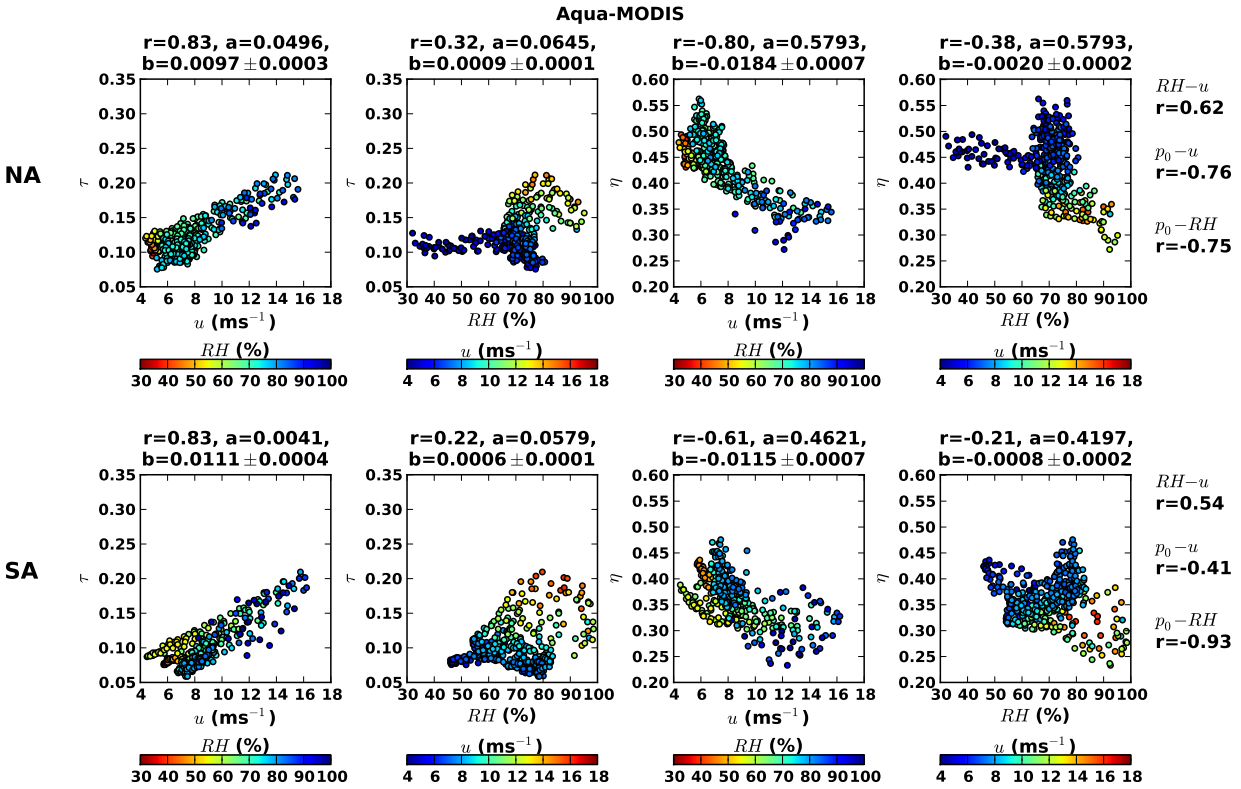

Figure C.1: Scatter plots of storm-centric composited Aqua-MODIS aerosol optical depth (τ) and fine-mode fraction (η) against wind speed (u) and relative humidity (RH) for the North Atlantic and South Atlantic oceans. Pattern correlation coefficients (r), linear regression slopes (b) and intercepts are provided above each scatter plot. Pattern correlation coefficients between u, RH and mean sea level pressure (p_0) are provided at the right-hand side.

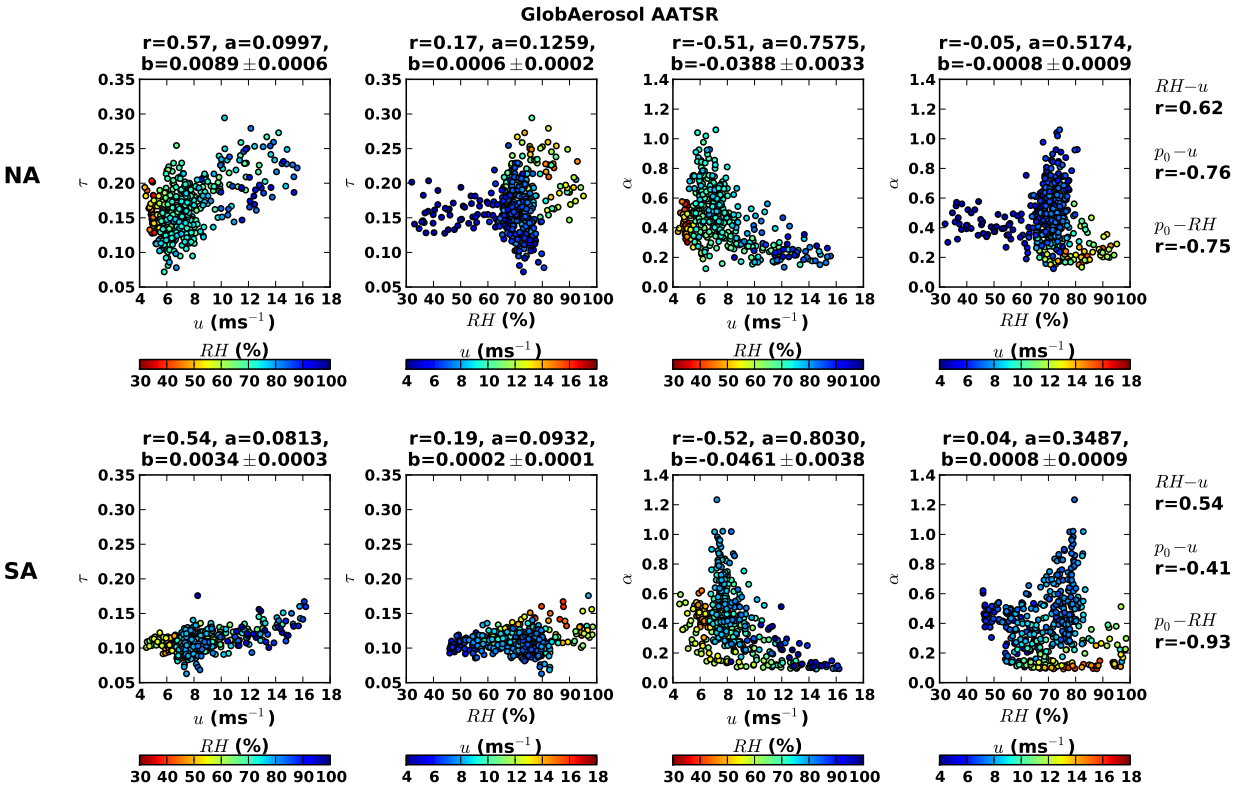

Figure C.2: Similar to Figure C.1, but for GlobAEROSOL AATSR aerosol optical depth (τ) and Ångström exponent (α).

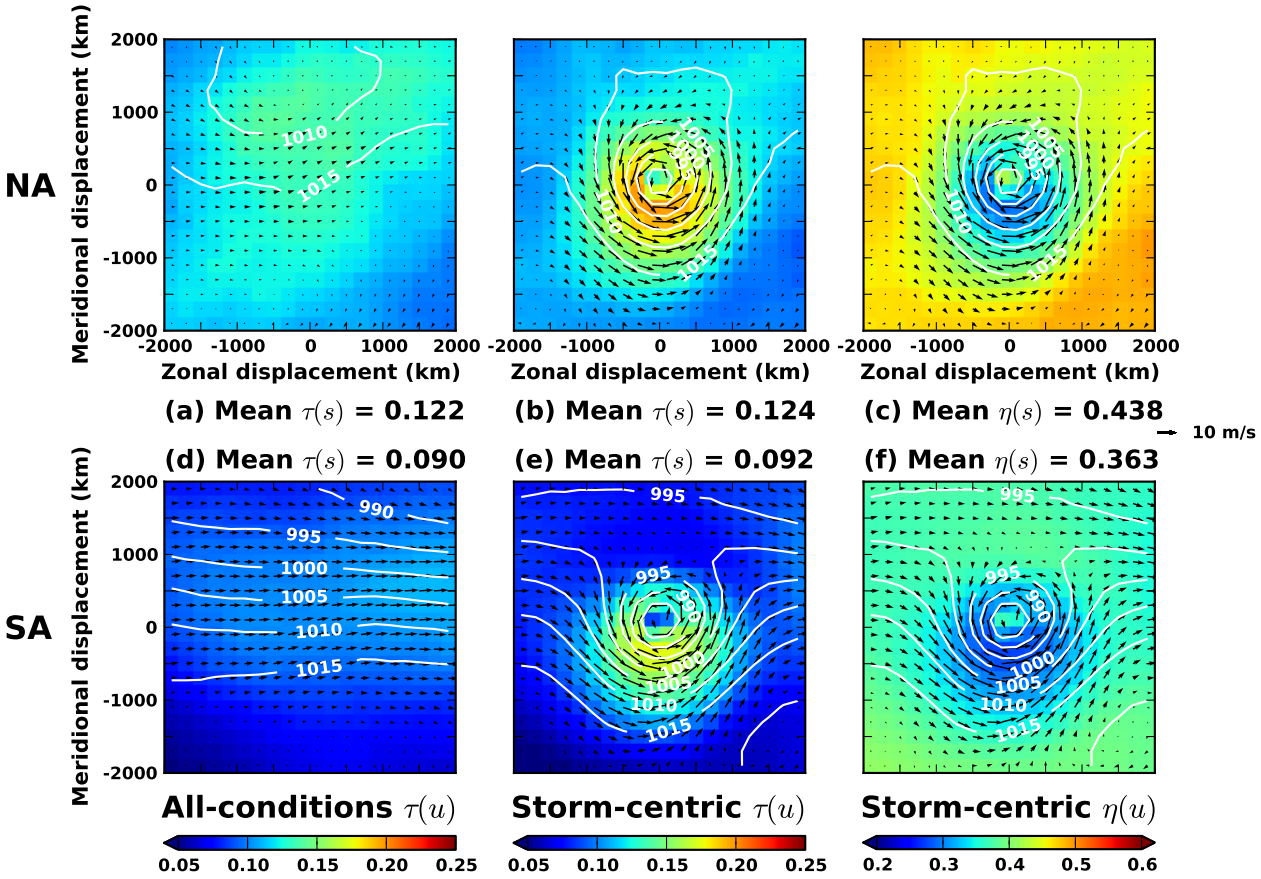

Figure C.3: Wind speed (u) fitted linear model of predicted aerosol optical depth (τ) and fine-mode fraction (η) based on the coefficients in Table 5.1 for Aqua-MODIS.

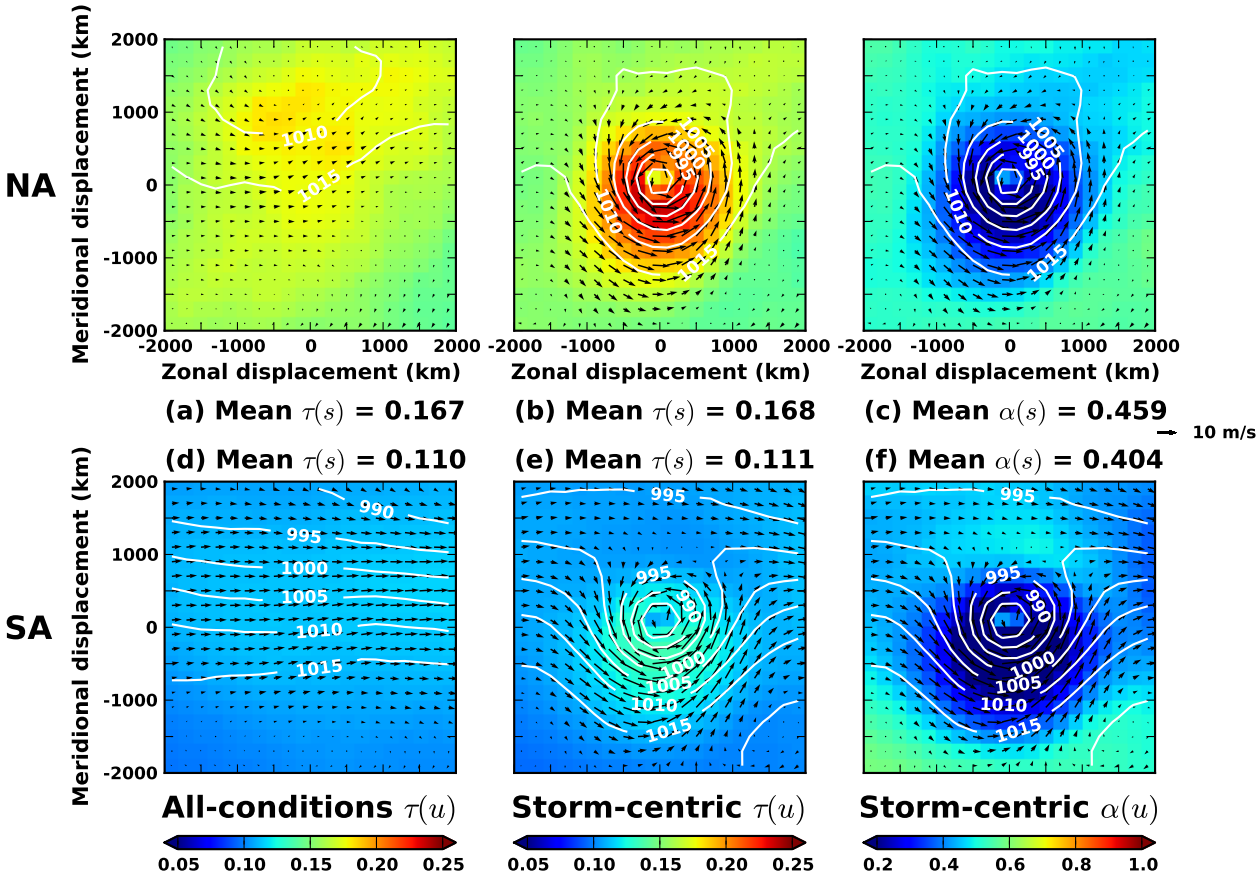

Figure C.4: Similar to Figure C.3, but for predicted aerosol optical depth (τ) and Ångström exponent (α) for GlobAerosol AATSR.

Appendix D

The contribution of extratropical cyclones to observed aerosol–cloud relationships

The figures in this appendix supplement the results and discussion of Chapter 6.

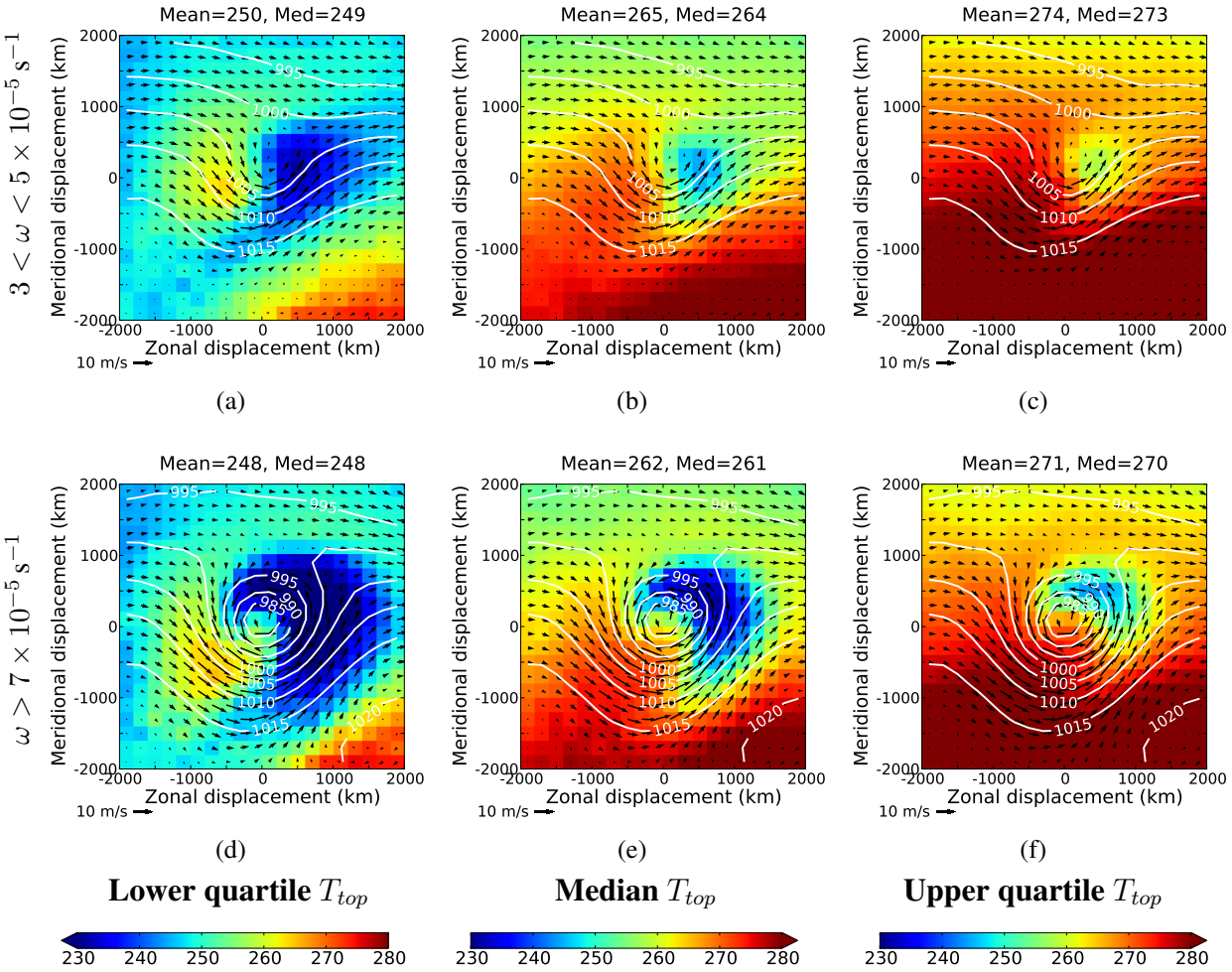

Figure D.1: Same as Figure 6.1, but for Aqua-MODIS cloud top temperature (T_{top}, K) over the South Atlantic ocean.

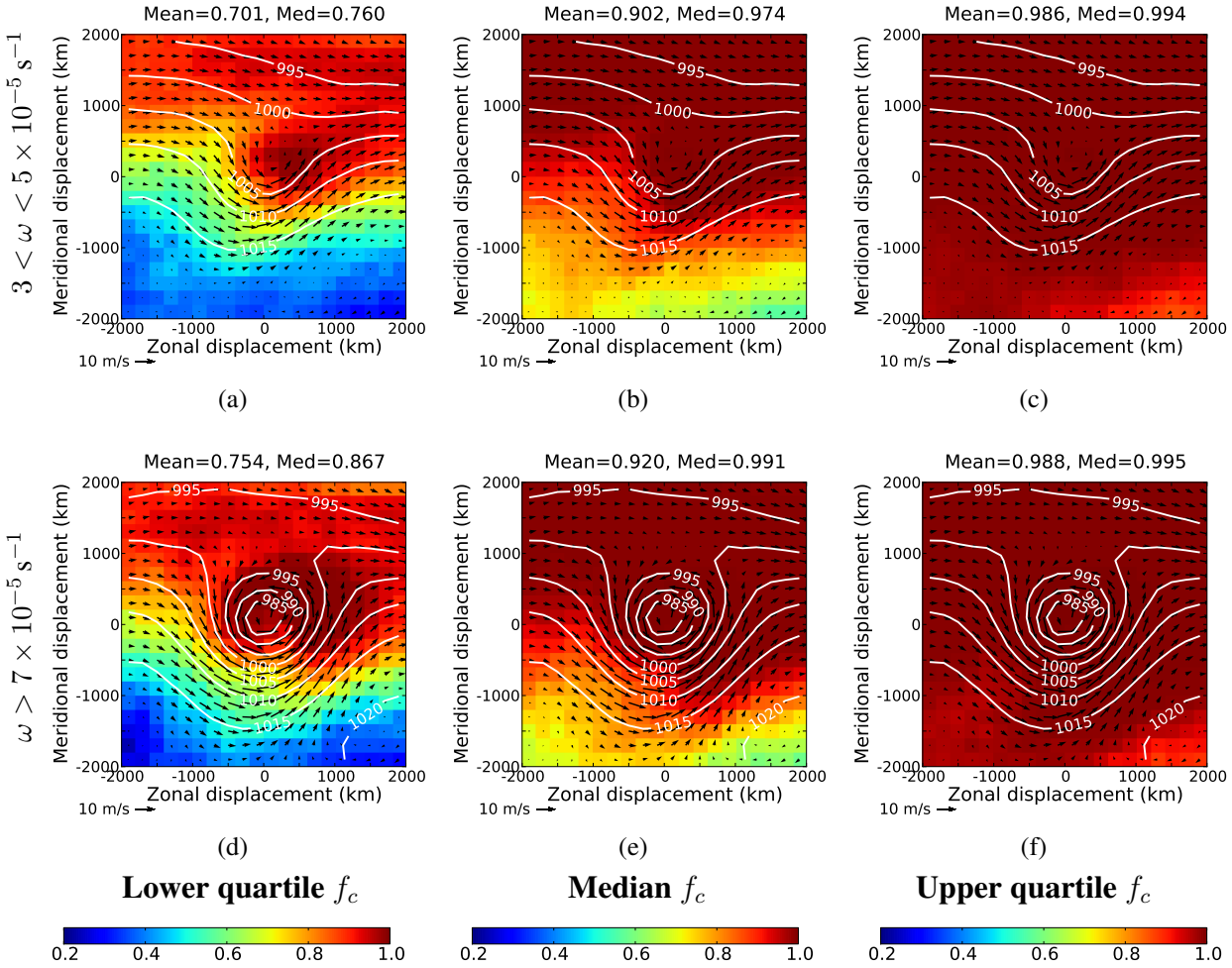

Figure D.2: Same as Figure 6.1, but for Aqua-MODIS cloud fraction (f_c) over the South Atlantic ocean.